Resilient Behavior and Permanent Deformations of Triaxial Geogrid Stabilized Bases over Weak Subgrade

By

Xiaohui Sun

Submitted to the graduate degree program in Civil, Environmental, and Architectural Engineering and the Graduate Faculty of the University of Kansas in partial fulfillment of the requirements for degree of Doctor of Philosophy

Dr. Jie Han, Chairperson

Dr. Masoud Darabi

Dr. Anil Misra

Dr. Robert L. Parsons

Dr. Hongguo Xu

Date defended: 05/14/2015

The dissertation Committee for Xiaohui Sun certifies that this is the approved version of the following dissertation:

Resilient Behavior and Permanent Deformations of Triaxial Geogrid Stabilized Bases over Weak Subgrade

Chairperson: Prof. Jie Han

Date approved:

Abstract

Geogrid has been playing an important role in solving geotechnical problems such as paved/unpaved roads constructed on weak subgrade. Geogrid provides lateral confinement to resist the lateral movement of aggregates by the interlocking action that occurs between geogrid apertures and surrounding aggregates. The inclusion of geogrid influences the resilient behavior of stabilized bases and benefits the stabilized bases by reducing permanent deformations (i.e. rutting). However, the resilient behavior and the accumulation mechanism of permanent deformations have not been well understood.

In this study, cyclic and static plate loading tests were conducted on test sections of geogrid stabilized bases over subgrade under various loading intensities. The test sections were constructed in a geotechnical box with dimensions of 2 m (W) × 2.2 m (L) × 2 m (H) at the University of Kansas. The vertical and horizontal pressures along the interface were monitored by earth pressure cells with varying distances away from the centerline of test sections. Permanent and resilient deformations were monitored by LVDTs installed at 0, 0.25, 0.5, and 0.75 m away from the center. The results show that both the vertical and horizontal stresses were redistributed due to the inclusion of geogrids. Vertical stresses were distributed to a wider area, while horizontal stresses were confined to a smaller area close to the loading plate. The presence of geogrids reduced permanent deformations but increased resilient deformations.

An analytical solution of the geogrid-stabilized layered elastic system was derived to evaluate the change of earth pressures induced by the inclusion of geogrids. Confinement effect and tensioned membrane effect were treated as external stresses

applied at the interface. The base course was treated as transversely-isotropic to capture the modulus degradation at the horizontal direction. Results show that vertical stresses at the interface decreased and horizontal stresses along the centerline increased due to the inclusion of geogrids. The geogrid stabilized sections had higher lateral earth pressure coefficients along the centerline.

A simple hypoplastic model was adopted to simulate the resilient behavior of stabilized soils (i.e. with higher lateral earth pressure coefficients). The results show that the soil sample under a stabilized condition had a higher resilient deformation under unloading as compared with that under an unstabilized condition. The confinement and tensioned membrane effect due to the inclusion of geogrids reduced the permanent deformations not only at the loading stage, but also at the unloading stage.

Acknowledgement

First of all, I would like to express my sincerest gratitude to my advisor, Prof. Jie Han, for his guidance, patience, support, and encouragement through my study at the University of Kansas. His knowledge, wisdom, and diligence impressed and influenced me significantly. He always tried his best to help me to develop my advantages, overcome my weaknesses, and prepare for my future career. The time of my study under the guidance of Prof. Han was short, but valuable, enjoyable and memorable.

I would like to thank my Ph.D. committee members, Profs. Masoud Darabi, Anil Misra, Robert L. Parsons, Hongguo Xu, and Yaozhong Hu for their valuable advices and also for serving as members of my graduate advisory committee.

This study was jointly funded by Tensar International and Kansas Department of Transportation. Dr. Mark Wayne and Dr. Jayhyun Kwon from Tensar provided great support and valuable advices during the study.

I am indebted to all the members of KUGS (Kansas University Geotechnical Society) for their great cooperation, advices, and help during the entire process of this study. Dr. Jitendra Thakur taught me the whole test procedures step by step. My lab assistant, Mr. Lee Crippen, helped me to construct most of the test sections. Mr. Matthew Maksimowiczat (laboratory manager) provided great technical support. Most of members in KUGS provided generous support during the construction of the roadway sections, who were Jun Guo, Fei Wang, Yan Jiang, Deep Khatri, Dan Chang, Meixiang Gu, Dr. Jingshan Jiang (visiting scholar from China), Dr. Zhen Zhang (visiting scholar from China), Dr.

Zhigang Cao (visiting scholar from China), and Dr. Hongguang Jiang (visiting scholar from China). Their support is greatly appreciated.

Finally, the gratitude is extended to my family for their support and encouragement throughout my study. During my Ph.D. study, I do not have too much time to get together with my wife. Her understanding is the most important driving for me to finish my study on time.

Table of Contents

List of Figures

List of Tables

Chapter 1. Introduction

1.1 Historical developments of roadways

Roadways have been constructed since ancient times. For example, stone-paved streets are found in the city of Ur in the Middle East dating back to 4000 BC and brick-paved streets were used in India as early as 3000 BC (Lay, 1992). More than 2000 years ago, Chinese people in Qin Dynasty constructed roadways over the country from its capital city. In 312 BC, the Roman Empire built stone Roman roads throughout Europe and North Africa (Hart-Davis, 2007). In 1879, Scotland constructed a Portland cement concrete road (Pasko, 1998), which may be considered as the first concrete road in the world. The first asphalt roadway in the United States was constructed in 1870 at Newark, New Jersey (Huang, 1993) and the first concrete pavement in US was built in Bellefontaine, Ohio in 1893 (Delatte, 2014). Prior to the early 1920s, the thickness of pavement was designed based purely on experience and the empiricism still plays a significant role in the current pavement design even though the current design method has gradually evolved from art to science (Huang, 1993).

1.2 Paved/unpaved roads

Roadways can be categorized as paved and unpaved. **Figure 1.1** shows the typical views of paved and unpaved roads and **Figure 1.2** demonstrates their typical cross-sections. Paved road has a surface layer of asphalt concrete or Portland cement concrete which can provide more structural strength. Therefore, the paved road can bear a heavier traffic volume. Unpaved road typically has an aggregate base course layer serving as

the surface layer. As compared with the asphalt concrete or Portland cement concrete, the aggregate base course is much weaker and, therefore, the unpaved roads are usually designed for low-volume roads. Even though the hierarchy of unpaved roads is relatively low, the majority of the road in the world are unpaved and low-volume (Tingle and Jersey, 2007).

(a) paved road (b) unpaved road

Figure 1.1 The view of paved and unpaved roads

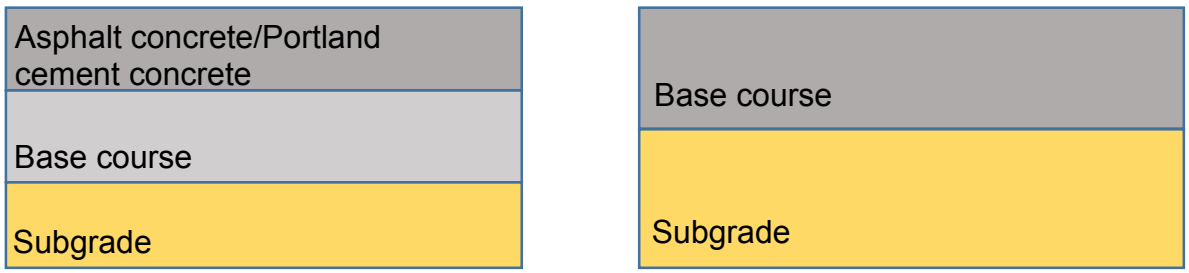

(a) paved road (b) unpaved road

Figure 1.2 The typical cross-sections of paved and unpaved roads

1.3 Geosynthetics stabilized unpaved roads

Geosynthetics, manufactured from polymeric materials, have been used for subgrade stabilization and base course reinforcement for the construction of unpaved structures since the 1970s (Giroud and Han, 2004a) and have been playing an important role in solving geotechnical problems (Qian et al., 2013; Wang et al., 2014). Geotextiles and geogrids are the two typical types of geosynthetics used in unpaved structures. The materials used to manufacture geogrid include polypropylene, high density polypropylene, and high-tenacity polyester. Geogrid can be a uniaxial, biaxial, or triaxial regular network of integrally connected tensile elements. **Figure 1.3** shows the three types of geogrid. In this study, the performance of the triaxial geogrid was studied.

(a) Uniaxial geogrid (b) Biaxial geogird (c) Triaxial geogrid

Figure 1.3 Geogrids with different shapes of apertures

Uniaxial geogrid can carry high tensile loads applied in one direction and mainly used for retaining walls, slopes, and embankments. Both biaxial and triaxial geogrid are appropriate for construction platforms, waste containment capping, paved and unpaved

roadways and railways. Geogrid can be placed within a base course or at the interface of base and subgrade to improve the subgrade and stabilize the base course. Geogrid provides lateral confinement to base course aggregates and resists the lateral movement of aggregate by the interlocking action that occurs between its apertures and surrounding aggregate (Giroud and Han, 2004a, 2004b). **Figure 1.4** illustrates this interlocking action.

Figure 1.4 Illustration of the interlocking between geogrid apertures and aggregates

1.4 Problem statement

Geogrid provides lateral confinement to base aggregates and resists the lateral movement of aggregates by the interlocking action that occurs between geogrid apertures and surrounding aggregates. The inclusion of geogrids influences the resilient behavior of roadways and benefits roadways by reducing permanent deformations (i.e. rutting). However, the resilient behavior and the accumulation of permanent deformations of geogrid stabilized bases have not been well understood.

1.5 Research objectives and scope

The objectives of this study are to investigate the resilient behavior and the accumulation of permanent deformations of geogrid-stabilized base courses over subgrade. Experimental study, elastic analysis, and hypoplastic model were the three major tools of this study. In this study,

(1) Cyclic/static plate load tests on geogrid stabilized base courses over subgrade were conducted to investigate stress distributions, permanent deformations, and resilient deformations with the inclusion of geogrids. Cyclic loading with various intensities was applied to simulate the real traffic loading.

(2) An analytical solution of the geogrid-stabilized layered elastic system was derived. In the derivation, the interface between geogrids and soils were considered as fully bonded. Confinement effect and tensioned membrane effect were treated as external stresses applied at the interface of the layered elastic system. The deformed shape of geogrids was assumed as a curve described by the Gauss function. The change of vertical and horizontal stresses induced by geogrids was evaluated based on the elastic solution.

(3) A hypoplastic model was adopted to simulate the resilient behavior of soils under the stabilization of geogrids.

1.6 Organization of this dissertation

This dissertation comprises of six chapters and one appendix. Following this chapter, a literature review of the previous studies is presented in Chapter two. Chapter three describes the laboratory tests conducted to investigate the performance of geogrid stabilized bases over subgrade. In Chapter four, the resilient behavior of stabilized soils

simulated by a hypoplastic model is presented. Chapter five describes the comparison of predicted and measured performance of test sections. Chapter six summarizes the conclusion drawn in this study and the recommendation proposed for further studies. Appendix A presents the derivation of the geogrid-stabilized transversely-isotropic layered elastic system.

Chapter 2. Literature Review

This chapter provides a literature review of geosynthetic-stabilized unpaved roads, including: mechanisms of geosynthetics in stabilizing paved/unpaved roads, laboratory/field evaluation of geosynthetic-stabilized unpaved roads, layered elastic system, tensioned membrane effect of geosynthetics, constitutive models for granular materials, soil damage model, and design methods of unpaved roads.

2.1 Mechanisms of geosynthetics in stabilizing paved/unpaved roads

Previous studies (Giroud and Noiray, 1981; Perkins and Ismeik, 1997) summarized three potential functions of geosynthetics as: lateral restraint, increased bearing capacity, and tensioned membrane effect. Figure 2.1 shows the primary functions of geogrids in stabilizing unpaved roads.

The confinement of geogrids results in a stiffer base course and a lower dynamic deflection of the pavement/roadbed structure during traffic loading (Giroud and Han, 2004a, 2004b). Geogrid changes the interface condition between weak subgrade and aggregate base. This phenomenon enhances the bearing capacity of the subgrade (Giroud and Noiray, 1981; Giroud and Han, 2004a). When an excessive amount of deformations is accumulated under the applied traffic load, the curved and tensioned reinforcement can develop an upward force to support the load (Giroud and Noiray, 1981; Sharma et al., 2009). In addition to the above mechanisms, geogrids at the interface between aggregate base and weak subgrade prevents base aggregates from punching

into the subgrade and fines in subgrade from migrating into base courses (Tingle and Jersey, 2005).

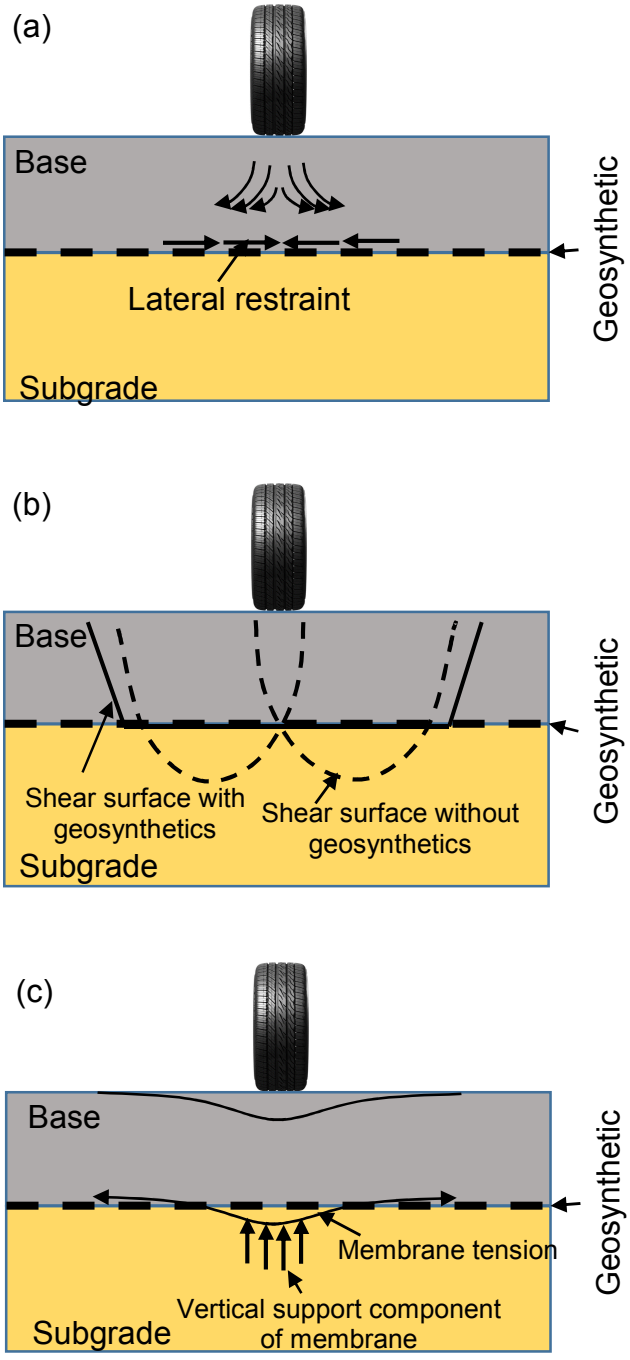

Figure 2.1 Mechanisms of geosynthetics in stabilizing paved/unpaved roads (Giroud and Noiray, 1981; Perkins and Ismeik, 1997)

2.2 Evaluation of geosynthetic-stabilized paved/unpaved roads

In the past decades, researchers have conducted many laboratory and field tests to investigate the geosynthetic-stabilized unpaved roads. The performance of geogrid-stabilized sections has been mainly evaluated in terms of an improved stress distribution and a corresponding reduction of permanent deformations. In general, 40 kN cyclic load was applied through a 300-mm diameter plate to simulate an equivalent single wheel load in a real traffic condition.

Haas et al. (1988) performed cyclic plate load tests in a 4.5 m × 1.8 m × 0.9 m box to investigate geogrid-reinforced roads. The base course thickness, subgrade strength, and location of geogrid were set as variables in the study. The surface deflection, vertical stress on the top of subgrade, and the strains in geogrids were monitored during the tests. The test results indicated that geogrid reinforcement increased the number of load cycles as compared with the unreinforced test sections. Al-Qadi et al. (1994) simulated a typical secondary road in Virginia constructed in a box with the dimensions of 3 m × 2.1 m × 1.8 m under cyclic loading applied through a steel plate with a diameter of 0.3 m. The surface deflections of road sections were monitored by LVDTs. Test results revealed that geogrid considerably reduced the deflections of the pavement sections over weak subgrade. Perkins (1999) performed plate load tests on the road sections constructed in a 2 m × 2 m × 1.5 m high box. A 40 kN cyclic load was applied on the test sections to simulate traffic load though a 0.305 m diameter steel plate. Various instruments were used to monitor the surface deformation, strains of geosynthetics, and stress in the soils. The test results revealed that the geogrid improved the performance of road sections with a subgrade CBR of 1.5% significantly. However, little improvement was observed for the

sections with a subgrade CBR of 20%. Leng and Gabr (2002) conducted cyclic plate load tests on the geogrid-reinforced aggregate over weak subgrade in a 1.5 m × 1.5 m × 1.35 m box. The cyclic load was applied through a steel plate with a diameter of 0.305 m and the contact pressure was set at 500 kPa. During the tests, surface deformations and vertical stresses at the interface were measured. The test results showed that geogrid reduced the surface deflection, improved the stress distribution, and mitigated the degradation of the aggregate base.

Tingle and Jersey (2005, 2009) evaluated the performance of geogrid reinforced aggregate roads in a full scale model test in terms of the surface deflection, subgrade deflection, and vertical stresses on the top of subgrade and found both the vertical deflection and vertical stress were reduced by geosynthetics. Chen et al. (2009) also studied the influence of the geogrid-stabilized pavements on subgrade deformation. The tests were conducted inside a test box with dimensions of 2.0×2.0×1.7 m^3 and a 40 kN cyclic load at a frequency of 0.77 Hz was applied on the test sections through a 305 mm diameter steel plate. The test results showed that the mechanically stabilized base course distributed the applied load to a wider area than the unstabilized control sections and reduced the permanent deformation of the subgrade. Indraratna et al. (2013) studied the lateral displacement response of geogrid-reinforced ballast under cyclic loading in a 0.8×0.6×0.65 m^3 box. In this study, one side-wall of which was replaced by a setup of five independent movable plates along the depth to measure the lateral displacement. The test results revealed that both the vertical and lateral deformation were influenced by the geogrid type and its placement location. The test results also demonstrated the ability of geogrid in arresting lateral displacement of ballast and reducing vertical settlement.

The resilient behavior of the geosynthetic-stabilized bases has not been well understood yet. Previous research shows some inconsistencies. Rahman et al. (2013) investigated the resilient moduli and permanent deformation characteristics of construction and demolition (C&D) materials stabilized with biaxial and triaxial geogrids. Repeated load triaxial (RLT) equipment was used to determine resilient modulus of the mechanically stabilized C&D specimens. The resilient modulus values of the geogrid-stabilized C&D materials were found to be higher than that of the respective unreinforced material. The permanent deformations of the geogrid-stabilized C&D materials were smaller than that of the respective unstabilized material. Abu-Farsakh et al. (2007) performed a series of laboratory triaxial tests and evaluate the effects of the geogrid properties, location, and number of layers on the resilient and permanent deformations of these samples under cyclic load. The test results demonstrated that neither the geogrid type nor the geogrid arrangement had a significant effect on the resilient strain values. Yang and Han (2012) proposed an analytical model to predict the resilient modulus and the permanent deformation of geosynthetic stabilized unbound granular materials under an RLT test. Both the test and the analytical results showed that the permanent strains of the geosynthetic stabilized samples were reduced significantly even though the resilient moduli of the samples slightly increased.

Load distribution acts radially at all levels within the pavement section. For geosynthetic stabilized roadways, traffic load creates a spreading motion of the aggregate, which causes tension in all directions in geosynthetics by the shear interaction between aggregate and geosynthetics (Perkins et al., 2011). When subjected to tension in all directions, triaxial geogrid exhibits more uniform stress and strain distribution over

traditional biaxial geogrids because biaxial geogrids have tensile stiffness predominantly in two directions whereas triaxial geogrids have the better ability to distribute load through 360 degrees with an additional principal direction of stiffness (Dong et al., 2011). **Figure 2.2** shows the strain distributions in ribs under 90°tension for geogrids with rectangular apertures and triangular apertures. It is clear to see that the geogrid with triangular apertures has more uniform tension in ribs. Therefore, triaxial geogrid is more effective and efficient in its ability to distribute tension and interact with granular material under traffic loading.

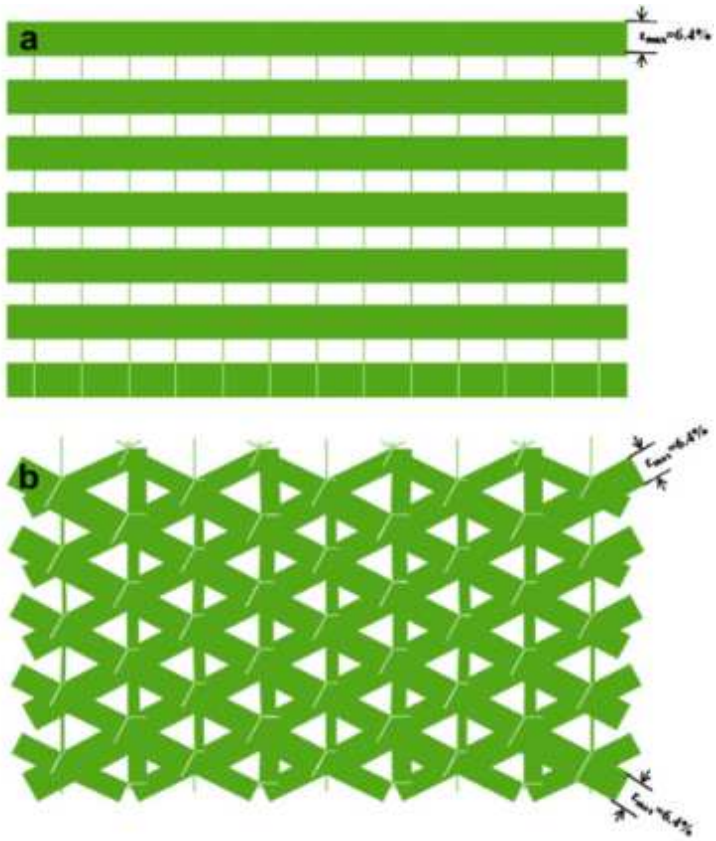

Figure 2.2 Strain distributions in ribs under 90° tension for: (a) geogrid with rectangular apertures and (b) geogrid with triangular apertures (Dong et al., 2011)

Qian et al. (2011a) investigated the triangular-aperture geogrid stabilized base courses over weak subgrade using cyclic plate load tests. The results showed that the vertical stresses at the interface between the base and the subgrade increased with the increase of the number of load cycles due to the deterioration of the base course and the inclusion of the geogrids reduced the rate of the deterioration.

In summary, the geogrid-stabilized paved/unpaved roads were investigated mainly by the cyclic plate load test under a constant maximum load magnitude and the performance of road sections was mainly evaluated in terms of the surface deflections and vertical stress distribution.

2.3 Layered elastic system

Roadways are typical layered systems. Layered elastic theory is the simplest model used to simplify the analysis of the road system. Base courses and subgrade of roads are usually assumed as linear elastic materials even though both the subgrade and base course layers exhibit non-linear stress-strain relationships. A single wheel load can be represented by a uniformly-distributed and static stress over a circular area in analysis and design.

Burmister introduced the layered elastic theory firstly, who developed an analytical solution for the two-layered system and extended it to a three-layered system in a further step (Burmister, 1945a, 1945b). Currently, the theory was extended for an arbitrary number of layers.

As pointed out by Burmister (1945b), all theories deal with ideal materials and ideal conditions. Layered elastic theory is based on the following assumptions (Wang, 2008):

The soils of each layers are homogeneous, isotropic, and linear elastic;

All layers are infinite in the horizontal direction;

All layers have constant thickness;

There are no discontinuities other than at the layer surface;

No body forces act in the system;

No initial stresses or strains are in the system; and

The applied load is distributed over a circular area.

A brief review of Burmister's solution is presented in this section. In developing the theory of the two-layer system, equations of elasticity for a three-dimensional problem in cylindrical coordinates were employed and axisymmetric condition was considered, as shown in **Figure 2.3**. **Equation 2.1** shows the equations of equilibrium of the element in **Figure 2.3**. By introducing a displacement function (the Love displacement function) and considering the general Hooke's law, the compatibility condition can be expressed as **Equation 2.2**. The stress and displacement of the element can be rewritten in terms of the displacement function, as shown in **Equation 2.3**. **Equation 2.4** shows the expression of the displacement function, which can be obtained by solving **Equation 2.2**.

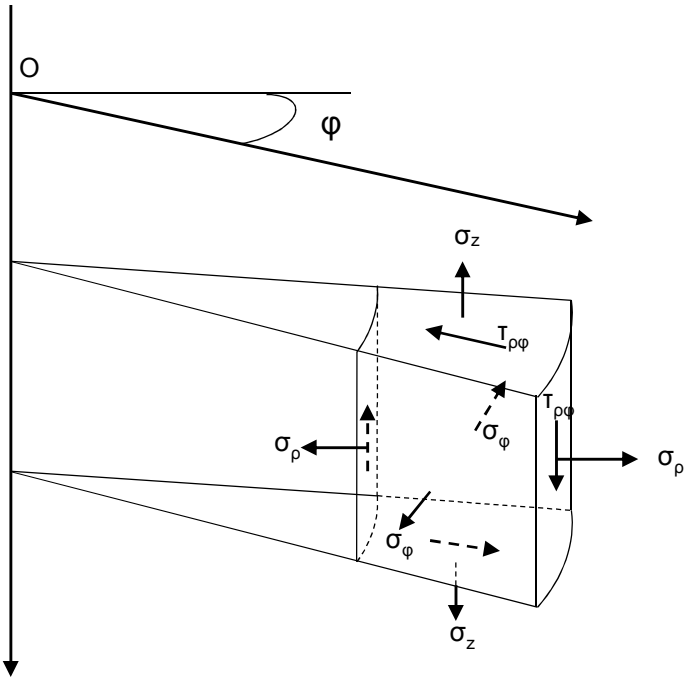

Figure 2.3 Axisymmetric coordinates

Equations of equilibrium:

$$\begin{cases} \dfrac{\partial \sigma_\rho}{\partial \rho} + \dfrac{\partial \tau_{\rho z}}{\partial Z} + \dfrac{\sigma_\rho - \sigma_\varphi}{\rho} = 0 \\ \dfrac{\partial \tau_{\rho z}}{\partial \rho} + \dfrac{\partial \sigma_z}{\partial Z} + \dfrac{\tau_{\rho z}}{\rho} = 0 \end{cases}$$

Equation 2.1

Equations of compatibility:

$$\nabla^4 \phi = \left(\frac{\partial^2}{\partial \rho^2} + \frac{1}{\rho} \frac{\partial}{\partial \rho} + \frac{\partial^2}{\partial z^2} \right)^2 \phi = 0$$

Equation 2.2

Elasticity equations of stress and displacement:

$$\begin{cases} \sigma_z = \dfrac{\partial}{\partial z}\left[(2-\mu)\nabla^2\phi - \dfrac{\partial^2\phi}{\partial z^2}\right] \\ \sigma_\rho = \dfrac{\partial}{\partial z}\left[\mu\nabla^2\phi - \dfrac{\partial^2\phi}{\partial \rho^2}\right] \\ \sigma_\varphi = \dfrac{\partial}{\partial z}\left[\mu\nabla^2\phi - \dfrac{1}{\rho}\dfrac{\partial\phi}{\partial\rho}\right] \\ \tau_{\rho z} = \dfrac{\partial}{\partial \rho}\left[(1-\mu)\nabla^2\phi - \dfrac{\partial^2\phi}{\partial z^2}\right] \\ w = \dfrac{1+\mu}{E}\left[(1-2\mu)\nabla^2\phi + \dfrac{\partial^2\phi}{\partial \rho^2} + \dfrac{1}{\rho}\dfrac{\partial\phi}{\partial\rho}\right] \\ u = -\dfrac{1+\mu}{E}\left[\dfrac{\partial^2\phi}{\partial\rho\partial z}\right] \end{cases} \qquad \textbf{Equation 2.3}$$

where ϕ is the displacement function:

$$\phi(\rho, z) = \int_0^\infty m\,(A_m e^{mz} + B_m e^{-mz} + C_m z e^{mz} + E_m z e^{-mz})\,J_0(m\rho)dm \qquad \textbf{Equation 2.4}$$

where $J_0(m\rho)$ is the zero order Bessel function. A_m, B_m, C_m, and E_m are the integral constants. Substituting the stress function into **Equation 2.3**, the stress and displacement can be obtained in terms of A_m, B_m, C_m, and E_m.

For a two-layer system as shown in **Figure 2.4**, the boundary and continuity conditions are as follows (The notation,1, represents the first layer and the notation, 2, represents the second layer).

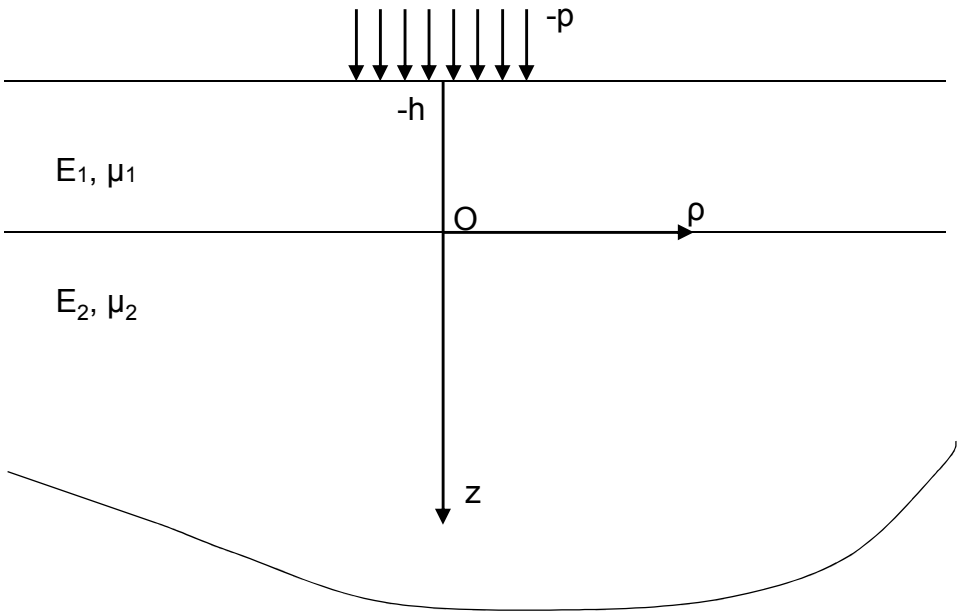

Figure 2.4 Two-layer elastic system

Boundary condition at z = -h,

Distribution of surface loading, $\sigma_z = -p$,

Shearing stress at the surface, $\tau_{\rho z} = 0$.

Continuity conditions at the interface, z = 0,

Vertical settlements must be equal, $w_1 = w_2$,

Horizontal displacements must be equal, $u_1 = u_2$,

Normal stresses, $\sigma_{z1} = \sigma_{z2}$,

Shearing stresses, $\tau_{\rho z1} = \tau_{\rho z2}$.

Boundary condition at the infinite depth,

Distribution of surface loading, $\sigma_z = 0$,

Shear stress at the surface, $\tau_{\rho z} = 0$.

Based on the boundary and continuity conditions, integral constants can be determined and therefore the solutions of the stress and displacement in the two-layer system can be obtained.

Vokas and Stoll (1987) developed an elastic model to describe the response of a layered elastic system containing one or more reinforcements based on the layered elastic system. In the analysis, the effect of reinforcement was included by specifying the interlayer continuity conditions based on the classical theory of thin plates. In this study, the continuity condition at the interface for the normal stress and shear stress was changed due to the inclusion of the reinforcement.

By applying the equilibrium equation in the radial direction of reinforcement and assuming plane stress conditions, the boundary condition of the shear stress at the interface yields

$$\frac{\partial N_\rho}{\partial \rho} + \frac{N_\rho - N_\varphi}{\rho} = \tau_{\rho z1} - \tau_{\rho z2} \qquad \textbf{Equation 2.5}$$

where N_ρ and N_φ are the forces per unit length of section within the reinforcement. Considering Hooke's law and the geometric equations, the expressions for the forces at the radial and tangential directions were derived in terms of the radial displacements at the bottom of the upper layer. **Equation 2.5** yields:

$$\frac{E_g h_g}{(1-\mu_g^2)}\left[\frac{\partial^2 u}{\partial \rho^2} + \frac{1}{\rho}\frac{\partial u}{\partial \rho} - \frac{u}{\rho^2}\right] = \tau_{\rho z1} - \tau_{\rho z2} \qquad \textbf{Equation 2.6}$$

Equation 2.7 shows the equilibrium at the vertical direction:

$$\frac{\partial N_{\rho z}}{\partial \rho} + \frac{N_{\rho z}}{\rho} = \sigma_{z1} - \sigma_{z2} \qquad \textbf{Equation 2.7}$$

Substituting the moment curvature equations in **Equation 2.7**, the equilibrium condition at the vertical direction yields:

$$\frac{E_g h_g^3}{12(1-\mu_g^2)}\left[\frac{\partial^4 w}{\partial \rho^4} + \frac{2}{\rho}\frac{\partial^3 w}{\partial \rho^3} - \frac{1}{\rho^2}\frac{\partial^2 w}{\partial \rho^2} + \frac{1}{\rho^3}\frac{\partial w}{\partial \rho}\right] = \sigma_{z1} - \sigma_{z2} \qquad \textbf{Equation 2.8}$$

With the continuity condition of the normal stress and shear stress at the interface, the reinforced layered elastic system was analyzed and the stress and displacement were calculated according to a numerical integral.

In reality, however, geosynthetics are commonly considered as membranes, which cannot bear moments in the vertical direction but tensions in the radial direction. Therefore, it is not appropriate to analyze the reinforced layered elastic system with the continuity condition described by **Equation 2.8**.

2.4 Hankel transforms of contact pressures

Hankel transforms are the basic mathematic tools to analyze the layered elastic systems in an axisymmetric coordinate system. **Equation 2.9** shows the Hankel transform of a function $\mathrm{f}(\rho)$ and **Equation 2.10** shows the inverse Hankel transform of the function.

$$\mathrm{f}(m) = \int_0^\infty \rho \mathrm{f}(\rho) J_n(m\rho) d\rho \qquad \textbf{Equation 2.9}$$

$$\mathrm{f}(\rho) = \int_0^\infty m \mathrm{f}(m) J_n(m\rho) dm \qquad \textbf{Equation 2.10}$$

where $J_n(m\rho)$ is the nth order Bessel function of the first kind.

To apply an external force to a layered elastic system, the external force needs to be transferred by the Hankel transform so that the integral constants can be determined in linear equations. The distribution of the contact pressure beneath a load plate depends on the stiffness of the load plate. **Figures 2.5** (a) and (b) show the distributions of the contact pressure beneath a rigid and flexible plate, respectively.

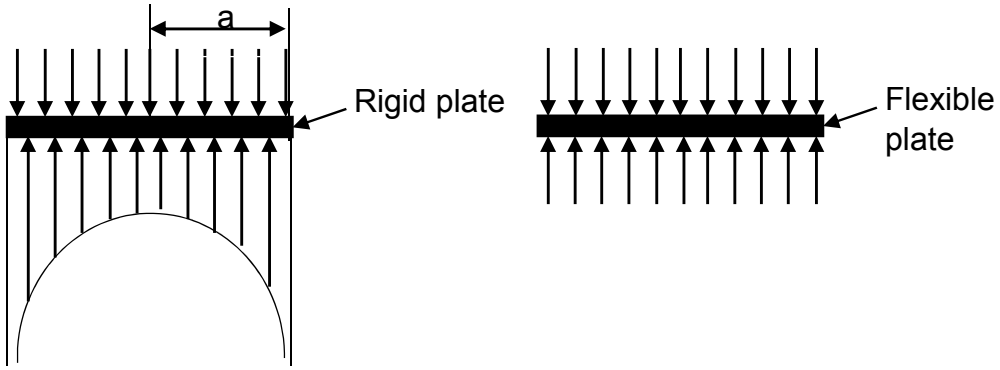

(a) (b)

Figure 2.5 Distributions of the contact pressure

As shown in **Figure 2.5 (a)**, the contact pressure under a rigid plate can be expressed as (Muki, 1960):

$$\sigma_z = \frac{p}{2\sqrt{(1-(\rho/a)^2)}} \qquad \textbf{Equation 2.11}$$

As shown in **Figure 2.5 (b)**, the contact pressure beneath a flexible plate can be expressed as:

$$\sigma_z = p \qquad \textbf{Equation 2.12}$$

The zero-order Hankel transforms of the contact pressure can be expressed as:

Under a rigid plate,

$$\sigma_z(m) = \frac{pa\sin(ma)}{2m} \qquad \textbf{Equation 2.13}$$

Under a flexible plate,

$$\sigma_z(m) = \frac{pa\,\mathrm{J}_1(ma)}{m} \qquad \textbf{Equation 2.14}$$

2.5 Transversely isotropic elasticity

In reality, the base course layer and subgrade may be transversely isotropic. During the loading process, base course can become stiffer in the vertical direction due to the vertical compression under traffic loading; however, the horizontal modulus of the base course will decrease due to the vertical shear of the traffic loading. In addition, the inclusion of the geosynthetics will amplify the characteristics of the transverse isotropy since the geosynthetics can only bear a tension force horizontally. Lekhnitskii (1981) developed the general equations for the axially symmetric transversely isotropy. The generalized Hooke's law equations are written in Cartesian system, as shown in **Figure 2.3**, namely:

$$\begin{cases} \varepsilon_\rho = a_{11}\sigma_\rho + a_{12}\sigma_\varphi + a_{13}\sigma_z, \\ \varepsilon_\varphi = a_{12}\sigma_\rho + a_{11}\sigma_\varphi + a_{13}\sigma_z, \\ \varepsilon_z = a_{13}\sigma_\rho + a_{13}\sigma_\varphi + a_{33}\sigma_z, \\ \gamma_{\varphi z} = a_{44}\tau_{\varphi z}, \\ \gamma_{\rho z} = a_{44}\tau_{\rho z}, \\ \gamma_{\rho\varphi} = 2(a_{11} - a_{12})\tau_{\rho\varphi}, \end{cases} \qquad \textbf{Equation 2.15}$$

where

$$a_{11} = \frac{1}{E}, a_{12} = -\frac{\mu}{E}, a_{33} = \frac{1}{E'}, a_{13} = -\frac{\mu'}{E'},$$

$$a_{44} = \frac{1}{G'}, 2(a_{11} - a_{12}) = \frac{2(1+\mu)}{E} = \frac{1}{G}. \qquad \textbf{Equation 2.16}$$

where E and E' are Young's moduli under tension and compression in the plane of isotropy and in a direction perpendicular to the isotropic plane, respectively;

μ is Poisson's ratio characterizing contraction in the plane of isotropy when tension is applied in this plane;

μ' is Poisson's ratio characterizing contraction in the plane of isotropy when tension is applied in a direction normal to the plane of isotropy;

G and $G'$are the shear moduli for the planes of isotropy and perpendicular planes.

It is clear to see that there are five independent parameters for a transverse isotropic body. As pointed out by Leknitskii, the shear modulus G' for planes normal to the plane of isotopy is an independent constant cannot be related to the other elastic constants. However, Leknitskii (1981) proposed an approximate formula correlating G' with other elastic constants, as shown in **Equation 2.17**.

$$G' = \frac{EE'}{E(1+2\mu')+E'} \qquad \textbf{Equation 2.17}$$

By introducing a displacement function $\phi(\rho, z)$, expressions of the stresses in terms of $\phi(\rho, z)$ for a transversely isotropic body are

$$\begin{cases} \sigma_\rho = -\dfrac{\partial}{\partial z}\left(\dfrac{\partial^2\phi}{\partial\rho^2} + \dfrac{b}{\rho}\dfrac{\partial\phi}{\partial\rho} + a\dfrac{\partial^2\phi}{\partial z^2}\right) \\ \sigma_\varphi = -\dfrac{\partial}{\partial z}\left(b\dfrac{\partial^2\phi}{\partial\rho^2} + \dfrac{1}{\rho}\dfrac{\partial\phi}{\partial\rho} + a\dfrac{\partial^2\phi}{\partial z^2}\right) \\ \sigma_z = \dfrac{\partial}{\partial z}\left(c\dfrac{\partial^2\phi}{\partial\rho^2} + \dfrac{c}{\rho}\dfrac{\partial\phi}{\partial\rho} + d\dfrac{\partial^2\phi}{\partial z^2}\right) \\ \tau_{\rho z} = \dfrac{\partial}{\partial\rho}\left(\dfrac{\partial^2\phi}{\partial\rho^2} + \dfrac{1}{\rho}\dfrac{\partial\phi}{\partial\rho} + a\dfrac{\partial^2\phi}{\partial z^2}\right) \end{cases}$$ **Equation 2.18**

where $a = \frac{a_{13}(a_{11}-a_{12})}{a_{13}a_{11}-a_{13}^2}, b = \frac{a_{13}(a_{13}+a_{44})-a_{12}a_{33}}{a_{13}a_{11}-a_{13}^2}, c = \frac{a_{13}(a_{11}-a_{12})+a_{11}a_{44}}{a_{13}a_{11}-a_{13}^2}, d = \frac{a_{11}^2-a_{12}^2}{a_{13}a_{11}-a_{13}^2}$.

Substituting **Equation 2.18** into the equilibrium equation, the compatible equation for the displacement function yields:

$$\left(\frac{\partial^2\phi}{\partial\rho^2} + \frac{1}{\rho}\frac{\partial\phi}{\partial\rho} + \frac{1}{s_1^2}\frac{\partial^2\phi}{\partial z^2}\right)\left(\frac{\partial^2\phi}{\partial\rho^2} + \frac{1}{\rho}\frac{\partial\phi}{\partial\rho} + \frac{1}{s_2^2}\frac{\partial^2\phi}{\partial z^2}\right) = 0 \qquad \textbf{Equation 2.19}$$

where

$$s_1 = \pm\sqrt{\frac{a + c + \sqrt{(a+c)^2 - 4d}}{2d}},$$
$$s_2 = \pm\sqrt{\frac{a + c - \sqrt{(a+c)^2 - 4d}}{2d}}.$$

When s_1 and s_2 are distinct, the displacement function $\phi(\rho, z)$ can be expressed as

$$\phi(\rho, z) = \int_0^\infty m(A_m e^{s_1 mz} + B_m e^{s_2 mz} + C_m e^{-s_1 mz} + D_m e^{-s_2 mz})J_0(m\rho)dm \qquad \textbf{Equation 2.20}$$

When $s_1 = s_2 = s$, the displacement function $\phi(\rho, z)$ can be expressed as

$$\phi(\rho, z) = \int_0^\infty m(A_m e^{smz} + B_m z e^{smz} + C_m e^{-smz} + D_m z e^{-smz})J_0(m\rho)dm \qquad \textbf{Equation 2.21}$$

where A_m, B_m, C_m,and D_m are the integral constants.

2.6 Tensioned membrane effect

Tensioned membrane effect has been studied by many researchers in the past decades (Bourdeau, 1989; Burd, 1995; Espinoza, 1994). The previous research on the analysis of the tensioned membrane effect has generally followed two broad approaches. One is to use an analytical model to represent the reinforcement mechanisms assumed to act within the system. The second is to use the numerical method to formulate and solve the compatibility, equilibrium, and constitutive equations for the complete system based on a suitable finite element method. Bourdeau (1989) consider the equilibrium conditions of the membrane as shown in **Figure 2.6**. The equilibrium in the horizontal direction implies:

$$T_H(x) + \int_0^x \tau_H(x)dx = T_0 \qquad \textbf{Equation 2.22}$$

where τ_H is the horizontal component of the frictional stress at the interface, $T_H(x)$ is the horizontal component of the tensile force in the membrane, and T_0 is the horizontal tensile force at the origin of coordinates.

In the vertical direction, the equilibrium in the vertical direction can be written as:

$$T_H(x)\frac{d^2w(x)}{dx^2} + k_s w(x) = S_{z,1}(x) \qquad \textbf{Equation 2.23}$$

where the $w(x)$ is the vertical deflection of the soil at the interface, k_s is the coefficient of subgrade reaction, and $S_{z,1}$ is the vertical stress on the top of the tensioned membrane.

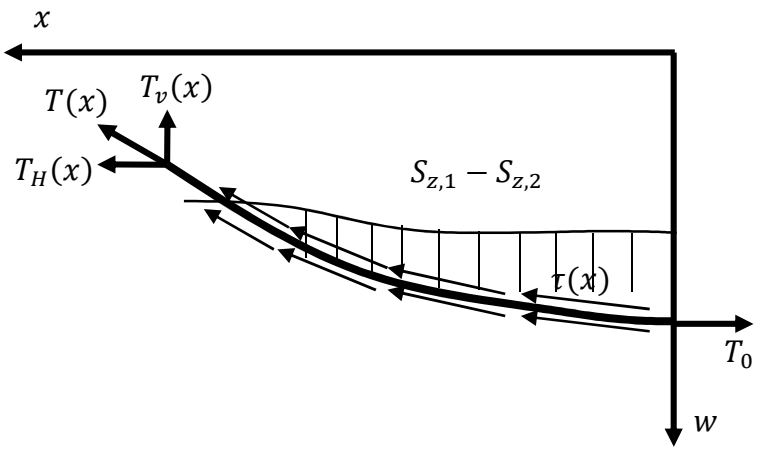

Figure 2.6 Forces acting on the deflected membrane (Bourdeau, 1989)

Figure 2.7 shows the assumed stresses acting on the reinforcement and the corresponding deformed layered system in the study of Burd (1995).

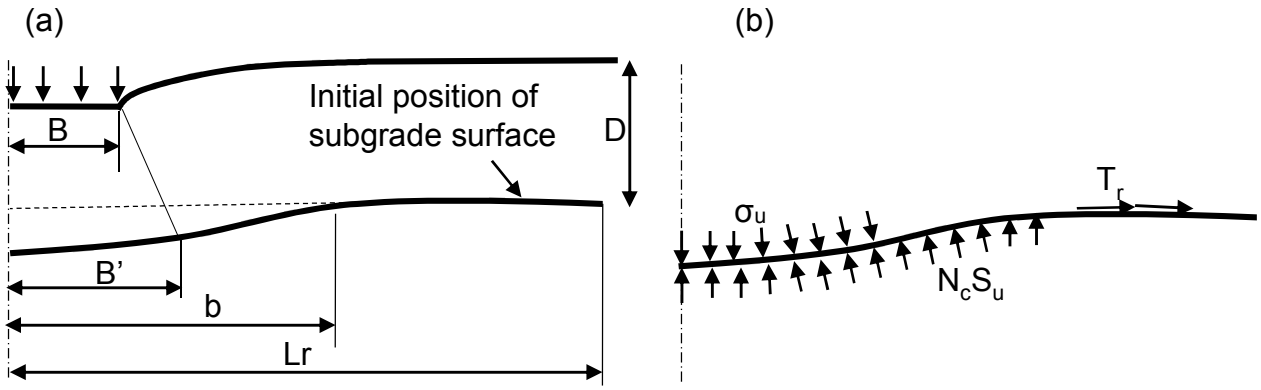

Figure 2.7 Assumed stresses acting on reinforcement and corresponding deformed shape. (a) Deformed shape of reinforcement. (b) Assumed stresses. (Burd, 1995)

The vertical stresses applied to the footing were assumed to be spread uniformly over a width 2B' at the bottom of base course, where B', as shown in **Figure 2.7**, was calculated using a load-spread model proposed by Love et al., (1987) and b was evaluated based

on the bearing capacity of subgrade. The tension in the geosynthetics was considered as constant.

In the study of Love et al. (1987), the deformed shape of geosynthetic was recorded photographically. As shown in **Figure 2.8**, the loading of width B was assumed to be spread through the base layer to give an increased width of loading B' on the surface of the clay. The effect was expressed in terms of a loading-spread angle, taken to be 25 – 30°. In the tests, the length of B' was measured directly. Points D and E were defined as the stationary points, between which the subgrade surface was moving downwards and outside which it was moving upwards. **Figure 2.9** shows the measured results of B', which were approximately constant for reinforced test sections and decreased in the unreinforced tests.

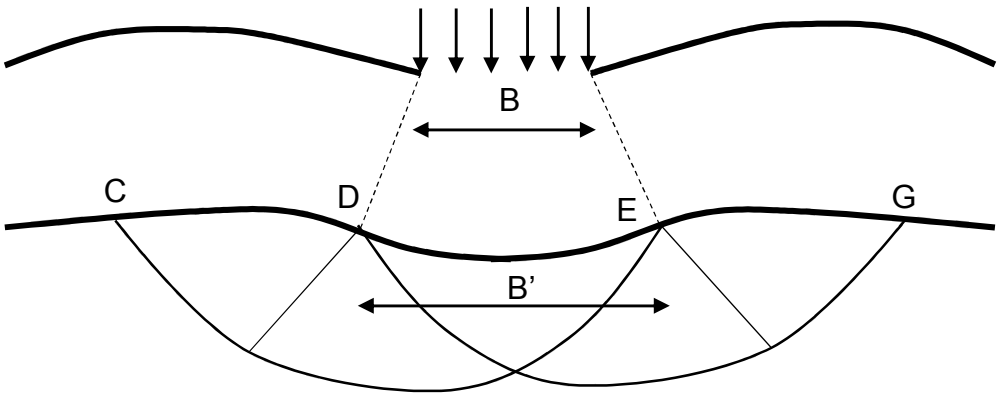

Figure 2.8 Failure mechanism in a reinforced test (Burd, 1995)

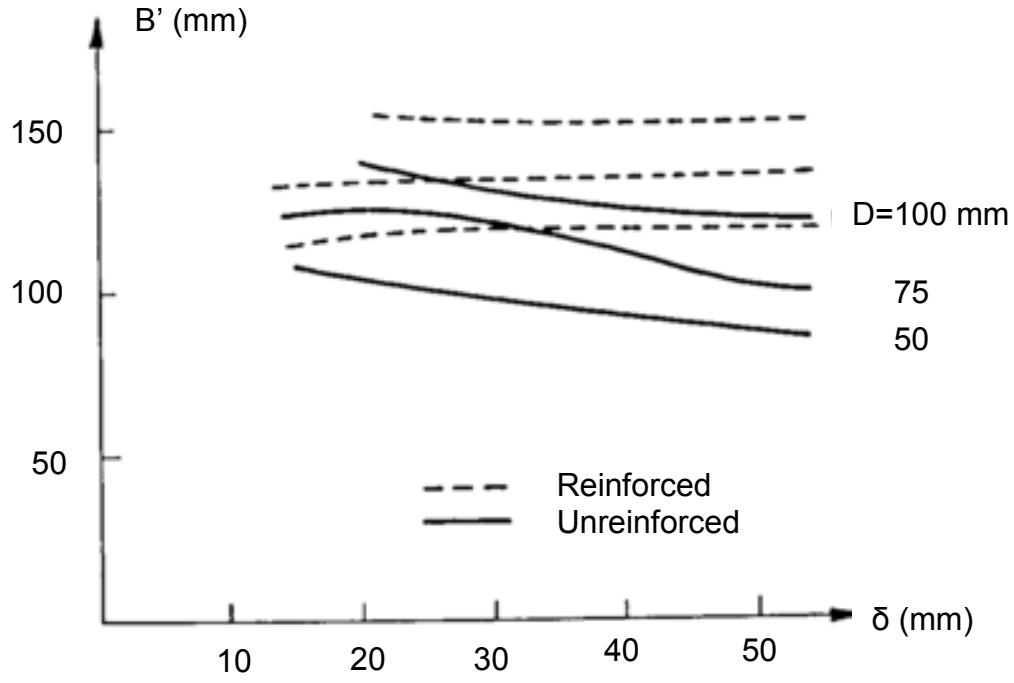

Figure 2.9 Variation of the length B' for different thicknesses of the base course (Burd, 1995)

In general, the previous analysis of the tensioned membrane effect was investigated separately and cannot reveal the influence to the stress and strain in soils in a layered elastic system. Additionally, assumptions were made to simplify the model and the strict equilibrium conditions may not be satisfied. Among those design methods considering the tensioned membrane effect, the shape of the geosynthetic deflection was assumed and the overall response of the geotextile support was evaluated subsequently. The shape of the deformed geosynthetics is commonly assumed a circular shape or a parabolic shape in the previous studies (Barenberg, 1980; Giroud and Noiray, 1981).

2.7 Constitutive model of granular materials

A constitutive model or equation is a mathematical relation between stress and strain for a particular material. The stress-strain relationship of soils depends on many factors, such as soil type, moisture content, density, stress level, and so on. Therefore, it is not feasible to capture all the characteristics of soils in a single constitutive model. The common constitutive models include: linear elastic model, nonlinear elastic model, elastoplastic model, and hypoplastic model.

Linear elastic model

Linear elastic model is the simplest model, including isotropic and anisotropic. The isotropic linearly elastic model has a stress-strain relationship which can be expressed in **Equation 2.24** (also known as the general Hooke's law).

$$\begin{cases} \varepsilon_x = \frac{1}{E}\left(\sigma_x - \mu\left(\sigma_y + \sigma_z\right)\right) \\ \varepsilon_y = \frac{1}{E}\left(\sigma_y - \mu(\sigma_x + \sigma_z)\right) \\ \varepsilon_z = \frac{1}{E}\left(\sigma_z - \mu\left(\sigma_x + \sigma_y\right)\right) \\ G = \frac{E}{2(1+\mu)} \end{cases} \qquad \textbf{Equation 2.24}$$

where E is the Young's modulus, G is the shear modulus, and μ is the Poisson's ratio.

The transversely isotropic elastic model, as one type of anisotropic, has been discussed in the previous paragraph. The property of elasticity is that the stress or strain history is immaterial and the deformation completely rebounds if the load is removed. As pointed out by Kolymbas (1999), elasticity cannot describe the following important properties of

soils: (a) plastic yield, i.e., the unlimited growth of the deformation under a constant stress; (b) dilatancy-contractancy; and (c) stress dependent stiffness.

Nonlinear elastic model

To account for the stress dependent property, i.e., the nonlinearity, a hyperbolic equation was proposed to fit the stress-strain curve obtained from the triaxial test (Kondner, 1963), as shown in **Equation 2.25**.

$$(\sigma_1 - \sigma_3) = \frac{\varepsilon_1}{\frac{1}{E_i} + \frac{\varepsilon_1}{(\sigma_1 - \sigma_3)_{ult}}} \qquad \textbf{Equation 2.25}$$

where $\mathrm{E_i}$ is the initial tangent modulus; $(\sigma_1 - \sigma_3)_{\mathrm{ult}}$ is the asymptotic value of the deviator stress; ε_1 is the axial strain.

Duncan et al. derived an equation for the tangent Young's modulus based on the hyperbolic model , as shown in **Equation 2.26**, by considering the Mohr-Coulomb failure criterion and the stress dependent initial Young's modulus .

$$E_t = \left[1 - \frac{R_f(1-\sin\emptyset)}{2c\cos\emptyset + 2\sigma_3 \sin\emptyset}\right]^2 K p_a \left(\frac{\sigma_3}{p_a}\right)^n \qquad \textbf{Equation 2.26}$$

where E_t is the tangent modulus; R_f is the failure ratio; and *K* is the modulus number; n is the modulus exponent; p_a is the atmospheric pressure; *c* is the cohesion; and ∅ is the friction angle. R_f is defined as **Equation 2.27** and can be determined based on the triaxial test.

$$R_f = \frac{(\sigma_1 - \sigma_3)_f}{(\sigma_1 - \sigma_3)_{ult}} \qquad \textbf{Equation 2.27}$$

where $(\sigma_1 - \sigma_3)_f$ can be calculated based on Mohr-Coulomb's failure criterion, as shown in **Equation 2.28**.

$$(\sigma_1 - \sigma_3)_f = \frac{2c\cos\emptyset + 2\sigma_3 \sin\emptyset}{(1-\sin\emptyset)} \qquad \textbf{Equation 2.28}$$

Elastoplastic model

Elastoplastic constitutive model is based on plasticity theories and describes the soil behavior by using various yield criteria, hardening/softening laws, and flow rules. Linearly-elastic perfectly-plastic model is one of the simplest models. Basically, the stress-strain curve can be divided into two portions, linearly elastic and perfectly plastic. For the linearly elastic portion, the Young's modulus is constant; for the perfectly plastic part, the modulus is zero. The Mohr-Coulomb yield criterion is chosen to separate the elastic and plastic behavior. The Mohr-Coulomb yield criterion can be expressed as **Equation 2.29**.

$$\sigma_1 - \sigma_3 = (\sigma_1 + \sigma_3)\sin\emptyset + 2c\cos\emptyset \qquad \textbf{Equation 2.29}$$

Hypoplastic model

In reality, there is no obvious division between the elastic and plastic status for soils. In other words, the elastic and plastic deformations always accompany with each other. Hypoplastic model can describe this property of soils without using yield surfaces, flow rules, hardening laws, etc. In addition, the loading and unloading are automatically accomplished by the model itself. The general form of the hypoplastic equation can be expressed as:

$$\dot{\boldsymbol{T}} = h(\boldsymbol{T}, \boldsymbol{D}) \qquad \textbf{Equation 2.30}$$

where $\dot{\boldsymbol{T}}$ is the Jaumann's stress rate tensor, $\boldsymbol{T}$ is the Cauchy stress tensor; and $\boldsymbol{D}$ is the Euler's stretching tensor (strain rate tensor). The bold font indicates a tensor variable and the normal font indicates a scalar variable.

The tensor function $h(\boldsymbol{T}, \boldsymbol{D})$ can be represented according to the general representation theorem, as shown in **Equation 2.31**.

$$h(\boldsymbol{T}, \boldsymbol{D}) = \varphi_1 \mathbf{1} + \varphi_2 \boldsymbol{T} + \varphi_3 \boldsymbol{D} + \varphi_4 \boldsymbol{T^2} + \varphi_5 \boldsymbol{D^2} + \varphi_6(\boldsymbol{TD} + \boldsymbol{DT}) + \varphi_7(\boldsymbol{TD^2} + \boldsymbol{DT^2}) + \varphi_8(\boldsymbol{T^2D} + \boldsymbol{D^2T}) + \varphi_9(\boldsymbol{T^2D^2} + \boldsymbol{D^2T^2}) \quad \textbf{Equation 2.31}$$

where φ_i are scalar functions of invariants and joint invariants of $\boldsymbol{T}$ and $\boldsymbol{D}$.

To consider the plastic behavior of soils, the function $h(\boldsymbol{T}, \boldsymbol{D})$ has to be non-linear in $\boldsymbol{D}$. In addition, it should be homogeneous in $\boldsymbol{T}$ and $\boldsymbol{D}$ to describe proportional stress-paths in case of proportional strain paths and the rate-independent behavior of soils. By trial and error, a function with four material parameters was found able to describe many aspects of soil behavior (Kolymbas, 2000).

$$\dot{\boldsymbol{T}} = C_1(tr\boldsymbol{T})\boldsymbol{D} + C_2 \frac{(tr\boldsymbol{TD})}{tr\boldsymbol{T}} \boldsymbol{T} + C_3 \frac{\boldsymbol{T^2}}{tr\boldsymbol{T}} \sqrt{tr\boldsymbol{D^2}} + C_4 \frac{\boldsymbol{T^{*2}}}{tr\boldsymbol{T}} \sqrt{tr\boldsymbol{D^2}} \quad \textbf{Equation 2.32}$$

where C_i are scalar material parameters; $tr()$ calculates the trace of a tensor; the deviator stress $\boldsymbol{T}^*$is defined as

$$\boldsymbol{T}^* = \boldsymbol{T} - \frac{1}{3}(tr\boldsymbol{T})\mathbf{1} \quad \textbf{Equation 2.33}$$

The hypoplastic constitutive equations have an alternative expression, which summarizes the linear terms by $\boldsymbol{LD}$, with $\boldsymbol{L}$ being a linear operate applied to $\boldsymbol{D}$, and nonlinear terms by

$\boldsymbol{N}|\boldsymbol{D}|$ with $|\boldsymbol{D}| = \sqrt{tr\boldsymbol{D}^2}$. The general form of the hypoplastic equation can be expressed as

$$\dot{\boldsymbol{T}} = \boldsymbol{L}\boldsymbol{D} + \boldsymbol{N}|\boldsymbol{D}| \qquad \textbf{Equation 2.34}$$

The hypoplastic model as shown above is capable to describe: (a) the triaxial test with a stiffness vanishes at the limit state and the contraction-dilation behavior and (b) unloading stiffness is much larger than that at loading. However, the limitation of this model is that the void ratio is not taken into account and therefore the model is not capable to describe the difference of the friction angle and stiffness between dense and loose soils. To overcome this problem, several new hypoplastic models have been proposed by introducing scalar factors to model the influences of the density and stress level.

Simplified Hypoplastic model

Fellin (2002) considered a simple one-dimensional hypoplastic model for non-cohesive soils under a triaxial condition. Three requirements were applied to the model: (a) different moduli for loading and unloading; and (b) modulus vanishing at the limit state; and (c) initial modulus, E_0. **Figure 2.9** shows the Mohr-Coulomb failure envelope. As shown in the figure, the Mohr-Coulomb failure criterion was chosen to describe the limit state of non-cohesive soils, as shown in **Equation 2.35**.

$$(\sigma_{1max} + \sigma_3)\sin\varphi = \sigma_{1max} - \sigma_3$$

$$(\sigma_{1min} + \sigma_3)\sin\varphi = \sigma_3 - \sigma_{1min} \qquad \textbf{Equation 2.35}$$

The deviator stress $\sigma_1 - \sigma_3$ and the sum of the principal stresses $\sigma_1 + \sigma_3$ control the limit state. The hypoplastic model was proposed with these two terms and two material parameters, m and n.

$$\dot{\sigma}_1 = m(\sigma_1 + \sigma_3)\dot{\varepsilon}_1 + n(\sigma_1 - \sigma_3)|\dot{\varepsilon}_1| \qquad \textbf{Equation 2.36}$$

for loading, $\dot{\varepsilon}_1 < 0$; for unloading, $\dot{\varepsilon}_1 > 0$.

Considering the conditions of the initial modulus and the vanishing modulus at the limit state, the material parameters, m and n, were determined. By substituting the m and n into **Equation 2.36**, the hypoplastic model yields

$$\dot{\sigma}_1 = \frac{E_0(\sigma_1+\sigma_3)}{2\sigma_3}\dot{\varepsilon}_1 + \frac{E_0(\sigma_1-\sigma_3)}{2\sigma_3 \sin\varphi}|\dot{\varepsilon}_1| \qquad \textbf{Equation 2.37}$$

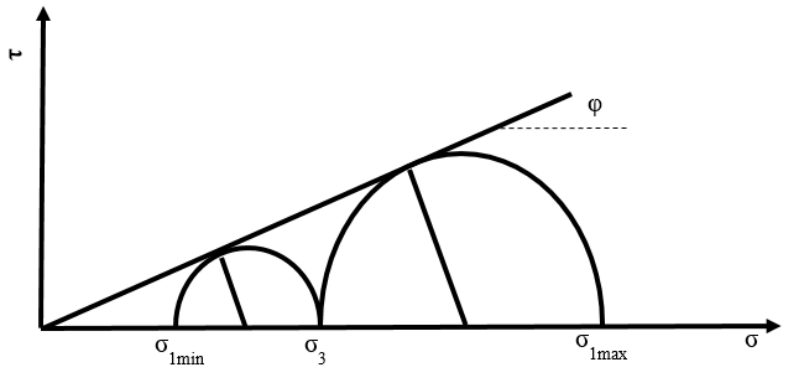

Figure 2.10 Mohr-Coulomb failure envelope

2.8 Damage models and MEPDG

In the literature reviews of Lekarp et al. (2000), several empirical permanent deformation models for granular materials were developed. Tseng and Lytton (1989) conducted cyclic triaxial tests on granular soils and developed a popular empirical permanent deformation

model by fitting the ratio of permanent strain to resilient strain ($\varepsilon_p/\varepsilon_r$) against the number of loading cycles. **Table 2.1** presents the permanent deformation models developed by different researchers.

The current Mechanistic Empirical Pavement Design Guide (MEPDG) used the modified form of the permanent deformation model developed by Tseng and Lyton (1989) to predict the permanent deformation of granular base materials. The model has been calibrated in the NCHRP Project-1-37a using a large amount of permanent deformation data collected from the Long Term Pavement Performance (LTPP) Program. **Equation 2.38** shows the calibrated permanent deformation model for granular base materials:

$$\begin{cases} PD = kh_{soil}\varepsilon_p = k \cdot h_{soil} \cdot \varepsilon_v \cdot \left(\frac{\varepsilon_0}{\varepsilon_r}\right) \cdot e^{-\left(\frac{\rho}{N}\right)^{\beta}} \\ Log\beta = -0.61119 - 0.017638W_c \\ \rho = 10^9 \cdot \left(\frac{-4.89285}{1-(10^9)^{\beta}}\right)^{\frac{1}{\beta}} \\ \left(\frac{\varepsilon_0}{\varepsilon_r}\right) = \frac{0.15 \cdot e^{\rho\beta} + 20 \cdot e^{\left(\frac{\rho}{10^9}\right)^{\beta}}}{2} \end{cases}$$

Equation 2.38

where, PD = accumulated permanent deformation in a layer;

β_{s1} = local calibration constant for the rutting in the unbound layers;

k_{s1} = global calibration coefficients (k_{s1} = 1.673 for granular materials and k_{s1} = 1.35 for fine-grained materials);

ε_v = average vertical strain in a layer which can be determined using layered elastic theory of pavement;

h_{soil} = layer thickness;

W_C = water content.

Table 2.1 Permanent deformation models for granular materials

Damage Models	
$\varepsilon_p = A + B \cdot \log N$	(Barksdale, 1972)
$\frac{\varepsilon_p}{\varepsilon_r} = A \cdot N^B$	(Veverka, 1979)
$\frac{\varepsilon_p}{\varepsilon_r} = \left(\frac{\varepsilon_0}{\varepsilon_r}\right) \cdot e^{-\left(\frac{\rho}{N}\right)^\beta}$	(Tseng and Lytton, 1989)
$\varepsilon_p = A \cdot N^B$	(Sweere, 1990)
$\varepsilon_p = A \cdot \left[1 - \left(\frac{N}{100}\right)^B\right]$	(Paute et al., 1994)

The development of the empirical method was based on the test results and/or the observations without the consideration of the pavement performance. In the Mechanistic-Empirical design method, the mechanistic analysis is used to evaluate the pavement response and the empirical damage model of soil is applied to estimate the pavement performance based on the mechanistic response of the pavement. The main advantages of ME design over the empirical methods are:

(1) It allows an evaluation of changes in traffic loading, climatic condition, pavement layer properties on pavement performance;

(2) Actual engineering properties are assigned to the materials used in the pavement; and

(3) Pavement responses related to actual modes of pavement failure are evaluated.

2.9 Design methods

Several design methods have been proposed on the planar geosynthetic reinforcement (especially the geotextile and geogrid) since the late 1970s. The first industrywide design standards for geotextile were established by Giroud and Noiray (1981). In 1985, FHWA published the Geotextile Engineering Manual. In 1990, Koerner published the Designing with Geosynthetics.

Giroud and Han (2004a and 2004b) developed and verified a design method for geogrid-reinforced unpaved roads in 2004. **Equation 2.39** presents the equation for determining the required base course thickness, h.

$$h = \frac{1 + k \log N}{\tan \alpha_0 \left[1 + 0.204 \left(R_E - 1 \right) \right]} \times \left(\sqrt{\frac{P}{\pi r^2 \left(\frac{s}{f_s} \right) \left\{ 1 - \xi \exp \left[-\omega \left(\frac{r}{h} \right)^n \right] \right\} N_c c_u}} - 1 \right) r \qquad \textbf{Equation 2.39}$$

where

r= radius of tire contact area (m);

N= number passes;

P = wheel load (kN);

c_u = undrained cohesion of the subgrade soil (kPa);

N_c = bearing capacity factor;

R_E = modulus ratio of base course to subgrade soil;

α_0 = reference stress distribution angle (degrees);

k = constant depending on base course thickness and reinforcement;

s = allowable rut depth (mm);

f_s = factor equal to 75 mm;

ξ, ω, n are constants.

In this design method, it is assumed that the 1/tan α and logN have a linear relationship between each other, as shown in **Equation 2.40**.

$$\frac{1}{\tan\alpha} = \frac{1 + k\log N}{\tan\alpha_1} \qquad \textbf{Equation 2.40}$$

where

α= stress distribution angle for the case where the number of passes is N;

α_1= stress distribution angle for the case where the number of passes is 1;

and k is a constant depending on the reinforcement and thickness of base course.

Giroud and Han (2004a) used the value of N_c = 3.14 for a unreinforced base, N_c = 5.14 for a geotextile-reinforced base, and N_c = 5.71 for a geogrid-reinforced base.

The limited modulus ratio of base course to subgrade is

$$R_E = \frac{E_{bc}}{E_{sg}} = \min\left(\frac{3.48CBR_{bc}^{0.3}}{CBR_{sg}}, 5.0\right) \qquad \textbf{Equation 2.41}$$

where E_{bc} = resilient modulus of base course (MPa);

E_{sg} = resilient modulus of subgrade soil (MPa);

CBR_{bc} = California Bearing Ratio (CBR) of base course; and

CBR_{sg} = CBR of subgrade.

The undrained shear strength of subgrade soil can be estimated by

$$c_u = f_c CBR_{sg} \qquad \textbf{Equation 2.42}$$

where f_c= factor equal to 30 kPa (Giroud and Noiray, 1981).

Perkins et al. (2004) proposed a design method for reinforced flexible pavements based on the M-E design procedure. An empirical model was developed to describe the growth of permanent shear stresses with traffic passes on test sections with three reinforcement materials. **Figure 2.10** shows the test results of one section.

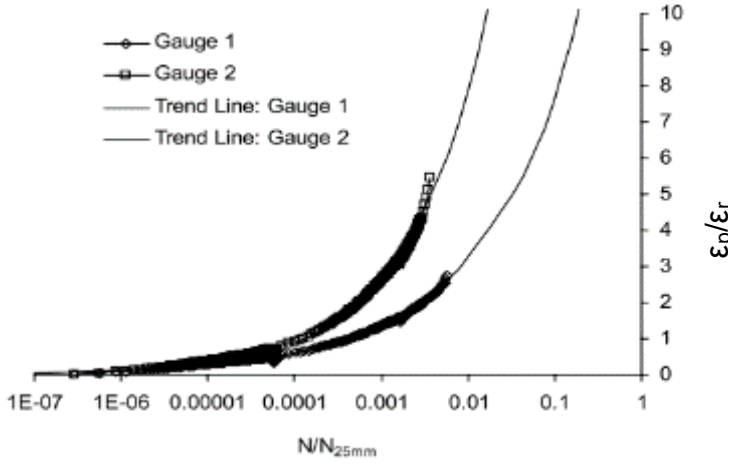

Figure 2.11 Permanent over resilient strain in geosynthetics versus normalized traffic load passes for a test section (Perkins et al., 2004)

The ratio of the permanent strain to the resilient strain in the reinforcement was correlated with the number of traffic passes, as shown in **Equation 2.43**.

$$\log\left(\frac{\varepsilon_p}{\varepsilon_r}\right) = \log(A) + B\log\left(\frac{N}{N_{25mm}}\right) \qquad \textbf{Equation 2.43}$$

where ε_p is the permanent strain in the reinforcement;

ε_r is the resilient strain in the reinforcement;

$N/N_{25\ mm}$ is the ratio of actual traffic passes to the passes necessary for 25 mm permanent deformation;

A and B are the regression constants.

In this study, the experimental data and theoretical derivation showed the equality between the ratio of the permanent strain to resilient strain in the reinforcement and the ratio of the permanent shear stress to resilient shear stress on the reinforcement-aggregate interface, as shown in **Equation 2.44**.

$$\tau_p = \tau_r \frac{\varepsilon_p}{\varepsilon_r} \qquad \textbf{Equation 2.44}$$

where τ_p is the permanent shear stress on the interface;

τ_r is the resilient shear stress on the interface.

The permanent interface shear stress was applied in the response model to account for confinement effects of the reinforcement on the base course layer during the traffic

loading. The permanent shear stress under N_{25mm} was considered as the maximum stress. The calibrated damage models were used to determine the surface permanent deformation versus load cycles for each $\varepsilon_p / \varepsilon_r$ ratio, as shown in **Figure 2.11**.

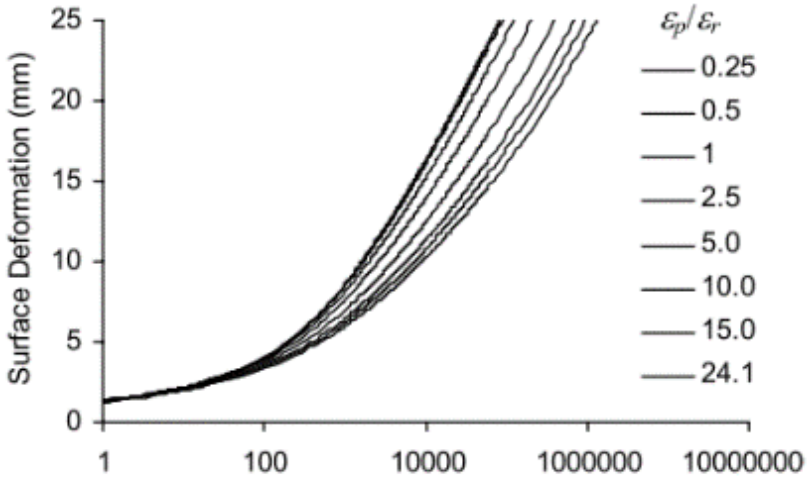

Figure 2.12 Permanent surface deformation vs. the number of load cycles (Perkins et al., 2004)

3.0 Summary

In this chapter, the past studies on the related areas of geosynthetic-stabilized bases over subgrade were reviewed in terms of laboratory and field tests, layered elastic theory, tensioned membrane effect, constitutive models, empirical soil damage model, and design methods. Based on the literature review, the following conclusions can be drawn:

(1) Geogrid is effective in reducing permanent deformations of bases over weak subgrade. With the inclusion of the geogrid, the vertical stress can be distributed to a wider area. In some studies, the resilient modulus of the geogrid stabilized bases were slightly increased.

However, some other studies showed that the geogrid stabilized bases had higher resilient deformations. Therefore, the resilient behavior of geogrid stabilized sections needs further investigation.

(2) There is not a feasible analytical solution available for the geogrid stabilized layered elastic system. The influence of the confinement and tensioned membrane effect to the stress and strain of soils is not clear.

Chapter 3 Experimental Study on Geogrid-Stabilized Bases over Subgrade

This chapter presents the laboratory tests conducted in the study, including triaxial tests, cyclic plate loading tests with increasing loading intensities, static plate loading tests, and cyclic plate loading tests with constant loading intensities. The test sections include base courses with various thicknesses over weak subgrade, base courses over subgrade in different CBRs, and subgrade-only sections.

3.1 Materials and test setup

3.1.1 Base course

In this study, the Kansas type AB aggregate (also referred to as the AB3 aggregate) was chosen as the base course material, as shown in **Figure 3.1**. The AB3 aggregate is commonly used as base course materials for low-volume roads in Kansas.

Figure 3.1 AB3 used in this study

Sieve analysis

Its physical properties are as follows: specific gravity (G_s) =2.69, mean particle size (d_{50}) =4.0 mm (Sun et al., 2014a, 2014b). **Figure 3.2** shows the grain size distribution curve of the AB3.

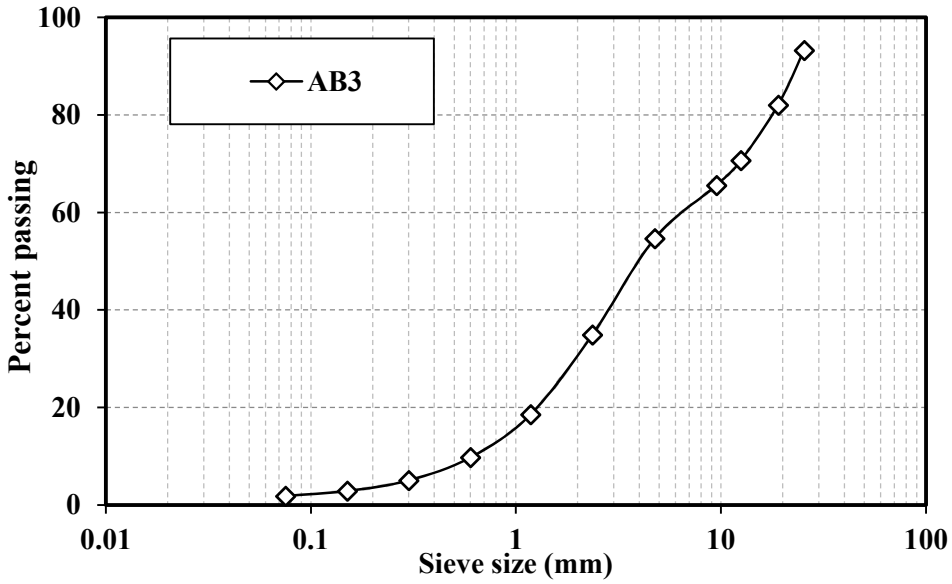

Figure 3.2 Grain size distribution of the AB3 in this study

Compaction and CBR tests

Five modified Proctor compaction tests were performed on the AB aggregate samples at varying moisture contents following ASTM D1557. In addition, the California Bearing Ratio (CBR) tests were performed on samples from the Proctor compaction tests following the ASTM D1188 standard. **Figure 3.3** shows the CBR test device. **Figure 3.4** presents the test results of the compaction test and CBR test.

Figure 3.3 CBR test setup

The maximum CBR value obtained from the test was 72% at a moisture content of 7.3%. For each large-scale test section, the CBR values of the base course were evaluated by the Dynamic Cone Penetration (DCP) test. Compacted at the same moisture content, however, the base course in each roadway test section reached the average CBR value at approximately 15%. The two reasons for this result are that: the confinement of the base course material was relatively low in the DCP test as compared with that in a steel mold in the CBR test and (2) the base course, when compacted over the weak subgrade, could not reach a state as dense as that in the CBR test.

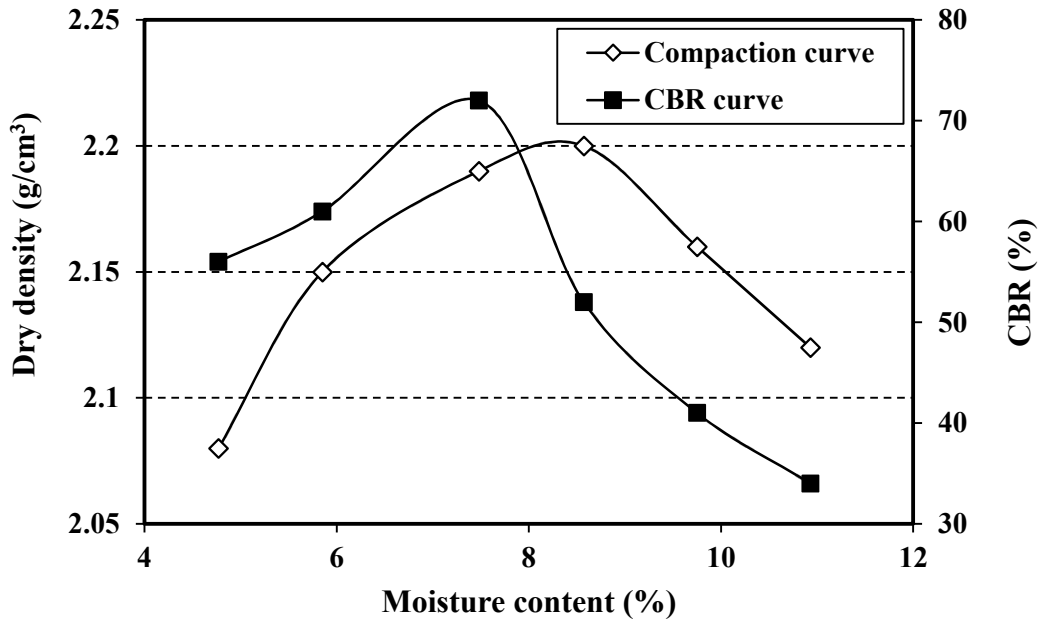

Figure 3.4 Modified Proctor compaction curve and CBR curve of base course (Sun et al., 2014b).

Triaxial test

The AB3 was tested under different confining pressures at its optimum moisture content, as shown in **Figure 3.5**. The dimension of test sample was 100 mm in diameter and 200 mm in height. In the test, the AB3 was not saturated to simulate the in-situ condition of the plate load test. Three confining pressures, 69, 138, and 207 kPa, were applied during the compression. **Figure 3.6** shows the stress-strain curves of the AB3 under different pressures. Considering the failure of the AB3 occurred at 5% strain, the failure envelope of the AB3 was analyzed, as shown in **Figure 3.7**. Based on the test results, the cohesion and friction angle of the AB3 were 45 kPa and 42^{o}, respectively.

Figure 3.5 The triaxial test setup

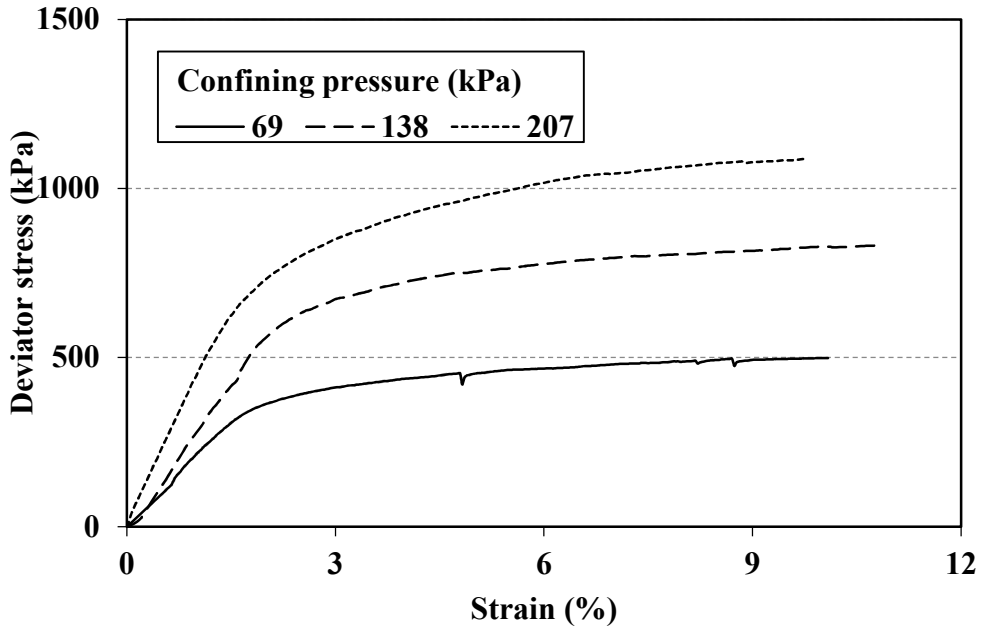

Figure 3.6 The stress-strain curve of the AB3

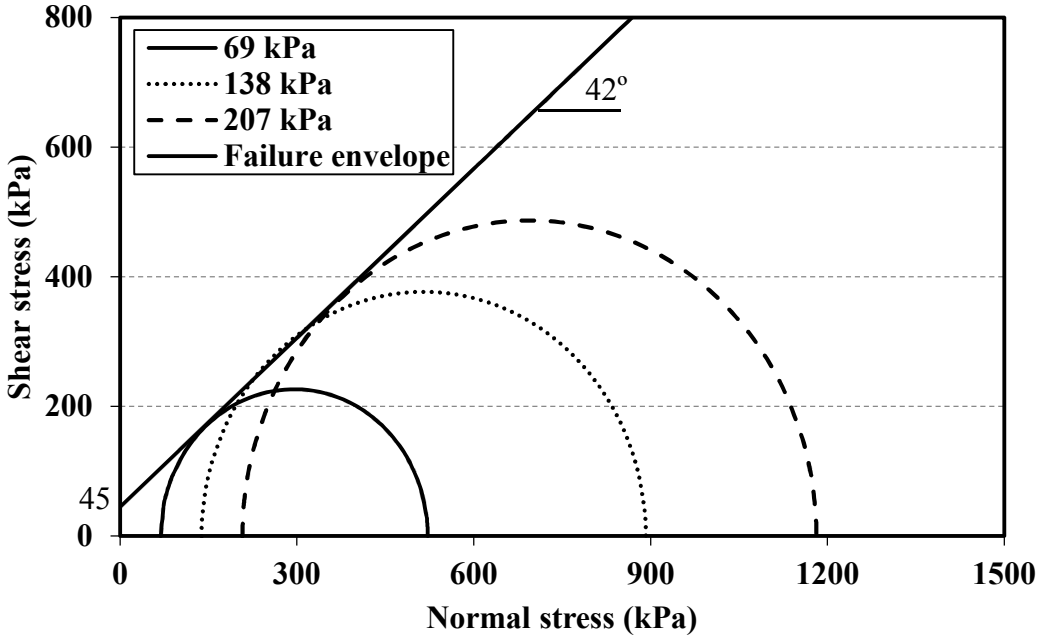

Figure 3.7 The failure envelope of the AB3

3.1.2 Subgrade

The subgrade material was made artificially by mixing 25% Kaolin and 75% Kansas River sand with water by weight, as shown in **Figure 3.8**. The Kansas River sand is a poorly-graded sub-rounded sand. **Figure 3.9** shows the grain size distribution of the Kansas River sand. Following the ASTM D4318-10 test standard, the plastic and liquid limits for the subgrade were determined to be 22% and 30%, respectively (Thakur et al., 2012). **Figure 3.10** shows the compaction curve and CBR curve versus the moisture content. Basically, the CBR of the subgrade increased with the decrease of the moisture content.

Figure 3.8 The failure envelope of the AB3

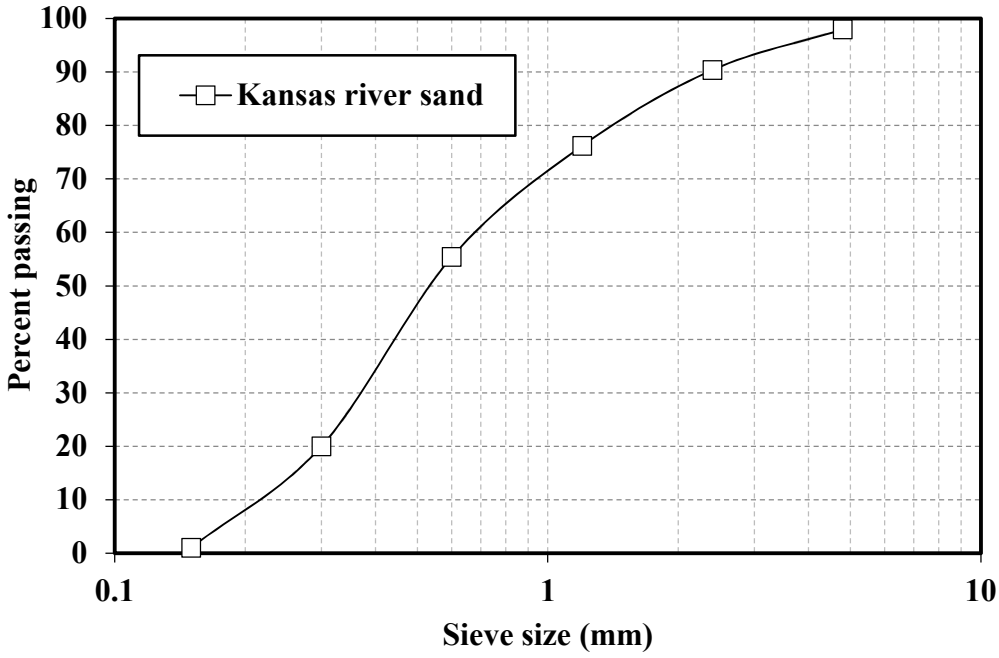

Figure 3.9 Grain size distribution of the Kansas River sand

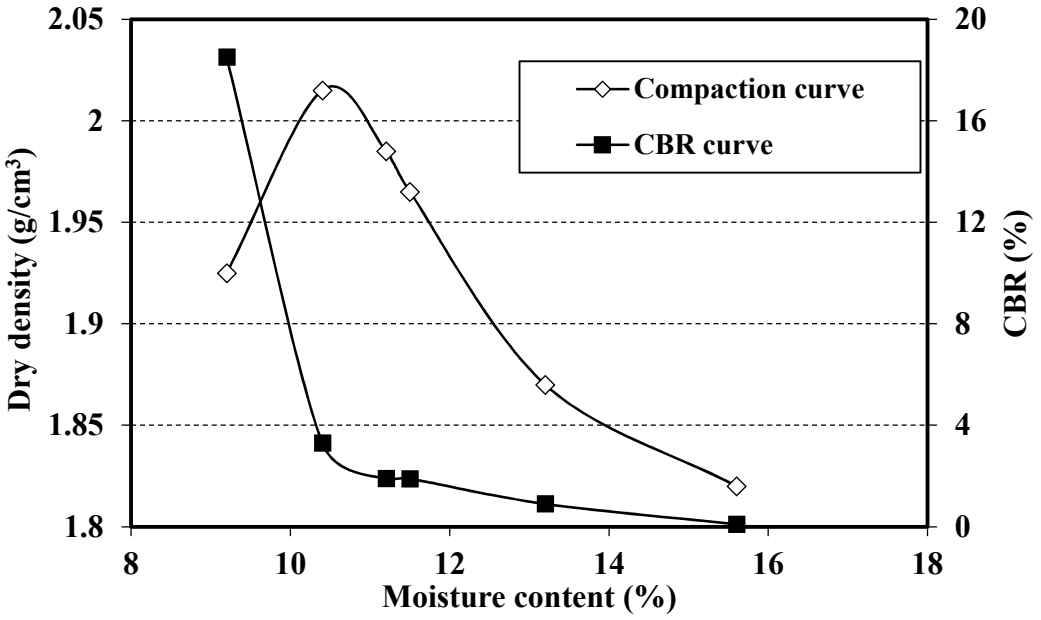

Figure 3.10 Modified Proctor compaction curve and CBR curve of subgrade (Pokharel, 2010).

Triaxial test

To identify the mechanical parameters of the subgrade, i.e., cohesion and friction angle, triaxial tests were conducted on the unsaturated samples of subgrade, as shown in **Figure 3.11**. The dimension of the samples was 71 mm in diameter and 152 mm in height. The CBR of the samples were controlled at 2, 3, and 5% with the corresponding moisture contents of 10.7, 10.2, and 9.6%, respectively. The triaxial tests were conducted under the confining pressures of 0, 34, 69, and 103 kPa. **Figure 3.12** shows the stress-strain curves of the subgrade under various confining pressures and moisture contents. **Figure 3.13** shows the corresponding failure envelopes of the subgrade with various moisture contents. As shown in **Figure 3.13**, with the moisture contents of 10.7, 10, and 9.6%, the

friction angles of the subgrade were 16º, 18º, and 28º, respectively; and the cohesion of the subgrade was 15, 30, and 35 kPa, respectively.

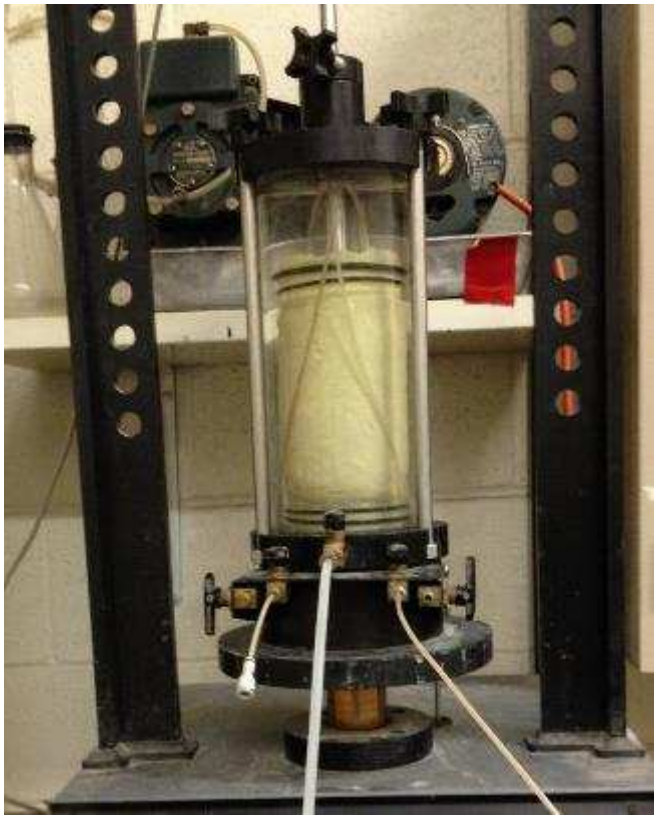

Figure 3.11 Triaxial test of the subgrade

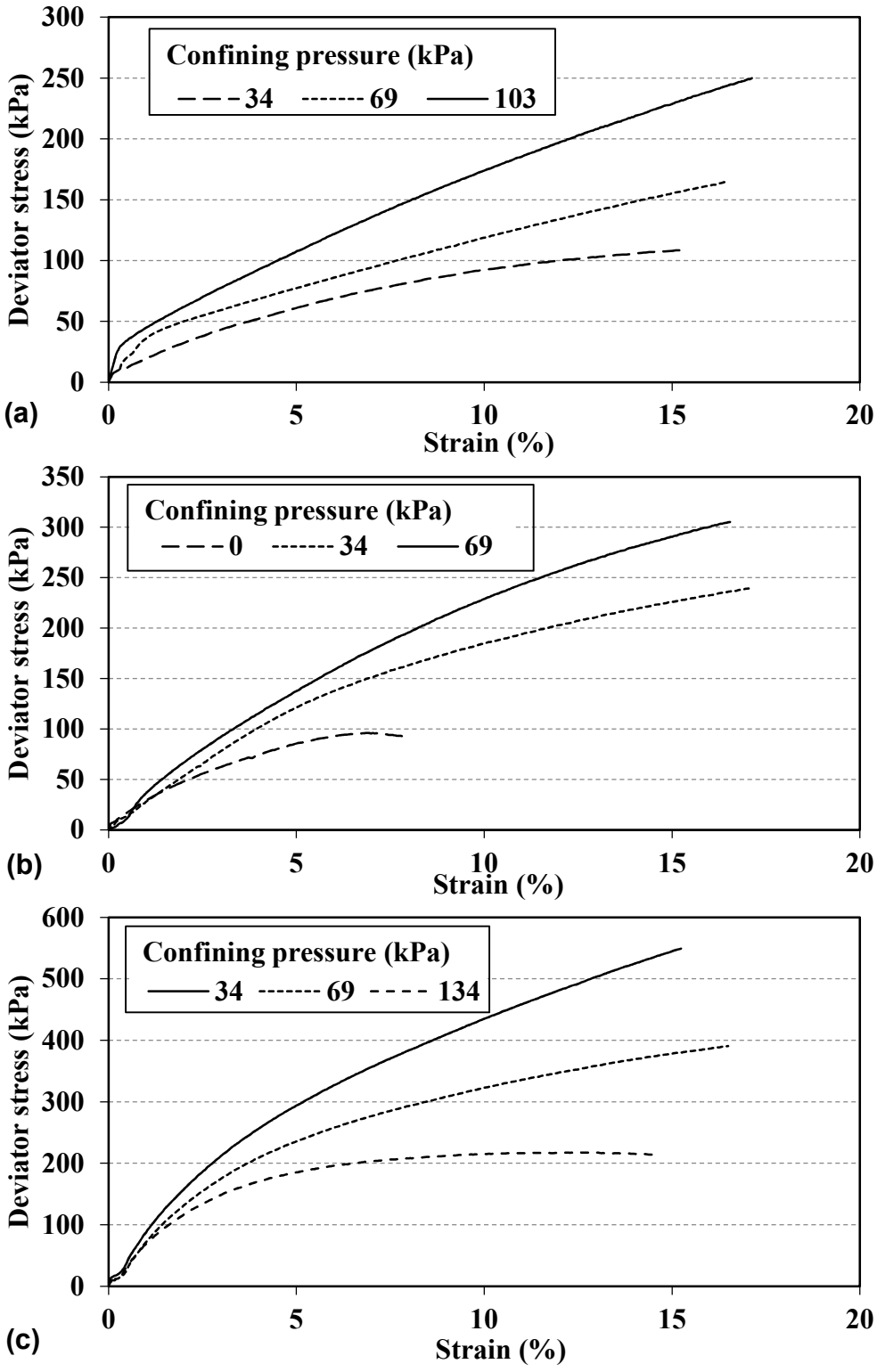

Figure 3.12 Stress-strain curves of subgrade with various moisture contents: (a) 10.7%; (b) 10.2%; and (c) 9.6%

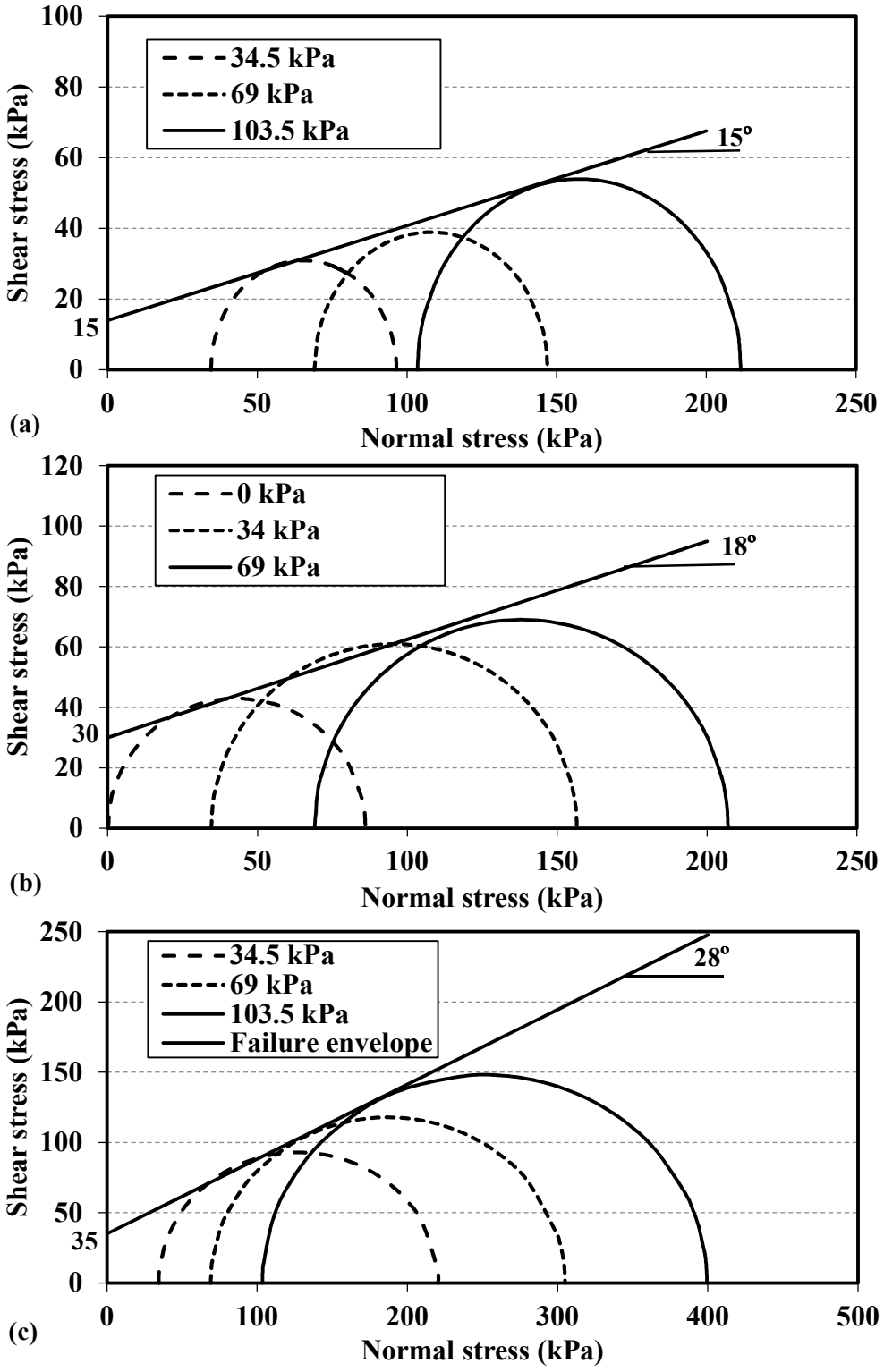

Figure 3.13 Failure envelope of subgrade with various moisture contents: (a) 10.7%; (b) 10.2%; and (c) 9.6%

The subgrade was prepared with a compacted thickness of each lift at 0.1 m and a targeted CBR value at approximately 2%. This subgrade is considered as weak subgrade so that the geosynthetic reinforcement is needed for road construction (Holtz et al., 1998). Vane shear test was used to control the quality of the subgrade after the compaction of each layer. The relationship between CBR and vane shear strength of this subgrade was established in the previous study as $\mathrm{CBR} = \frac{c_u}{20.5}$, where, c_u is the undrained shear strength evaluated by the vane shear test (kPa) (Pokharel, 2010).

3.1.3 Geogrid

In this study, two extruded triaxial geogrids with triangular shaped aperture (i.e., a standard-duty grade, T1, and a heavy-duty grade, T2) were used to stabilize the AB3 aggregate course, as shown in **Figure 3.14**.

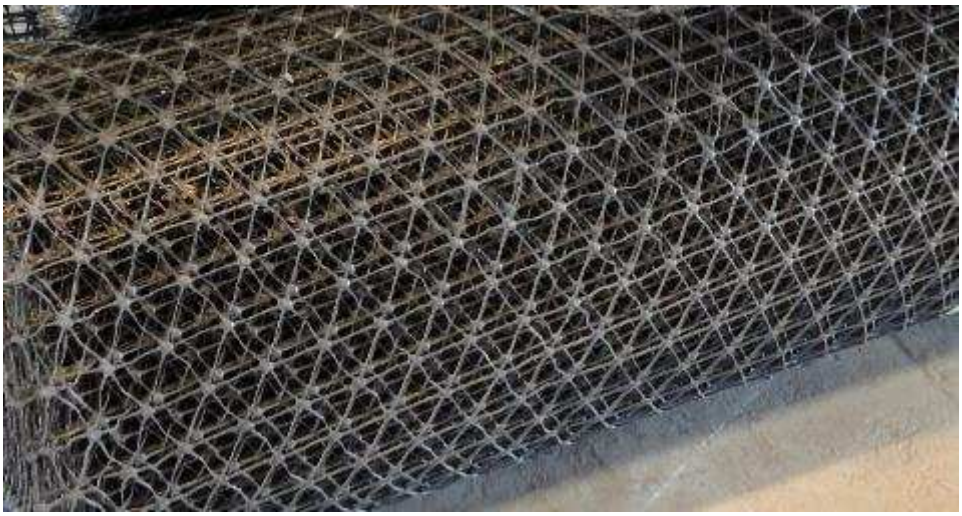

Figure 3.14 The geogrid used in this study

The two types of geogrid were made of polypropylene and had the same manufacturing type. The difference between these two types of geogrid is the thicknesses of the original

sheet used to manufacture the two kinds of products. **Table 3.1** lists the physical properties of the two geogrid products used in this study. The radial stiffness of the two types of geogrid, T1 and T2, was 270 and 365 kN/m, respectively, at 0.5% radial strain.

Table 3.1 Properties of triaxial geogrids used in this study (Sun et al., 2014a)

Geogrid type	Rib pitch - longitudinal (mm)	Rib pitch - diagonal (mm)	Mid-depth - diagonal (mm)	Mid-depth - transverse (mm)	Mid-width - diagonal (mm)	Mid-width - transverse (mm)
T1	40	40	1.3	1.2	0.9	1.2
T2	40	40	2.0	1.6	1.0	1.3

3.1.4 Test equipment

Large-scale geotechnical box

A large geotechnical test box with dimensions of 2 m (W) × 2.2 m (L) × 2 m (H) at the University of Kansas was used in this study, as shown in **Figure 3.15**. The roadway sections were constructed in the box and a cyclic/static load was be applied to the test sections via a 300-mm diameter steel plate. The frequency of the cyclic loading applied in this study was 0.77 Hz. To complete a load cycle, the cyclic loading wave started with a seating load of 0.5 kN, linearly increased to a peak load in 0.3 seconds, maintained for 0.2 seconds, decreased to a trough load of 0.5 kN linearly, and maintained for another 0.5 seconds (Qian et al., 2013).

Figure 3.15 The geotechnical box at the University of Kansas

Earth pressure cells and displacement transducers

Figure 3.16 shows the earth pressure cell and displacement transducers used in this study. The portable pressure cells had a thickness of 11.3 mm, an outer diameter of 50 mm with the sensing area diameter of 46 mm, and total weight of 160 g. The displacement transducers were strain gauge type sensors with 50 or 100 mm measurement range.

(a) (b)

Figure 3.16 (a) Earth pressure cell and (b) displacement transducer

3.2 Cyclic plate load tests with increasing load magnitudes

3.2.1 Introduction and test setup

In this study, a total of nine test sections were prepared in a large geotechnical test box (2 m × 2.2 m × 2 m). The base course thicknesses were 0.15, 0.23, and 0.3 m, respectively. Three test sections, unstabilized, T1 stabilized, and T2 stabilized, were prepared for each base course thickness. **Figure 3.17** shows the test setup.

Displacement transducers were installed at the distances of 0, 0.25, 0.50, and 0.75 m from the center of the load plate to monitor the surface deformations. The subgrade deformation at the center was measured by a displacement transducer placed on a telltale seated on the top of the subgrade. For each loading cycle, resilient deformation was

estimated from the difference between the maximum and minimum deformations in the cycle. Vertical stresses at the interface of the base course and subgrade were monitored by earth pressure cells. The earth pressure cells were installed at 0, 0.18, 0.25, and 0.38 m away from the center. Radial stresses close to the bottom of the base course were monitored at the distances of 0.25 and 0.38 m from the center and those near the top of the subgrade were monitored by the pressure cells placed at 0.18, 0.25, and 0.38 m away from the center. To monitor the radial stresses, earth pressure cells were placed vertically so that their sensitive surfaces were perpendicular to the directions of the radial stresses. **Figure 3.18** shows the top view of the arrangements of the earth pressure cells.

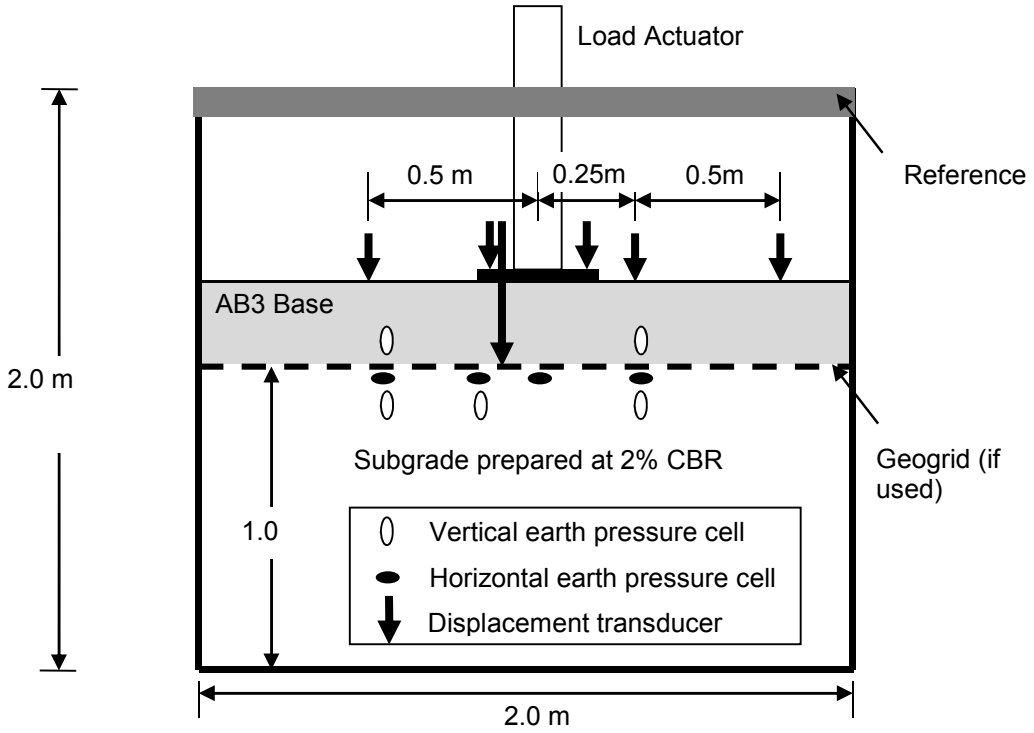

Figure 3.17 Test setup (Sun et al., 2014a).

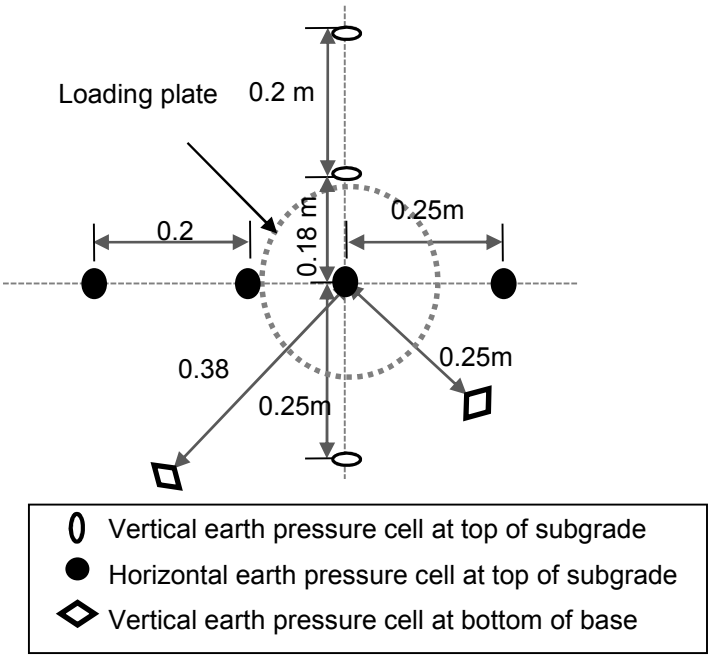

Figure 3.18 Top view of the arrangements of the earth pressure cells (Sun et al., 2014a).

A cyclic load was applied to the test section via a 300-mm diameter steel plate. The intensity of the load increased from 5 to 50 kN with an increment of 5 kN, aimed to simulate the varying single wheel loads in reality, as shown in **Figure 3.19**. For every loading increment, 100 cycles were applied on the test sections. A surface permanent deformation greater than 75 mm was considered as failure of the test section.

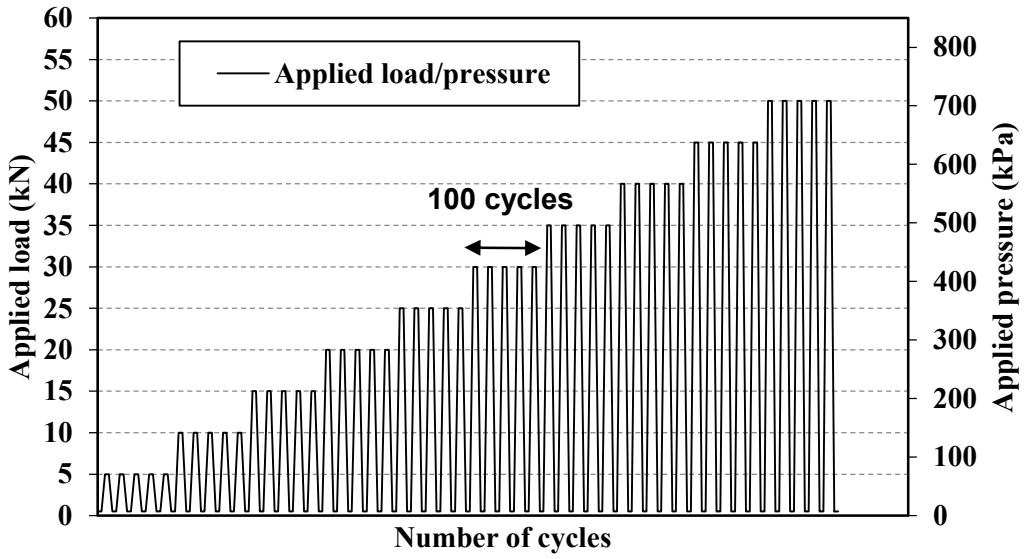

Figure 3.19 The intensities of cyclic load (Sun et al., 2014a, 2014b).

3.2.2 Results and discussion

CBR values

Dynamic cone penetration (DCP) tests were conducted to evaluate the CBR values of the test sections. The CBR values were determined by the following formula (Webster, 1993):

$$\mathrm{CBR} = 292/(\mathrm{DCPI})^{1.12} \qquad \textbf{Equation 3.1}$$

where DCPI = Penetration Index (mm/blow).

Table 3.2 presents the average CBR values of the base and the subgrade. The CBR ratio of base course to subgrade was approximately 6.6.

Table 3.2 Average CBR values of each test section based on DCP tests

Base thickness (m)	Stabilized condition	CBR (%)	
		Subgrade	Base course
0.15	Unstabilized Section	2.1	15.2
	Stabilized Section (T1)	2.2	14.9
	Stabilized Section (T2)	2.0	15.6
0.23	Unstabilized Section	2.3	14.2
	Stabilized Section (T1)	2.4	15.4
	Stabilized Section (T2)	2.3	14.9
0.30	Unstabilized Section	2.3	15.2
	Stabilized Section (T1)	2.3	14.8
	Stabilized Section (T2)	2.4	14.5

Maximum vertical stresses

Figure 3.20 shows the measured maximum vertical stresses at the interface of the base course and subgrade located at the center of the loading plate versus the number of load cycles for the test sections with the base thicknesses of 0.15, 0.23, and 0.30 m, respectively. Generally, the vertical stress at the interface increased with the increase of

the load magnitude proportionally. At a loading stage with a lower load magnitude, the vertical stress did not change much with the increase of load cycles, whereas it increased significantly in the loading stage with a higher load magnitude. This phenomenon is because that the deterioration of the quality of the base course under a lower load magnitude was not as drastic as that under a higher load magnitude. Under the same load magnitude, the maximum vertical stresses at the subgrade decreased with the increase of the base thickness. The geogrid confined aggregate resulted in a stiffer base course and a lower subgrade vertical stress. The depth of influence from the geogrid in granular materials was limited and the stiffness improvement within the influence zone depended on the quality of the aggregate and the geogrid type. The reduction of the vertical stresses in the geogrid stabilized sections was more obvious in the 0.15-m thick base section. The influence of the geogrid decreased with the increase of the base course thickness. When a heavier-duty geogrid (i.e., T2) was used, the reduction of the vertical stresses became more apparent since the geogrid with the heavier duty was more effective in maintaining the stiffness of the base course as compared with the geogrid with the lower duty (i.e., T1), as pointed out by Qian et al. (2013).

Vertical stress distribution

Figure 3.21 shows the measured maximum vertical stresses along the base-subgrade interface versus the distance from the center for the test sections with 0.15, 0.23, and 0.3 m thick base courses under 500, 700, and 900 load cycles, respectively. The load cycles correspond with the maximum load cycles applied on the unstabilized test sections with 0.15, 0.23, and 0.3 m thick base courses, respectively. The distances from the center to the measured locations were 0, 0.18, 0.25, and 0.38 m. **Figure 3.21** shows that the

vertical stresses were distributed in a wider area in the stabilized sections as compared with those in the unstabilized sections. The unstabilized sections had a sudden decrease in the vertical stresses at 0.18 to 0.25 m from the center, indicating the punching failure of the subgrade, whereas the vertical stresses along the radial distance decreased gradually in the stabilized sections.

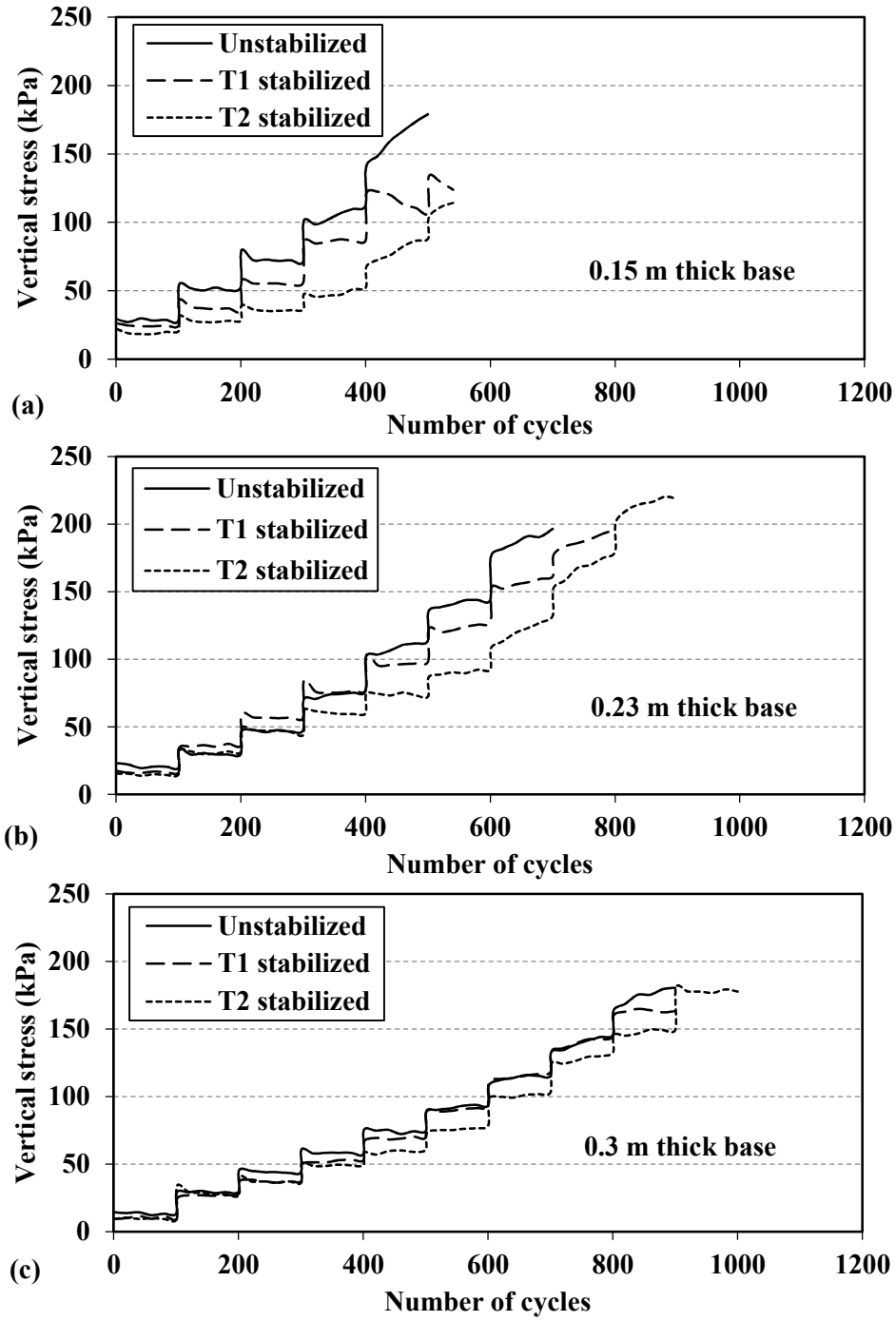

Figure 3.20 Maximum vertical stresses at the interface vs. number of load cycles for: (a) 0.15-m-thick; (b) 0.23-m-thick; (c) 0.30-m-thick base course.

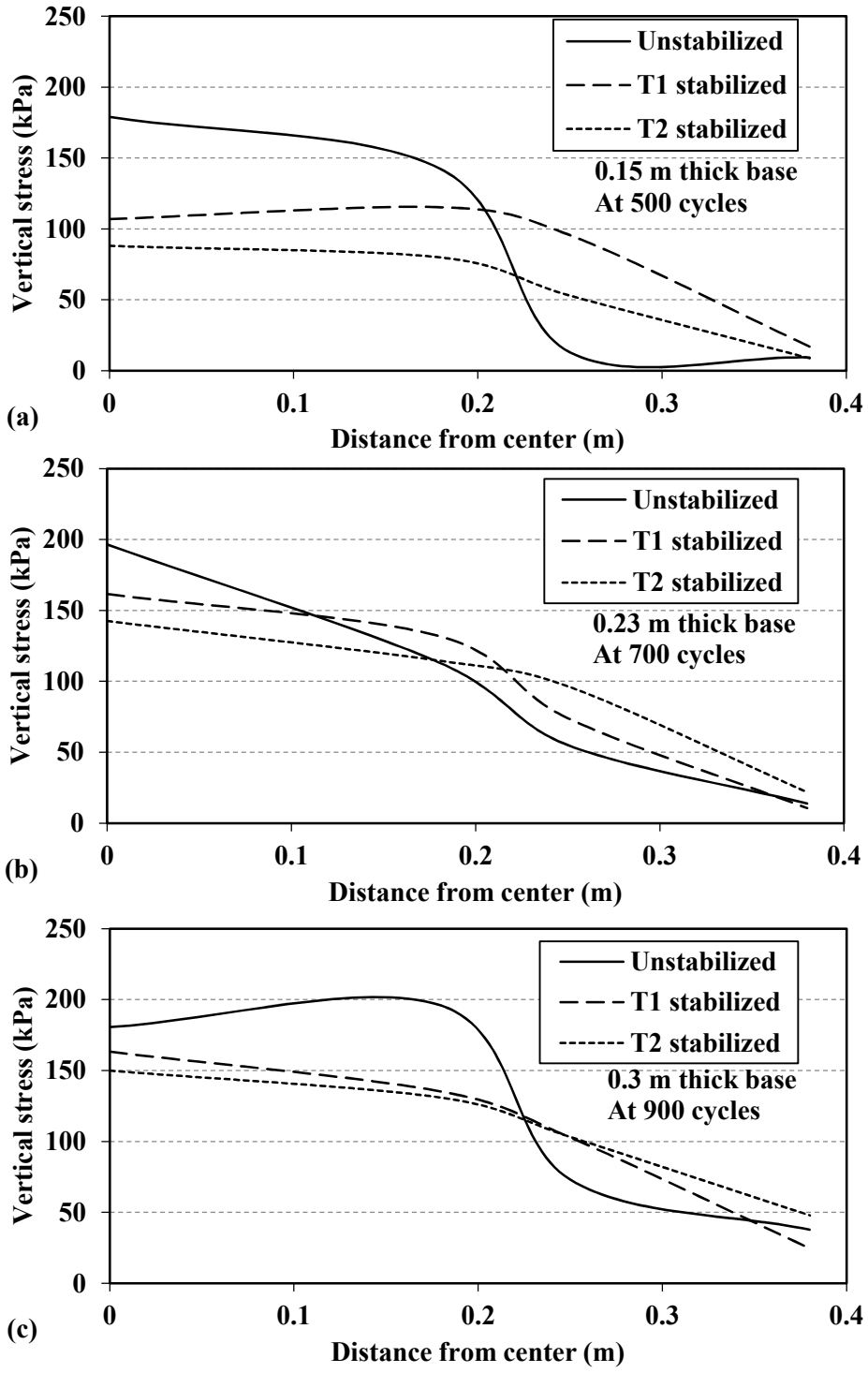

Figure 3.21 Maximum vertical stresses at the interface vs. distance from center for: (a) 0.15-m-thick; (b) 0.23-m-thick; (c) 0.30-m-thick base course.

Radial stresses

To evaluate the confinement effect of the geogrid in the stabilized sections, the radial stresses in the base course and subgrade were monitored. **Figures 3.22** and **3.23** present the measured radial stresses at the bottom of the base course with the distances from the load center of 0.25 and 0.38 m, respectively. In general, the radial stresses increased with the increase of the load magnitude. As shown in **Figure 3.22**, the geogrid-stabilized test sections exhibit higher radial stresses within the base course than the unstabilized section with a distance of 0.25 m from the load center. This phenomenon gives a direct indication of the lateral restraint mechanism, in which the lateral confinement of the geogrid strengthened the unbound aggregate horizontally. After a certain number of load cycles, the radial stresses dropped rapidly in most test sections. The stress reduction indicates the deterioration of the base course.

At a distance of 0.38 m from the center of the loading plate, the trend that the radial stresses increased with the increase of load magnitude was maintained. As compared with those at a distance of 0.25 m from the center for the unstabilized sections, the radial stresses decreased at a distance of 0.38 m from the center of the loading plate in the test sections with 0.15 and 0.23 m thick unstabilized bases, but increased in the unstabilized section with the base thickness of 0.3 m. This phenomenon indicates that the radial stresses were distributed to a wider area with the increase of base course thickness. As shown in **Figure 3.23**, at a distance of 0.38 m from the center of the loading plate, the measured radial stresses at the bottom of the base course in the geogrid stabilized sections were lower than those in the unstabilized sections. This trend is different from that at the location of 0.25 m from the load center. This phenomenon reveals that the

presence of the geogrid tends to change the radial stress distribution and confine the radial stresses at the bottom of the base course to a smaller area around the loading plate.

Figures 3.24, **3.25**, and **3.26** present the measured radial stresses on the top of the subgrade with the varying distances from the center of the loading plate of 0.18, 0.25, and 0.38 m, respectively. Basically, the radial stresses increased with the increase of the load magnitude. Compared with those at the bottom of the base course, the radial stresses on the top of the subgrade were much lower. Considering the continuity condition at the interface, the radial stresses are expected to be less than those at the bottom of the base course with the same lateral deformation since the subgrade modulus is much lower than that of the base course. Burmister (1945b) described this discontinuity. In **Figure 3.24**, the stabilized test sections had higher radial stresses as compared with those in the unstabilized sections at the location with a distance of 0.18 m from the center of the loading plate, except the test section stabilized by T2 geogrid with a base thickness of 0.15 m, as shown in **Figure 3.24** (a). In **Figures 3.25** and **3.26**, however, the stabilized test sections had lower radial stresses as compared with the unstabilized test sections. These results indicate that the radial stress distribution on the top of the subgrade was changed by the inclusion of the geogrid and the radial stress was concentrated into a zone close to the loading plate. This trend is similar to that at the bottom of the base course. In other words, the confinement of the geogrid could not only influence the distribution of the radial stresses at the bottom of the base course, but also influence that on the top of the subgrade and therefore contributed to the improved performance of the stabilized test sections.

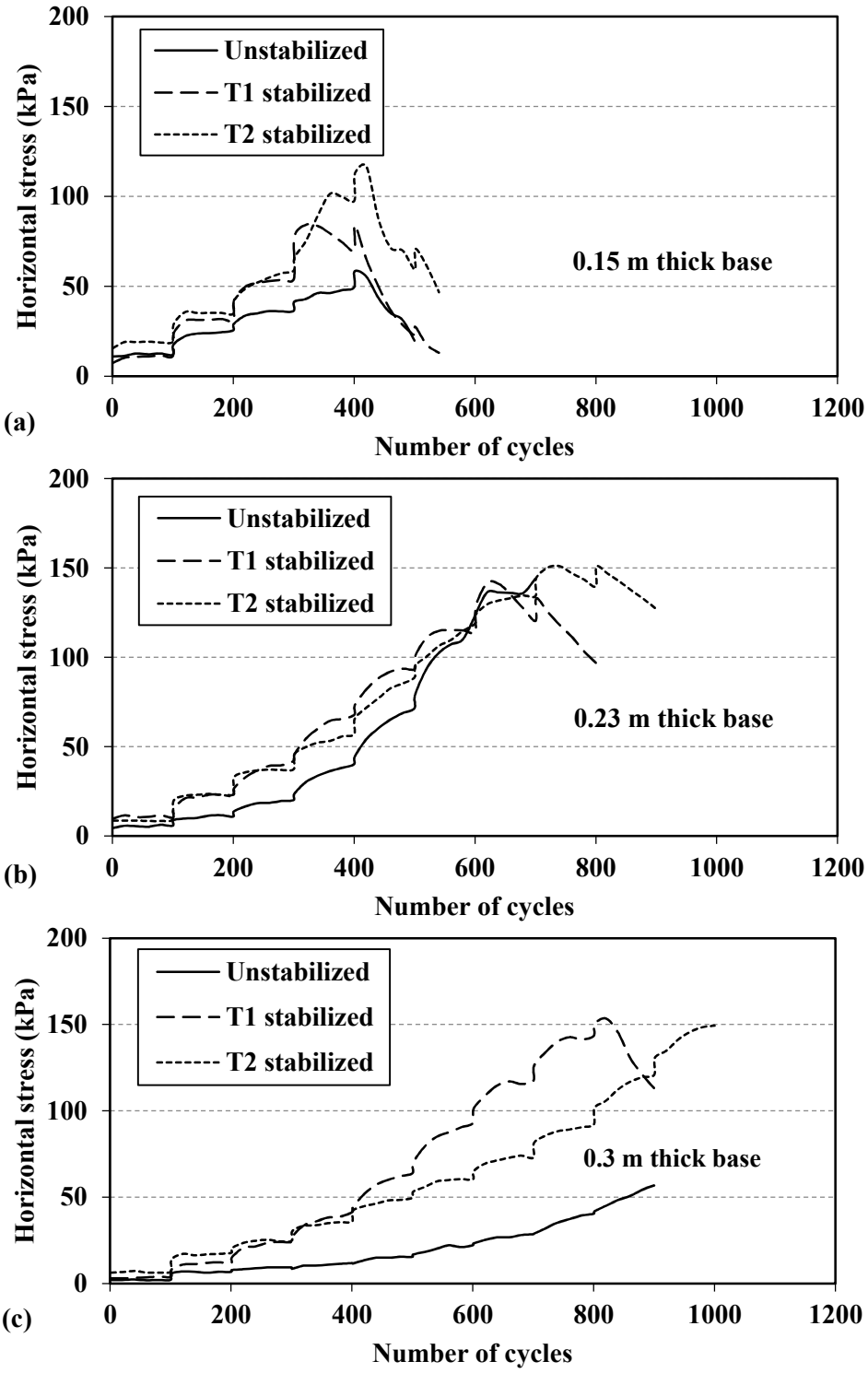

Figure 3.22 Maximum radial stress at the bottom of base course with a distance of 0.25 m from the center vs. number of load cycles for: (a) 0.15-m-thick; (b) 0.23-m-thick; (c) 0.30-m-thick base course.

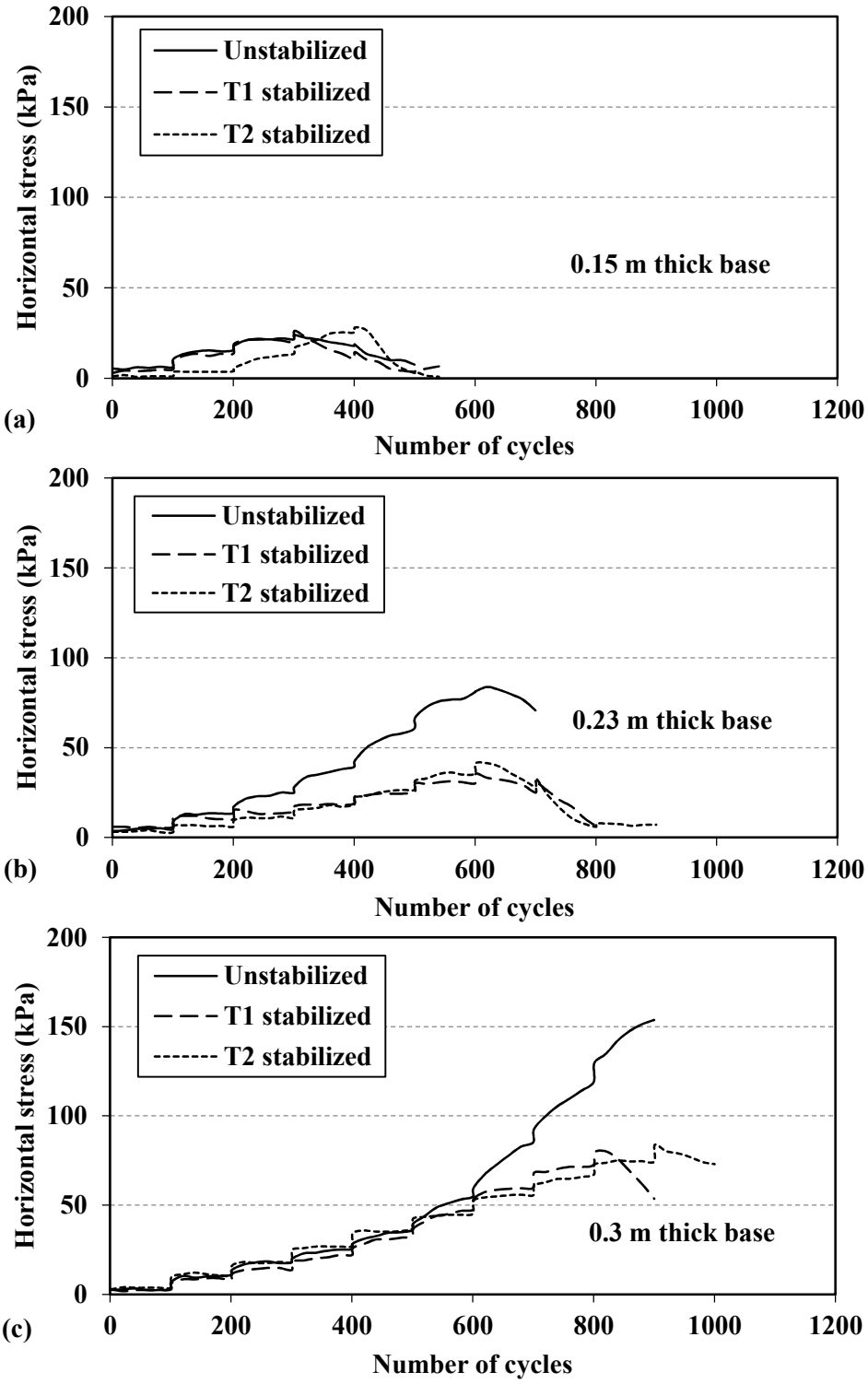

Figure 3.23 Maximum radial stress at the bottom of base course with a distance of 0.38 m from the center vs. number of load cycles for: (a) 0.15-m-thick; (b) 0.23-m-thick; (c) 0.30-m-thick base course.

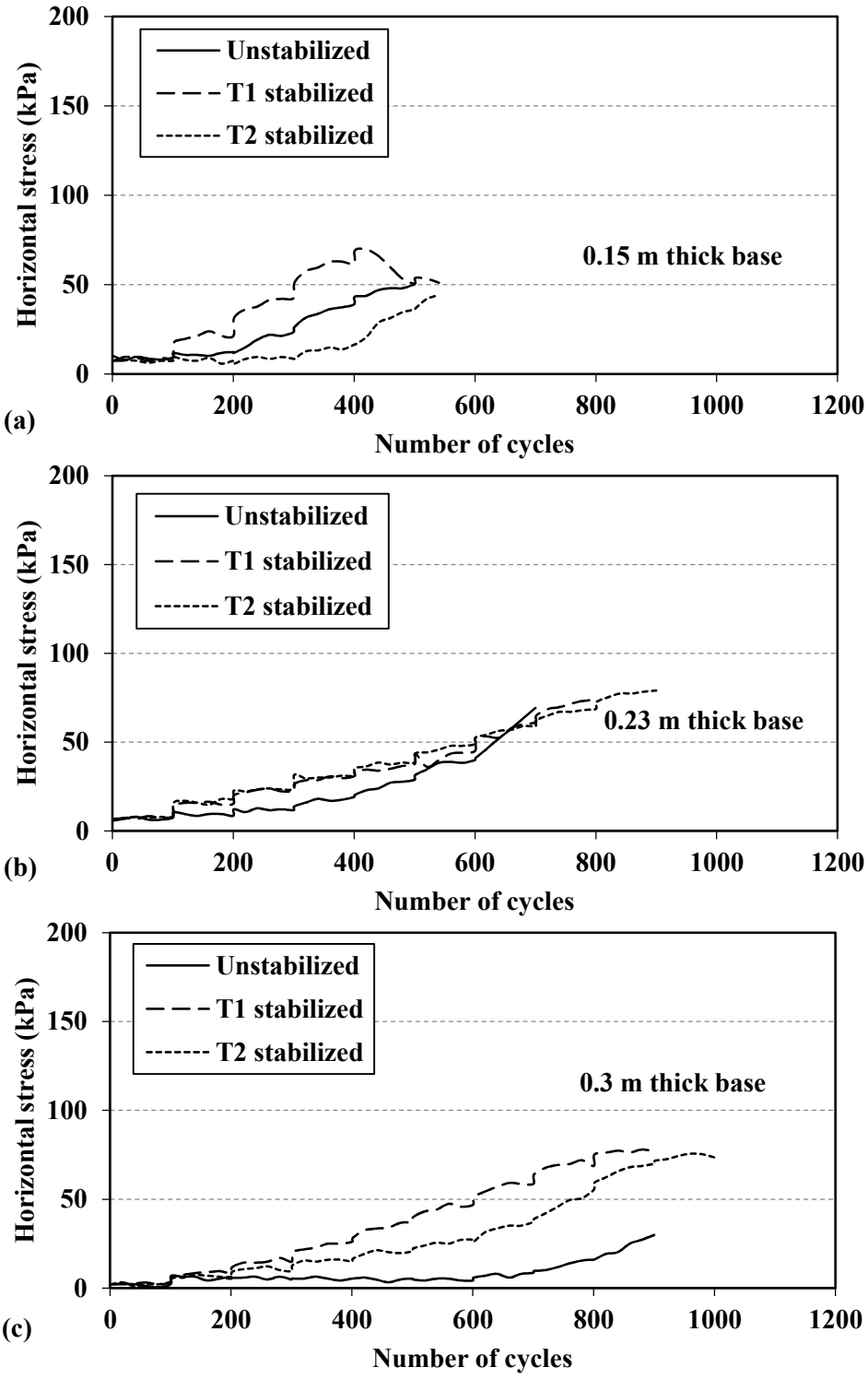

Figure 3.24 Maximum radial stress on top of subgrade with a distance of 0.18 m from the center vs. number of load cycles for: (a) 0.15-m-thick; (b) 0.23-m-thick; (c) 0.30-m-thick base course.

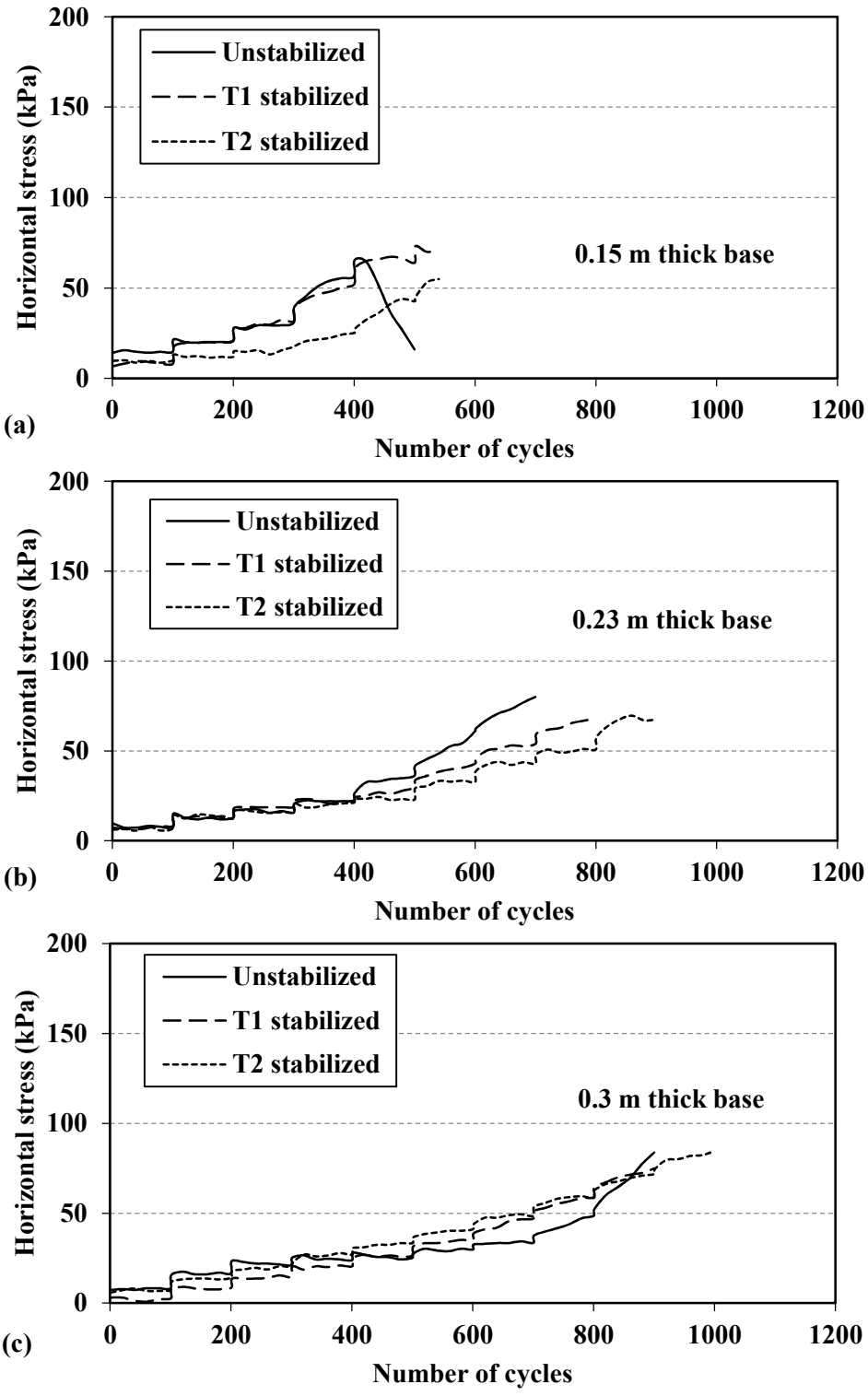

Figure 3.25 Maximum radial stress on top of subgrade with a distance of 0.25 m from the center vs. number of load cycles for: (a) 0.15-m-thick; (b) 0.23-m-thick; (c) 0.30-m-thick base course.

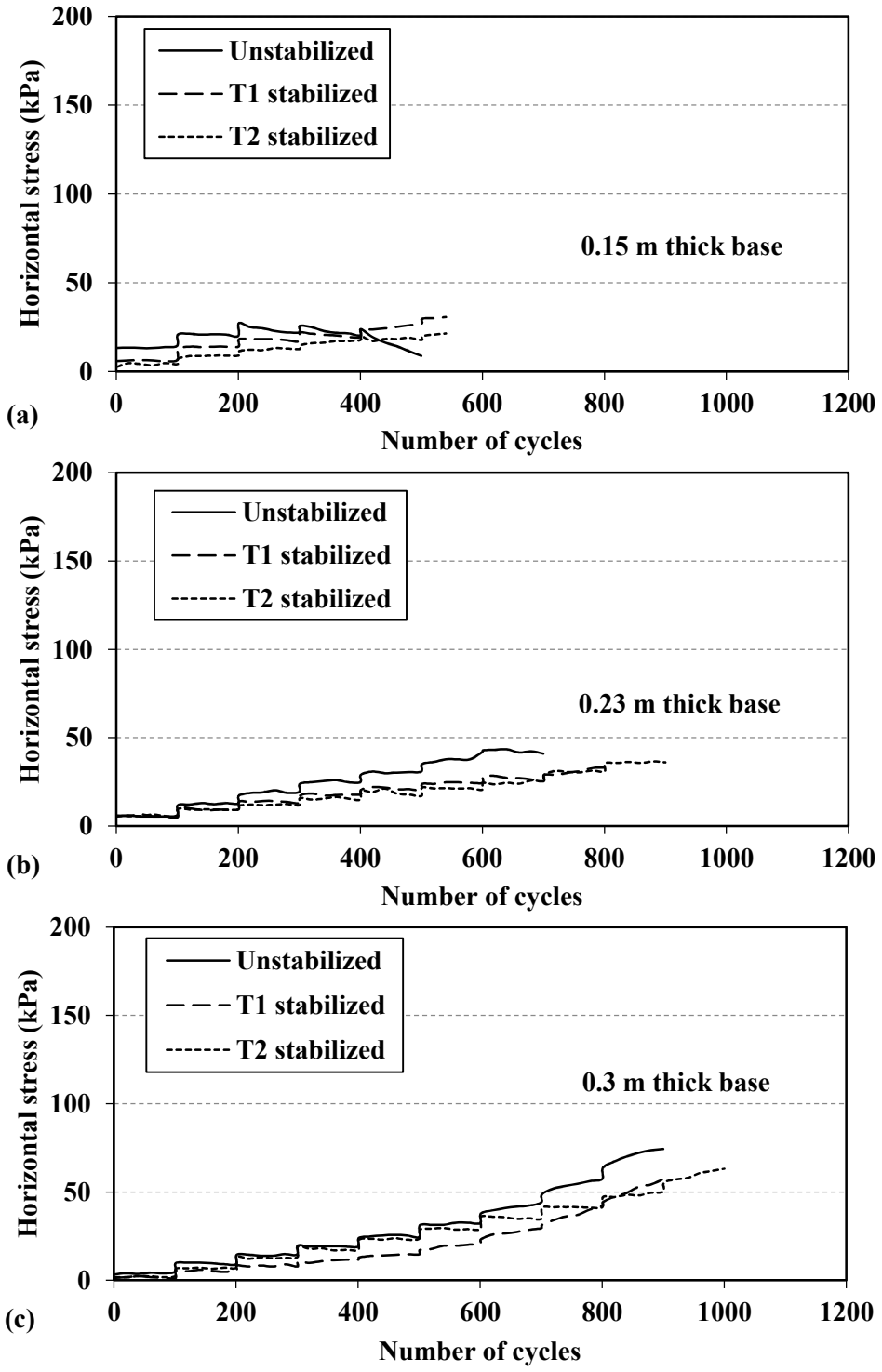

Figure 3.26 Maximum radial stress on top of subgrade with a distance of 0.38 m from the center vs. number of load cycles for: (a) 0.15-m-thick; (b) 0.23-m-thick; (c) 0.30-m-thick base course.

Permanent deformations

Figure 3.27 shows the measured surface permanent deformations in all the test sections. **Figure 3.28** presents the subgrade and base course permanent deformations in all the test sections. The subgrade permanent deformation was measured by the displacement transducer connected with a telltale seated on the top of the subgrade. The base course permanent deformations were estimated as the difference between the measured surface and subgrade permanent deformations.

Figure 3.27 shows that the permanent deformations in the stabilized test sections were reduced by the inclusion of the geogrid as compared with those in the unstabilized test sections. The reduction was not obvious when the load magnitude was relatively low, whereas it became significant at the higher load magnitude due to the mobilization of the geogrid. With the increase of the load magnitude, the rate of the accumulation of the permanent deformation increased pronouncedly. Under each load stage, the accumulation of the permanent deformation decelerated with the increase of the number of load cycles. This result indicates the strain hardening of soils. When the load magnitude was comparatively low, the trend agreed with the damage model developed by Tseng and Lytton (1989). Under the higher load magnitude, the trend was different from Tseng and Lytton's model, in which the accumulation of the permanent deformation would stop eventually. The reason for this disagreement is that the applied load exceeded the bearing capacities of the test sections, so that the deformation became unstable. When a heavier duty geogrid (i.e. T2) was included, the reduction of the permanent deformation became more obvious, especially in the test sections with the base course thicknesses of 0.15 and 0.23 m, as shown in **Figure 3.27** (a) and (b).

In **Figure 3.28**, the subgrade permanent deformation had a similar trend to the surface permanent deformation. Under a lower load magnitude, the rate of the accumulation of the subgrade permanent deformation under each load stage decreased with the increase of load cycles. Under a higher load magnitude, however, the rate of the accumulation of the subgrade permanent deformation increased significantly. In **Figure 3.28**, it is obvious that the surface permanent deformation was mainly contributed by the subgrade. Under the lower load magnitude, the accumulation of the permanent deformation in the base course was quite slow so that it can be neglected. Under the higher load magnitude, however, the deformation in the base course accelerated with the increase of load cycles. There are two reasons for this phenomenon: (1) the quality of base course was much deteriorated after hundreds of load cycles and (2) the load magnitude was high enough so that the test section was close to or experienced a bearing failure. As shown in **Figure 3.28**, the geogrid reduced the surface permanent deformation by reducing both the permanent deformations of the subgrade and the base course. In addition, the heavy duty geogrid showed more benefit in reducing the permanent deformations of the subgrade and the base course.

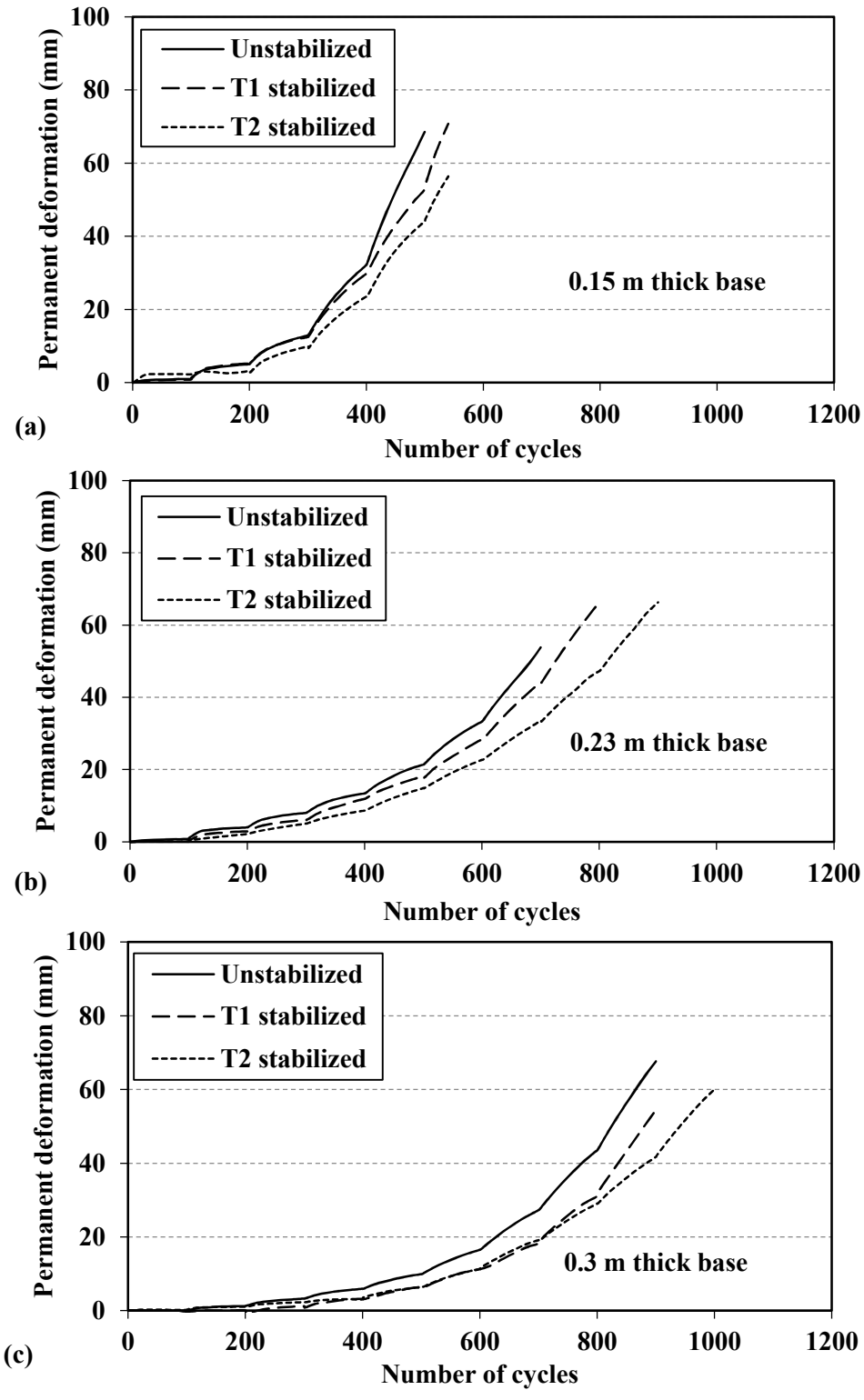

Figure 3.27 Surface permanent deformation vs. number of load cycles for: (a) 0.15-m-thick; (b) 0.23-m-thick; (c) 0.30-m-thick base course.

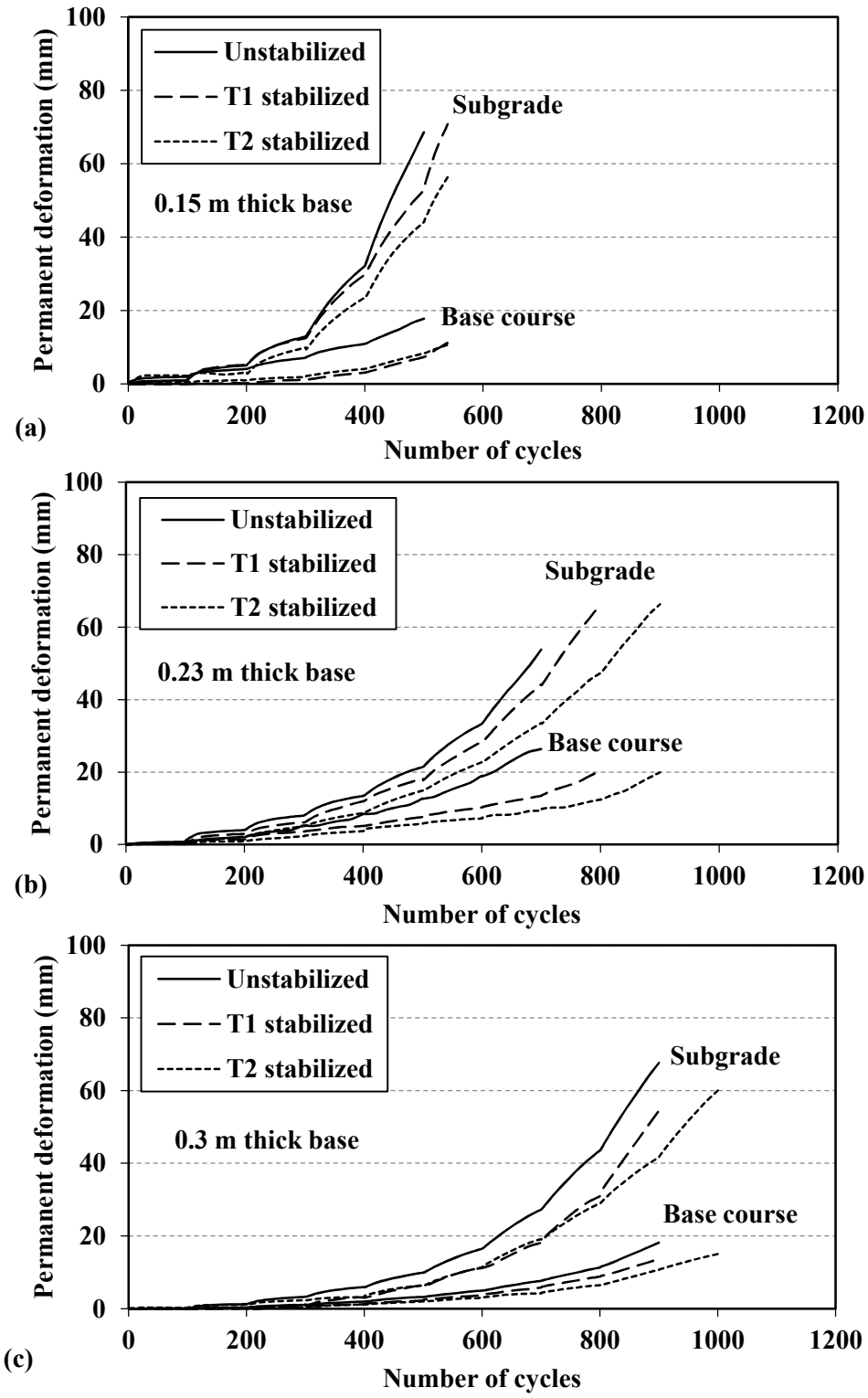

Figure 3.28 Subgrade permanent deformation vs. number of load cycles for: (a) 0.15-m-thick; (b) 0.23-m-thick; (c) 0.30-m-thick base course.

Resilient deformations

Figures 3.29 and **3.30** present the measured surface and subgrade resilient deformations in all the test sections, respectively. In **Figure 3.29**, the resilient deformations in the unstabilized sections increased proportionally with the load magnitude. For the stabilized sections, the resilient deformations increased proportionally with the increase of the load magnitude at the relatively lower load magnitude, but accelerated significantly at the higher load magnitude. By comparing the test sections with three different base course thicknesses, it is clear to see that the resilient deformations of the test sections decreased with the increase of base course thickness under the same load magnitude. This result indicates that the equivalent modulus of the section with a thicker base course was increased. Under a certain load magnitude, the resilient deformations in both the stabilized and unstabilized sections were maintained in a similar level when the number of cycles was relatively low. For the test sections with a 0.15 m thick base course, the stabilized test sections had slightly higher resilient deformations as compared with the unstabilized test sections. For the test sections with a 0.23 m thick base course, the resilient deformations of the stabilized and unstabilized sections were close to each other. With the 0.3 m thick base course, the test section stabilized by the T2 geogrid showed a similar resilient deformation as the unstabilized section, but that stabilized by the T1 geogrid had a relatively large variation.

In general, the geogrid stabilized sections had the greater resilient (recoverable) deformations than the unstabilized sections. This phenomenon is due to the lateral confinement of the geogrid and the recovery of the lateral deformation of the aggregate particles during the unloading stage. Under a higher load magnitude, the resilient

deformations in the stabilized sections increased significantly and were larger than those of the unstabilized sections.

Figure 3.30 shows the resilient deformations of the subgrade in all the test sections. The comparison of **Figure 3.29** with **Figure 3.30** shows that the surface resilient deformations of the test sections were mainly contributed by the subgrade. Therefore, the subgrade resilient deformations showed a similar trend to the surface resilient deformations as shown in **Figure 29**. Under the lower number of load cycles, the subgrade in the stabilized sections exhibited the slightly higher resilient deformations as compared with those of the unstabilized sections due to the confinement of the geogrid at the unloading stage as mentioned in the previous paragraph. Under the higher number of load cycles, the subgrade resilient deformations of the stabilized sections increased drastically and were much higher than those of the unstabilized sections.

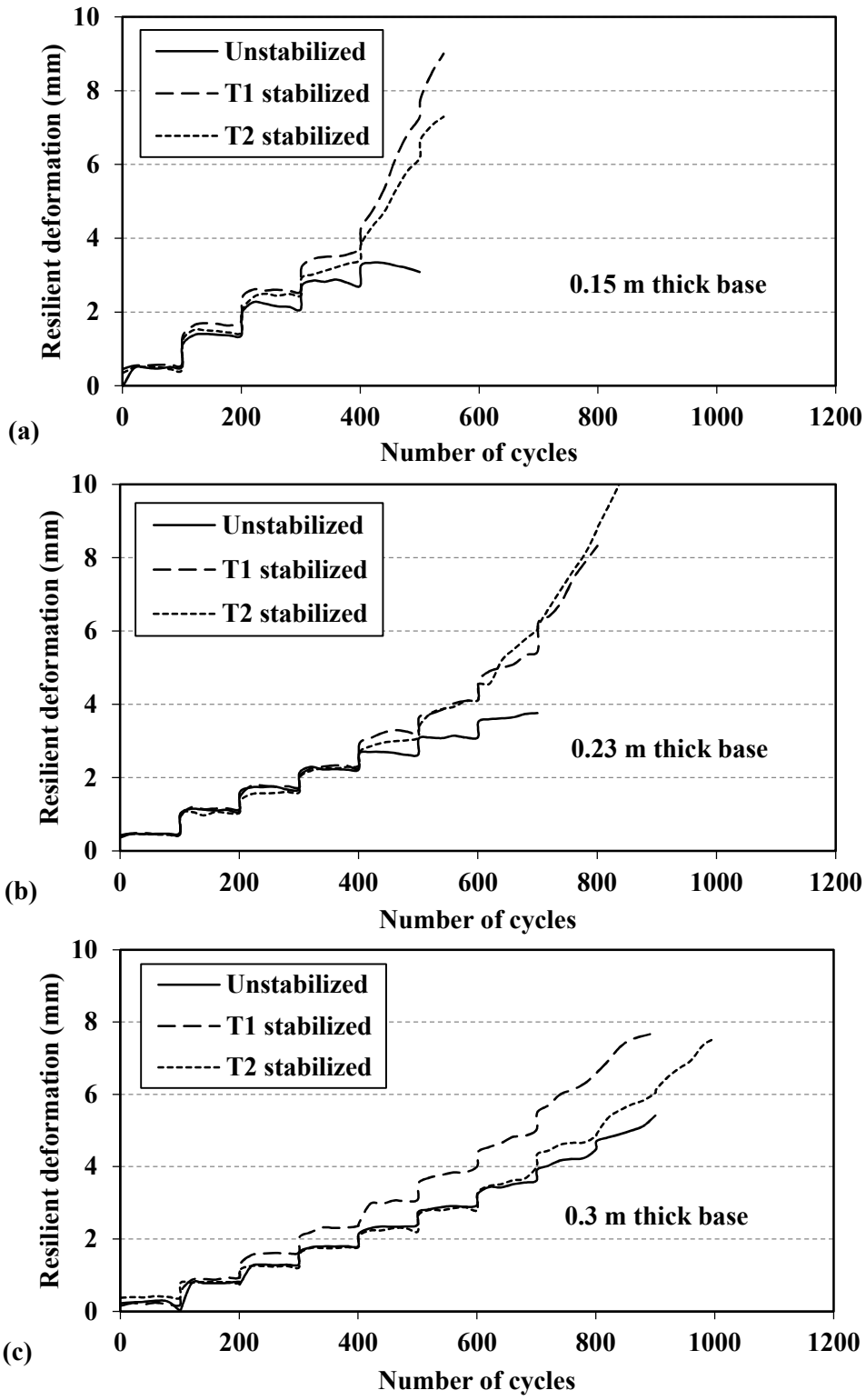

Figure 3.29 Measured surface resilient deformation vs. number of load cycles for: (a) 0.15-m-thick; (b) 0.23-m-thick; (c) 0.30-m-thick base course.

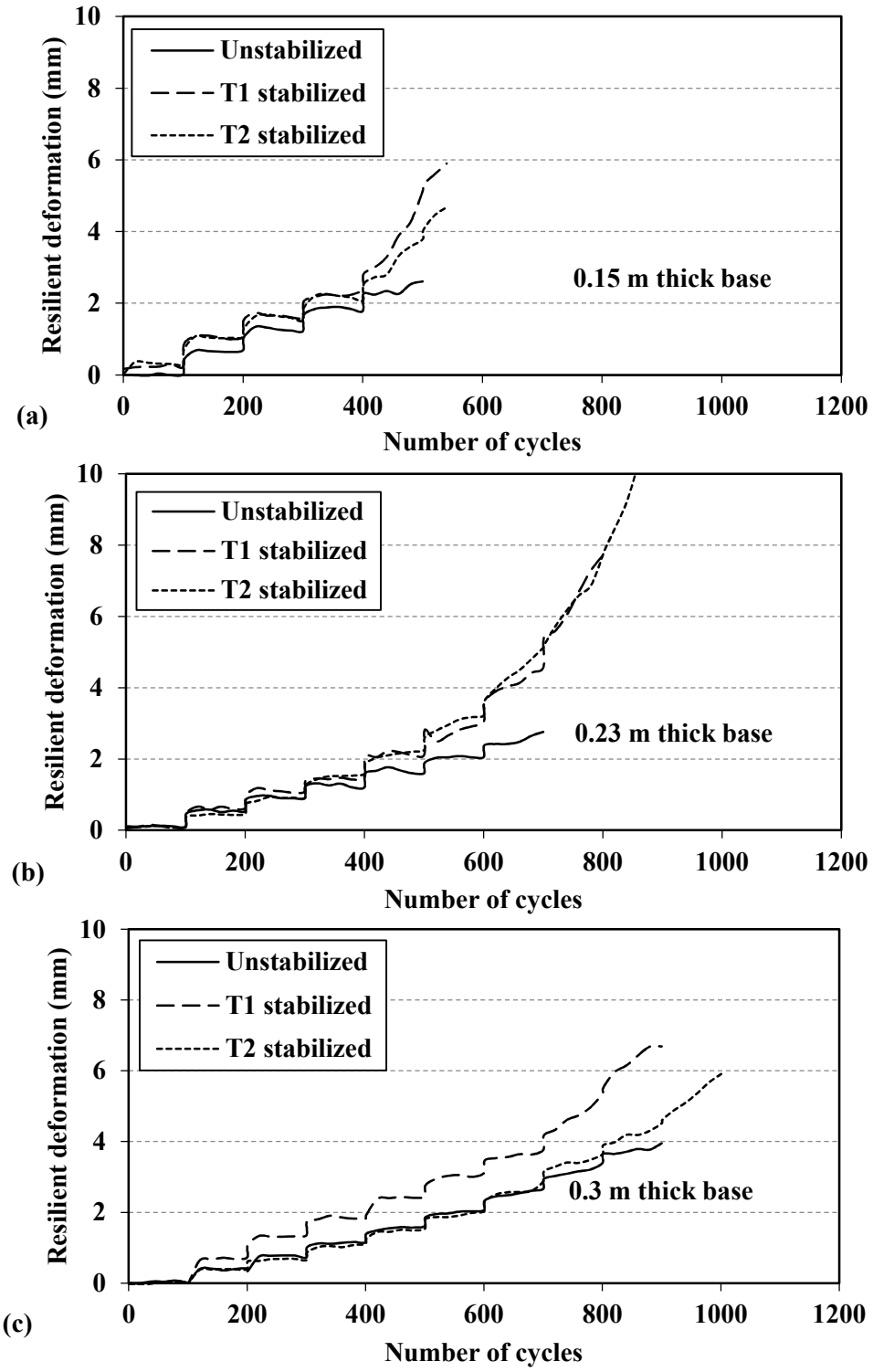

Figure 3.30 Measured subgrade resilient deformation vs. number of load cycles for: (a) 0.15-m-thick; (b) 0.23-m-thick; (c) 0.30-m-thick base course.

3.2.3 Summary

In this study, nine large-scale cyclic plate load tests were conducted to study the stress distribution, the permanent deformation, and the resilient behavior of the triaxial geogrid stabilized base courses over the weak subgrade. In the test sections, the base course layers were prepared with three different thicknesses (i.e. 0.15, 0.23, and 0.3 m) and the subgrade was prepared to have a CBR value approximately at 2%. Two types of triaxial geogrid (T1, a light duty, and T2, a heavy duty) were used to evaluate the influence of the geogrid type on the performance of the stabilized unpaved road sections. The changes in the vertical and horizontal stresses as well as the deformations at the surface and the subgrade under varying load magnitudes were monitored. From this study, the following conclusions can be drawn:

1) The vertical stress at the interface was reduced by the inclusion of geogrid; the reduction became more obvious when a heavier duty of geogrid was included. The distribution area of the vertical stress was widened due to the presence of the geogrid.

2) Under a relatively small load, the vertical stress did not change much with the increase of load cycles. Under a higher load magnitude, the vertical stress increased apparently with the increase of load cycles. This result indicates the deterioration of the base course due to the heavier load.

3) With the increase of base course thickness, the vertical stresses at the interface were reduced in both the stabilized and unstabilized sections, but the reduction of the vertical stresses at the interface contributed by the presence of the geogrid

decreased since the influence of the geogrid was reduced by the increase of base course thickness.

4) With the inclusion of the geogrid, the radial stress at the bottom of base course at 0.25 m from the center of the loading plate was increased, but that at 0.38 m from the center of the loading plate decreased. This result indicates that the lateral confinement of the geogrid changed the stress distribution of the radial stress and confined the radial stress into a smaller area close to the center.

5) The radial stress on the top of the subgrade at 0.18 m from the center increased, but those at 0.25 m and 0.38 m from the center decreased. In other words, the radial stress distribution on the top of the subgrade was confined by the geogrid as well.

6) The radial stresses in the base course and the subgrade increased with the increase of load magnitude. The radial stress in the base course increased drastically at a higher number of load cycles, indicating a large lateral movement of aggregate particles at the bottom of the base course.

7) The surface permanent deformation was reduced by the inclusion of the geogrid and the higher reduction in the permanent deformation was observed with the heavier duty geogrid. Both the subgrade and base course permanent deformations decreased in the stabilized sections. The surface permanent deformations mainly resulted from the subgrade deformations.

8) The rate of the surface permanent deformation increased with the increase of load magnitude. At a lower load magnitude, the rate of the accumulation decreased

with the increase of load cycles. At a higher load magnitude, however, the permanent deformation kept increasing with a higher accumulation rate. This result indicates that the test sections experienced a bearing failure.

9) The surface resilient deformation was mainly contributed by the subgrade as well. The lateral displacements of the aggregate particles under a load were restricted by the geogrid; therefore, the lateral deformations of the aggregate were recovered during the unloading stage in the stabilized sections while the unstabilized sections failed due to the progressive lateral displacements.

3.3 Repetitive static plate load test

3.3.1 Introduction

Most of the research that has been performed so far focused on the performance of geogrid-stabilized base courses under cyclic loading. However, cyclic plate load tests require special and expensive equipment (i.e., an actuator and a controller). Repetitive static plate load tests can be more easily done. However, it is unknown how repetitive static plate load results are compared with cyclic plate load tests, especially for geosynthetic-stabilized base courses over weak subgrade.

In this study, static plate load tests were conducted on 0.23-m thick unstabilized and geogrid-stabilized base courses over weak soil with a CBR of 2.0% constructed in the geotechnical testing box. In these tests, surface deformations, subgrade deformations, and vertical and horizontal stresses at the interface between base and subgrade were monitored by transducers placed at varying distances from the center of the loading plate.

The test results are compared with the results under cyclic plate loads with increasing load magnitudes.

3.3.2 Test materials and test setup

The test materials were the AB3 and subgrade, as discussed in the Section 3.1. The test setup was the same as that shown in **Figure 3.15**.

However, the loading wave was different. Three repetitive static plate load tests were conducted on the 0.23-m thick stabilized and unstabilized test sections to investigate the performance of the test sections under a static load. **Figure 3.31** shows the load intensity of the repetitive static load. The intensities of loading applied on a steel plate of 0.30 m in diameter were increased from 5 to 55 kN with each load increment of 5 kN. **Table 3.3** shows the average contact pressure under the steel loading plate, which can be calculated by the applied load divided by the area of the plate.

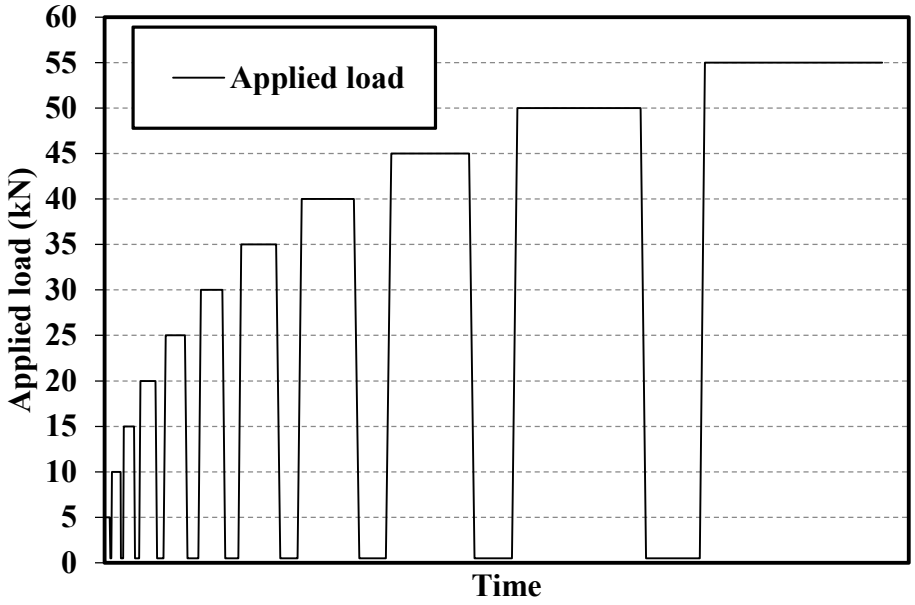

Figure 3.31 Load intensities of the repetitive static load test

Table 3.3 Average Contact pressures at different load intensities

Load (kN)	5	10	15	20	25	30
Average contact pressure (kPa)	71	141	212	283	354	424
Load (kN)	35	40	45	50	55	
Average contact pressure (kPa)	495	566	637	707	778	

Each load was maintained constantly until the rate of displacement was not more than 0.03 mm per minute at least for 3 minutes successively and then unloaded until the rebound met the same requirement (ASTM, 2009). The same procedure was repeated for all the load intensities until the maximum load was reached.

To compare with the performance of the test sections under cyclic loading, six cyclic plate load tests were conducted on the 0.23-thick stabilized and unstabilized test sections with increasing loading intensities. In the six cyclic plate load test sections, three of them were reported in Section 3.1, which had 100 cycles for each load magnitude; and the other three test sections were newly constructed and tested with 1000 cycles per load magnitude. The cyclic load waves are shown in **Figure 3.32**. The test was terminated if the permanent deformation was higher than 75 mm, which is considered as the failure criterion.

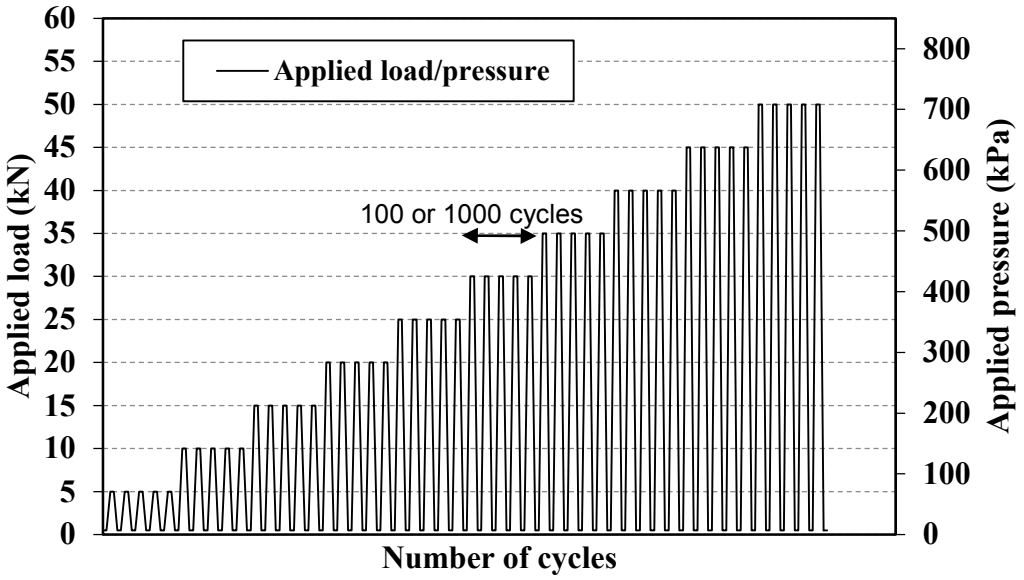

Figure 3.32 Load intensities of the cyclic load test

3.3.3 Test results and discussions

DCP test

Dynamic cone penetration (DCP) test was conducted to investigate the CBR values of the test sections for the repetitive static load test and the cyclic plate load test. For each test section, DCP tests were performed at 4 different locations and the CBR results at each location were calculated by Equation 3.2. The average CBR values for base course and subgrade in each test section are summarized in Table 3. For comparison purposes, the CBR results of test sections under cyclic plate loads with 100 cycles per load magnitude are presented again.

Table 3.4 Average CBR values of each test section from DCP tests

Loading type	Stabilized condition	CBR (%)	
		Subgrade	Base course
Repetitive static load	Unstabilized	2.1	15.3
	T1 stabilized	2.2	15.9
	T2 stabilized	2.2	15.7
Cyclic load (100 cycles for each load magnitude)	Unstabilized	2.3	14.2
	T1 stabilized	2.4	15.4
	T2 stabilized	2.3	14.9
Cyclic load (1000 cycles for each load magnitude)	Unstabilized	2.3	14.9
	T1 stabilized	2.4	14.7
	T2 stabilized	2.6	14.1

Vertical stresses

Figure 3.33 shows the vertical stresses at the interface between base course and subgrade. **Figures 3.33** (a), (b), and (c) represent the results under the repetitive static load, the cyclic load with 100 cycles per load magnitude, and the cyclic load with 1000 cycles per load magnitude, respectively. The vertical stresses at the end of each loading stage are chosen as the representative vertical stresses. As demonstrated in the figure, the vertical stresses at the interface of the stabilized test sections were reduced as compared with those in the unstabilized test sections and the reduction was more obvious in the test section stabilized by the geogrid of the higher duty. In addition, the increase of the average contact pressure signified the reduction of the vertical stresses in the stabilized test sections. This phenomenon indicates the mobilization of the geogrid. The

vertical stresses of test sections under the static load and the cyclic load had a similar trend. However, the test sections under a repetitive load needed a higher applied load to mobilize the geogrid. Taking the vertical stresses under 30 kN applied load as an example, as shown in the figure, the reduction of the vertical stress under the repetitive static load due to the geogrid was much lower than that under the cyclic load. The reason is that the geogrid was much mobilized in the test section under the cyclic load. In addition, the vertical stress under the cyclic load was higher than that under the repetitive static load for the unstabilized section. This result indicates that the deterioration of the base course under a cyclic load was more severe than that under the repetitive static load.

Figure 3.34 shows the comparison of the vertical stresses under the repetitive static load vs. those under the cyclic load with the same magnitude of the applied load. Basically, the results can be divided into two groups, Group A under relatively lower load magnitudes and Group B under higher load magnitudes. In Group A, the vertical stresses under the cyclic load were higher than those under the repetitive static load. The reason is that the deterioration of the base course under the dynamic load was more severe as compared with that under the repetitive static load. In Group B, vertical stresses under the cyclic load had no significant difference from those under the static load statistically. The reason for this phenomenon is that the cyclic load was more effective to mobilize the geogrid as compared with the repetitive static load so that the vertical stresses of test sections under the cyclic load decreased further. Geogrid confines the base course through the interlock between the aggregates and its apertures. Under a dynamic load, the interlock would become stronger as compared with that under a static load.

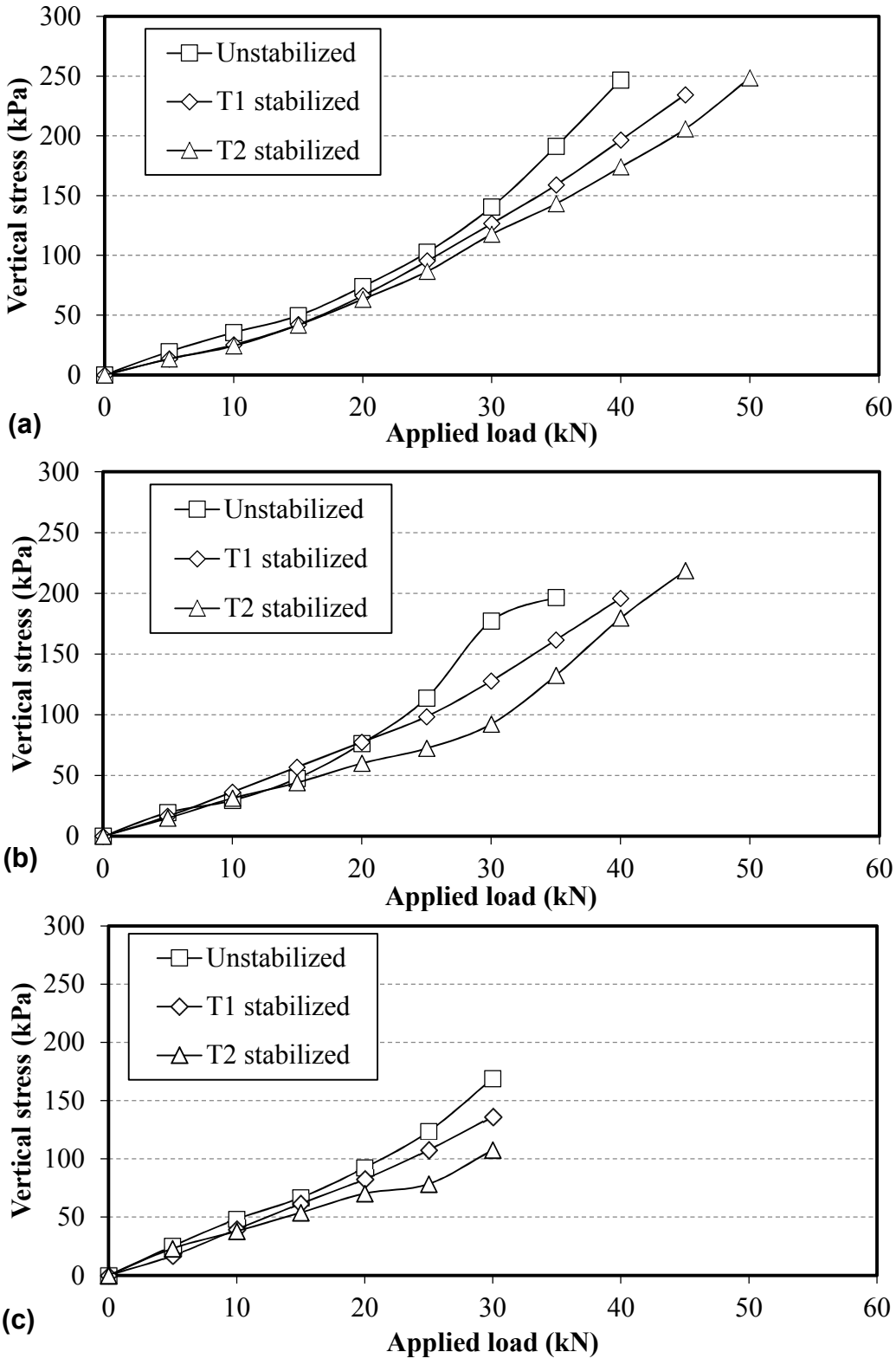

Figure 3.33. Maximum vertical stress at the interface under: (a) repetitive static load; (b) cyclic load with 100 cycles per load magnitude; and (c) cyclic load with 1000 cycles per load magnitude

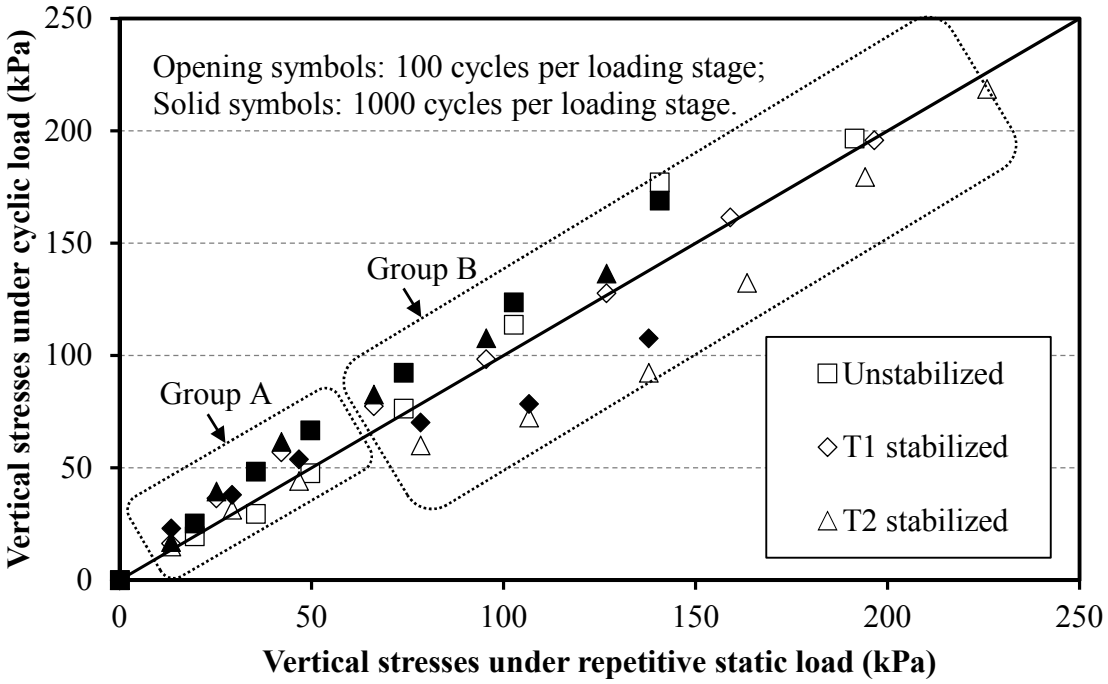

Figure 3.34. Vertical stresses under repetitive static load vs. those under cyclic load

Horizontal stresses

Figures 3.35, **3.36**, and **3.37** demonstrate the horizontal stresses near the bottom of the base course and the top of the subgrade at distances of 0.18, 0.25 and 0.38 m, respectively, from the center of the loading plate. In each figure, (a), (b) and (c) represent the horizontal stresses under a repetitive static load, a cyclic load with 100 cycles per load magnitude, and a cyclic load with 1000 cycles per load magnitude, respectively. In **Figure 3.35**, the horizontal stresses at the top of the subgrade increased with the presence of the geogrid at a distance of 0.18 m away from the center. In **Figure 3.36**, the horizontal stresses at the bottom of the base course at a distance of 0.25 m away from the center increased with the inclusion of the geogrid. At the same distance from the center, however, the horizontal stresses at the top of the subgrade decreased due to the inclusion of the geogrid. In **Figure 3.37**, the horizontal stresses both at the bottom of the base

course and at the top of the subgrade decreased due to the inclusion of the geogrid. The phenomenon that the horizontal stresses increased at a distance of 0.25 m from the center but decreased at a distance of 0.38 m away from the center at the bottom of the base course indicates the geogrid changed the distribution of the horizontal stresses in the base courses and tended to concentrate the horizontal stresses to an area closer to the loading plate. The geogrid confinement had a similar effect on the distribution of the horizontal stresses in the subgrade. For the horizontal stresses at all the locations (0.18, 0.25, and 0.38 m, away from the center), the test sections under the static and cyclic loading had a similar trend. This result indicates that the loading type would not change the distribution of the stresses.

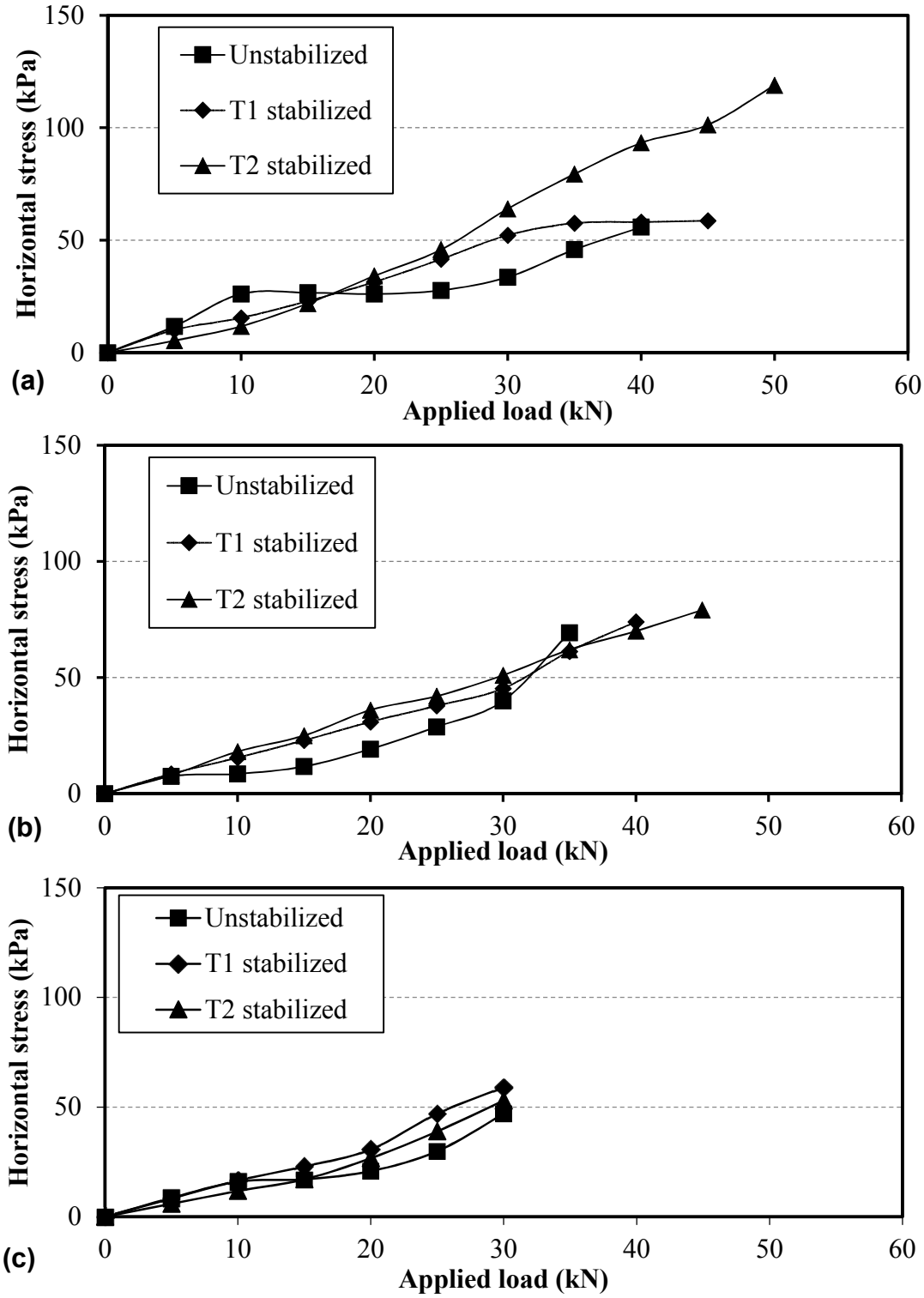

Figure 3.35. Horizontal stresses at the top of the subgrade with a 0.18 m away from the center under: (a) repetitive static load; (b) cyclic load with 100 cycles per load magnitude; and (c) cyclic load with 1000 cycles per load magnitude

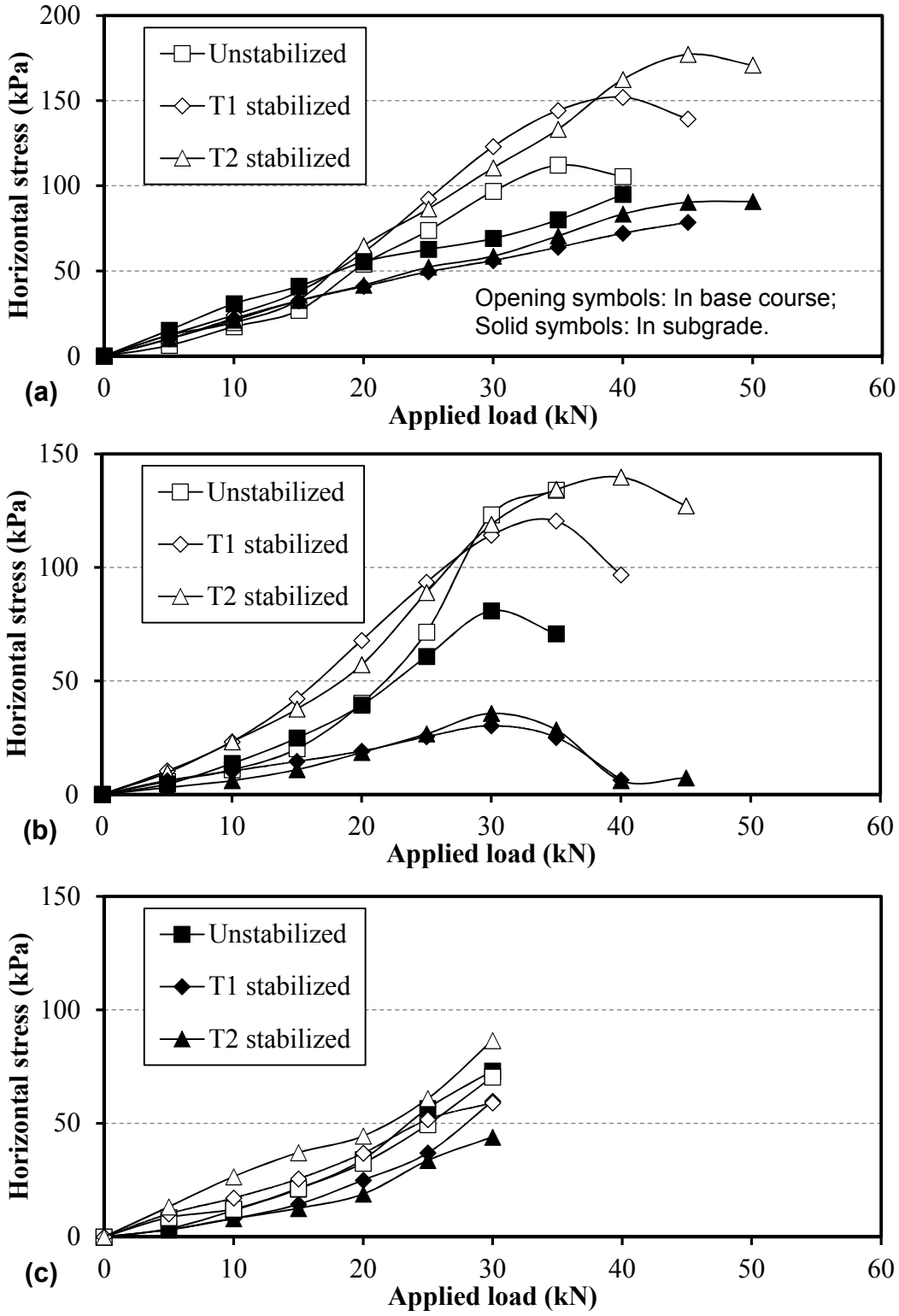

Figure 3.36. Horizontal stresses at a distance of 0.25 m from the center under: (a) repetitive static load; (b) cyclic load with 100 cycles per load magnitude; and (c) cyclic load with 1000 cycles per load magnitude

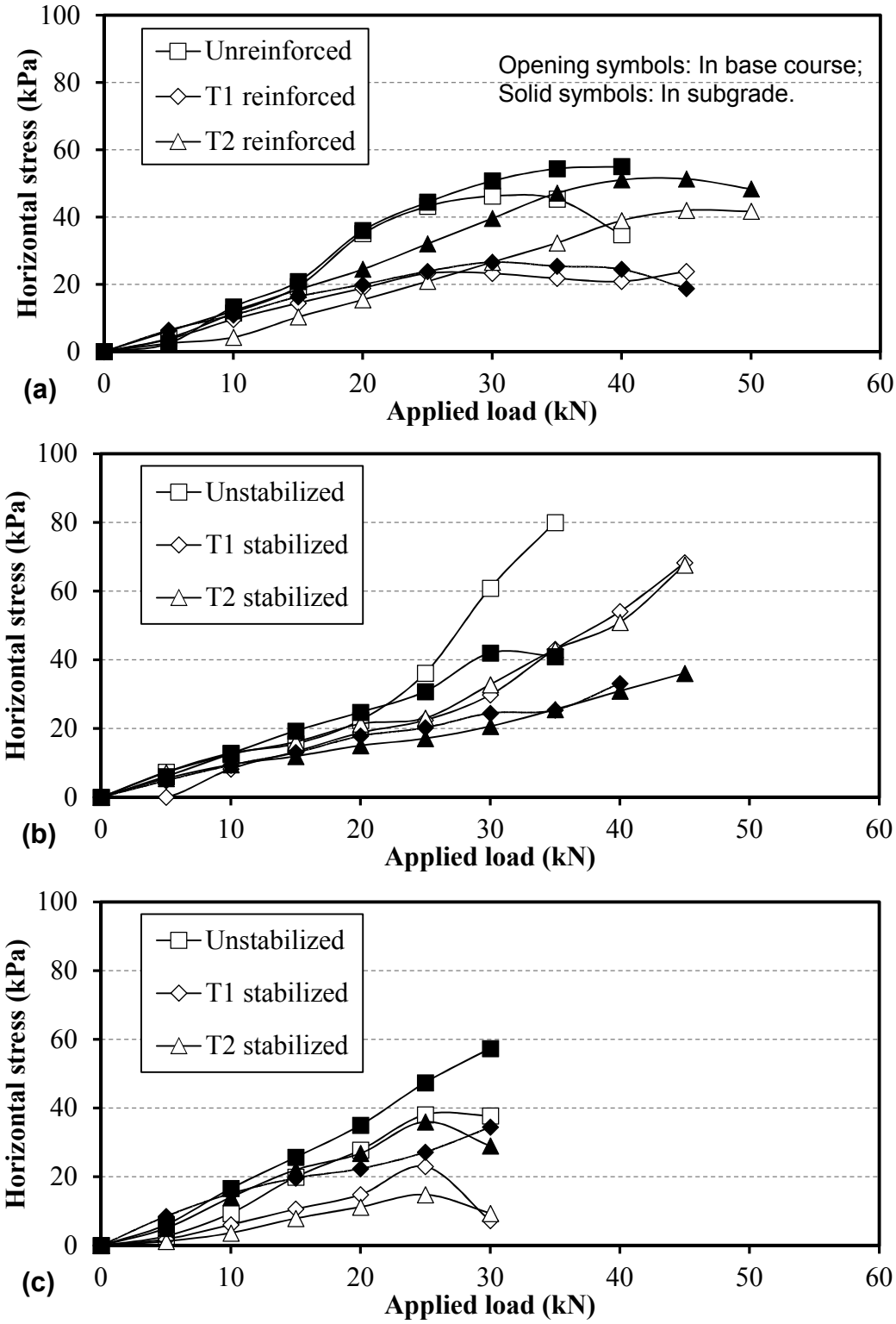

Figure 3.37. Horizontal stresses at a distance of 0.38 m from the center under: (a) repetitive static load; (b) cyclic load with 100 cycles per load magnitude; and (c) cyclic load with 1000 cycles per load magnitude

Resilient deformations

Figure 3.38 shows the surface resilient deformations of unstabilized, T1 stabilized, and T2 stabilized test sections. **Figures 3.38** (a), (b) and (c) show the results of test sections under the repetitive static load, the cyclic load with 100 cycles per loading stage, and the cyclic load with 1000 cycles per loading stage, respectively. As shown in the figure, the resilient deformations increased with the increase of the applied load. Under a relatively low load, the resilient deformations of unstabilized and stabilized test sections were close to each other. Under a higher magnitude of load, however, the resilient deformation of the stabilized sections increased significantly as compared with that of unstabilized sections. The two probable reasons for this phenomenon are that, firstly, the higher horizontal stresses in the base course restrained the soil and consequently led to the surface rebound at the unloading stage, and secondly, the tensioned geogrid not only supported the base course under the loading plate but also pushed the heaved subgrade soil around the loading plate back, which added more rebound of the stabilized test sections. The resilient deformations of the test sections under the repetitive static load and cyclic load shared a similar trend with the increase of the applied load. The resilient deformations of unstabilized test sections under the repetitive static load and cyclic load matched each other well. This result indicates that the loading type had no much influence on the resilient deformations of the test sections. The geogrid stabilized test sections under the repetitive static load had larger resilient deformations as compared with those under the cyclic load with 100 or 1000 cycles per loading stage. The reason for this phenomenon is that the deformations of the test sections under the repetitive static

load took longer to recover at the unloading stage as compared with those under the cyclic load.

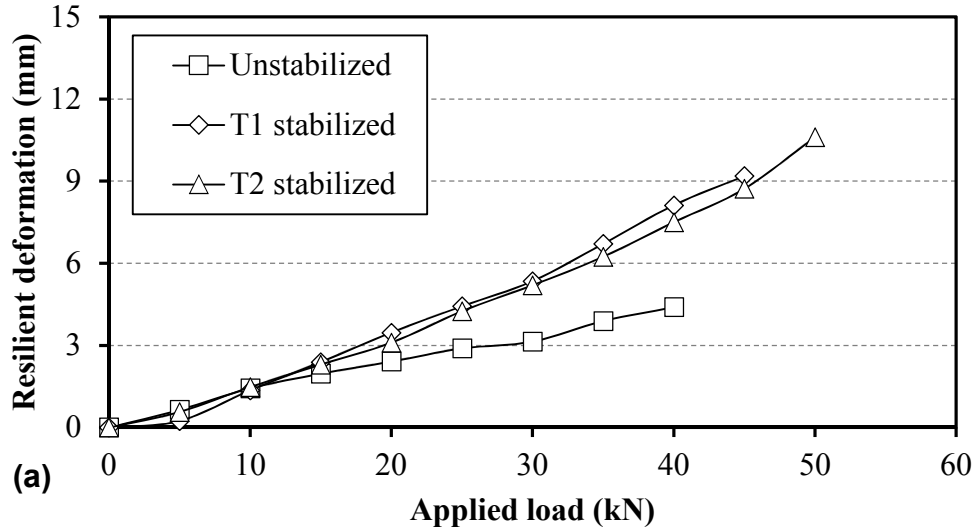

(a)

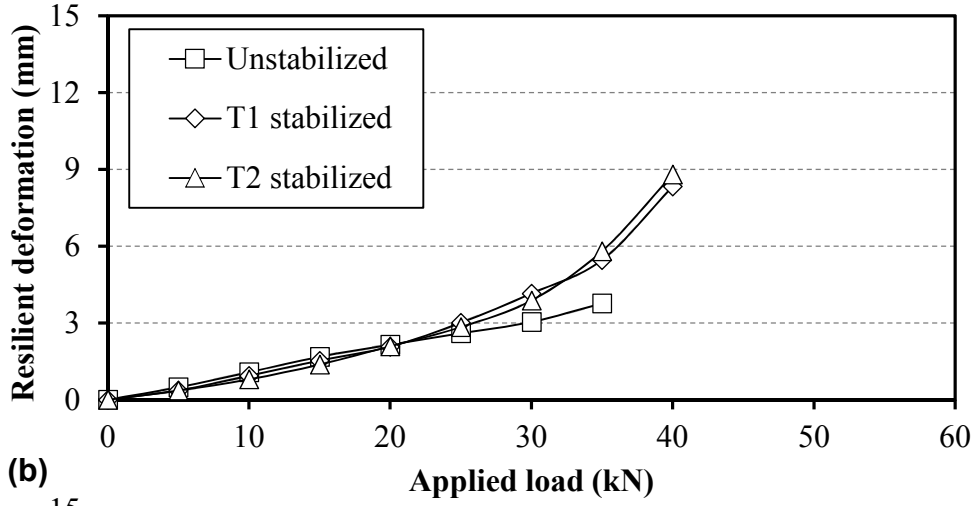

(b)

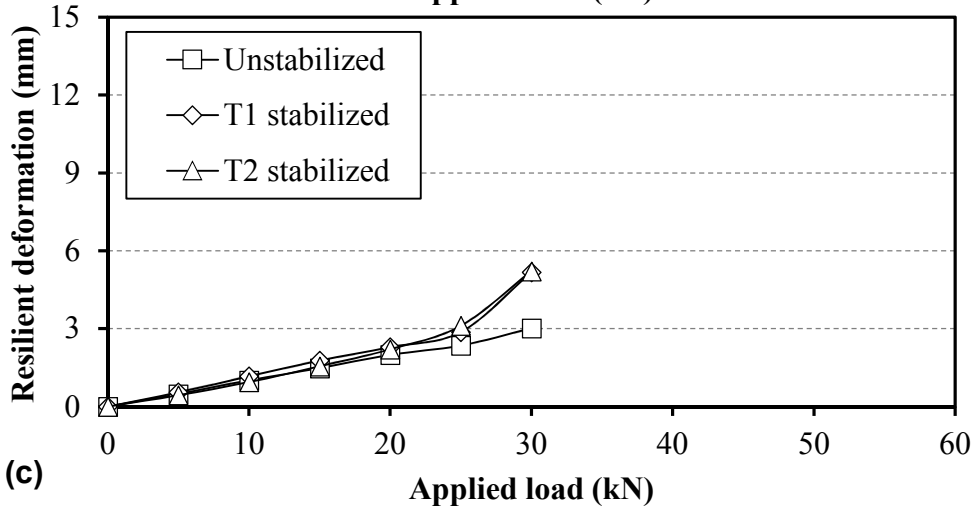

(c)

Figure 3.38. Surface resilient deformation under: (a) repetitive static load; (b) cyclic load with 100 cycles per load magnitude; and (c) cyclic load with 1000 cycles per load magnitude

Permanent deformations

Permanent deformation is one of the most important performance parameters for stabilized or unstabilized bases over weak subgrade. **Figure 3.39** shows the surface and subgrade permanent deformations of the unstabilized and stabilized test sections under the repetitive static load, the cyclic load with 100 cycles per loading stage, and the 1000 cycles per loading stage, respectively. With the increase of the applied load, the permanent deformations increased at the accelerated rate for all the test sections. For the stabilized test sections, the permanent deformations were reduced as compared with those of the unstabilized section and the amount of reduction increased with the increase of the applied load. This result indicates that the mobilization of the geogrid required a relatively large deformation. When the higher duty geogrid was used, the decrease of the surface permanent deformations was more obvious at the same magnitude of the applied load. The subgrade permanent deformations in all the test sections exhibited the same trend and the surface permanent deformations were mainly contributed by the subgrade permanent deformations. The difference between the surface and subgrade permanent deformation is the base permanent deformation. The base permanent deformation is usually neglected in the design of unpaved roads.

The loading type influenced the permanent deformations of the test sections significantly. As shown in the figure, the increasing rate of the permanent deformations for the test sections under the cyclic loading was much larger than that for the test sections under static loading, especially under a relatively higher applied load. The reason is that the

higher applied loads were close to the bearing capacities of the test sections so that the deformations became unstable.

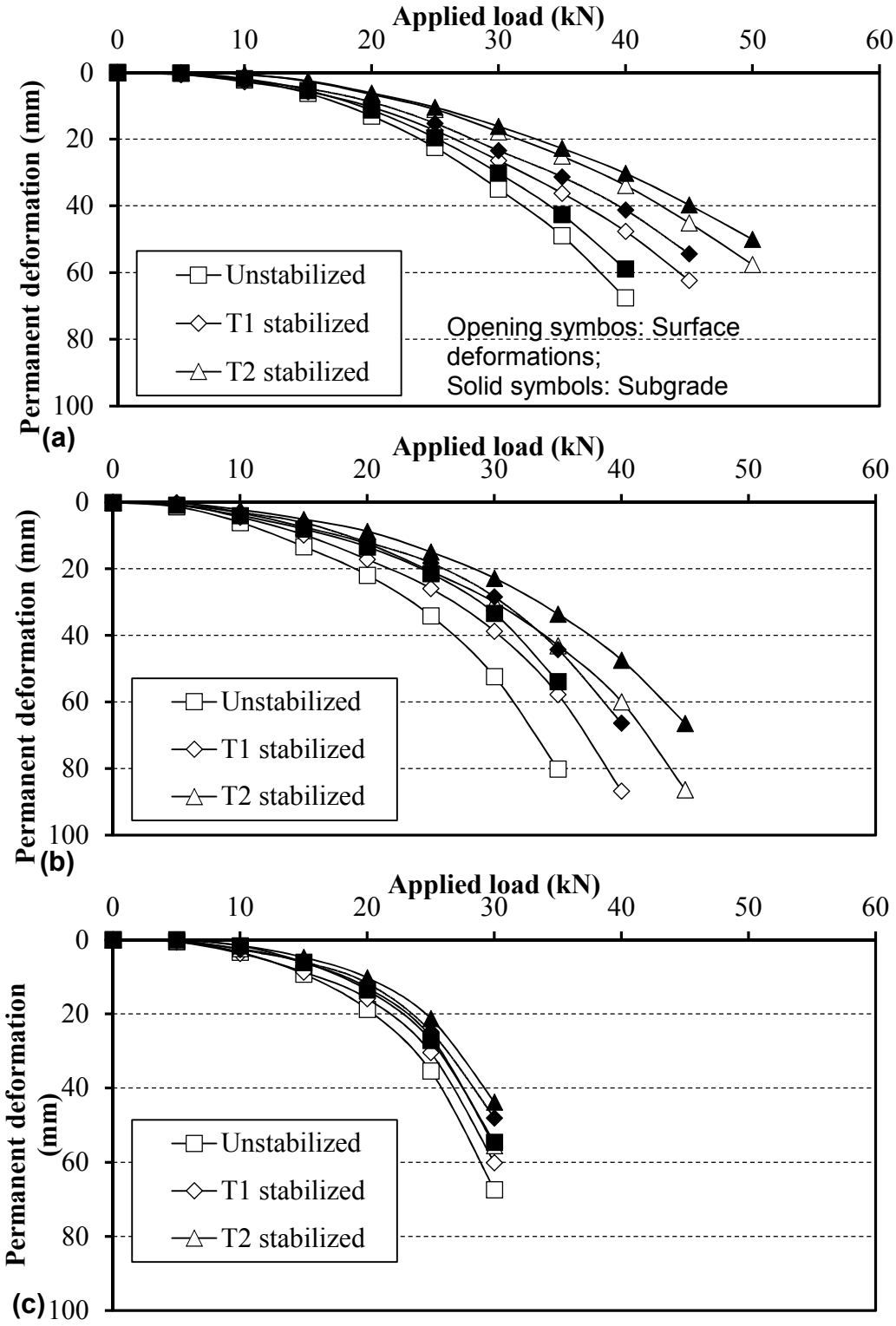

Figure 3.39. Surface/Subgrade permanent deformation under: (a) repetitive static load; (b) cyclic load with 100 cycles per load magnitude; and (c) cyclic load with 1000 cycles per load magnitude

Comparison of permanent deformations under repetitive static and cyclic loads

The permanent deformations under the repetitive static loading were compared with those under the cyclic loading with 100 or 1000 cycles per loading stage at the same loading intensities, as shown in **Figure 3.40**.

As shown in **Figure 3.40**, the permanent deformations of the test sections under the cyclic loading were much higher than those under the repetitive static loading at the same loading intensity. The permanent deformations of the test sections under the cyclic loading with 1000 cycles per loading stage were even higher. The correlation of the permanent deformations under cyclic loading and static loading can be expressed as **Equation 3.2**.

$$\mathrm{PD}_{c,100} = 1.7\mathrm{PD}_s$$

$$\mathrm{PD}_{c,1000} = 2.0\mathrm{PD}_s \qquad \textbf{Equation 3.2}$$

where $\mathrm{PD}_{c,100}$ = Permanent deformations under cyclic loading with 100 cycles at each loading intensity; $\mathrm{PD}_{c,1000}$ = Permanent deformations under cyclic loading with 1000 cycles at each loading intensity; and PDs = Permanent deformations under static loading.

Since the permanent deformation under cyclic loading is influenced significantly by the number of loading cycles, the comparison of the deformation with the higher number of loading cycles to that under static loading may need to be investigated to fully understand the correlation. However, the correlation shown in **Equation 3.2** is reliable if the applied load is relatively low so that the test sections will not experience a bearing failure. As

shown in **Figure 3.40**, the ratio of the permanent deformations under cyclic loading to those under static loading had no significant difference and ranged from 1.7 to 2.0.

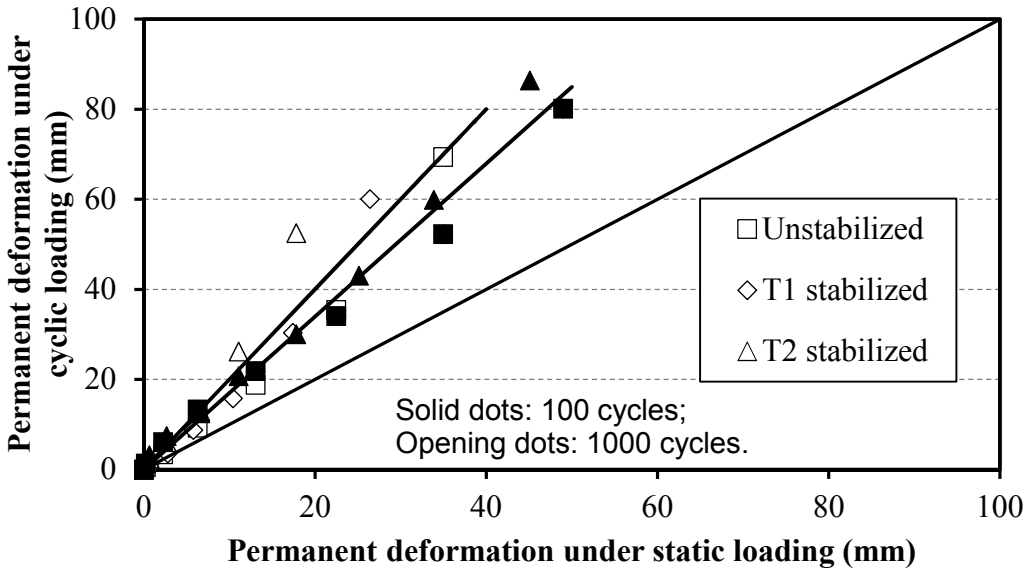

Figure 3.40. Permanent deformations under static loading vs. cyclic loading at the same loading intensities

3.3.4 Summary

Based on the experimental study in this section, the findings can be summarized as follows:

(1) Under the repetitive static load, the vertical stresses at the interface were reduced with the inclusion of the geogrid. The distribution of the horizontal stress in the base course was changed by the inclusion of the geogrid. The horizontal stresses at the bottom of the base course at a distance of 0.25 m from the center were increased and those at the distance of 0.38 m from the center decreased. This result indicates the influence of the geogrid confinement on the distribution of the horizontal stress in the base course. The

distribution of the horizontal stress in subgrade was changed as well. The horizontal stresses at the top of the subgrade at a distance of 0.18 m from the center were increased, while those at the distances of 0.25 and 0.38 m from the center decreased.

(2) The vertical and horizontal stress distributions in the test sections under the repetitive static load had no much difference from those in the test sections under the cyclic load. However, the loading type had a significant influence on the permanent deformations.

(3) The permanent deformations of the test sections under the repetitive static load were much lower than those under the cyclic load. The ratio of the permanent deformations under cyclic loading to those under static loading at the same loading intensity increased with the increase of the number of cycles per loading stage, but the increasing rate decreased.

(4) The ratio of the permanent deformations under cyclic loading to those under static loading at the same loading intensity ranged from 1.7 to 2.0 if the number of cycles per loading stage increased from 100 to 1000.

(5) The resilient deformations of stabilized test sections were higher than those of unstabilized test sections under the repetitive static load due to the recovery of the lateral movement of the soil under the confinement of the geogrid. The stabilized sections under the repetitive static load had higher resilient deformations as compared with those under the cyclic load. The reason is that the test sections under the repetitive static load had a longer period of unloading so that the soil would recover more under the confinement of the geogrid.

3.4 Geogrid-stabilized bases under a 40-kN cyclic load

3.4.1 Introduction

For the sections of geogrid-stabilized bases over subgrade, the base quality and the subgrade CBR influence the performance significantly. Firstly, the base quality and the subgrade CBR are relevant to the modulus ratio in a two layer system. According to the layered theory, the vertical stress distribution between the base and the subgrade is dominated by the modulus ratio. Therefore, the accumulation rate of the subgrade rutting (i.e., permanent deformation) varies. Secondly, the bearing capacity of subgrade changes if the subgrade CBR changes. Therefore, the test section will experience a bearing failure if the vertical stress at the interface is higher than the bearing capacity of subgrade. The accumulation of the subgrade rutting changes as well. Additionally, the resilient behavior of the test sections with varying base course and subgrade CBRs has not been well investigated yet. In this study, therefore, test sections with different base course and subgrade conditions were prepared and tested under a 40 kN cyclic load, which is the standard wheel load.

3.4.2 Test materials and test setup

The AB3 and Kaolin-sand mixture as discussed in Section 3.1 were used in this study as the base course and subgrade materials as well. To obtain a base course with lower quality, the AB3 was mixed with turf soil at a ratio of 1:1 by weight. The base course was named as the AB3-soil mixture. During the preparation of the test sections, subgrade was compacted at two different moisture contents with the corresponding CBRs of subgrade at 3% and 5%, respectively. These two base courses were compacted to the

degree of compaction of 95%. The thickness of the base course was controlled at 0.15 m. Totally, eight test sections were constructed and tested in this study.

The test setup was the same as that shown in **Figure 3.41**. Four pressure cells were installed at the interface between the base course and the subgrade with the distances from the center of 0, 0.18, 0.25, and 0.38 m, respectively. Displacement transducers were installed at the surface of the test sections with the distances from the center of 0, 0.25, 0.5 m, respectively. To measure the deformation of subgrade, a displacement transducer was installed on a telltale, the bottom of which was seated on the top of subgrade. During the plate load test, a cyclic load with a magnitude of 40 kN was applied on the test sections. **Figure 3.42** shows the load intensity of the repetitive static load.

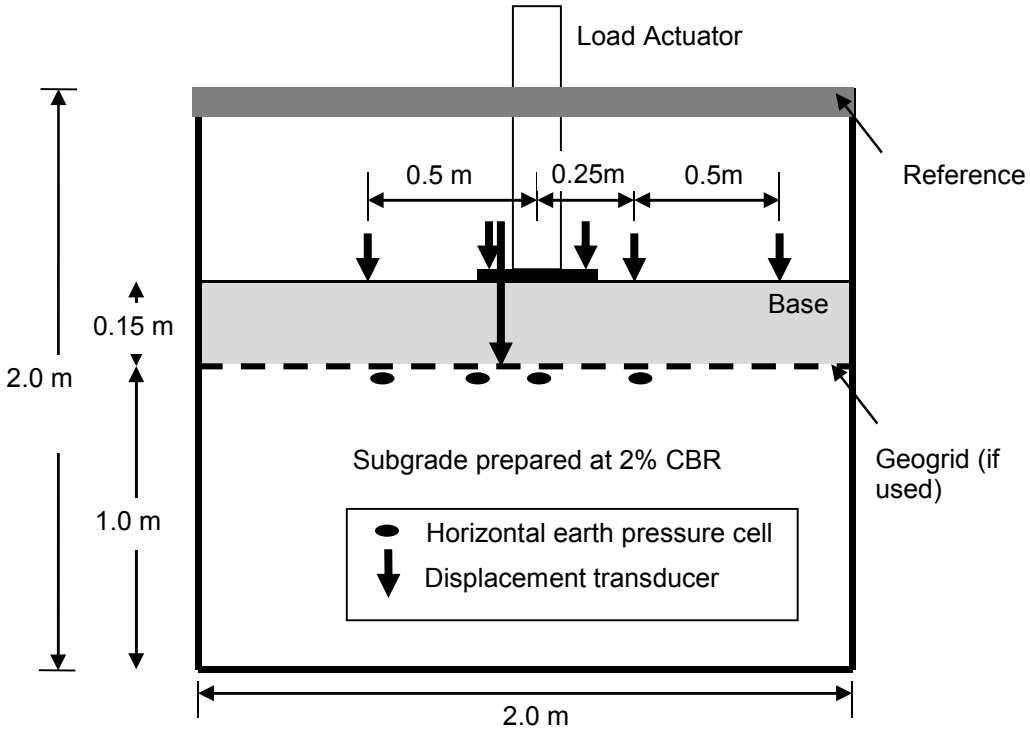

Figure 3.41 Test setup

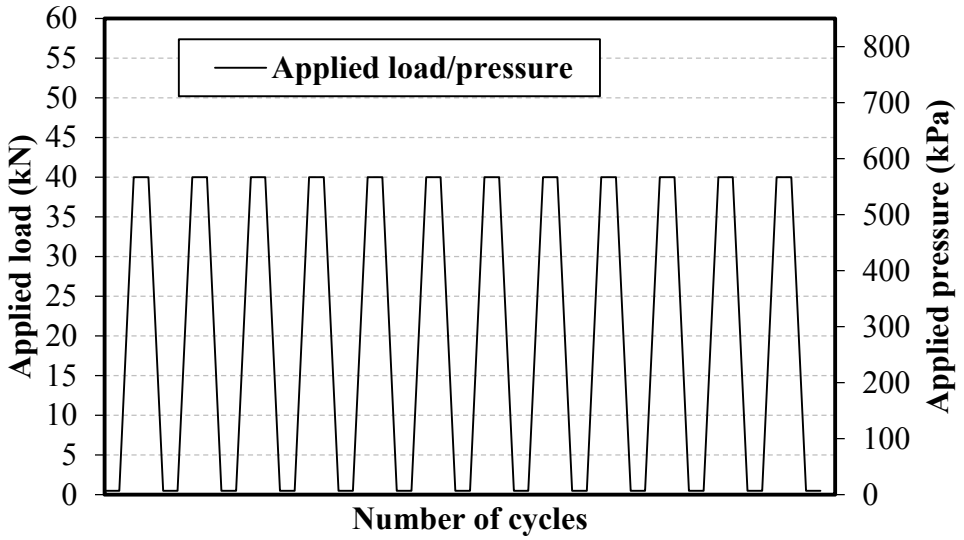

Figure 3.42 Load wave with the magnitude of 40 kN

3.4.3 Test results and discussions

DCP test

Dynamic cone penetration (DCP) tests were conducted to investigate the CBR values of the test sections for the 40 kN cyclic plate load test. The test procedures were the same as mentioned in the previous study and the CBR values were calculated by **Equation 3.1**. The average CBR values for base course and subgrade in each test section are summarized in **Table 3.5**. As shown in **Table 3.5**, the subgrade had a CBR value close to 3% or 5%. The CBR values of the AB3 and AB3-soil mixture were around 14% and 10%, respectively.

Table 3.5 Average CBR values from DCP tests

Loading type	Stabilized condition	CBR (%)		
		Subgrade	Base course	
			AB3	AB3-soil mixture
40 kN cyclic load	Unstabilized	3.3	14.3	
	T1 stabilized	3.5	13.7	
	Unstabilized	3.1		10.5
	T1 stabilized	3.4		9.8
	Unstabilized	4.8	14.6	
	T1 stabilized	5.2	15.5	
	Unstabilized	4.6		9.5
	T1 stabilized	4.9		10.2

Vertical stresses

Figures 3.43 and **3.44** show the vertical stresses at the interface in all the test sections. Overall, the vertical stresses decreased with the inclusion of the T1 geogrid. This phenomenon is similar to that observed in the previous sections of this study. With the increase of the load cycles, the vertical stresses increased gradually. This result indicates the deterioration of the base course. However, the increasing rate of the vertical stresses decreased with the increase of the number of cycles.

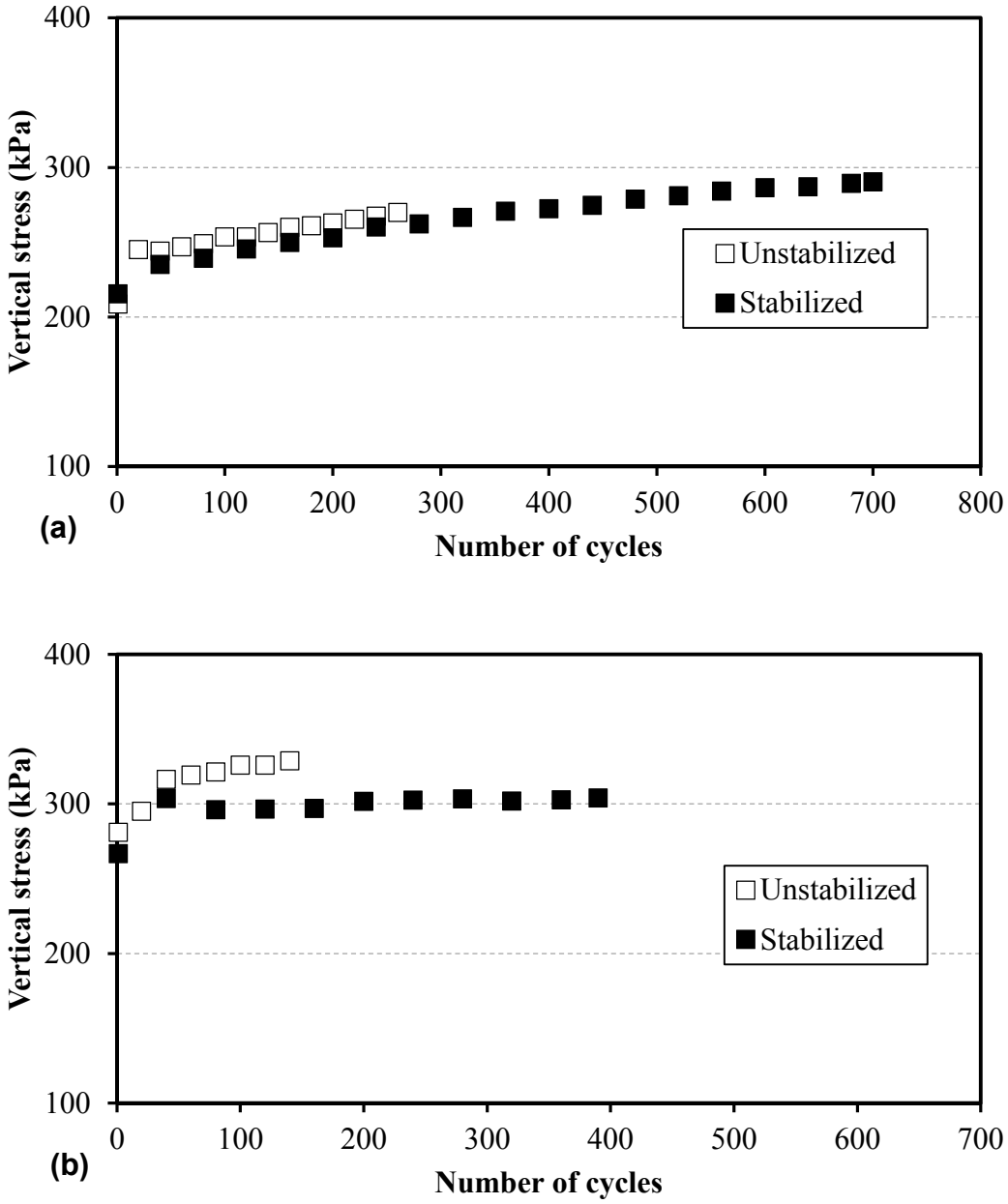

Figure 3.43 Vertical stress at the interface vs. number of cycles for the test section with subgrade CBR of 3% and: (a) AB3 base and (b) AB3-soil mixture base

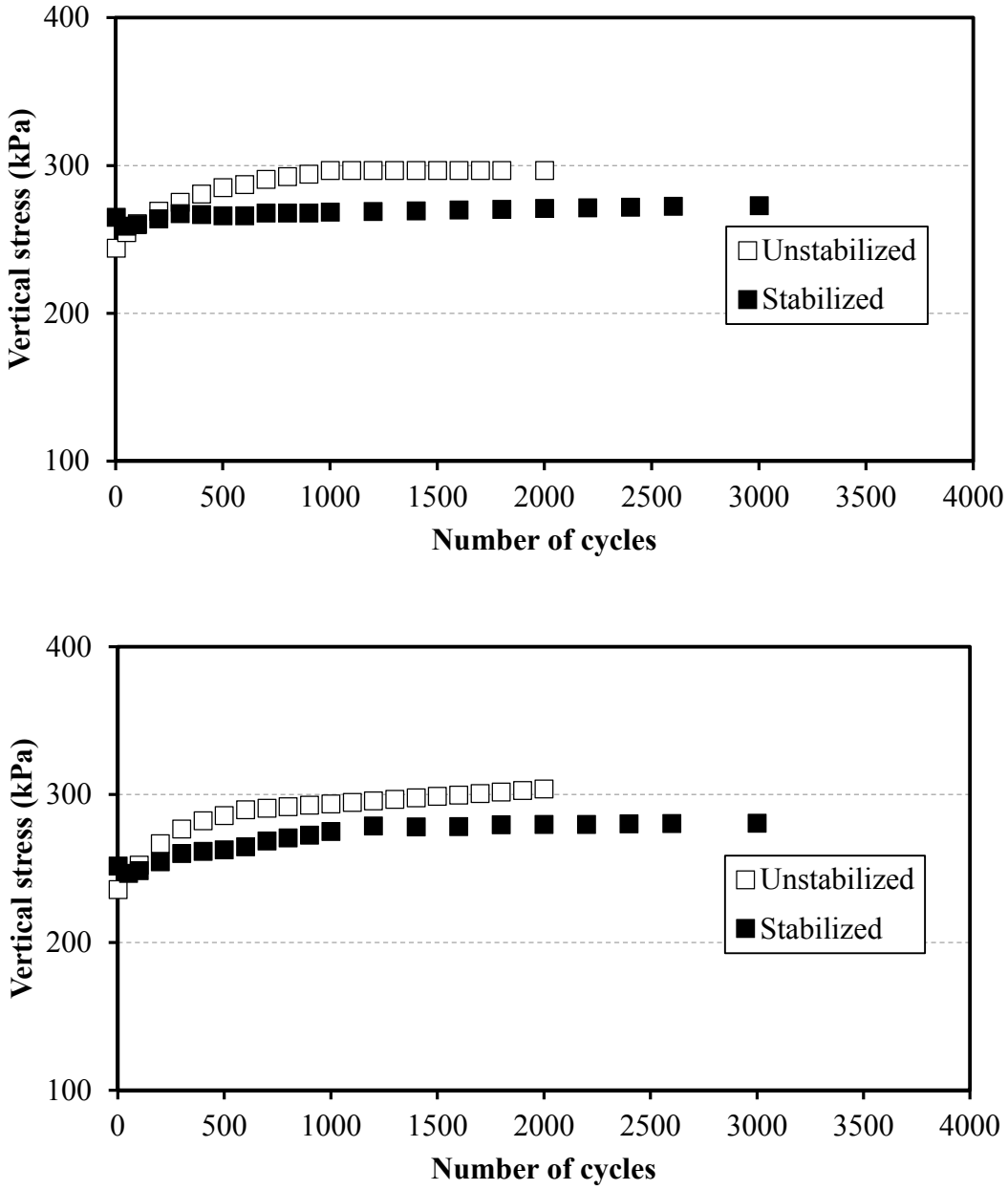

Figure 3.44 Vertical stress at the interface vs. number of cycles for the test section with subgrade CBR of 5% and: (a) AB3 base and (b) AB3-soil mixture base

As compared with those of the test sections with AB3 bases, the vertical stresses of the test sections with AB3-soil mixture bases were higher because the modulus of the AB3-soil mixture base was lower than that of the AB3 base. According to the layered elastic

theory, the decrease of the modulus ratio of the base course to subgrade results in the increase of the vertical stress at the interface. Similarly, the increase of the subgrade modulus causes the decrease of the modulus ratio as well. Therefore, the vertical stresses of the test sections with the subgrade CBR at 5% were higher than those of the test sections with the subgrade CBR at 3%. The vertical stresses shown in **Figure 3.44** were higher those shown in **Figure 3.43**.

Figures 3.43 and **3.44** show that the average maximum vertical pressures in the test sections with the subgrade CBR values at 3% and 5% were 260 and 290 kPa, respectively. The bearing capacity of the subgrade can be evaluated by **Equation 3.3** :

$$q = N_c c_u \qquad \textbf{Equation 3.3}$$

where q = bearing capacity, kPa; N_c = bearing capacity factor, 3.14; and c_u = undrained shear strength, kPa.

The undrained shear strength, c_u, of each test section was approximately deduced from CBR value of the subgrade soil using **Equation 3.4** (Han et al., 2011).

$$c_u = 20CBR \qquad \textbf{Equation 3.4}$$

Therefore, the bearing capacities of the subgrade with the average CBR values at 3% and 5% were 190 and 310 kPa, respectively. As compared with the average vertical stresses, 260 and 290 kPa, the test sections with the subgrade CBR at 3% likely experienced a bearing failure.

Permanent deformations

Figures 3.45 and **3.46** show the surface and subgrade permanent deformations of all the test sections. The increase rate of the permanent deformation at the initial stage was high and decreased with the increase of the loading cycles. The surface permanent deformation mainly came from the deformation of the subgrade. As shown in **Figure 3.45**, the permanent deformations were significantly reduced by the inclusion of the geogrid. The test sections with the AB3-soil mixture base course were much weaker than those with the AB3 base course in terms of the number of cycles to reach the same permanent deformation. For the test sections with the subgrade CBR at 5%, as shown in **Figure 3.46**, the number of cycles increased significantly to reach the same permanent deformations as compared with the test sections with the subgrade CBR at 3%. In addition, the T1 stabilized test sections had lower permanent deformations. The surface and subgrade permanent deformations of the test sections with the AB3-soil mixture bases were slightly higher those of the test sections with the AB3 bases. However, their differences were not as significant as those of the test sections with the subgrade CBR at 3%, as shown in **Figure 3.46**. This result indicates that, for a test section with stronger subgrade, the quality of the base course was not as significant as that for a test section with weak subgrade. The main reason is that the test sections with stronger subgrade could avoid a bearing failure so that the accumulation of the permanent deformation became stable, while that of the test sections with weaker subgrade was unstable.

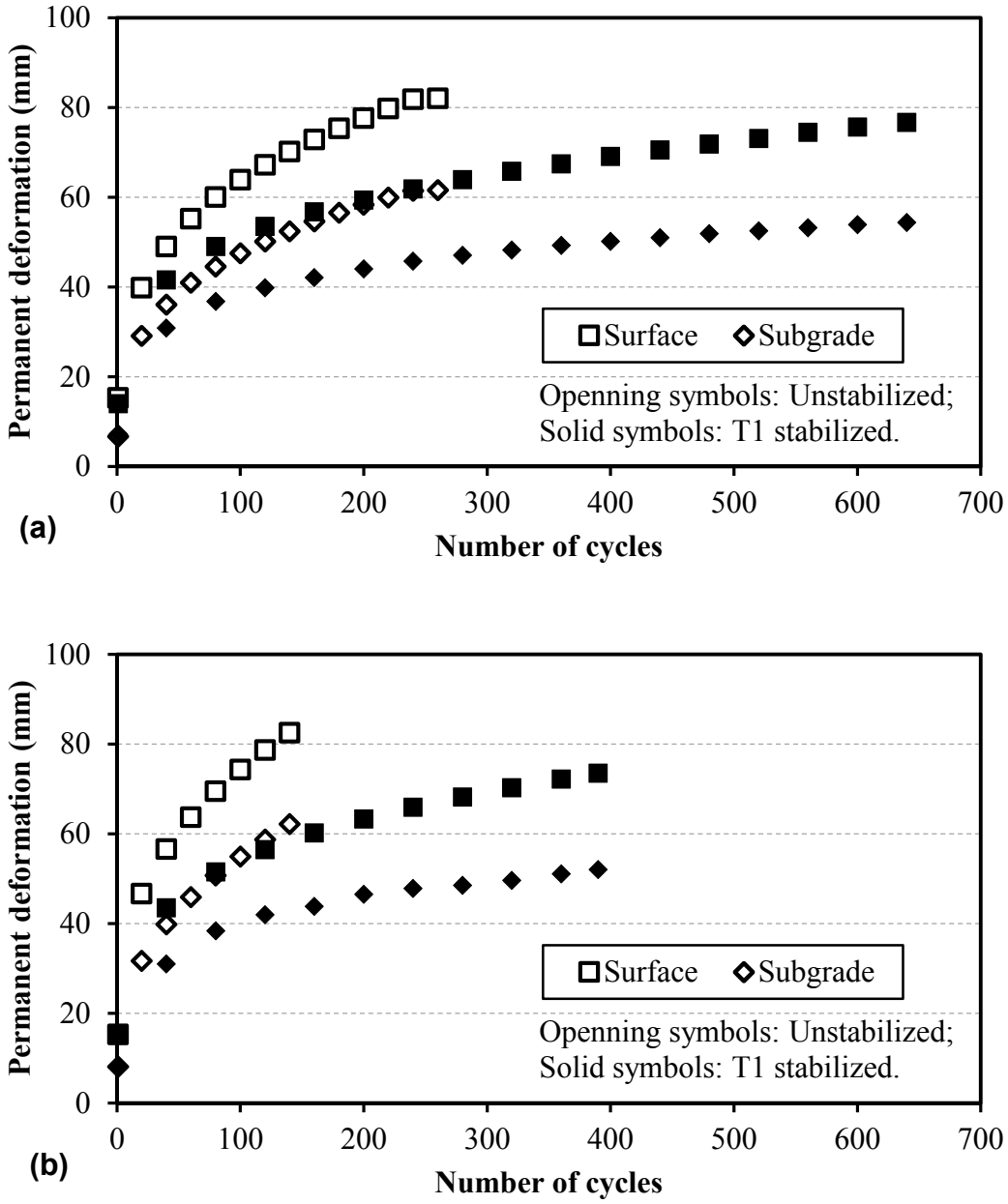

Figure 3.45 Permanent deformations vs. number of cycles for the test section with subgrade CBR of 3% and: (a) AB3 base and (b) AB3-soil mixture base

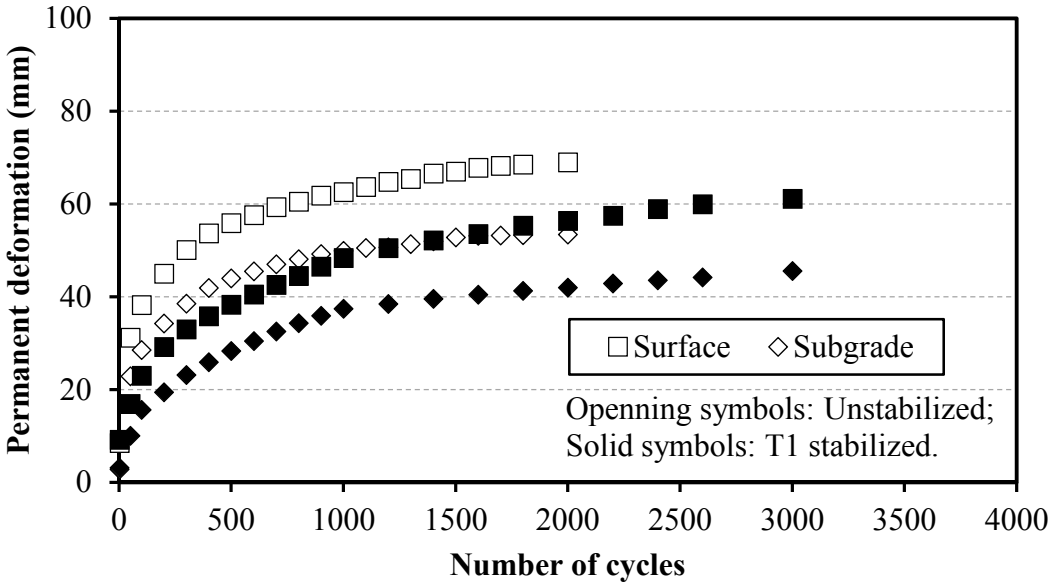

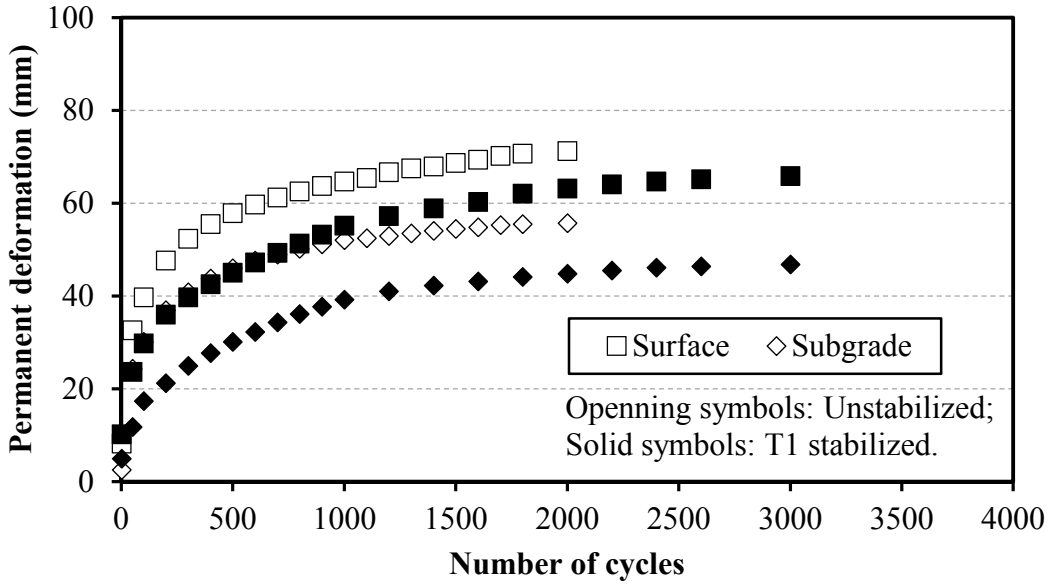

Figure 3.46 Permanent deformations vs. number of cycles for the test section with subgrade CBR of 5% and: (a) AB3 base and (b) AB3-soil mixture base

Resilient deformations

Figures 3.47 and **3.48** show the surface and subgrade permanent deformations of all the test sections. For all the unstabilized test sections with the subgrade CBR values of 3%

and 5%, the surface resilient deformations decreased with the increase of the number of loading cycles. This result indicates the strain-hardening characteristic of the test sections. The subgrade resilient deformations of the test sections with a CBR of 3% increased with the increase of the loading cycles at the initial stage and became stable at a higher number of loading cycles. The reason for this phenomenon is that the test sections had not reached a stable condition at the initial loading stage since the subgrade was weak. The subgrade resilient deformations of the test sections with a CBR of 5% decreased with the increase of the loading cycles at the initial stage and became stable at a higher number of loading cycles. This phenomenon indicates the strain-hardening property of the subgrade.

For the geogrid-stabilized test sections, the behavior of the resilient deformations was totally different from that of the unstabilized test sections. As shown in **Figures 3.47** and **3.48**, both the surface and subgrade resilient deformations of the stabilized test sections increased with the increase of the loading cycles. Moreover, the resilient deformations of the geogrid-stabilized test sections were much higher than those of unstabilized sections at the same permanent deformation. This phenomenon is consistent with the observations regarding the resilient behavior of the geogrid-stabilized test sections in the previous sections. The possible reasons for this phenomenon are that: (1) the confinement and the tensioned membrane effect of the geogrid were applied to the soils at the unloading stage and increased the resilient deformations and (2) due to the discontinuity at the interface of the base course and the subgrade under a large deformation, it is possible that the geogrid-stabilized base course was separated from subgrade under unloading.

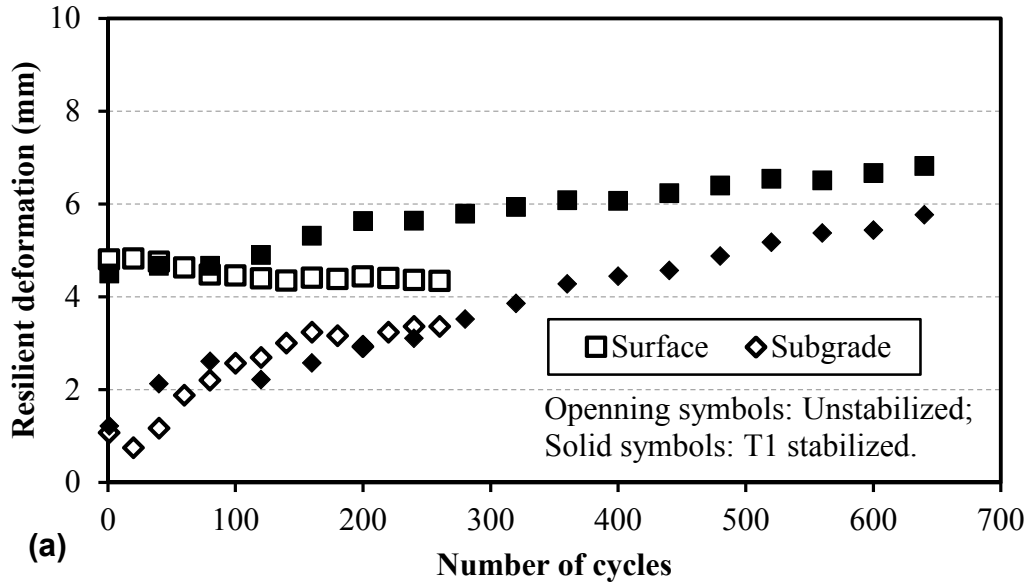

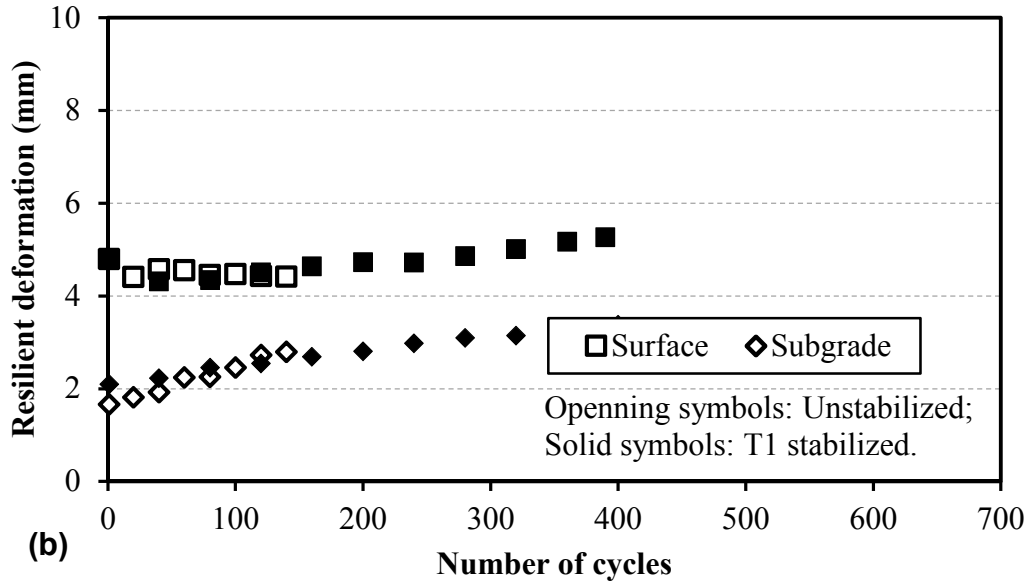

Figure 3.47 Resilient deformations vs. number of cycles for the test section with subgrade CBR of 3% and: (a) AB3 base and (b) AB3-soil mixture base

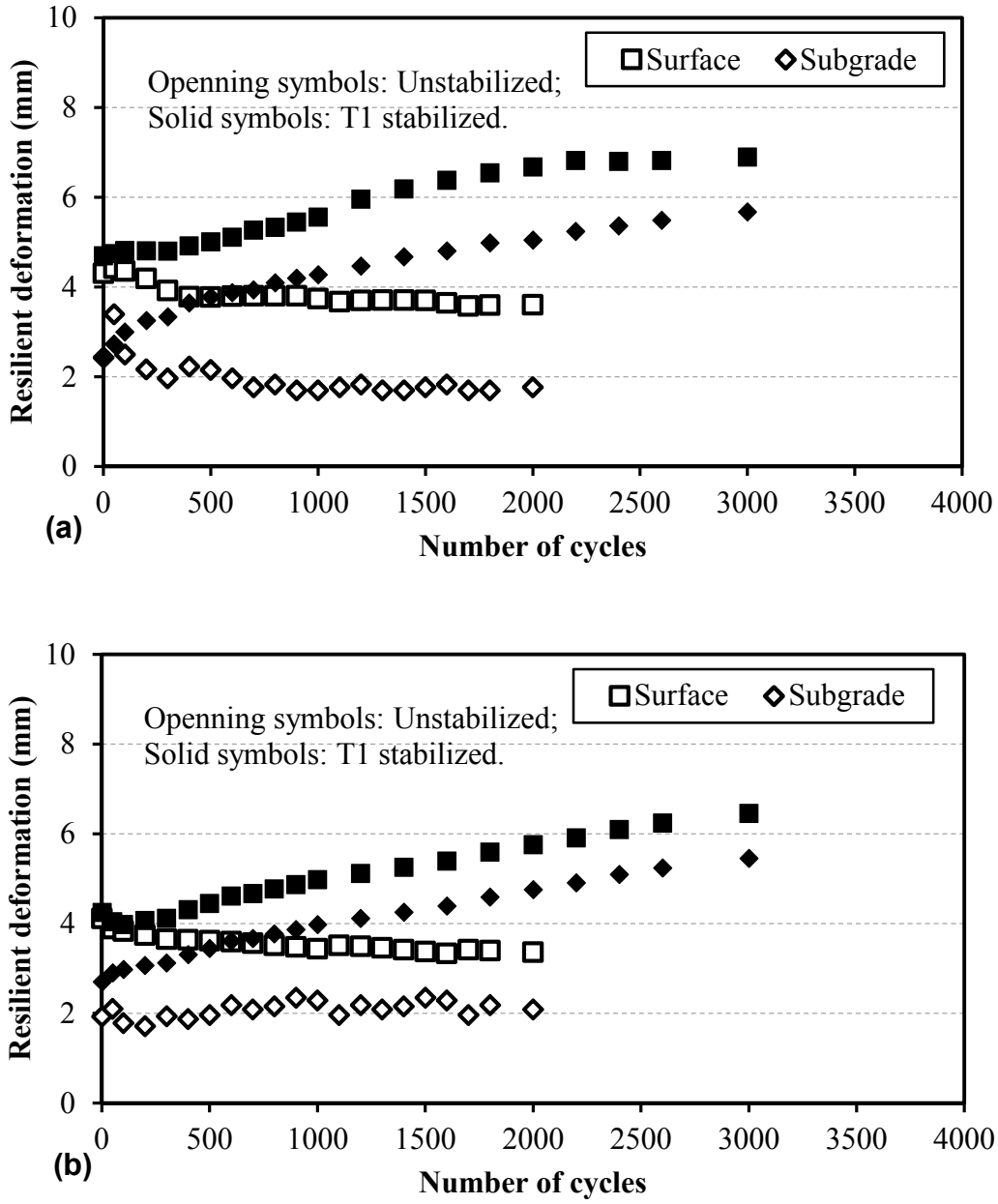

Figure 3.48 Resilient deformations vs. number of cycles for the test section with subgrade CBR of 5% and: (a) AB3 base and (b) AB3-soil mixture base

3.4.4 Summary

In this study, the cyclic plate load tests were conducted on the test sections with different base course and subgrade CBR values under the 40 kN cyclic load. The vertical stresses

at the interface and the permanent/resilient deformations at the surface and subgrade were monitored by earth pressure cells and displacement transducers. The following conclusions can be summarized based on the test results:

(1) The decrease of the base quality caused the increase of the vertical stresses at the interface. This result indicates that the base course with lower quality has less capability in protecting subgrade. Similarly, the increase of the subgrade CBR caused the increase of the vertical stresses at the interface. The inclusion of the geogrid would reduce the vertical stresses at the interface. This effect of the geogrid can be equivalent to the increase of the base course quality.

(2) The inclusion of the geogrid and the increase of the subgrade CBR reduced the permanent deformation significantly. The surface permanent deformations were mainly contributed by subgrade. The test sections with the subgrade CBR at 3% had bearing failure so that the increase rate of the permanent deformations was relatively higher at a higher number of loading cycles, while the permanent deformations of the test sections with the subgrade CBR at 5% became stable at a higher number of loading cycles. For the test sections with a higher subgrade CBR, the quality of the base course would not influence the permanent deformations as much as that for the test sections with the weak subgrade.

(3) The surface resilient deformations for unstabilized test sections decreased with the increase of the loading cycles, while those for stabilized test sections increased. The main reason for the increase of the resilient deformation in the stabilized test sections is that the confinement and the tensioned membrane effect were applied to the soils at the unloading stage and increased the resilient deformations.

3.5 Calibration of the MEPDG soil damage model

3.5.1 Introduction

The performance of subgrade soils under traffic loading is an important factor in the design of pavement systems. In the current Mechanistic Empirical Pavement Design Guide (MEPDG), subgrade resilient modulus, M_r, is one of the most significant input parameters for the design of pavements. The resilient modulus laboratory testing involves cyclic triaxial testing under a constant confining pressure, σ_3, and with a deviator stress cycled between the hydrostatic state and a positive deviator stress ($\sigma_1 - \sigma_3$). At this condition, the resilient modulus is defined as **Equation 3.5**:

$$M_r = \frac{\sigma_d}{\varepsilon_r} \qquad \textbf{Equation 3.5}$$

where M_r = resilient modulus; σ_d = deviator stress, ($\sigma_1 - \sigma_3$); and ε_r = resilient strain.

For mechanistic-empirical design, the resilient modulus is estimated by using the following generalized model as shown in **Equation 3.6** to describe the stress dependency of the resilient modulus:

$$M_r = k_1 P_a \left(\frac{\theta}{P_a}\right)^{k_2} \left(\frac{\tau_{oct}}{P_a} + 1\right)^{k_3} \qquad \textbf{Equation 3.6}$$

where k_1, k_2, k_3 are regression parameters; θ = bulk stress = $\sigma_1 + \sigma_2 + \sigma_3$; σ_1 = major principal stress; $\sigma_2 = \sigma_3$ = intermediate principal stress; P_a = atmosphere pressure; and τ_{oct} = octahedral shear stress. Khazanovich et al. (2006) found that the subgrade modulus is mostly affected by k_1-parameter, followed by the k_3-parameter.

This study aimed to back-calculate the resilient modulus of the fine-grained subgrade under different loading intensities based on its performance under cyclic plate loading tests and predicted the permanent deformations by modifying the damage model in the current MEPDG. Seven cyclic plate loading tests were conducted on the fine-grained subgrade with CBR ranging from 2.9% to 15.8% under increasing load intensities.

3.5.2 Test material and setup

The subgrade material used in the previous study was chosen in this study. **Figure 3.49** shows the test setup.

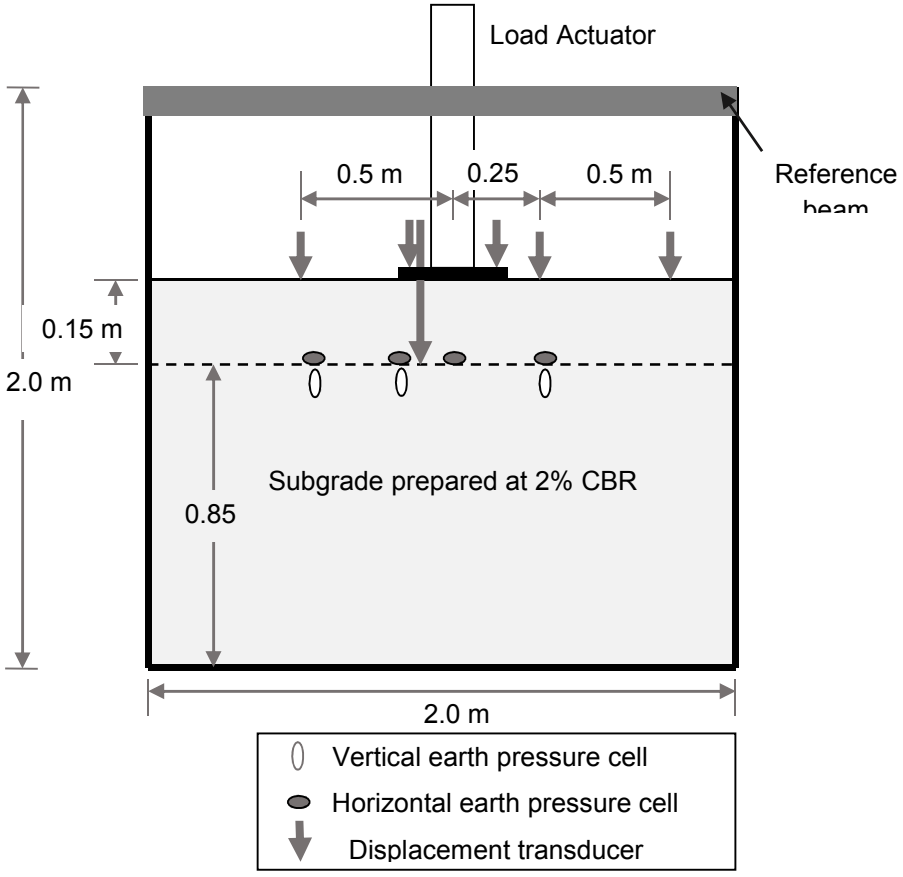

Figure 3.49 Test setup

The intensities of cyclic loading changed from 5 to 70 kN with an increment of 5 kN. For each loading magnitude, 100 cycles were performed on the test sections. In this study, surface deformations were monitored by transducers at the distances of 0, 0.25, 0.5, and 0.75 m from the center of the loading plate. For the subgrade-only section, the deformation at the depth of 0.15 m was measured by a transducer placed on a telltale. At this depth, vertical stresses were monitored by earth pressure cells placed at 0, 0.18, 0.25, and 0.38 m away from the center. **Figure 3.50** shows the top view of the arrangements of the earth pressure cells.

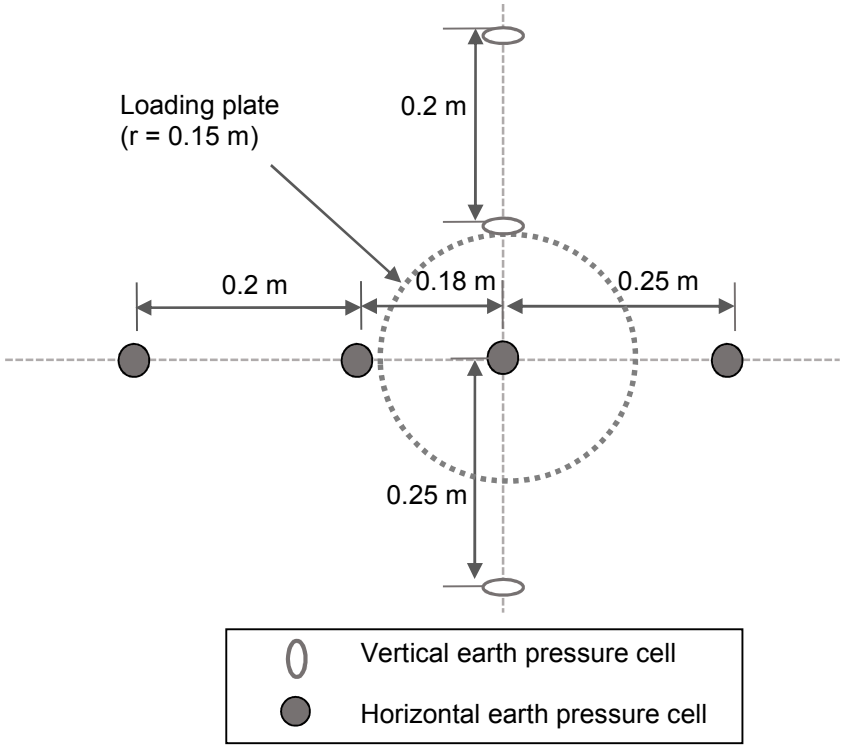

Figure 3.50 The arrangement of earth pressure cells

3.5.3 Results and discussion

Subgrade CBR and dynamic modulus

For each test section, DCP tests were performed at four locations after the preparation and the average dynamic cone penetration index (DCPI) profiles were calculated, as shown in **Figure 3.51**. The dynamic moduli were measured by LWD tests at each DCP test location as well. The CBR of each test section was estimated using the average DCPI profile based on **Equation 3.1**.

The average CBR value and the moisture content for each test section are shown in **Table 3.6**, which indicates that the CBR values of the subgrade material are sensitive to moisture content. The correlation between CBRs and dynamic moduli (based on LWD tests) is shown in **Figure 3.52**. The correlation can be expressed as **Equation 3.7** by fitting with a linear trend line.

$$CBR = 0.327\mathrm{E}_{\mathrm{vd}} \qquad \textbf{Equation 3.7}$$

where E_{vd} = the dynamic modulus of the fine-grained subgrade based on LWD tests (MPa); and CBR = California Bearing Ratio (%). **Figure 3.52** also shows the comparison between the correlations developed by other studies (Abu-Farsakh et al., 2004; Kavussi et al., 2010; Rao et al., 2008) and that of this study and a reasonable match can be observed. However, considering the physical concept of CBR and Dynamic modulus, the intercept of the trend line was set as zero in this study.

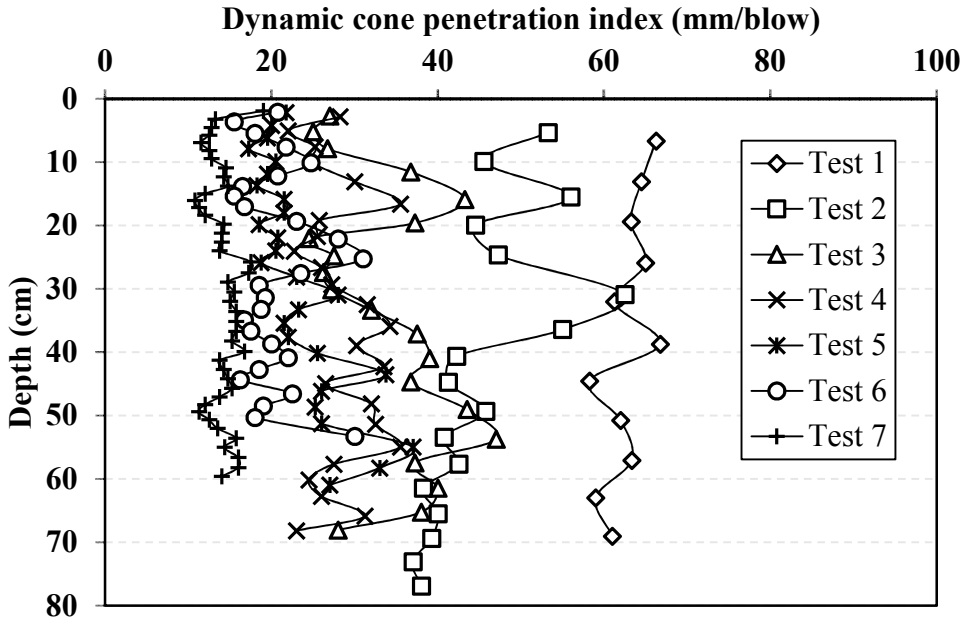

Figure 3.51 DCPI profiles

Table 3.6 Moisture contents and CBR values of test sections

No. of test	Test 1	Test 2	Test 3	Test 4	Test 5	Test 6	Test 7
Moisture content (%)	10.6	10.2	10.0	9.9	9.6	9.4	9.1
CBR (%)	2.9	4.4	6.2	7.4	9.5	11.0	15.8

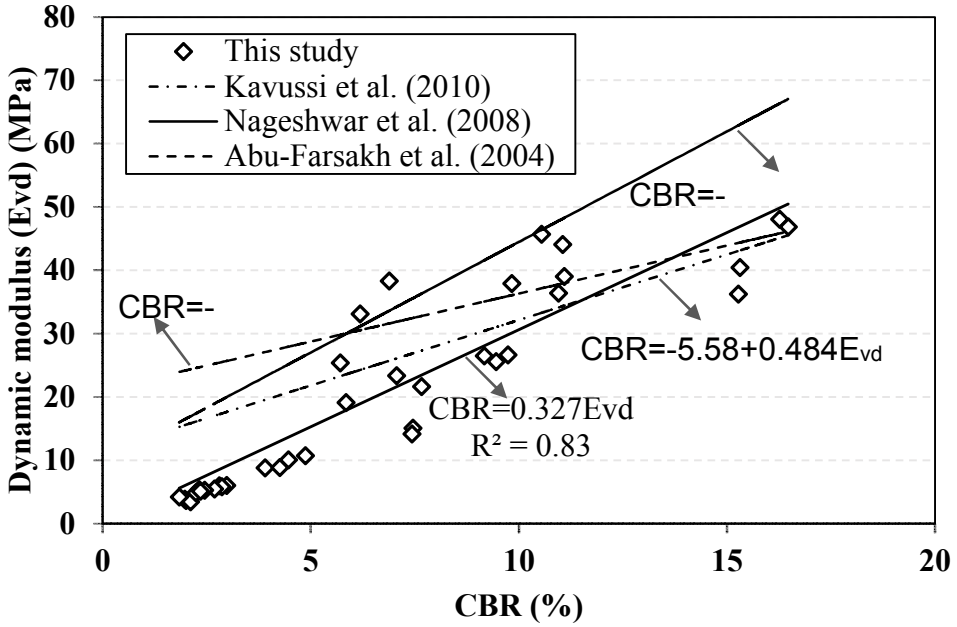

Figure 3.52 Dynamic modulus based on LWD tests vs. CBR

Vertical pressure and resilient deformations

Considering the rigig loading plate, the actual contact pressure beneath the loading plate can be expressed as **Equation 3.8**.

$$p(r) = \begin{cases} \frac{p_{av}}{2} \frac{1}{\sqrt{1-\frac{r^2}{\delta^2}}} & r < \delta \\ 0 & r > \delta \end{cases} \qquad \textbf{Equation 3.8}$$

where p(r) = the contact pressure; p_{av} = the average contact pressure; r = the distance between the calculated point to the center of the loading plate; and δ = the radius of the loading plate. **Table 3.7** shows the average contact pressure, p_{av}, under each loading**.**

Table 3.7 The average contact pressure of each loading stage

The range of the number of loading cycles	1-100	101-200	201-300	301-400	401-500	501-600	601-700
p_{av} (kPa)	71	141	212	283	354	424	495
The range of the number of loading cycles	701-800	801-900	901-1000	1001-1100	1101-1200	1201-1300	1301-1400
p_{av} (kPa)	566	637	707	778	849	920	990

The vertical pressure at the depth of 0.15 m (the same as the radius of the rigid loading plate) equals to $p_{av}/2$ based on the elastic theory. **Figure 3.53** shows the elastic solution of the vertical pressure and the corresponding results measured at the center of the loading plate with the depth of 0.15 m.

As demonstrated in **Figure 3.53**, the measured results roughly match the theoretical solution; however, the measured results exhibit that the vertical pressure at the same location tend to decrease with the increase of the CBRs of test sections, which is inconsistent with the elastic solution. Based on the elastic theory, the pressure distribution in a uniform elastic mass is independent to the elastic modulus of the mass. The inconsistency might be due to the plastic properties of the soil and the stress redistribution in soil resulting from the uneven accumulation of permanent deformations in both horizontal and vertical directions.

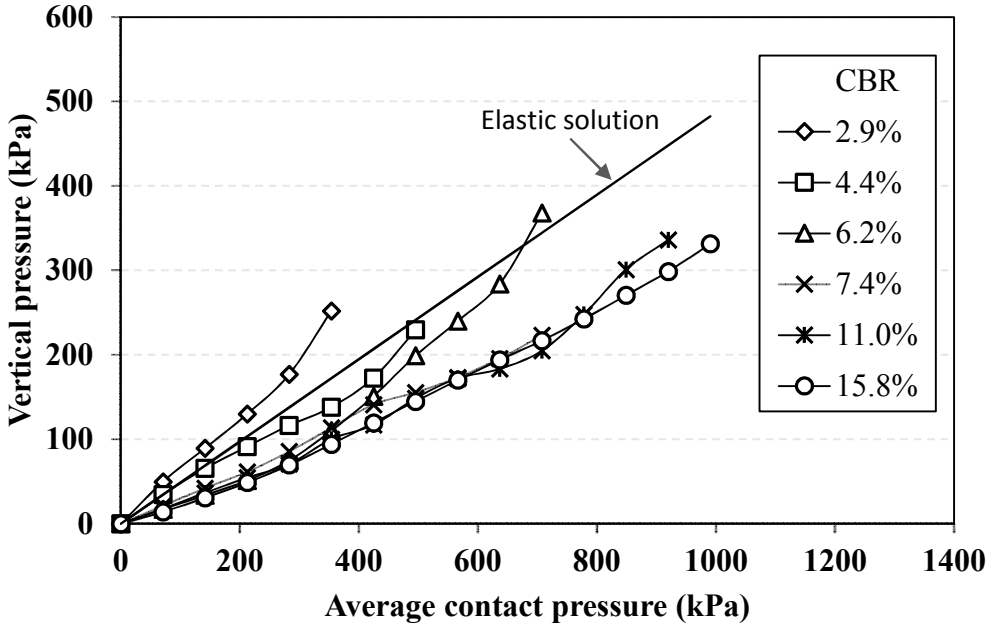

Figure 3.53 Vertical pressure at the center with depth of 0.15 m vs. the average contact pressure

Figure 3.54 shows the resilient deformation of the fine-grained subgrade versus the average contact pressure of the loading plate. The resilient deformation was obtained from the last cycle of each loading intensity. As shown in **Figure 3.54**, the increase of the average contact pressure increased the resilient deformations for all the test sections, but reduced the increase rate. This reduction was more obvious for test sections with higher subgrade CBRs. Under the same average contact pressure, the resilient deformations decreased with the increase of the subgrade CBRs, which indicates the increase of the resilient modulus in the test sections with the higher CBRs based on the elastic solution.

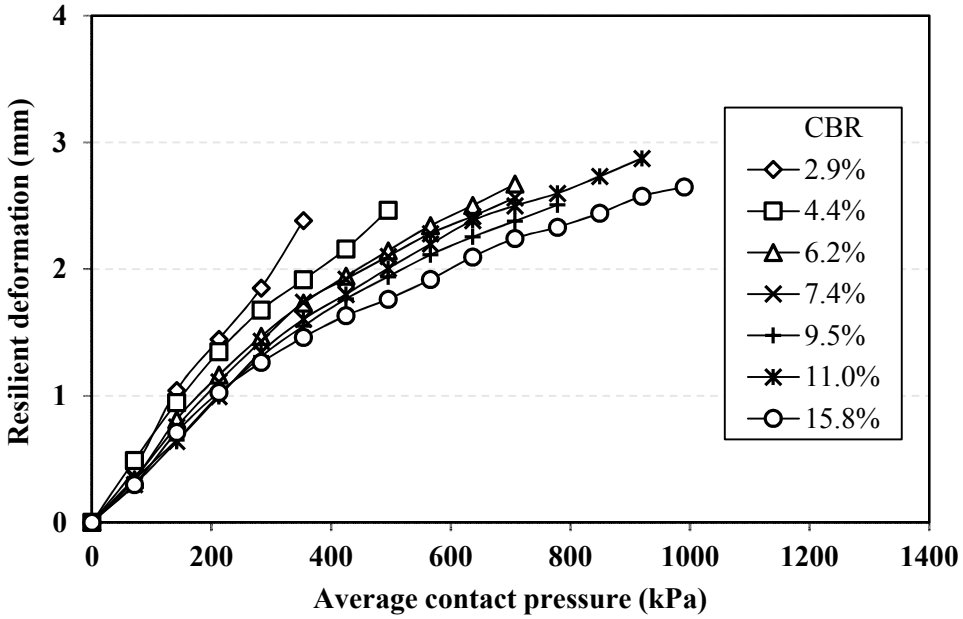

Figure 3.54 Resilient deformation vs. the average contact pressure

Back-calculation of resilient modulus of fine-grained subgrade

Equation 3.9 shows the elastic solution for the deformation at the center of the rigid loading plate at a certain depth of the semi-infinite elastic mass:

$$w = \frac{(1+\mu)\cdot p\cdot \delta}{2\cdot E}\left(2\cdot(1-\mu)\cdot \arctan\left(\frac{\delta}{z}\right) + \frac{\frac{z}{\delta}}{1+\left(\frac{z}{\delta}\right)^2}\right) \qquad \textbf{Equation 3.9}$$

where w = elastic deformation; μ = Poisson's ratio (assuming 0.35 in this study); p_{av} = average contact pressure; E = elastic modulus; δ = radius of the loading plate; and z = depth. When z equals to zero, **Equation 3.10** yields

$$w = \frac{\pi}{4}\frac{\left(1-\mu^2\right)\cdot p\cdot 2\delta}{E} \qquad \textbf{Equation 3.10}$$

Based on **Equation 3.10** and the resilient deformations measured on the surface of the test sections, the resilient moduli of the test sections were back-calculated, as shown in **Figure 3.55**.

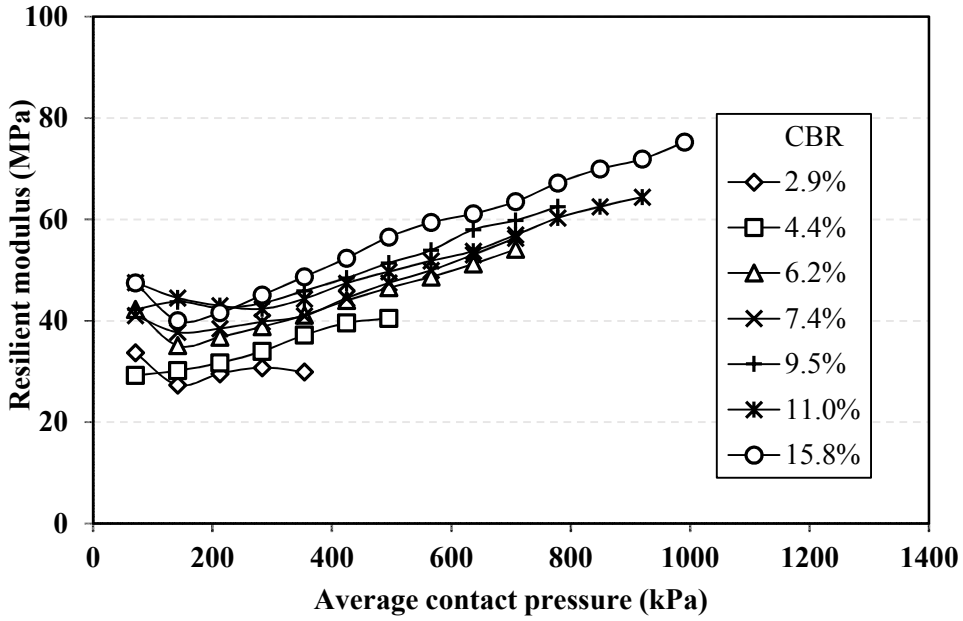

Figure 3.55 Resilient modulus of the fine-grained subgrade vs. the average contact pressure

It can be noted that the resilient modulus of the fine-grained subgrade increased with the increase of the applied pressure on the loading plate and the CBRs of the test sections. The correlation between the maximal resilient modulus obtained in this study and the CBR of each test section, as shown in **Equation 3.11**, is compared with the correlations developed in other studies (Heukelom and Klomp, 1962; Qian et al., 2011b), as shown in **Figure 3.49**.

$$M_r\ (\text{psi}) = 2555\text{CBR}^{0.55} \qquad \textbf{Equation 3.11}$$

where M_r = resilient modulus (psi). The correlation developed in this study matches that adopted in the current MEPDG well for the test sections with lower CBRs. As shown in **Figure 3.56**, the difference between the correlation obtained in this study and that in the current MEPDG enlarged with the increase of the CBRs.

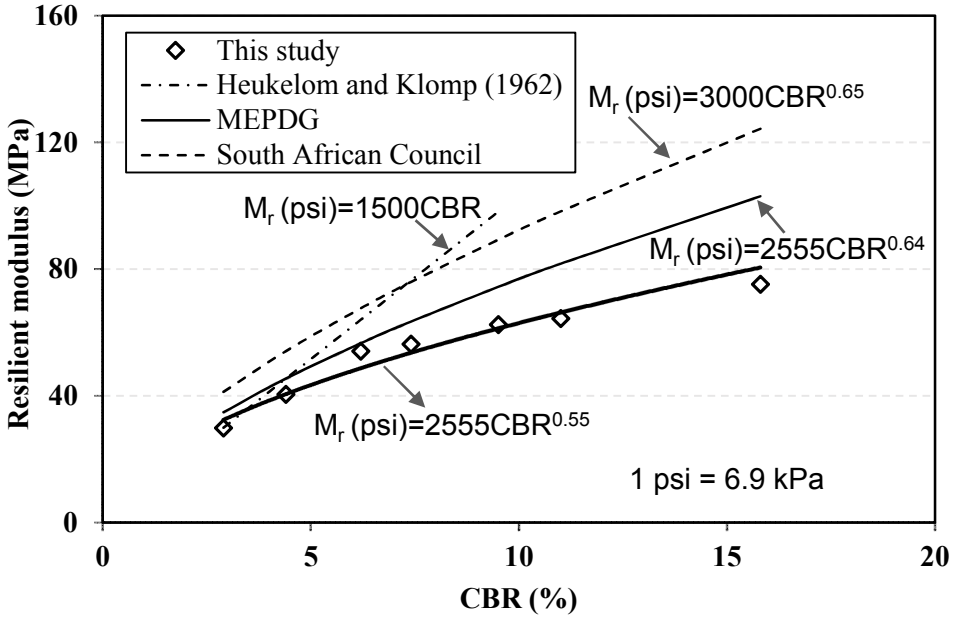

Figure 3.56 Comparison of the correlations between resilient modulus and CBR of subgrade

Permanent deformation

The damage model adopted in the current MEPDG, as shown in **Equation 3.12**, was chosen to predict the permanent deformations of the test sections constructed in this study.

$$\begin{cases} PD = k \cdot h_{soil} \cdot \varepsilon_v \cdot \left(\frac{\varepsilon_0}{\varepsilon_r}\right) \cdot e^{-\left(\frac{\rho}{N}\right)^{\beta}} \\ Log\beta = -0.61119 - 0.017638W_c \\ \rho = 10^9 \cdot \left(\frac{-4.89285}{1-(10^9)^{\beta}}\right)^{\frac{1}{\beta}} \\ \left(\frac{\varepsilon_0}{\varepsilon_r}\right) = \frac{0.15 \cdot e^{\rho^{\beta}} + 20 \cdot e^{\left(\frac{\rho}{10^9}\right)^{\beta}}}{2} \end{cases}$$ **Equation 3.12**

where PD = permanent deformation; h_{soil} = thickness of soil layer; ($\varepsilon_0/\varepsilon_r$), ρ, and β = parameters of unbound materials; k = calibration factor; ε_v = average vertical strain; W_c = water content (%); and N = number of traffic repetitions.

To predict the permanent deformations of the test sections, the vertical strains of soil layers at the center of the loading plate, ε_v, are needed in **Equation 3.12**. By applying partial derivative of **Equation 3.13**, ε_v yields

$$\varepsilon_v = \frac{\partial w}{\partial z} = \frac{p_{av}\delta^2(1+\mu)\left(\left(-\frac{1}{2}+\mu\right)\delta^2+\left(-\frac{3}{2}+\mu\right)z^2\right)}{(z^2+\delta^2)^2 E}$$ **Equation 3.13**

Based on the back-calculated resilient modulus of each test section at a certain loading stage, as shown in **Figure 3.55**, the vertical strain at any depth of soil can be calculated by **Equation 3.13**. Since the vertical strain varying through the depth of soil, the whole subgrade layer can be divided into layers to calculate the total permanent deformations. In this study, the subgrade was divided into 10 layers with each thickness of 0.1 m and the total permanent deformation was calculated by summing up the calculated permanent deformation of each layer. From the surface to the bottom, the layers were labeled as layers 1−10. The test section with 2.9% CBR was chosen to demonstrate the procedure for the prediction of the permanent deformation. The vertical strains of the test section with 2.9% CBR calculated based on **Equation 3.13** are shown in **Figure 3.57**.

In these calculations, the test section was assumed to be uniform and therefore had a constant resilient modulus in different layers. The strain at the middle point of each layer was considered as the representative vertical strain of the layer. By substituting the available vertical strain and soil parameters (water content) of the test section into **Equation 3.12**, the permanent deformation of each layer can be calculated. The total permanent deformation of the entire test section can be obtained by **Equation 3.14**.

$$TPD = \sum PD_i \qquad \textbf{Equation 3.14}$$

where TPD = total permanent deformation and PD_i = permanent deformation of the i^{th} layer.

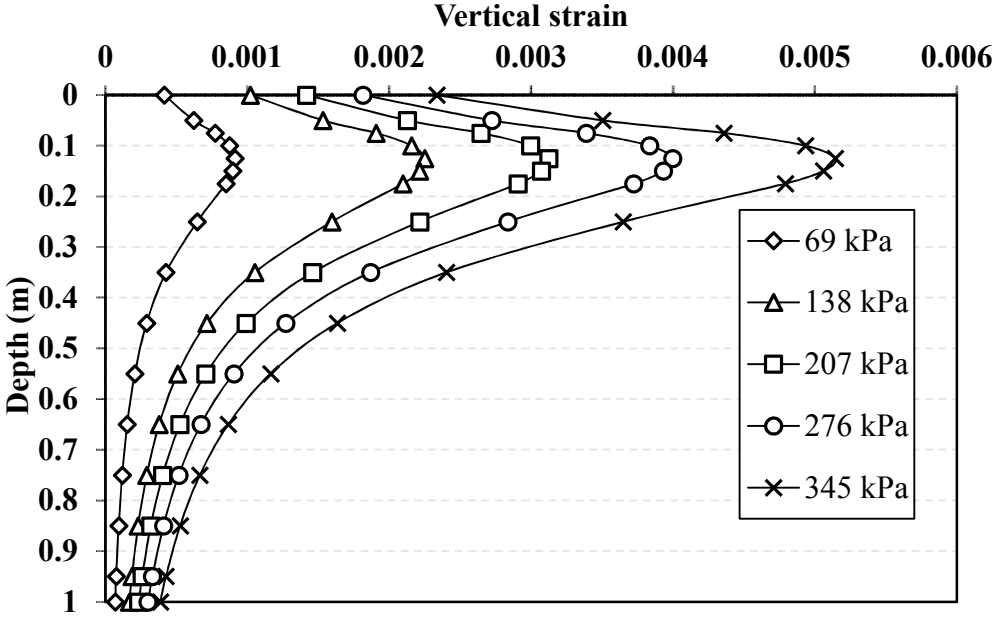

Figure 3.57 Vertical strain at the central line of the test section with 2.9% CBR subgrade

For the test section with 2.9% CBR subgrade, the surface permanent deformation predicted by the MEPDG model with the calibration factor as 1 and the measured

permanent deformations at surface and 0.15 m are shown in **Figure 3.51**. It can be observed that the predicted permanent deformation based on the MEPDG model was much lower than the measured results. This result indicates that the MEPDG model needs to be calibrated to fit the measured results. Following the same procedure, the predicted surface permanent deformations based on the MEPDG model were evaluated for the test sections with the subgrade CBR values of 4.4%, 6.2%, 7.4%, 9.5%, 11.0% and 15.8%, as shown in **Figures 3.59**, **3.60**, **3.61**, **3.62**, **3.63**, and **3.64**, respectively. In these figures, the measured permanent deformations at the surface and 0.15 m depth are presented. For the test section with the subgrade CBR of 9.5%, the permanent deformation at 0.15 m depth was not available since the telltale was not installed in this test section.

The rate of the permanent deformations increased with the increase of loading intensities for all the test sections. In addition, the measured permanent deformations decreased significantly with the increase of the subgrade CBRs under the same loading intensity. When the loading intensities were higher, the offsets between the predicted permanent deformations and the measured results became larger. The reason is that the damage model in the current MEPDG considers that the accumulation of the permanent deformations will level off eventually, which is indicated by the fact that the permanent deformation will become constant when the repetitions of traffic loading, N, approach to ∞. When the loading intensities are beyond the bearing capacities of the test sections, however, the increase rates of the surface permanent deformations accelerate significantly in laboratory, in contrary to becoming constant as demonstrated in the current damage model.

Therefore, to predict the permanent deformation more accurately, the model shown in **Equation 3.11** needs to be modified by introducing the stiffness and bearing capacity as additional parameters.

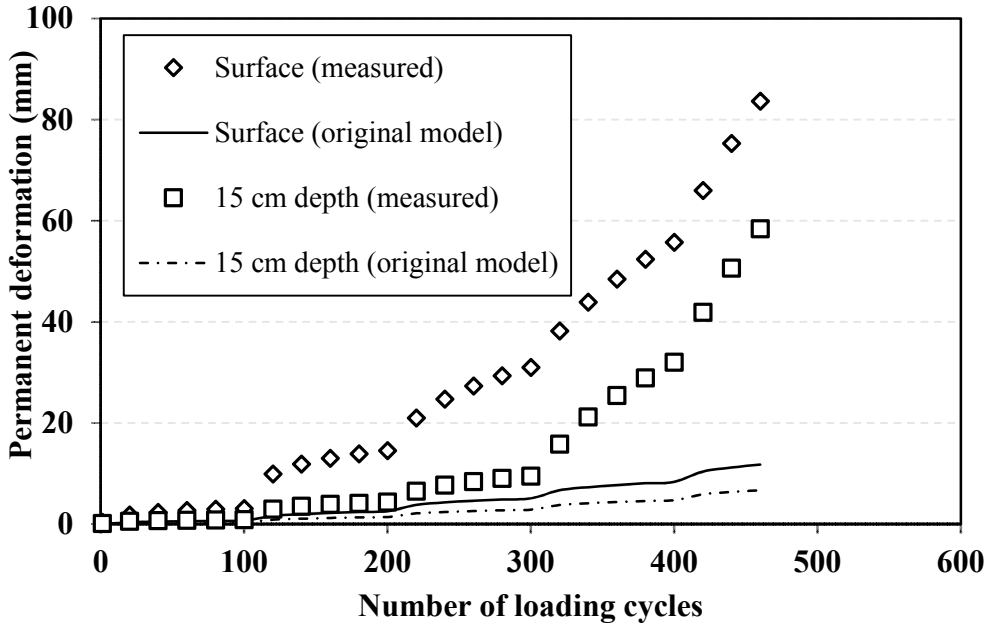

Figure 3.58 Permanent deformation vs. number of loading cycles of the test section with 2.9% CBR subgrade

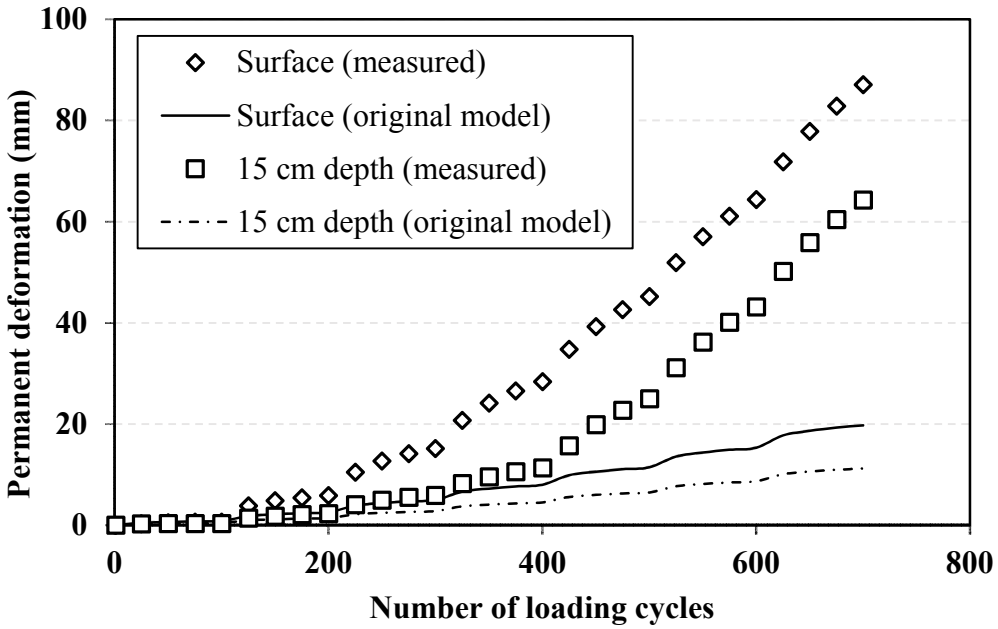

Figure 3.59 Permanent deformation vs. number of loading cycles of the test section with 4.4% CBR subgrade

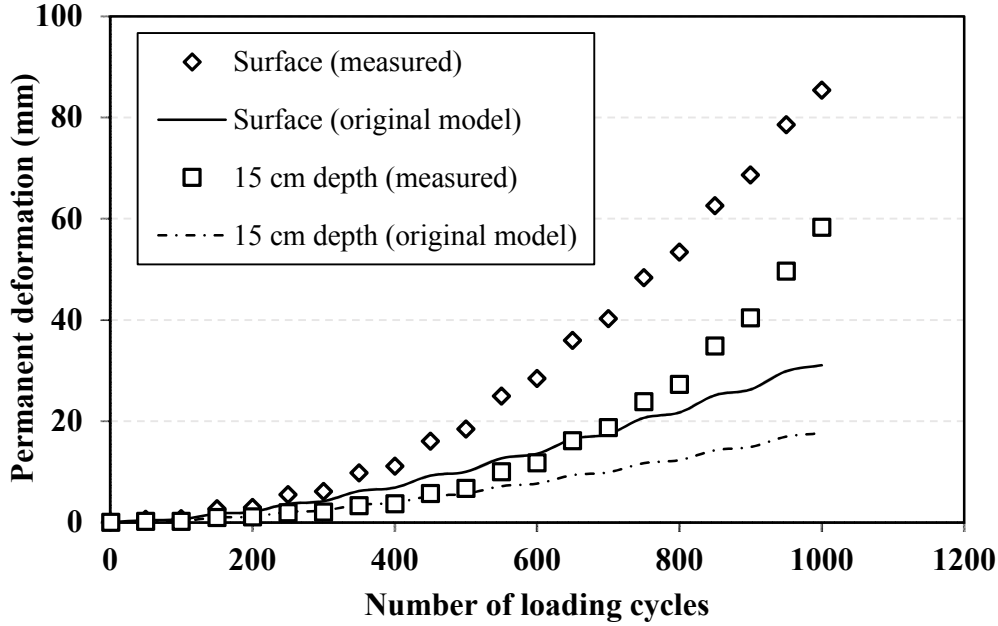

Figure 3.60 Permanent deformation vs. number of loading cycles of the test section with 6.2% CBR subgrade

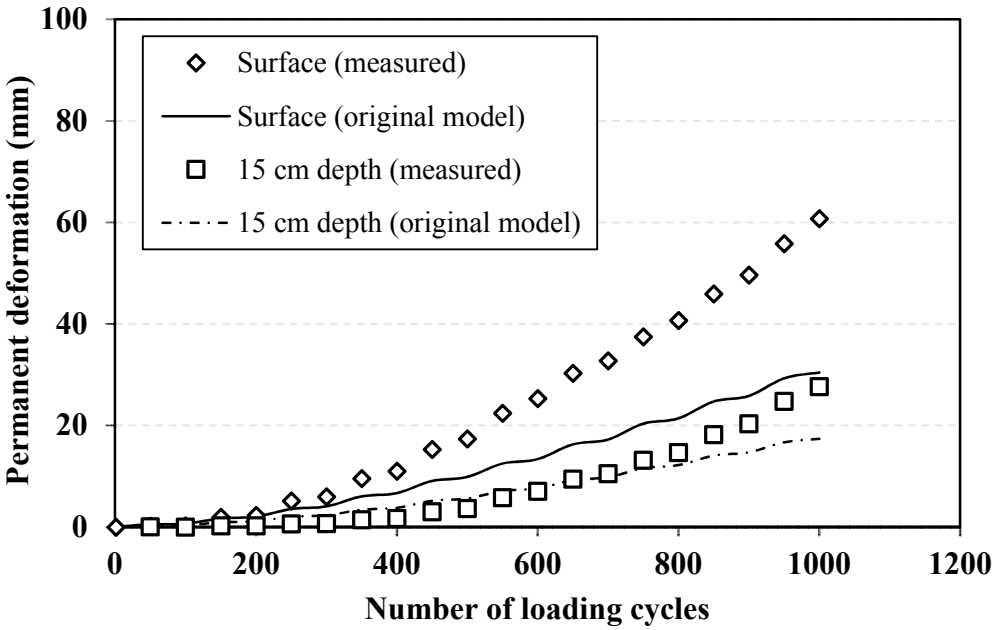

Figure 3.61 Permanent deformation vs. number of loading cycles of the test section with 7.4% CBR subgrade

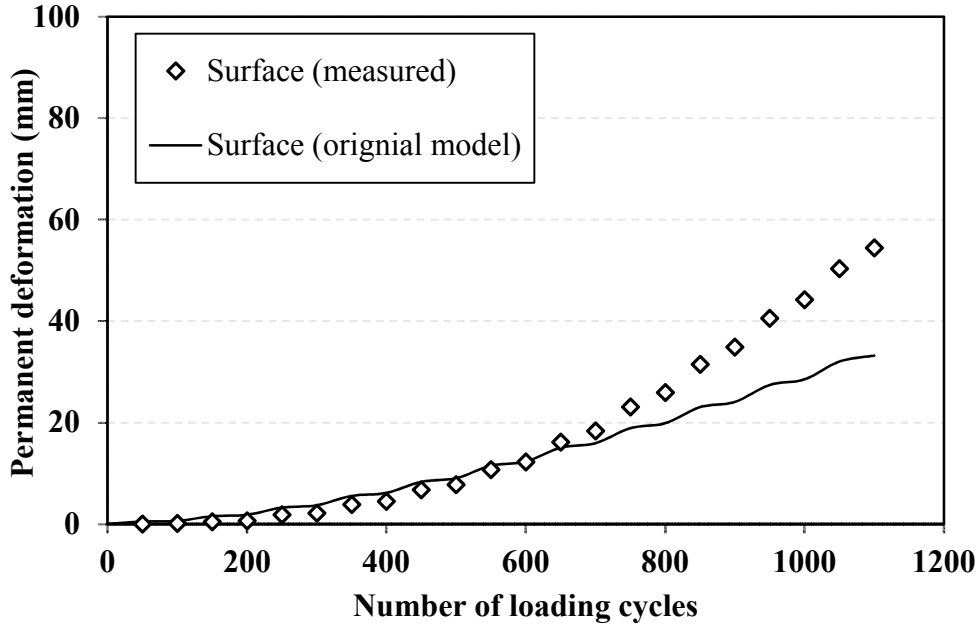

Figure 3.62 Permanent deformation vs. number of loading cycles of the test section with 9.5% CBR subgrade

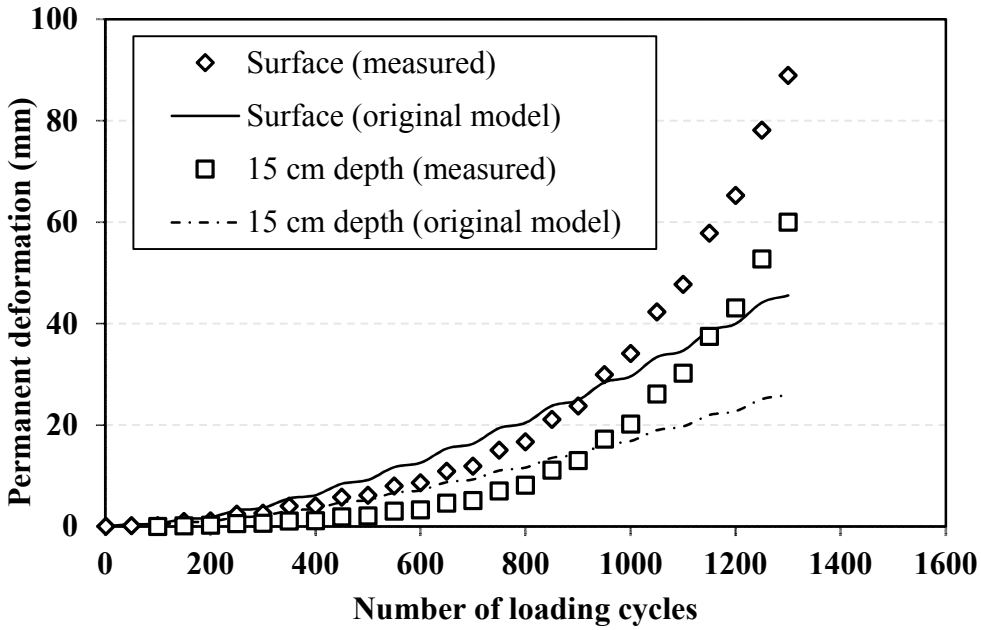

Figure 3.63 Permanent deformation vs. number of loading cycles of the test section with 11.0% CBR subgrade

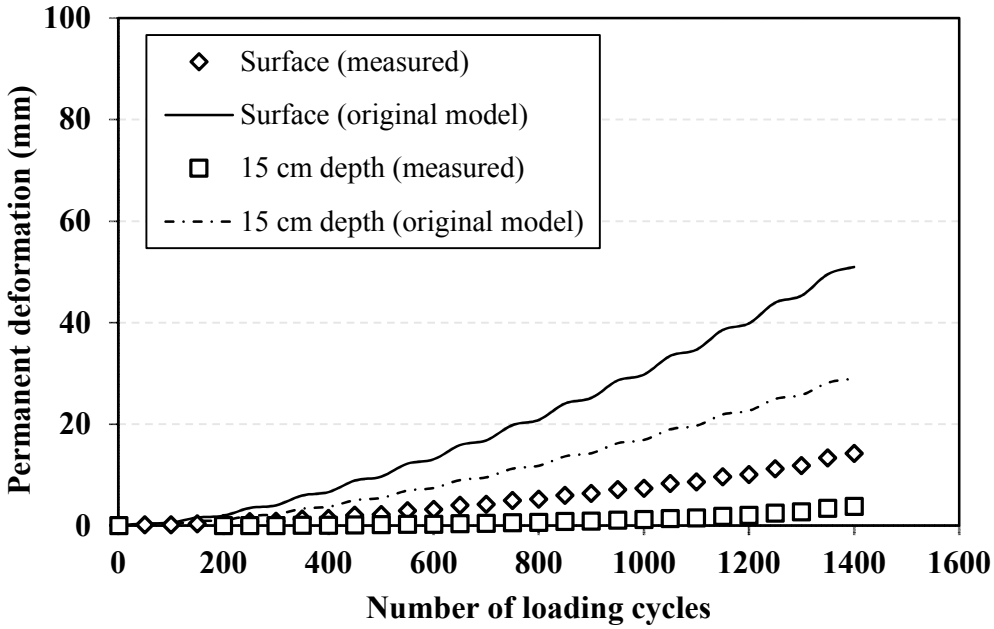

Figure 3.64 Permanent deformation vs. number of loading cycles of the test section with 15.8% CBR subgrade

Modification of the damage model in the MEPDG

As mentioned above, the load intensity and the CBR of the test section influenced the prediction of the original damage model. These two factors can be clearly demonstrated in **Figure 3.65**. **Figure 3.65** shows the curves of the contact pressure vs. the permanent deformation of two types of subgrade, Subgrade 1 and Subgrade 2, under the static plate load test. As shown in **Figure 3.65**, the permanent deformation of the subgrade was linearly related to the contact pressure when the pressure was lower than the elastic-limit bearing capacity. In addition, the subgrade stiffness (i.e. CBR) influenced the accumulation of the permanent deformation. To capture the influence of the two factors on the accumulation of the permanent deformation, the calibration factor, k, was expressed in a special form, as shown in **Equation 3.15**:

$$k = a \cdot CBR^{(-b)} \frac{p}{N_c c_u} \qquad \textbf{Equation 3.15}$$

where k = calibration factor; a = parameter; b = parameter; CBR = California bearing ratio; N_c = bearing capacity factor (i.e. 3.14); c_u = undrained shear strength; and p = contact pressure. The undrained shear strength, c_u, of each subgrade was approximately deduced from the CBR value of the subgrade soil (Han et al., 2011).

$$c_u = 20CBR \qquad \textbf{Equation 3.16}$$

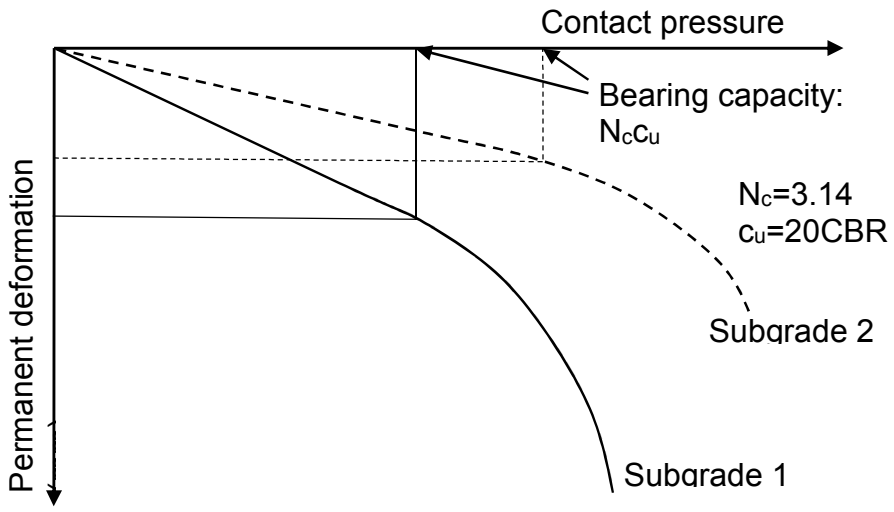

Figure 3.65 Contact pressure vs. permanent deformation of subgrade under the static plate load test

The original damage model was modified by introducing **Equation 3.15** into **Equation 3.12.** The modified damage model was calibrated to minimize the bias between the measured permanent deformation and the predicted permanent deformation. The bias is defined as:

$$\text{Bias} = \sum \left(\text{deformation}_{\text{predicted}} - \text{deformation}_{\text{measured}}\right) \qquad \textbf{Equation 3.17}$$

By adjusting the calibration factors, a and b, the bias was minimized. **Figures 3.66** and **3.67** show the comparison of the calibrated permanent deformation and the measured permanent deformation at the surface and the depth of 0.15 m, respectively. **Table 3.8** summarizes the calibration factors and the coefficient of determination, R^2.

Table 3.8. Calibration factors and the coefficient of determination

Calibration factors	Statistical analysis

		Location	R^2
a	10	At the surface	0.925
b	0.187	At the depth of 0.15 m	0.876

Equation 3.18 shows the modified soil damage model.

$$\begin{cases} PD = k \cdot h_{soil} \cdot \varepsilon_v \cdot \left(\frac{\varepsilon_0}{\varepsilon_r}\right) \cdot e^{-\left(\frac{\rho}{N}\right)^{\beta}} \\ Log\beta = -0.61119 - 0.017638 W_c \\ \rho = 10^9 \cdot \left(\frac{-4.89285}{1-(10^9)^{\beta}}\right)^{\frac{1}{\beta}} \\ \left(\frac{\varepsilon_0}{\varepsilon_r}\right) = 10 \cdot \mathrm{CBR}^{(-0.187)} \frac{p}{N_c c_u} \cdot \frac{0.15 \cdot e^{\rho\beta} + 20 \cdot e^{\left(\frac{\rho}{10^9}\right)^{\beta}}}{2} \end{cases}$$

Equation 3.18

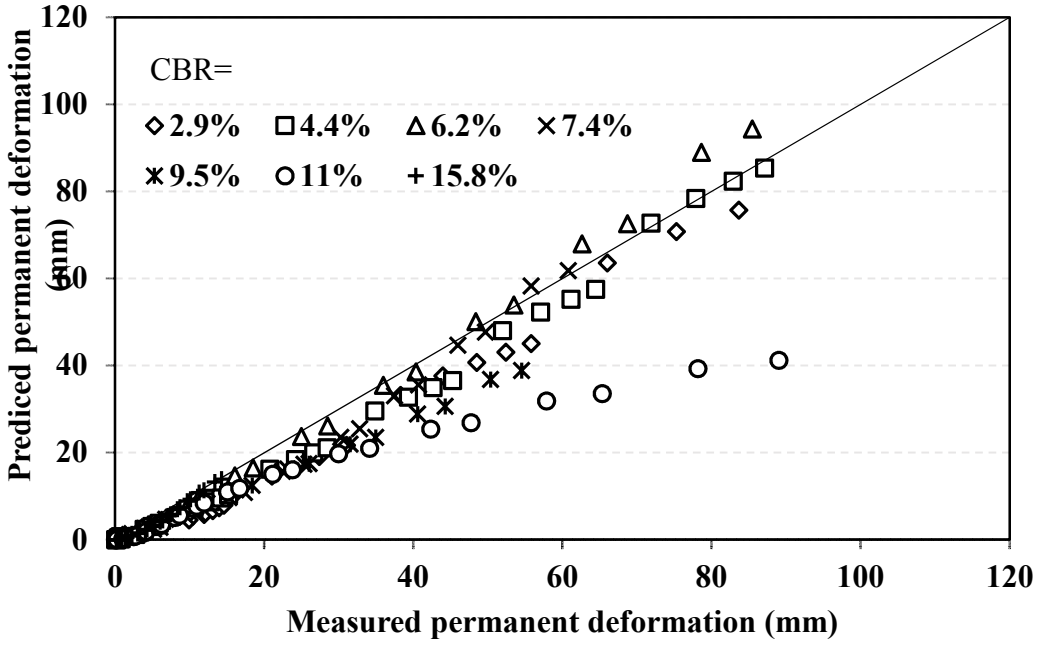

Figure 3.66 Measured surface permanent deformation vs. predicted permanent deformation with the modified damage model

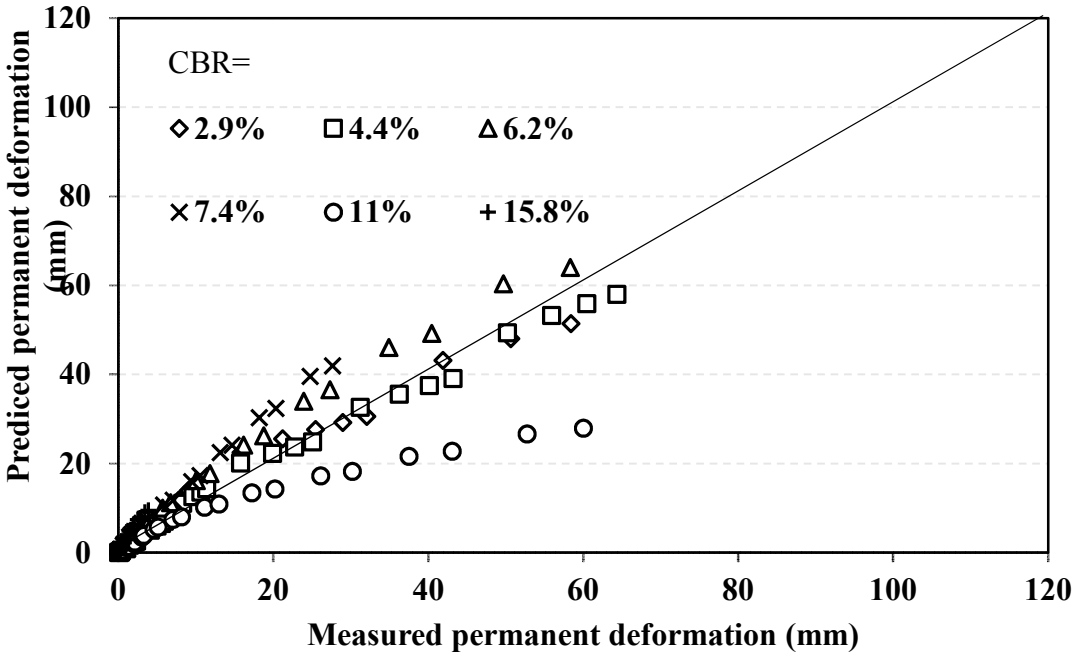

Figure 3.67 Measured permanent deformation at 0.15 m depth vs. predicted permanent deformation with the modified damage model

The predicted permanent deformations at surface and 0.15 m depth for all the test sections using the modified damage model in **Equation 3.18** are shown in **Figures 3.68 - 3.74**. As compared with the permanent deformations predicted by the original MEPDG model, the predicted permanent deformations based on Equation 3.18 matched the measured results well.

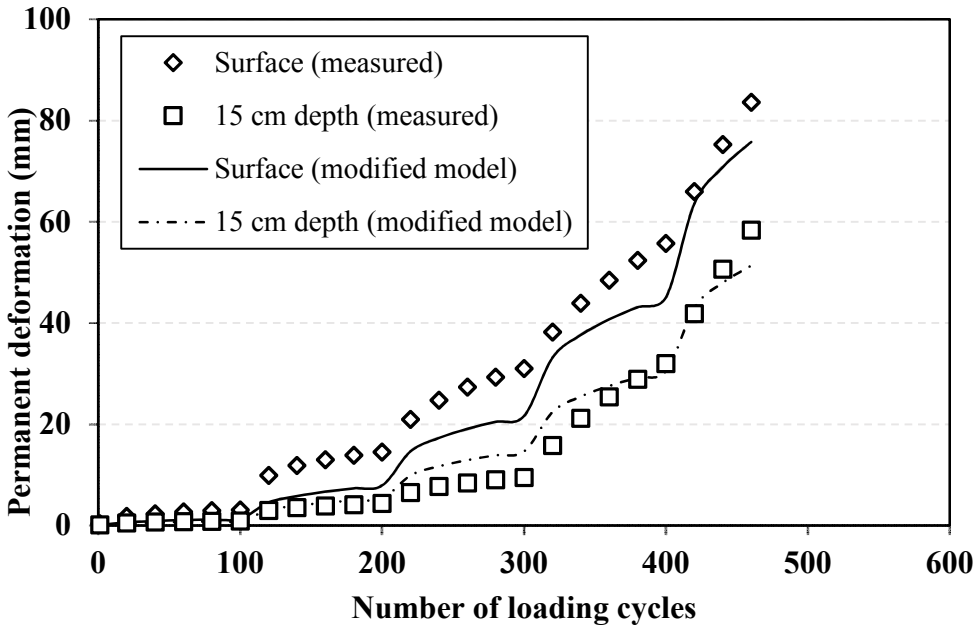

Figure 3.68 Permanent deformation vs. number of loading cycles of the test section with 2.9% CBR subgrade

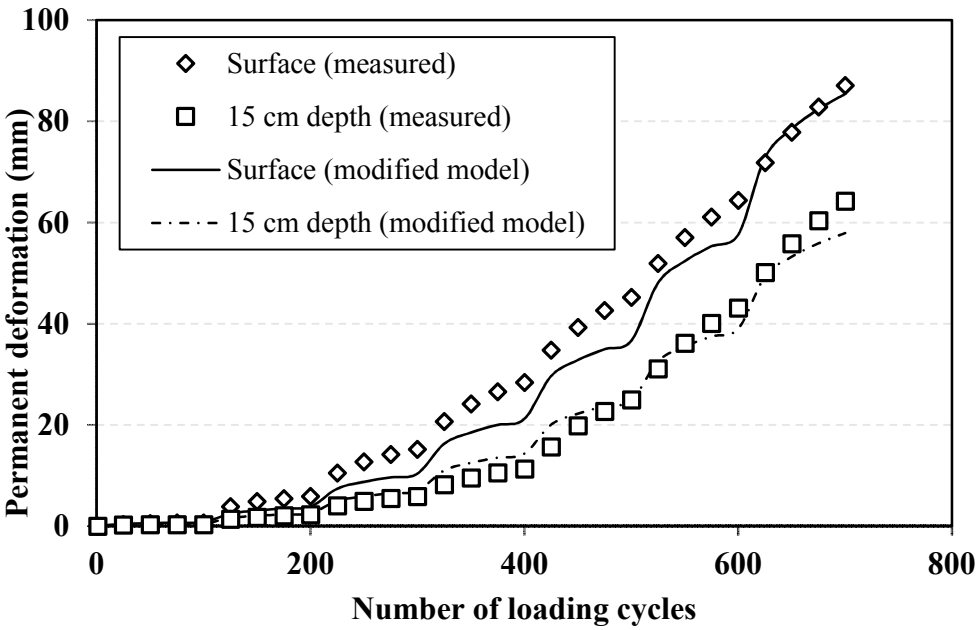

Figure 3.69 Permanent deformation vs. number of loading cycles of the test section with 4.4% CBR subgrade

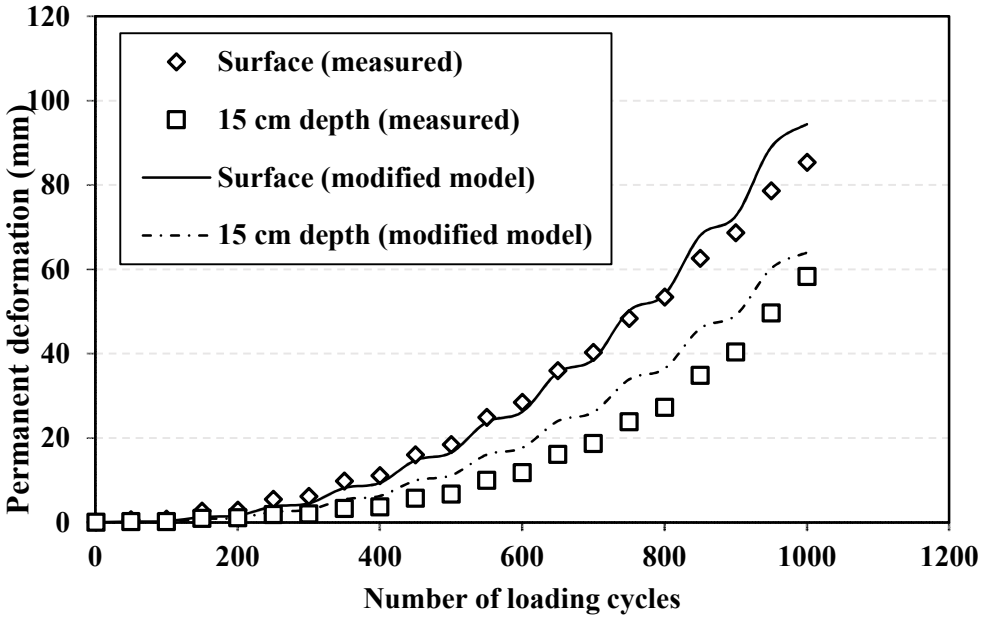

Figure 3.70 Permanent deformation vs. number of loading cycles of the test section with 6.2% CBR subgrade

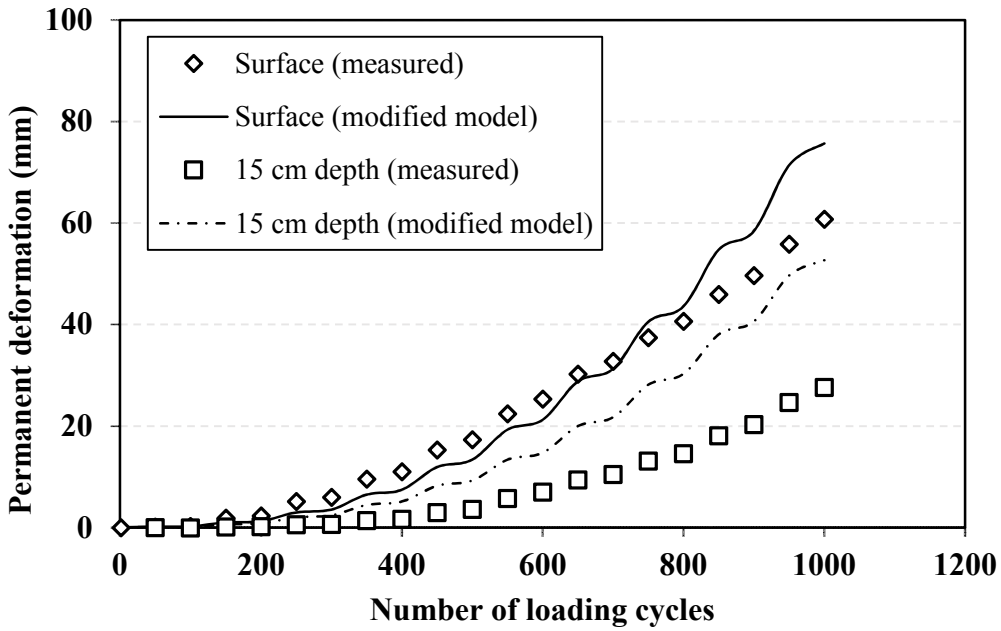

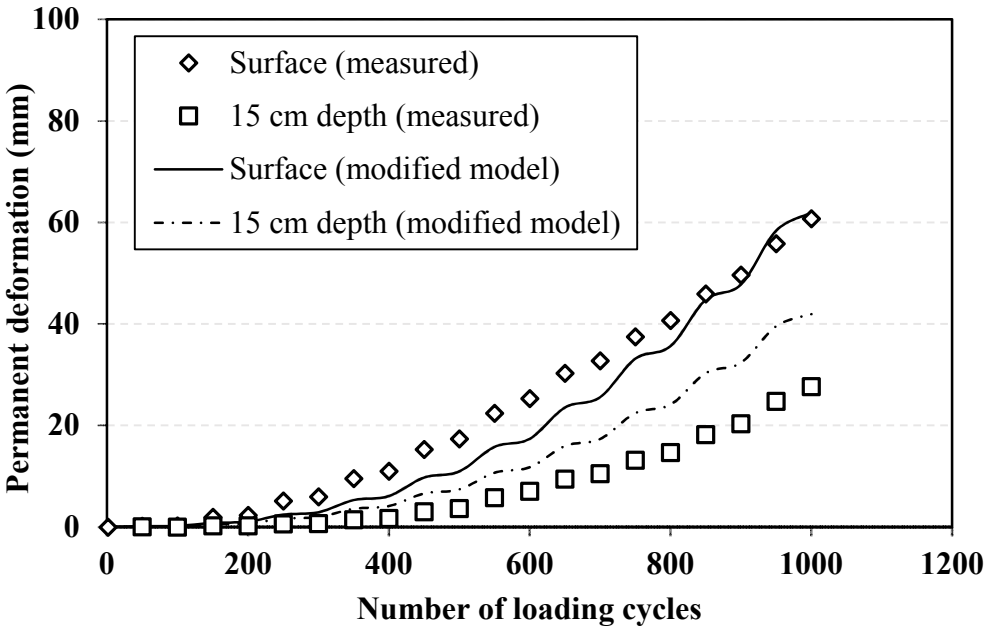

Figure 3.71 Permanent deformation vs. number of loading cycles of the test section with 7.4% CBR subgrade

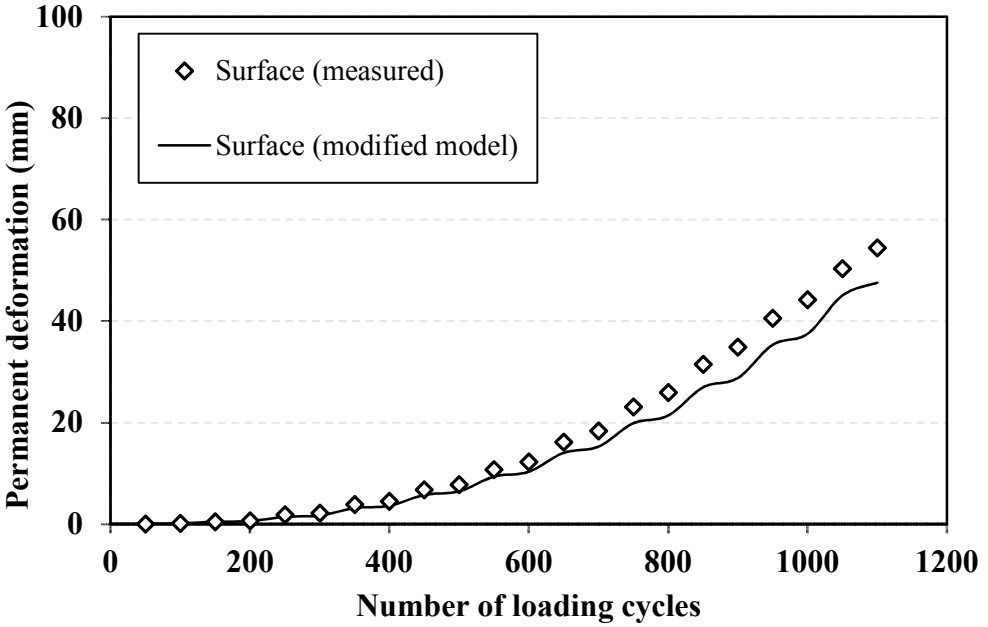

Figure 3.72 Permanent deformation vs. number of loading cycles of the test section with 9.5% CBR subgrade

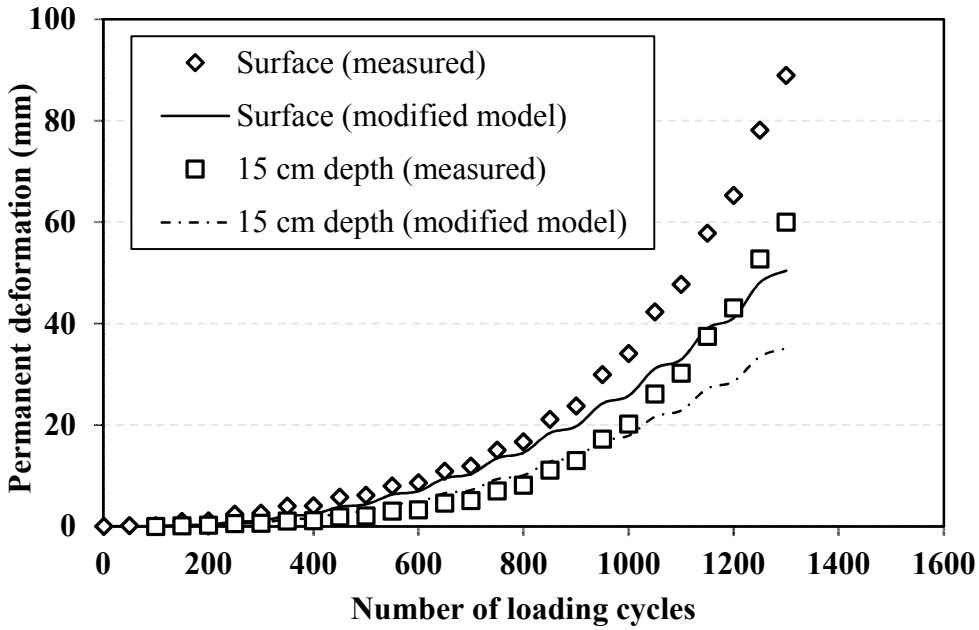

Figure 3.73 Permanent deformation vs. number of loading cycles of the test section with 11% CBR subgrade

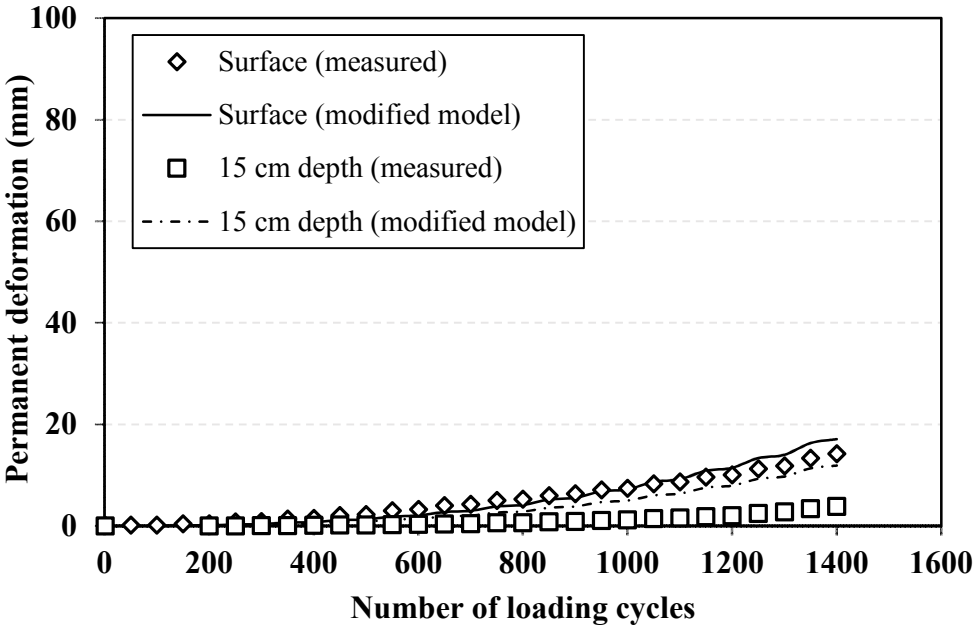

Figure 3.74 Permanent deformation vs. number of loading cycles of the test section with 15.8% CBR subgrade

3.5.4 Summary

The following conclusions can be drawn from this study:

1. The correlation between the dynamic modulus and the CBR for the fine-grained subgrade material can be expressed in the following equation:

$$E_{vd} = 3.07CBR$$

where E_{vd} = the dynamic modulus of the fine-grained subgrade based on the LWD test (MPa); CBR = California Bearing Ratio (%).

2. The resilient deformations of subgrade increased with the increase of loading intensities, but the increase rate decreased in the process. This result demonstrates the characteristic of the strain-hardening of subgrade. In addition, the resilient deformations decreased with the increase of the CBR.
3. The back-calculated resilient moduli of all test sections demonstrated a stress-dependent feature. The resilient moduli increased with the increase of the loading intensities. The correlation between back-calculated resilient moduli and CBRs for the fine-grained subgrade was developed as the following equation:

$$M_r\,(MPa) = 18.3CBR^{0.54}$$

where M_r = resilient modulus (MPa).

4. The permanent deformation of the subgrade accumulated with the increase of the load cycles. The increase rate of the permanent deformation increased significantly with the increase of the loading intensities. The original damage model of the MEPDG could not predict the permanent deformation well since the stiffness of subgrade and the ratio of the contact pressure to the bearing capacity were not considered.

5. The damage model in the current MEPDG was modified by introducing two factors: the stiffness of subgrade and the ratio of the contact pressure to the bearing capacity. The predicted permanent deformations of subgrade by the modified damage model matched the measured permanent deformations well.
6. The verification of the modified damage model indicates that the modified damage model can be used to evaluate the subgrade permanent deformations of the sections with base courses over subgrade.

3.6 Summary

In this chapter, cyclic/static plate loading tests were conducted on the test sections with varying base thicknesses and subgrade CBRs. The MEPDG soil damage model was calibrated based on the cyclic plate loading tests applied on the subgrade-only sections. The major findings are summarized below:

(1) Both the vertical stress and horizontal stress distributions were changed by the inclusion of geogrids. The vertical stresses at the interface were distributed to a wider area and the horizontal stresses were confined to a smaller area close to the loading plate.

(2) Resilient deformations increased with the presence of geogrids. One reason is that the additional lateral earth pressure induced by geogrids pushed soils back at the unloading stage. Another reason is that base course and subgrade may not be in contact at the end of the unloading stage.

(3) The ratio of the permanent deformations under cyclic loading to those under static loading at the same loading intensity ranged from 1.7 to 2.0 if the number of cycles per loading stage increased from 100 to 1000.

(4) The inclusion of the geogrid and the increase of the subgrade CBR reduced the permanent deformation significantly. The surface permanent deformations were mainly contributed by subgrade. The test sections with subgrade CBR at 3% had bearing failure so that the increase rate of the permanent deformations was relatively higher at a higher number of loading cycles, while the permanent deformations of the test sections with subgrade CBR at 5% became stable at a higher number of loading cycles.

(5) The damage model in the current MEPDG was modified by introducing two factors: the stiffness of subgrade and the ratio of the contact pressure to the bearing capacity. The predicted permanent deformations of subgrade by the modified damage model matched the measured permanent deformations well.

Chapter 4 Analytical Model for the Resilient Behavior of Geogrid-stabilized Bases

4.1 Introduction

In pavement design, resilient modulus is an important design parameter. If two unstabilized test sections constructed with the same material had different permanent deformations under the same loading condition, it would be expected that the test section with a higher permanent deformation has a lower resilient modulus, and vice versa. Meanwhile, the test section with a higher resilient modulus would show a lower resilient deformation. As shown in Chapter 3, the inclusion of the geogrid reduced the permanent deformations of test sections. Therefore, it is likely for one to assume that the geogrid-stabilized test sections had higher resilient moduli and lower resilient deformations than those unstabilized test sections. In fact, there is no doubt that the confinement effect and the tensioned membrane effect improved the stiffness of the stabilized bases at the loading stage; however, the resilient deformations of geogrid-stabilized sections were not lower but even higher than those of unstabilized test sections. The reason is that the confinement effect and the tensioned membrane effect recovered the soils during the unloading stage. The recovery of the resilient deformation indicates the reduction of the permanent deformation.

In this chapter, a hypoplastic model was adopted to simulate the resilient behavior of the geogrid stabilized bases. The hypoplastic model has been reviewed in Chapter 2.7.

4.2 Analysis by a hypoplastic model

4.2.1 Simple hypoplastic model

The resilient behavior of soils is a nonlinear behavior. Resilient deformation and permanent deformation always occur at the same time even under a very small magnitude of load. A hypoplastic model can easily capture this behavior of soil and describe the loading and unloading with one single formula. Since this is a nonlinear and plastic model, it is not feasible to give a closed form of solution for a layered system with a certain boundary condition. However, it is possible to investigate a soil element under a triaxial condition by a hypoplastic model.

For a triaxial soil element, as shown in **Figure 4.1**, the Mohr-Coulomb failure envelope is shown in **Figure 4.2**. The limit states of the soil element under the triaxial condition can be expressed by **Equation 4.1**.

$$(\sigma_{1max} + \sigma_3 + 2c\cot\varphi)\sin\varphi = \sigma_{1max} - \sigma_3$$
$$(\sigma_{1min} + \sigma_3 + 2c\,cot\,\varphi)\,sin\,\varphi = \sigma_3 - \sigma_{1min} \qquad \textbf{Equation 4.1}$$

where c and φ are the cohesion and friction angle of the soil element.

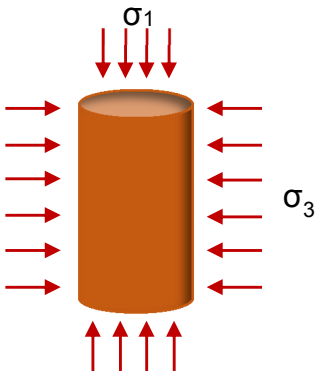

Figure 4.1 Soil element under a triaxial condition

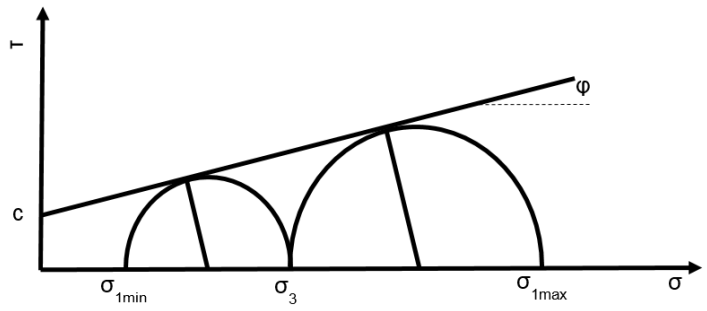

Figure 4.2 Mohr-Coulomb failure envelope

It is known that the stiffness of soil is stress-dependent and $(\sigma_1 + \sigma_3 + 2c\cot\varphi)$ and $(\sigma_1 - \sigma_3)$ control the limit state of soil, as shown in **Equation 4.1**. **Equation 4.2** expresses a hypoplastic model using two terms.

$$\dot{\sigma}_1 = m(\sigma_1 + \sigma_3 + 2c\,cot\,\varphi)\dot{\varepsilon}_1 + n\,(\sigma_1 - \sigma_3)|\dot{\varepsilon}_1| \qquad \textbf{Equation 4.2}$$

where m and n are soil parameters, $\dot{\sigma}_1$ and $\dot{\varepsilon}_1$ are the stress rate and strain rate in the axial direction. $\dot{\varepsilon}_1$ can be negtive and positive to differentiate the loading and unloading processes, respectively.

Under a loading condition, $\dot{\varepsilon}_1 < 0$

$$\dot{\sigma}_1 = \left[m(\sigma_1 + \sigma_3 + 2c\cot\varphi) - n\,(\sigma_1 - \sigma_3)\right]\dot{\varepsilon}_1 \qquad \textbf{Equation 4.3}$$

$\left[m(\sigma_1 + \sigma_3 + 2c\cot\varphi) - n\,(\sigma_1 - \sigma_3)\right]$ is the modulus of soil at a loading stage;

Under an unloading condition, $\dot{\varepsilon}_1 > 0$

$$\dot{\sigma}_1 = \left[m(\sigma_1 + \sigma_3 + 2c\cot\varphi) + n\,(\sigma_1 - \sigma_3)\right]\dot{\varepsilon}_1 \qquad \textbf{Equation 4.4}$$

$\left[m(\sigma_1 + \sigma_3 + 2c\cot\varphi) + n\,(\sigma_1 - \sigma_3)\right]$ is the modulus of soil at an unloading stage.

4.2.2 Triaxial condition with constant confinement

To simulate a triaxial test, the initial condition and the failure need to be considered.

At the initial point, $\sigma_1 = \sigma_3$

$$E_0 = 2m(\sigma_3 + c\cot\varphi) \qquad \textbf{Equation 4.5}$$

Therefore,

$$m = \frac{E_0}{2(\sigma_3 + c\cot\varphi)} \qquad \textbf{Equation 4.6}$$

At failure, $\sigma_1 = \sigma_{1,max}$,

Considering the limit state of soil, as shown in **Equation 4.1,**

$$\frac{m}{n} = \sin\varphi \qquad \textbf{Equation 4.7}$$

Therefore,

$$n = \frac{E_0}{2\sin\varphi(\sigma_3 + c\cot\varphi)} \qquad \textbf{Equation 4.8}$$

By substituting m and n into **Equation 4.3** and **Equation 4.4** and integrating the equations,

at the loading stage,

$$\frac{1}{A}\ln[(A\sigma_1 + C)/(A\sigma_3 + C)] = \varepsilon_1 \qquad \textbf{Equation 4.9}$$

at the unloading stage,

$$\frac{1}{B}\ln[(B\sigma_{max} + D)/(B\sigma_1 + D)] = \varepsilon_{max} - \varepsilon_1 \qquad \textbf{Equation 4.10}$$

where, $A = m - n$;

$B = m + n$;

$C = m(\sigma_3 + 2c\cot\varphi) + n\sigma_3$;

$D = m(\sigma_3 + 2c\cot\varphi) - n\sigma_3$.

The measured results obtained from triaxial tests were simulated by the hypoplastic model, as shown in **Figures 4.3, 4.4,** and **4.5**. As shown in the figure, the predicted results matched the measured ones under 5% strain.

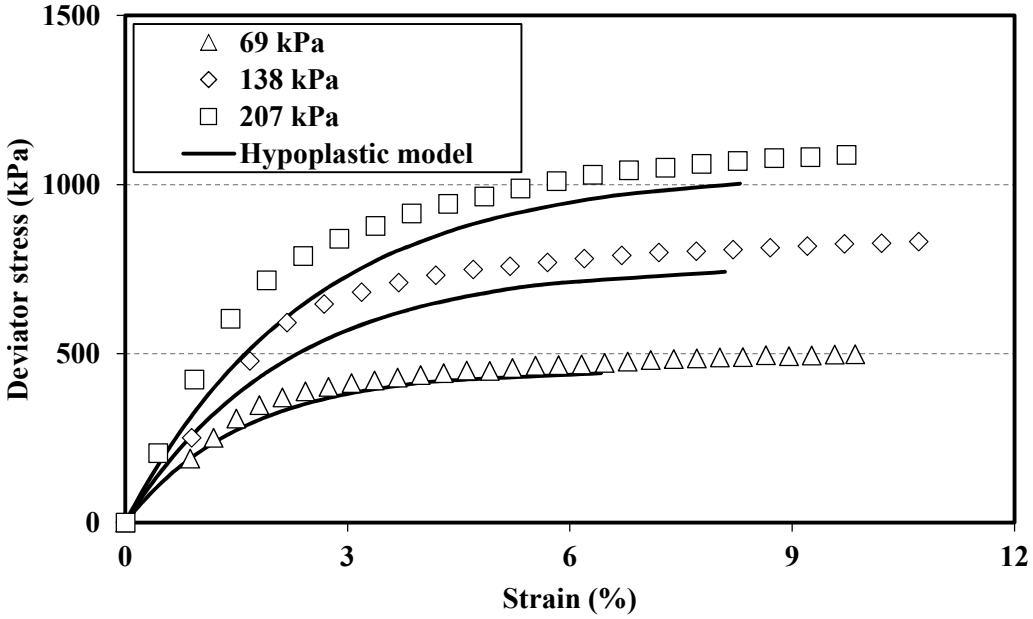

Figure 4.3 Comparison of the hypoplastic model with the experimental data for AB3

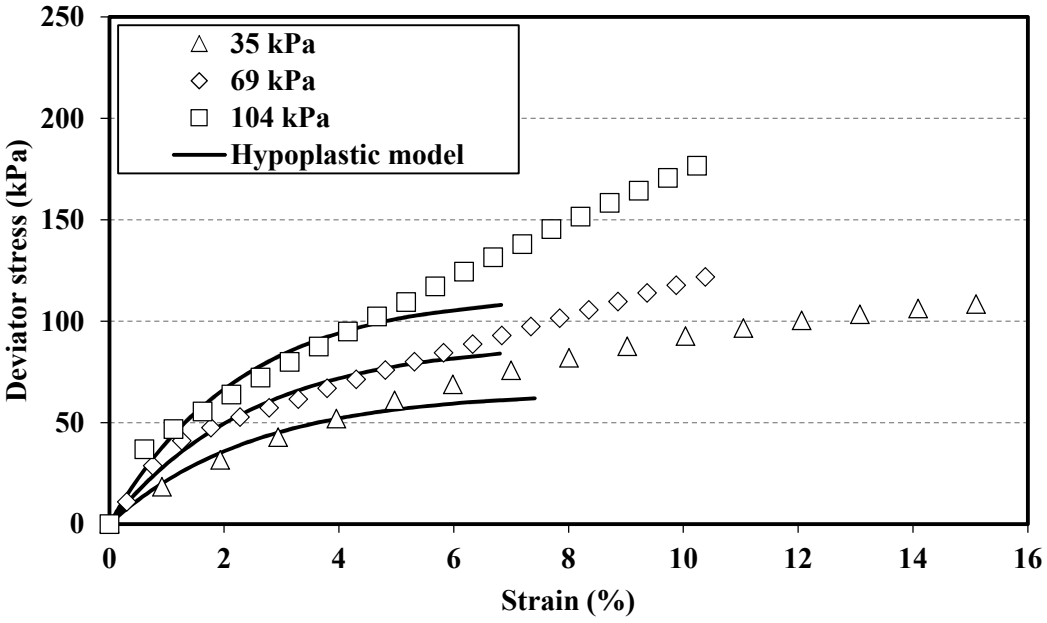

Figure 4.4 Comparison of the hypoplastic model with the experimental data for subgrade at 2% CBR

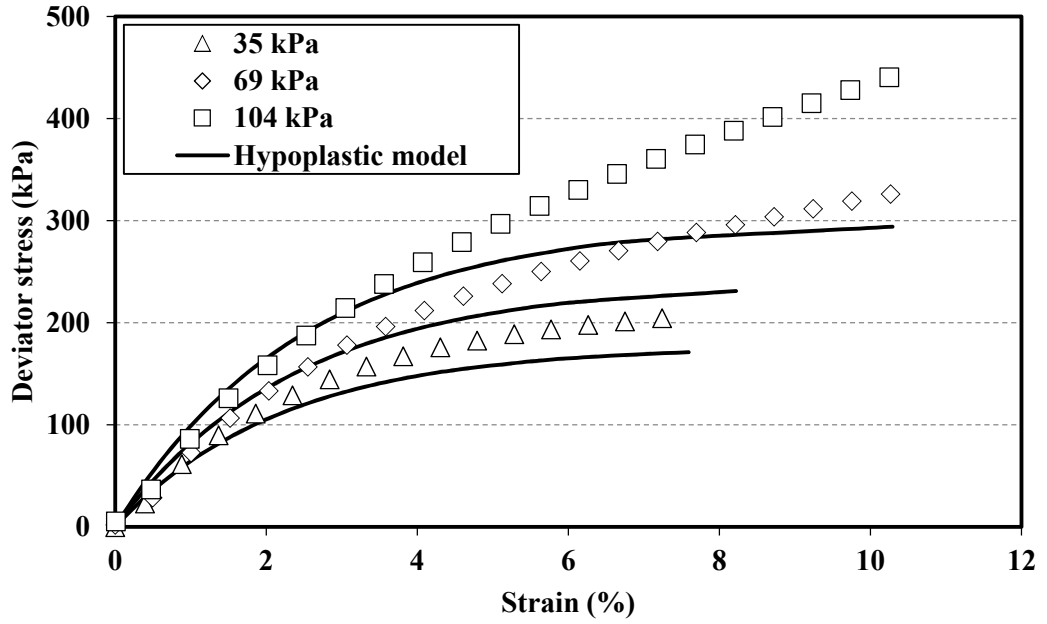

Figure 4.5 Comparison of the hypoplastic model with the experimental data for subgrade at 5% CBR

4.2.3 Triaxial condition with changing confinement

For the soil at the centerline of the layered sections, the lateral earth pressure can be considered as

$$\sigma_3 = k\sigma_1 \qquad \textbf{Equation 4.11}$$

where k is the lateral earth pressure coefficient. By substituting **Equation 4.11** into **Equation 4.3** and **Equation 4.4**, the following equations can be obtained.

At the loading stage,

$$\dot{\sigma}_1 = \sigma_1 \left[m \left((1+k) + \frac{2c\cot\varphi}{\sigma_1} \right) - n(1-k) \right] \dot{\varepsilon}_1 \qquad \textbf{Equation 4.12}$$

At the unloading stage,

$$\dot{\sigma}_1 = \sigma_1 \left[m \left((1+k) + \frac{2c\cot\varphi}{\sigma_1} \right) + n(1-k) \right] \dot{\varepsilon}_1 \qquad \textbf{Equation 4.13}$$

To express the soil parameters, m and n, the intial state and the final state of the soil should be taken into consideration.

At the initial stage,

$$E = E_0 \qquad \textbf{Equation 4.14}$$

$$\sigma_3 = k\sigma_{v0} \qquad \textbf{Equation 4.15}$$

$$\sigma_1 = \sigma_{v0} \qquad \textbf{Equation 4.16}$$

where E is the modulus of soil; E_0 is the initial modulus; k is the lateral earth pressure coefficient during a loading cycle (for the unstabilized condition, k is k_0; for the stabilized condition, k is $k_0 + \Delta k$); and σ_{v0} is the overburden stress.

At failure,

$$E = 0 \qquad \textbf{Equation 4.17}$$

Therefore, the soil parameters, m and n, can be determined based on the above conditions at the initial stage and at failture.

$$m = \frac{E_0 \sin\varphi}{\sigma_{v0}\left[\sin\varphi\left(1+k+\frac{2c\cot\varphi}{\sigma_{v0}}\right)-(1-k)\right]} \qquad \textbf{Equation 4.18}$$

$$n = \frac{E_0}{\sigma_{v0}\left[\sin\varphi\left(1+k+\frac{2c\cot\varphi}{\sigma_{v0}}\right)-(1-k)\right]} \qquad \textbf{Equation 4.19}$$

To obtain the stress-strain relationship, **Equation 4.12** and **Equation 4.13** need to be integrated. Considering the axial stress increases from σ_{v0} to σ_1 at the loading stage and decreases from σ_{max} to σ_1 at the unloading stage, the stress-strain relationship can be expressed as:

At the loading stage,

$$\frac{1}{A}\ln[(A\sigma_1 + C)/(A\sigma_{v0} + C)] = \varepsilon_1 \qquad \textbf{Equation 4.20}$$

At the unloading stage,

$$\frac{1}{B}\ln[(B\sigma_{max} + C)/(B\sigma_1 + C)] = \varepsilon_{max} - \varepsilon_1 \qquad \textbf{Equation 4.21}$$

where,

$$A = m(1 + k) - n(1 - k)$$

$$B = m(1 + k) + n(1 - k)$$

$$C = 2cm \cot \varphi \ .$$

In a geogrid stabilized base, the confinement and tensioned membrane effects of the geogrid will increase the lateral earth pressure coefficient, k. Therefore, the k value will be higher in the geogrid stabilized sections as compared with that in the unstabilized sections. During the loading and unloading processes, k is not a constant since the mobilization of the geogrid changes during the loading and unloading processes. For the unstabilized sections, the lateral earth pressure coefficient along the centerline can be considered as a constant (i.e., k_0). **Figure 4.6** shows the additional lateral earth pressure induced by the inclusion of the geogrid along the centerline of a road section.

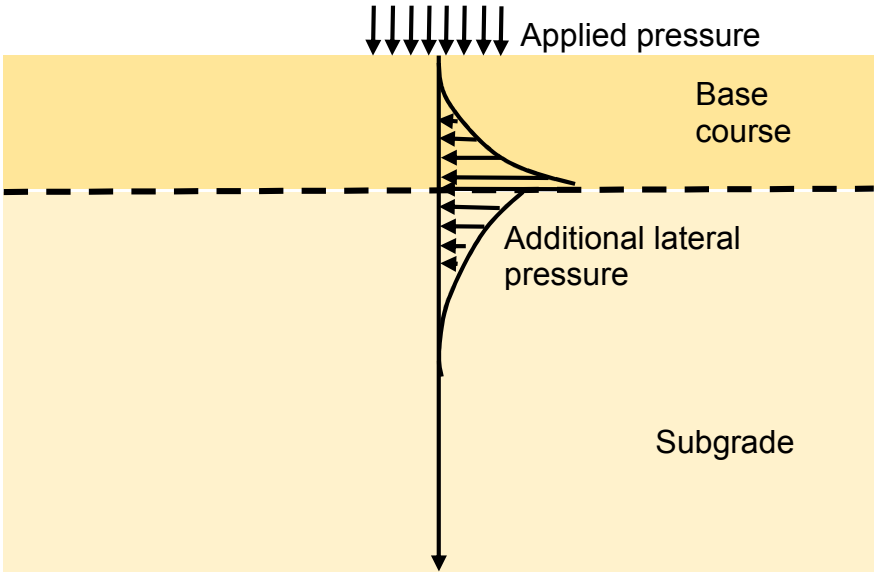

Figure 4.6 Additional lateral earth pressure along the centerline due to the geogrid

By substituting soil parameters determined from the triaxial test into **Equation 4.20** and **Equation 4.21**, the stress-strain relationship of the soil at the centerline of the test section under a plate loading test was obtained. For the unstabilized condition, k_0 was chosen as the lateral earth pressure coefficient. For demonstration purposes, the lateral earth pressure coefficient was increased by 0.1 and considered as a constant for the stabilized condition. The deviator stress increases from 0 to 300 kPa for AB3 and from 0 to 200 kPa for subgrade. **Table 4.1** summaries the input soil parameters. **Figures 4.7**, **4.8** and **4.9** show the stress-strain curves generated from the hypoplastic model.

Table 4.1 Soil parameters used in the model

Soil type	Cohesion (kPa)	Friction angle (°)	Initial modulus (kPa)	k for unstabilized condition	k for the stabilized condition
AB3	45	42	25000	0.33	0.43
Subgrade at 2% CBR	15	16	3000	0.74	0.84
Subgrade at 5% CBR	35	28	10000	0.53	0.63

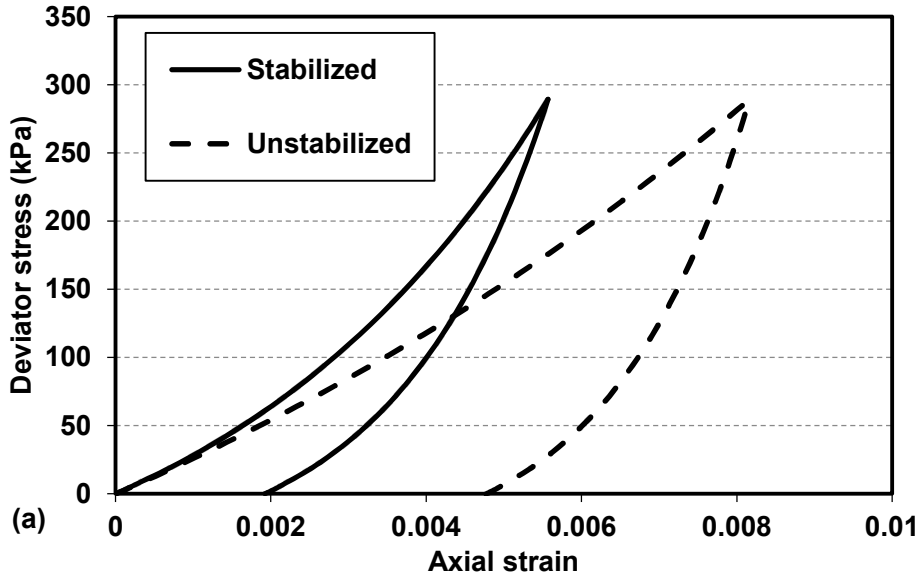

Figure 4.7 Hypoplastic model of stabilized and unstabilized base courses under loading and unloading

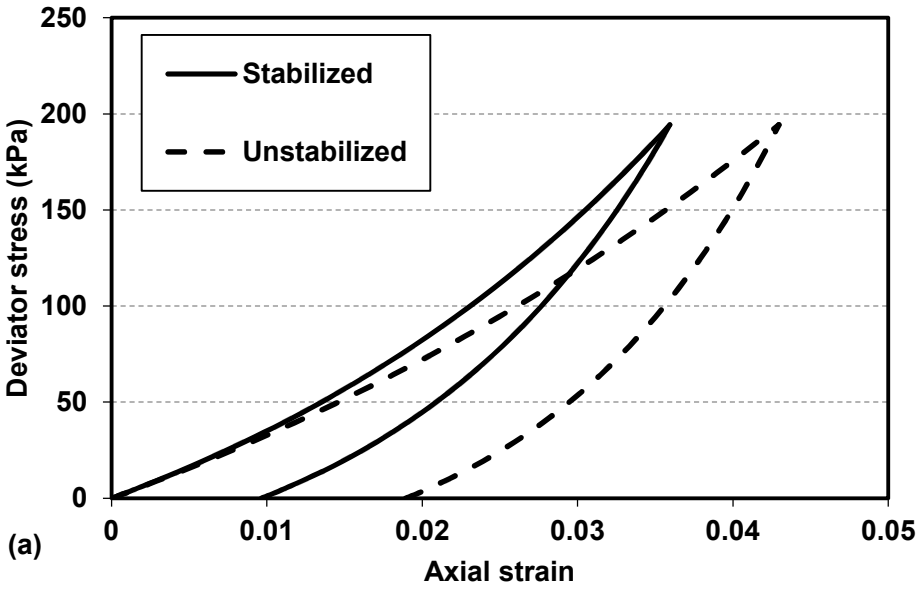

Figure 4.8 Hypoplastic model of the subgrade at 2% CBR under loading and unloading

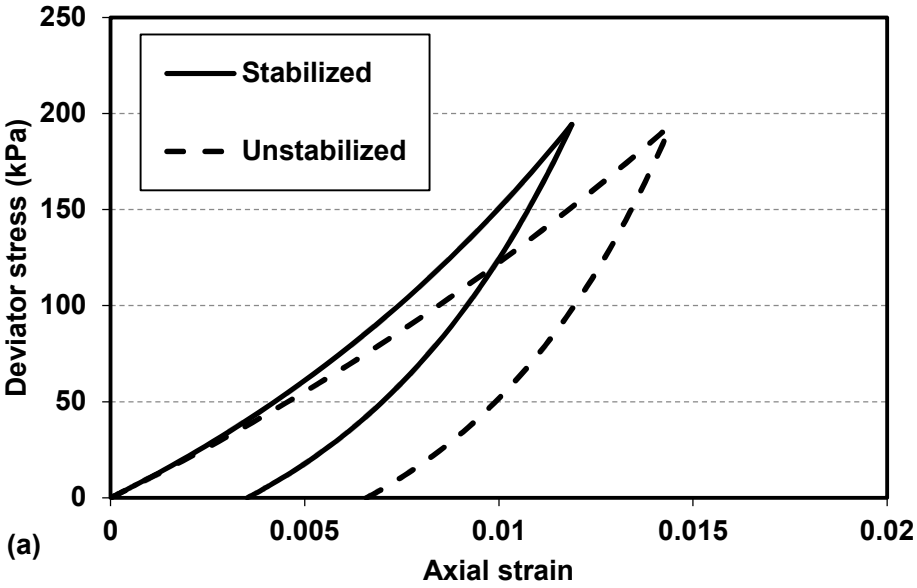

Figure 4.9 Hypoplastic model of the subgrade at 5% CBR under loading and unloading

As shown in **Figures 4.7**, **4.8** and **4.9**, it is obvious that the increase of the lateral earth pressure due to the inclusion of the geogrid improved the stiffness of the soil during the

loading stage and the axial strain (or total strain) was reduced significantly under the same deviator stress; however, at the unloading stage, the recovered or resilient strain was increased due to the additional lateral earth pressure induced by the inclusion of the geogrid. The reason for this phenomenon is that the effect of the additional lateral earth pressure induced by the geogrid increased the rebound at the unloading stage.

A qualitative schematic diagram, as shown in **Figure 4.10**, demonstrates the behavior of soils under stabilized and unstabilized conditions. At the loading stage, the stress-strain curve shifts from curve 1 to curve 2 due to the inclusion of the geogrid. This phenomenon is mainly due to the confinement effect of the geogrid. At the unloading stage, if the ratio of the permanent strain to the resilient strain is considered as the same as that of the unstabilized condition, the stress-strain curve will develop along the curve 2a and the stabilized soil will show a lower resilient strain as compared with the unstabilized soil. However, due to the additional lateral stress induced by the geogrid at the unloading stage, the stress-strain curve will go along the curve 2b. This shift between the curve 2a and curve 2b is referred to as the confinement effect at the unloading stage. With this effect, the resilient strain is even higher than the soil under the unstabilized condition. As compared with the unstabilized condition, both the confinement effect and the rebound effect benefit the stabilized soil by reducing the permanent strain. In **Figure 4.10**, $\varepsilon_{e,1}$ and $\varepsilon_{p,1}$ represent the resilient and permanent strains for the unstabilized condition; $\varepsilon_{e,2}$ and $\varepsilon_{p,2}$ represent the resilient and permanent strains for the stabilized condition without considering the confinement effect of the geogrid at the unloading stage; and $\varepsilon_{e,3}$ and $\varepsilon_{p,3}$ represent the resilient and permanent strains for the stabilized condition with considering

the confinement effect of the geogrid at the unloading stage. The relationship between these strains under different conditions can be expressed as follows:

$$\varepsilon_{e,2} < \varepsilon_{e,1} < \varepsilon_{e,3}$$

$$\varepsilon_{p,3} < \varepsilon_{p,2} < \varepsilon_{p,1}$$

$$\frac{\varepsilon_{p,1}}{\varepsilon_{e,1}} = \frac{\varepsilon_{p,2}}{\varepsilon_{e,2}}$$

$$\varepsilon_{p,2} + \varepsilon_{e,2} = \varepsilon_{p,3} + \varepsilon_{e,3}$$

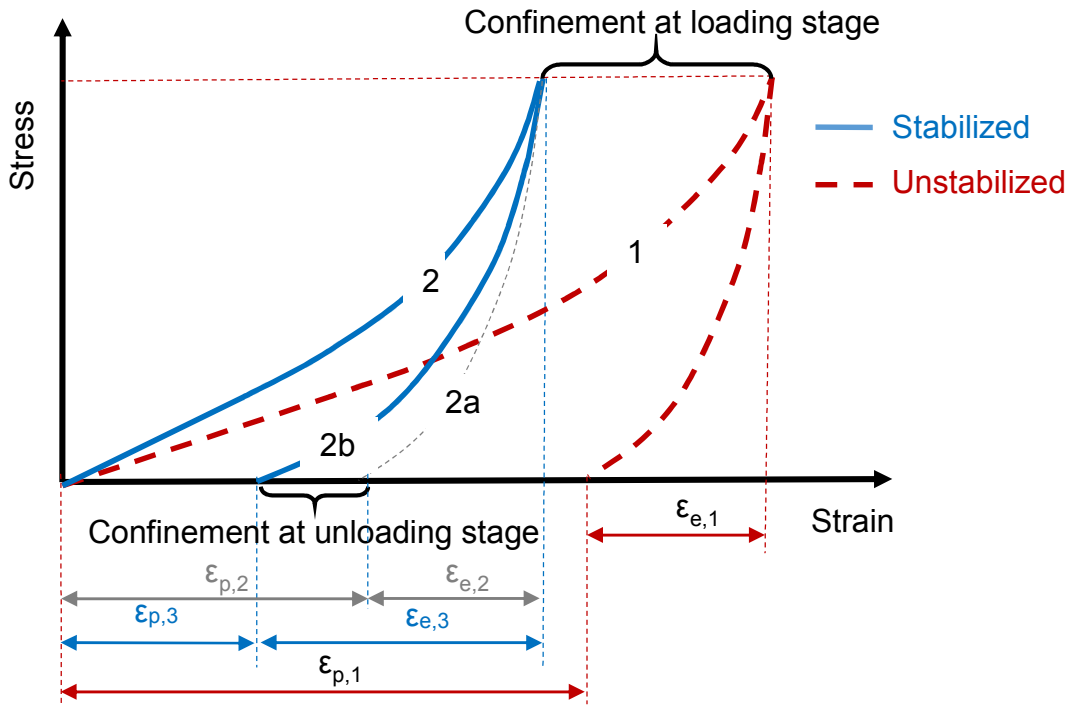

Figure 4.10 Confinement effect and rebound effect of the geogrid

4.2.4 Evaluation of the permanent and resilient strains

The permanent strain at each cycle can be estimated by the hypoplastic model with the initial modulus, cohesion, and friction angle of soil. However, under a cyclic loading

condition, the initial modulus of the soil changes with cycles due to the change of its void ratio.

In the current MEPDG design, the permanent strain is accumulated based on the elastic (resilient) strain and the number of loading cycles. The soil damage model adopted in the MEPDG has been discussed in the previous chapter and is presented here again.

$$\frac{\varepsilon_p}{\varepsilon_e} = k_{calibration} \cdot \left(\frac{\varepsilon_0}{\varepsilon_r}\right) \cdot e^{-\left(\frac{\rho}{N}\right)^{\beta}}$$

Equation 4.22

where ε_p is the accumulated permanent strain,ε_e is the elastic (resilient) strain, N is the number of loading cycles, $k_{calibration}$ is a calibration factor, and other parameters are about the soil properties. From **Equation 4.22**, it is obvious to see that the ratio of the permanent strain to resilient strain is considered as a constant for a soil under a certain physical state (e.g., moisture content) and loading cycles.

In the previous hypoplastic model, the ratio of the permanent strain to resilient strain for an unstabilized condition yields

$$\frac{\varepsilon_{p,1}}{\varepsilon_{e,1}} = \frac{\varepsilon_{p,2}}{\varepsilon_{e,2}} = \frac{B}{A}\frac{ln[(A\sigma_{max} + C)/(A\sigma_{v0} + C)]}{ln[(B\sigma_{max} + C)/(B\sigma_{v0} + C)]} - 1$$

Equation 4.23

where,

$A = m(1 + k) - n(1 - k)$

$B = m(1 + k) + n(1 - k)$

$C = 2cm\cot\varphi$

$k = k_0$, for the unstabilized condition.

For the stabilized condition,

$$\frac{\varepsilon_{p,3}}{\varepsilon_{e,3}} = \frac{B}{A}\frac{ln[(A\sigma_{max}+C)/(A\sigma_{v0}+C)]}{ln[(B\sigma_{max}+C)/(B\sigma_{v0}+C)]} - 1$$

Equation 4.24

where,

$$A = m(1+k) - n(1-k)$$

$$B = m(1+k) + n(1-k)$$

$$C = 2cm\cot\varphi$$

$$k = k_0 + \Delta k;$$

Δk is the increase of the lateral earth pressure coefficient induced by geogrid.

In **Equation 4.23** and **Equation 4.24**, the ratios of the permanent strain to resilient strain are independent to the initial modulus and the physical state of the soil. By considering the equation that

$$\varepsilon_{p,2} + \varepsilon_{e,2} = \varepsilon_{p,3} + \varepsilon_{e,3}$$

Equation 4.25

$\frac{\varepsilon_{p,3}}{\varepsilon_{p,2}}$ and $\frac{\varepsilon_{e,3}}{\varepsilon_{e,2}}$ can be derived as the following equations:

$$\frac{\varepsilon_{p,3}}{\varepsilon_{p,2}} = \frac{\frac{\varepsilon_{p,3}}{\varepsilon_{p,3}+\varepsilon_{e,3}}}{\frac{\varepsilon_{p,2}}{\varepsilon_{p,2}+\varepsilon_{e,2}}} = \frac{\frac{\varepsilon_{p,3}/\varepsilon_{e,3}}{\varepsilon_{p,3}/\varepsilon_{e,3}+1}}{\frac{\varepsilon_{p,2}/\varepsilon_{e,2}}{\varepsilon_{p,2}/\varepsilon_{e,2}+1}}$$

Equation 4.26

$$\frac{\varepsilon_{e,3}}{\varepsilon_{e,2}} = \frac{\frac{\varepsilon_{e,3}}{\varepsilon_{p,3}+\varepsilon_{e,3}}}{\frac{\varepsilon_{e,2}}{\varepsilon_{p,2}+\varepsilon_{e,2}}} = \frac{\varepsilon_{p,2}/\varepsilon_{e,2}+1}{\varepsilon_{p,3}/\varepsilon_{e,3}+1}$$

Equation 4.27

Equation 4.26 and **Equation 4.27** can be reorganized as follows:

$$\varepsilon_{p,3} = f_p \cdot \varepsilon_{p,2} \qquad \textbf{Equation 4.28}$$

$$\varepsilon_{e,3} = f_e \cdot \varepsilon_{e,2} \qquad \textbf{Equation 4.29}$$

where the two modified factors, f_p and f_e are expressed as:

$$f_p = \frac{\frac{\varepsilon_{p,3}/\varepsilon_{e,3}}{\varepsilon_{p,3}/\varepsilon_{e,3}+1}}{\frac{\varepsilon_{p,2}/\varepsilon_{e,2}}{\varepsilon_{p,2}/\varepsilon_{e,2}+1}}$$

$$f_e = \frac{\varepsilon_{p,2}/\varepsilon_{e,2}+1}{\varepsilon_{p,3}/\varepsilon_{e,3}+1}$$

In **Equation 4.28** and **Equation 4.29**, $\varepsilon_{p,3}/\varepsilon_{e,3}$ and $\varepsilon_{p,2}/\varepsilon_{e,2}$ can be determined from **Equation 4.23** and **Equation 4.24**.

To obtain $\varepsilon_{p,3}$ and $\varepsilon_{e,3}$, the following variants are needed: (1) Δk; (2) $\varepsilon_{p,2}$; and (3) $\varepsilon_{e,2}$. In fact, based on the MEPDG soil damage model, $\varepsilon_{p,2}$ can be obtained if $\varepsilon_{e,2}$ is known. Therefore, Δk and $\varepsilon_{e,2}$ are two remaining parameters need to be determined.

In this study, a theoretical solution for the geogrid-stabilized transversely-isotropic layered elastic system was derived, as presented in Appendix A. With the solution available, the elastic strains, $\varepsilon_{e,2}$, along the centerline of the geogrid-stabilized test section can be calculated. In the theoretical derivation, the geogrid-soil interface was considered as fully bonded. Geogrid induced lateral earth pressure was evaluated by considering the lateral confinement, which was caused by the tension in the geogrid due to the lateral permanent

deformation of the soil. Additionally, the tensioned membrane effect of the geogrid, due to the large differential vertical deformation of subgrade, was taken into account.

Figure 4.11 shows the force diagram of a soil element taken from the centerline of the layered system.

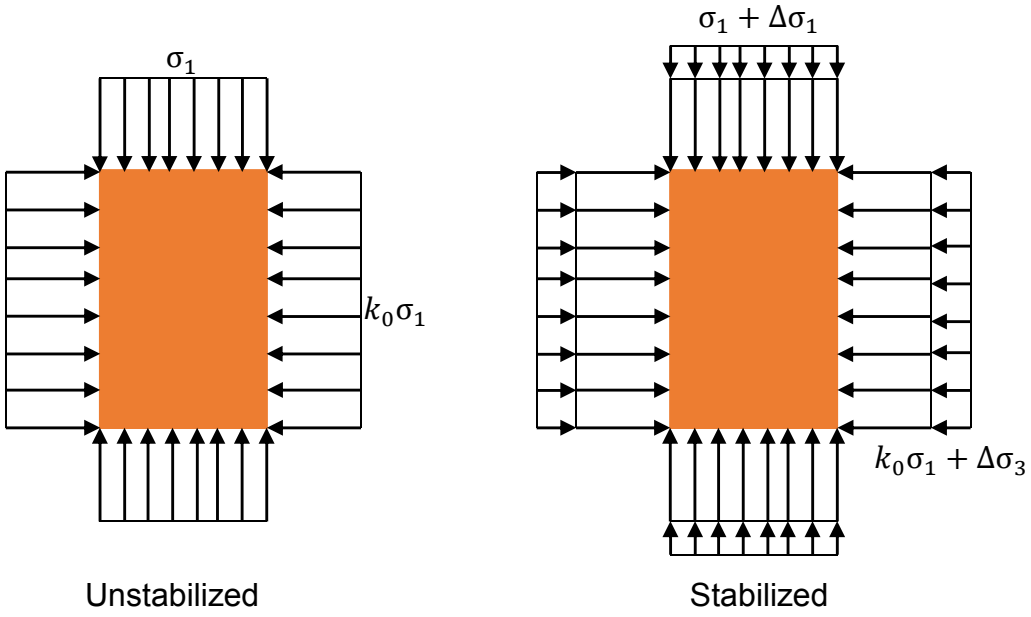

Figure 4.11 Force diagram of a soil element at the centerline

As shown in **Figure 4.11**, additional lateral pressure, $\Delta\sigma_3$, and additional vertical pressure, $\Delta\sigma_1$, are applied on the soil element. $\Delta\sigma_3$ and $\Delta\sigma_1$ can be determined by the difference of the stresses between the unstabilized and stabilized elastic layered systems. Therefore, Δk can be determined as:

$$\Delta k = \frac{k_0\sigma_1 + \Delta\sigma_3}{\sigma_1 + \Delta\sigma_1} - k_0 = \frac{k_0\Delta\sigma_1 + \Delta\sigma_3}{\sigma_1 + \Delta\sigma_1}$$

Equation 4.30

During a loading cycle, σ_1, $\Delta\sigma_3$, and $\Delta\sigma_1$ change with the loading wave. To be simplified, Δk is determined at the maximum applied pressure, $\sigma_{1,max}$, with the corresponding additional pressures obtained from the elastic theory under a static condition. With all the available parameters, the permanent and resilient strains can be estimated for the geogrid stabilized layered elastic system.

4.3 Degradation of the base course

As observed in the laboratory tests, the vertical stresses at the interface of the base courses and subgrade increased with the increase of loading cycles. This phenomenon indicates that the modulus ratio of the base courses to subgrade decreased. In other words, the modulus of base courses decreased if the subgrade modulus is considered as no change. The reason for the degradation of the base course is due to the shear of the base courses under cyclic shear stresses. **Figure 4.12** shows the shear failure of the base course. In the vertical direction, the base course was compressed and the modulus would increase. To be conservative, the modulus in the vertical direction can be considered as constant. Due to the vertical shear of the cyclic loading, the modulus in the horizontal direction would decrease. Therefore, the base course can be considered as transversely-isotropic, as shown in **Figure 4.13**. In **Figure 4.13**, the vertical shear modulus G_v within the shear zone degrades with the accumulation of the shear strain. The vertical modulus E_v will not degrade since the base course is compressed under the k_0 condition. Therefore, it can be assumed that E_v keeps constant during the cyclic loading.

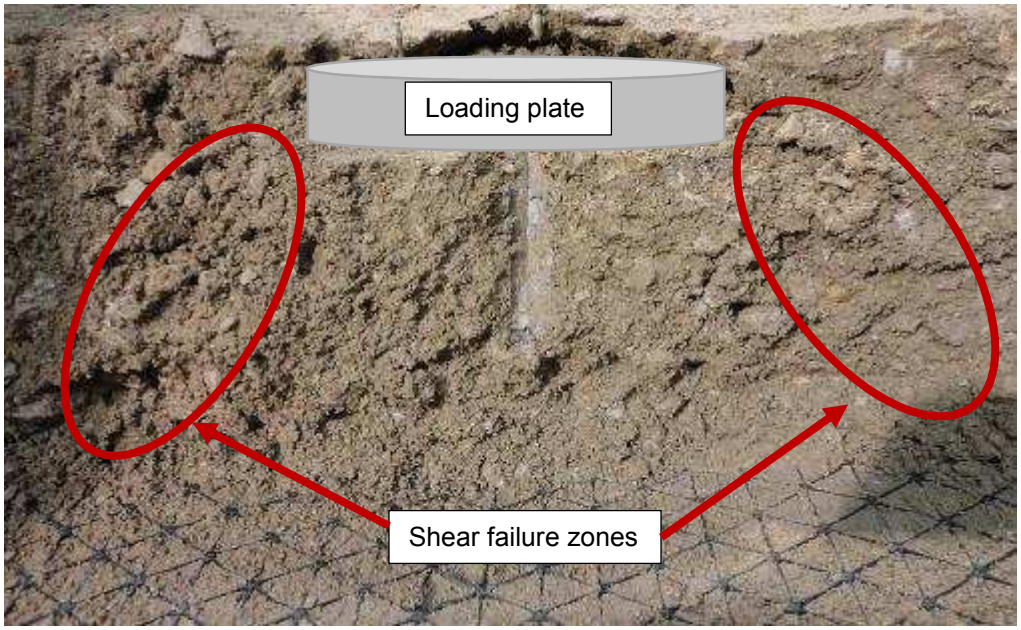

Figure 4.12 The shear failure of the base course in the cross-section

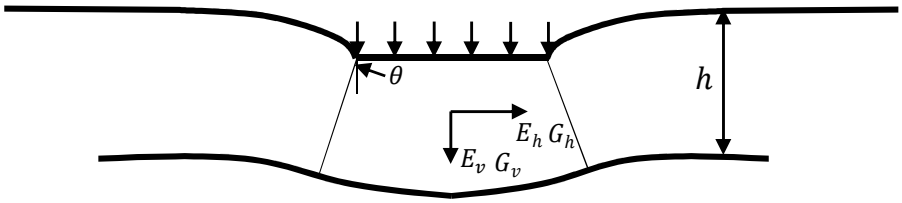

Figure 4.13 The transversely-isotropic property of the base course

Considering the approximate relationship between shear modulus and elastic modulus as Lekhnitskii (1981) suggested, as shown in **Equation 2.17**, the horizontal modulus of the base course, E_h, decreases with the decrease of the vertical shear modulus G_v.

$$E_h = \frac{G_v E_v}{E_v - G_v(1 + 2\mu')}$$

Equation 4.31

where μ' is the Poisson's ratio characterizing the contraction in the isotropic plane when tension is applied to a plane normal to the plane of isotropy.

Additionally,

$$G_h = \frac{E_h}{(1+2\mu)} \qquad \textbf{Equation 4.32}$$

where μ is the Poisson's ratio characterizing the contraction in the isotropic plane when tension is applied in the plane of isotropy.

Hyperbolic relationship, as shown in **Figure 4.14**, is a good approximation between the shear stress and the shear strain under dynamic loading, as shown in **Equation 4.33**.

$$\tau = \frac{\gamma}{a+b\gamma} \qquad \textbf{Equation 4.33}$$

where τ and γ are the stress and strain on the shear surface; a and b are soil parameters.

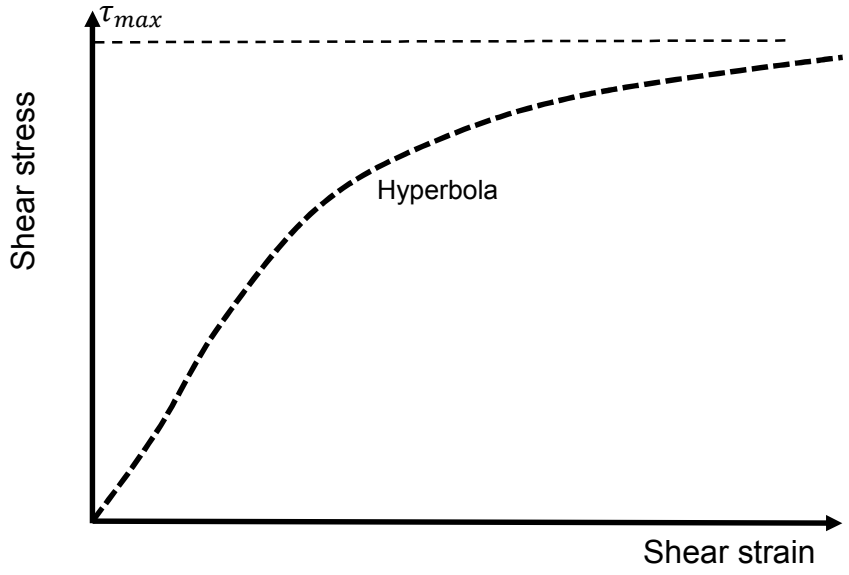

Figure 4.14 The typical shear stress and shear strain curve

According to Hardin and Drnevich (1972), the degradation of the secant shear modulus of a soil can be expressed as the following formula:

$$\frac{G_v}{G_{v,0}} = \frac{1}{\left(1+\frac{\gamma}{\gamma_{ref}}\right)} \qquad \textbf{Equation 4.34}$$

where γ_{ref} is the reference shear strain, $\gamma_{ref} = \frac{\tau_{max}}{G_{v,0}}$ and τ_{max} is the shear stress at infinite strain.

For the degradation of base courses under cyclic loading, Hardin and Drnevich's formula was adopted in this study. However, the shear strain was changed to the accumulated shear strain and γ_{ref} was defined as the maximum accumulated shear strain. Therefore, γ_{ref} can be determined as the maximum shear strain at the rut depth of 75 mm in the center. 75 mm rutting at the interface is considered as the failure in the design of unpaved roads. With the known rut depths at the top of subgrade and base course, the vertical shear modulus of the base course can be estimated. Subsequently, the elastic modulus in the horizontal direction, E_h, can be determined as well.

A base course may degrade with the number of loading cycles but reach a residual state. In other words, there is a residual modulus existing for the base course. In this study, the horizontal modulus of the base course was considered not lower than the modulus of the subgrade.

4.4 Summary

Based on the analysis shown in this chapter, the findings can be summarized as follows:

(1) The phenomenon that geogrid-stabilized sections had higher resilient deformations as compared with unstabilized sections was due to the confinement effect during the unloading stage.

(2) The hypoplastic model can be adopted to model the confinement during the unloading stage. To consider the confinement effect during the unloading stage, the MEPDG soil damage model was modified to estimate the permanent deformation of the geogrid stabilized section.

(3) The degradation of a base course was considered as the shear modulus degradation with the increase of the number of cycles. The accumulation of the shear strain in the base course, due to the increase of the number of cycles, caused the degradation of the base course. The shear modulus degradation curve was assumed being hyperbolic.

Chapter 5 Model Validation and Predicted Performance of the Geogrid-stabilized Base Courses over Subgrade

5.1 Introduction

In the previous chapters, the base course degradation model and the modified soil damage model were developed. These models needs to be verified by the experimental data as shown in Chapter 3. In this chapter, a MATLAB code was programed to predict the performance of the unstabilized and geogrid-stabilized sections. The geogrid confinement effect during the loading/unloading stage and the base degradation were taken into consideration in this program. The additional lateral earth pressure induced by the geogrid, the vertical pressures at the interface, the permanent deformations, and the resilient deformations were investigated and discussed.

5.2 Proposed method

The evaluation of the performance of a base course over subgrade was programed in Matlab 2013. In this program, the resilient modulus of soil, Poisson's ratio, layer thickness and geosynthetic stiffness need to be input. At a certain cycle, the stress and the resilient strain of a roadway were estimated based on the geosynthetic-stabilized layered elastic solution with the confinement effect and the tensioned membrane effect obtained from the previous cycle. With the obtained roadway responses, the MEPDG soil damage model and the reduction factor due to the confinement during the unloading stage were taken into account to determine the accumulated rutting. By assuming no volume change in the base course, the lateral deformation of the base course was estimated based on

the accumulated rutting. The accumulated rutting and the lateral deformation were be used to consider the confinement effect and the tensioned membrane effect of the geogrid for the next cycle. **Figure 5.1** shows the flow chart of the program.

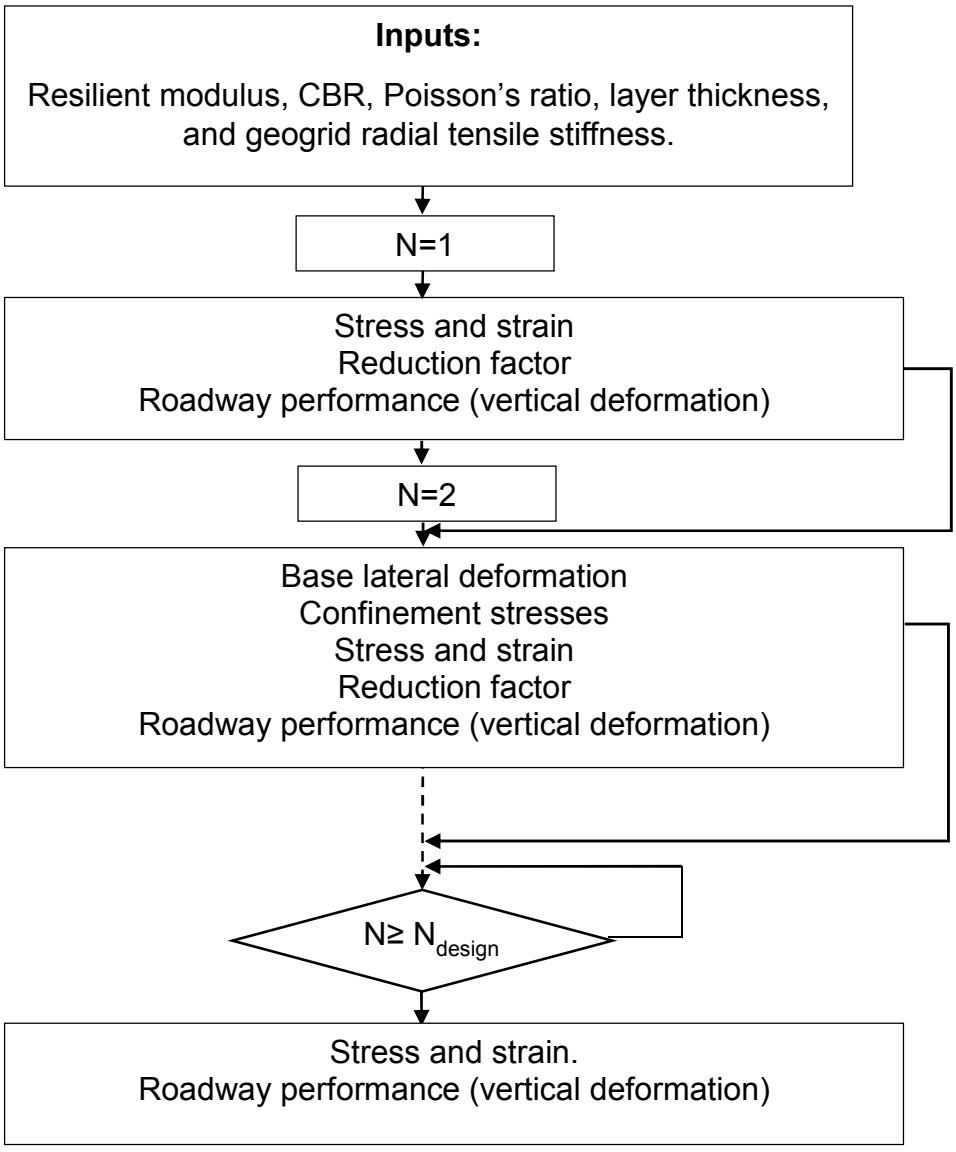

Figure 5.1 The procedure for the evaluation of the roadway performance

5.3 Input parameters

The test sections under cyclic loading with an increasing load magnitude, which are presented in Chapter 3.2, and the test sections under cyclic loading of 40 kN, which are presented in Chapter 3.4, were modeled to verify the models developed in Chapter 4. The CBR inputs in Table 3.2 and Table 3.5 were used to determine the resilient moduli of the base courses and subgrade. The modulus ratios of base courses to subgrade were evaluated based on the following equation (Giroud and Han, 2004a):

$$R_E = \frac{E_{bc}}{E_{sg}} = \min\left(\frac{3.48 CBR_{bc}^{0.3}}{CBR_{sg}}, 5.0\right) \qquad \textbf{Equation 5.1}$$

where E_{bc} = resilient modulus of base course (kPa);

E_{sg} = resilient modulus of subgrade soil (kPa);

CBR_{bc} = California Bearing Ratio (CBR) of base course; and

CBR_{sg} = CBR of subgrade.

The subgrade resilient modulus was estimated based on **Equation 3.11**.

The geogrid stiffness values for T1 and T2 as shown in Chapter 3 were used to in the calculation. The cohesion and friction angle of base courses and subgrade were obtained based on the triaxial tests, as discussed in the previous section. **Table 5.1** summaries the parameters.

Table 5.1 Soil parameters used in the model

Soil type	Cohesion (kPa)	Friction angle (°)	Resilient modulus (MPa)	k for unstabilized condition (1-sinφ)
AB3	45	42	R_e*E_{sg}	0.33
Subgrade at 2% CBR	15	16	$18.3\mathrm{CBR}^{0.54}$	0.74
Subgrade at 3% CBR	30	18	$18.3\mathrm{CBR}^{0.54}$	0.69
Subgrade at 5% CBR	35	28	$18.3\mathrm{CBR}^{0.54}$	0.53

5.4 Additional lateral earth pressure coefficient

5.4.1 Changes of the vertical stresses and the lateral stresses

With the increase of loading cycles, the lateral and vertical deformations of a geogrid accumulate and therefore tension develops in geogrid. Due to the interlock between the geogrid and the soils, the tension in the geogrid is applied to the soils and induces the changes of lateral and vertical earth pressures. For demonstration purposes, **Figure 5.2** and **Figure 5.3** show the changes of the vertical stresses and the lateral stresses along the centerline of the test sections with the T2-stabilized base course. In each figure, the curves from the left to the right are referred to as the changes of the stresses from 100 to 1000 cycles with an increment of 100 cycles. In these figures, the geogrid was located at the depth of zero.

Figure 5.2 and **Figure 5.3** show that the change of the vertical stresses and the lateral stresses increased with the increase of the loading cycles. This result indicates that the tension in the geogrid increased with the accumulation of deformations. Under the same

number of loading cycles, the change of the vertical/lateral stresses was higher in the sections with a thinner base course. The reason is that the geogrid was easily mobilized in a section with a thinner base course.

In addition, the influence depth of the geogrid can be observed in **Figure 5.2** and **Figure 5.3**. As shown in **Figure 5.2**, the influence depth of the geogrid to the vertical stresses was 0.15 m below the interface. As shown in **Figure 5.3**, the influence depth of the geogrid to the lateral stresses increased with the increase of the tension in geogrid. Approximately, the influence depth of the geogrid on the lateral stresses in the base was 75% of the thickness of the base and that in the subgrade was around 0.3 m.

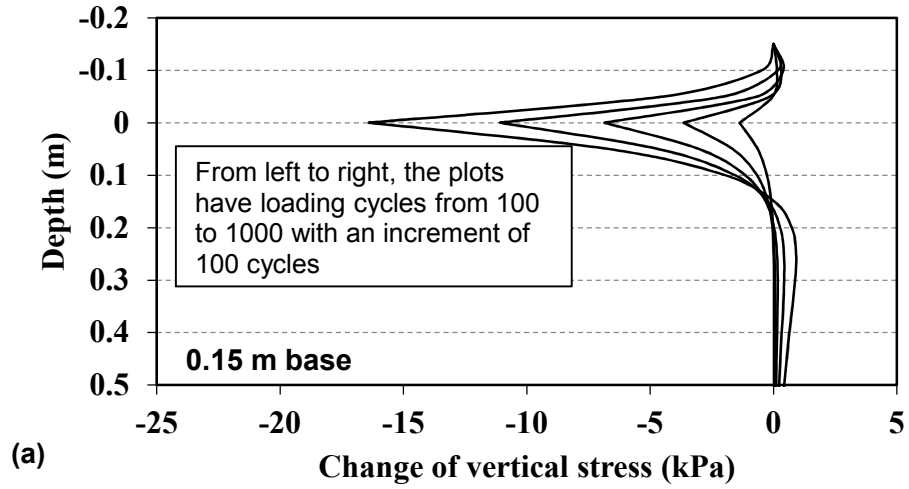

(a)

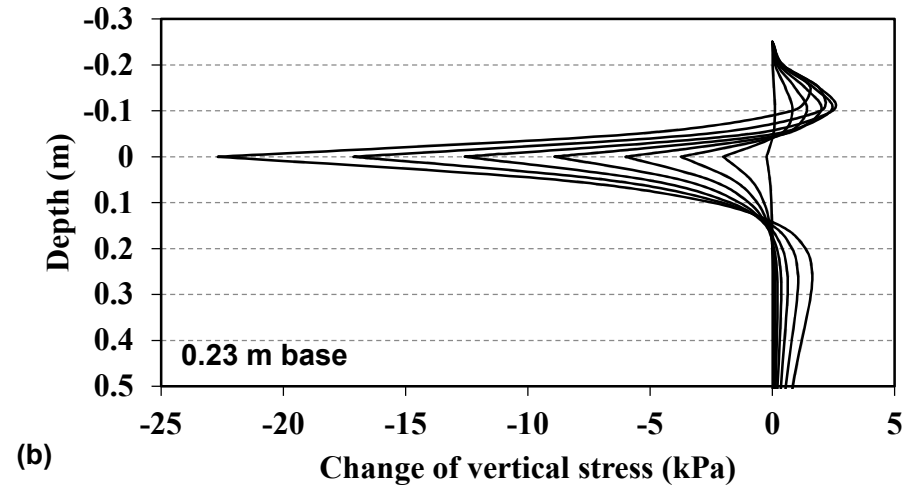

(b)

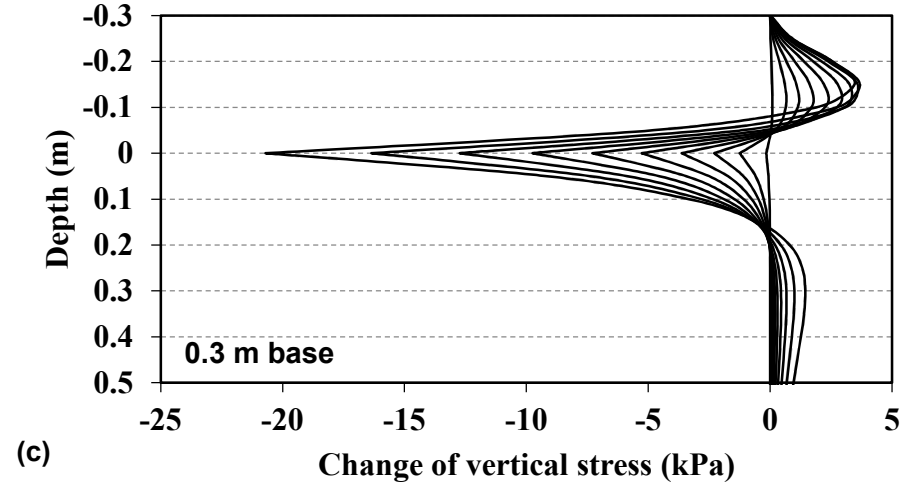

(c)

Figure 5.2 Change of the vertical stresses along the centerline with the inclusion of T2 geogrid

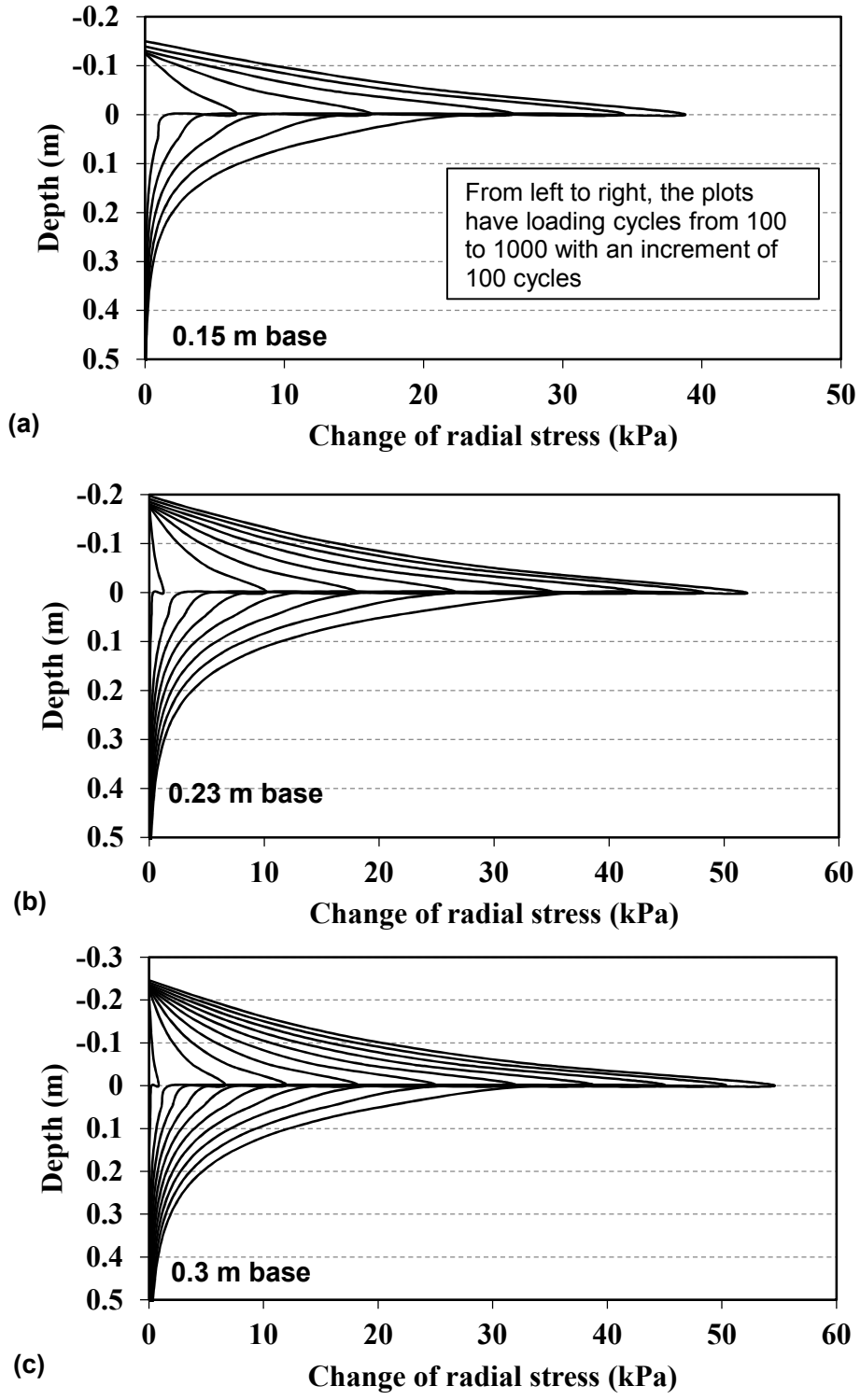

Figure 5.3 Change of the lateral stresses along the centerline with the inclusion of T2 geogrid

5.4.2 The increase of the lateral earth pressure coefficient

The decrease of the vertical stresses and the increase of the lateral stresses due to the inclusion of the geogrid result in the increase of the lateral earth pressure coefficient. Under a static condition, the additional lateral earth pressure coefficient can be evaluated based on **Equation 4.21**. **Figure 5.4** shows the additional lateral earth pressure coefficient induced by the inclusion of the geogrid with the increasing number of loading cycles. As shown in **Figure 5.4**, the additional lateral earth pressure coefficient increased with the number of loading cycles. In addition, the additional lateral earth pressure coefficient was higher in the base course than that in the subgrade. The reason is that the lateral earth pressure induced by the geogrid was much higher in the base course than that in the subgrade along the centerline. Under cyclic loading, the additional lateral earth pressure coefficient changed with the loading cycle; however, it was simplified as a constant during a loading cycle in this study.

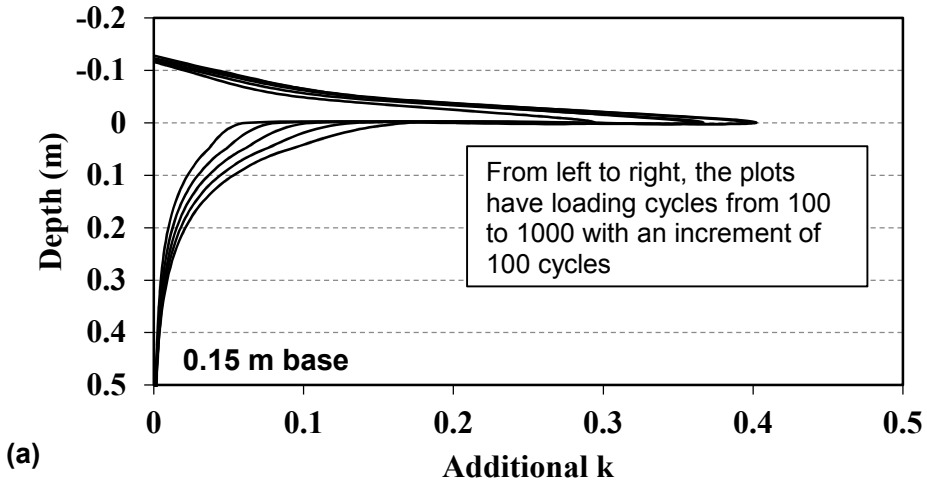

(a)

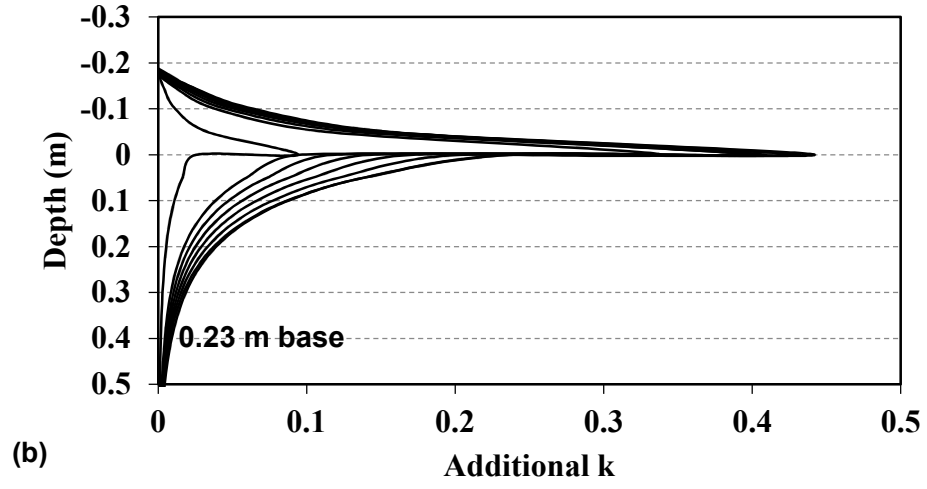

(b)

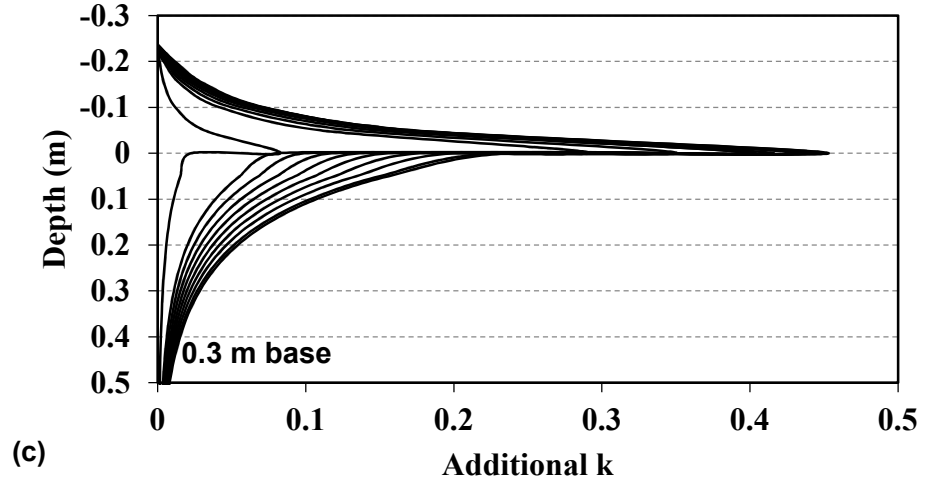

(c)

Figure 5.4 Additional lateral earth pressure coefficient

5.4.3 Permanent strain reduction factor and resilient strain increase factor

With the available soil parameters and the additional lateral earth pressure coefficient, the permanent strain reduction factors and the resilient strain increase factors were determined based on **Equation 4.19** and **Equation 4.20**. **Figures 5.5** and **5.6** show the reduction factors and the increase factors for the test sections stabilized by T2 geogrid. As shown in the figures, the reduction factors for permanent strains were less than one. This result indicates that the permanent strains were reduced. Similarly, the resilient strains were increased.

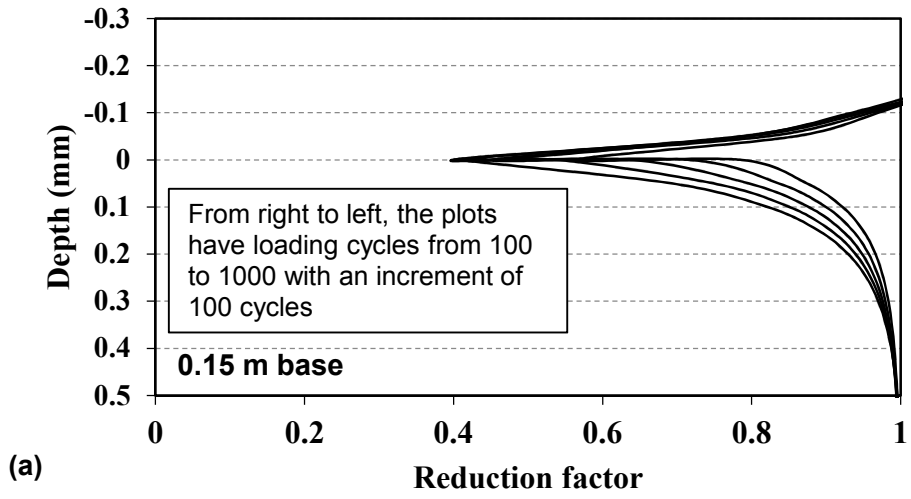

(a)

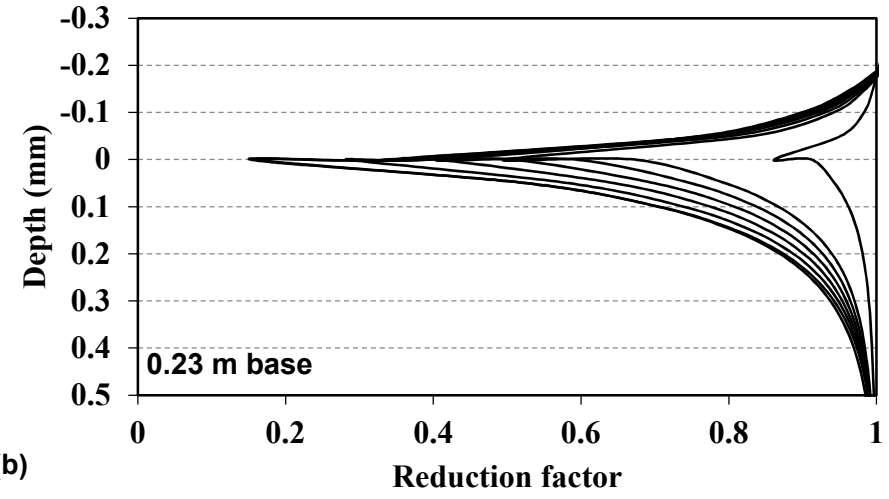

(b)

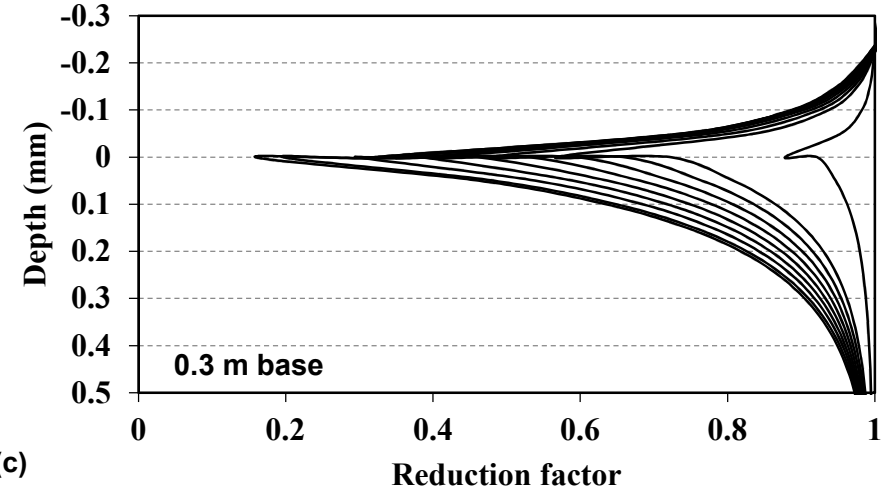

(c)

Figure 5.5 Permanent strain reduction factor

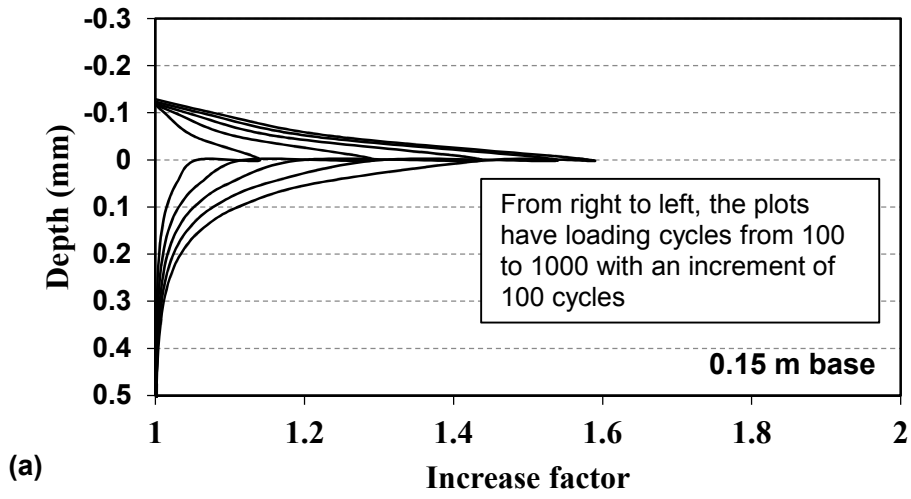

(a)

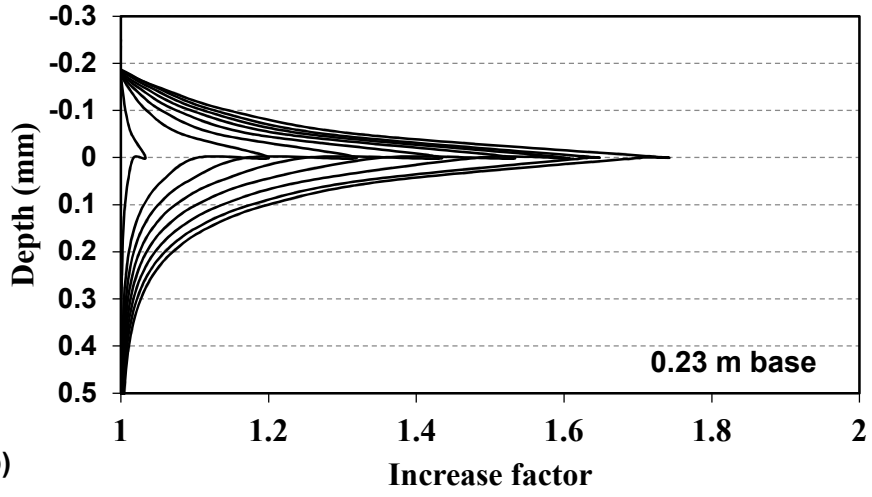

(b)

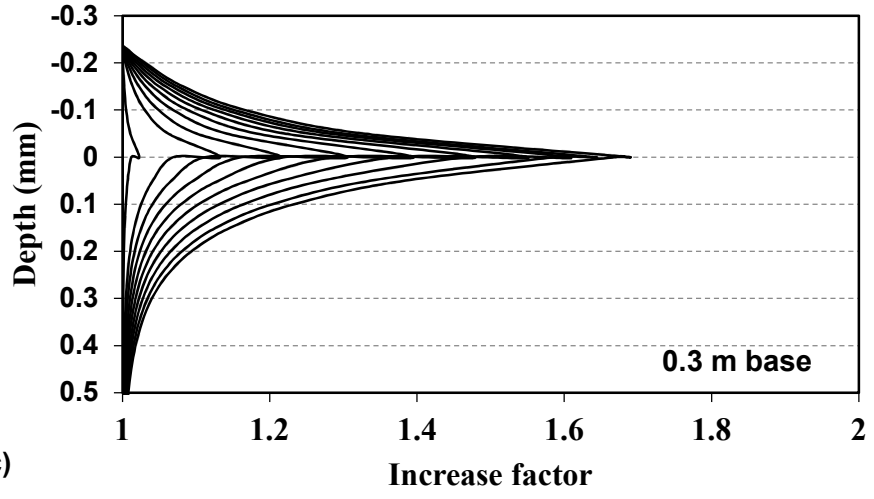

(c)

Figure 5.6 Resilient strain increase factor

5.5 Comparison of measured and predicted roadway performances

5.5.1 Vertical stresses

Figure 5.7 shows the comparison between the measured and predicted vertical stresses at the interface. As shown in the figure, overall, the predicted vertical stresses for the unstabilized sections reasonably matched with the measured stresses. The predicted results overestimated the vertical stresses in the stabilized sections. In other words, the benefit of the geogrid was underestimated. As compared with the 0.15 m thick base, the predicted results for the sections with 0.23 and 0.3 m thick bases matched the measured results comparatively well. Several reasons may influence the prediction: 1) The dilation of the base course material was not taken into consideration and 2) the resilient moduli of the base course and subgrade were estimated based on the empirical correlation between the resilient modulus and CBR values. The base course degradation model showed the phenomenon that the vertical stresses increased with the increase of the number of loading cycles.

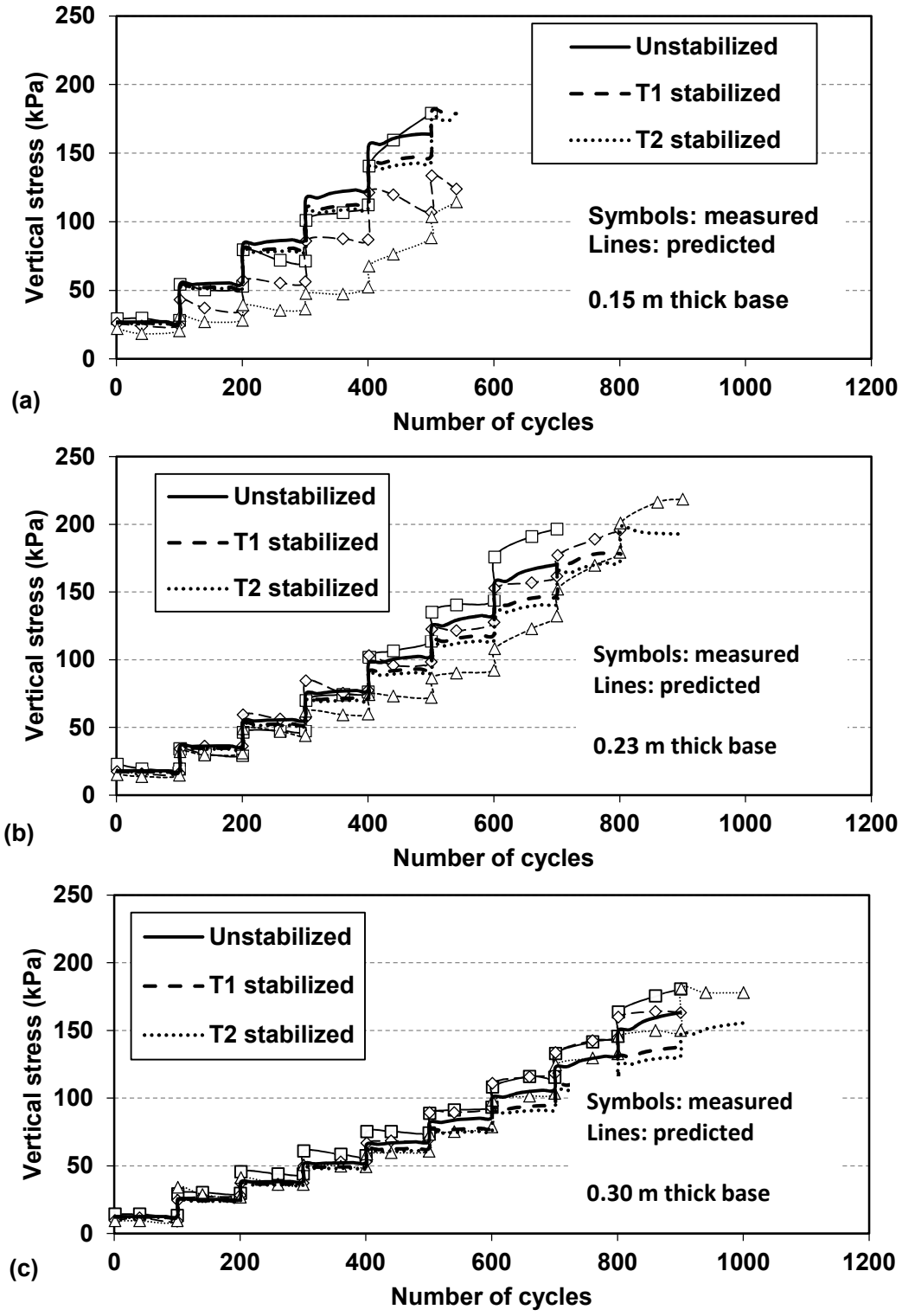

Figure 5.7 Comparison of the measured and predicted vertical stresses at the interface

5.5.2 Resilient deformations

Figures 5.8 and **5.9** show the comparison of the predicted and measured resilient deformations at the surface and the top of the subgrade, respectively. The measured resilient deformations were higher than the predicted resilient deformations, especially for the geogrid stabilized sections. The predicted resilient deformations of the geogrid stabilized sections were higher than those of the unstabilized sections; however, the increase of the predicted resilient deformations in the stabilized sections was much lower than that of the measured resilient deformations due to the inclusion of geogrids. At the top of the subgrade, the increase of the predicted resilient deformation was even less. Theoretically, the additional lateral earth pressure during the unloading stage increased the resilient deformation. In reality, the increase of the resilient deformation was much higher based on the measured results. The possible reason is that, at the end of the unloading stage, the base course and the subgrade might not be in contact due to the tension in the geogrid. Therefore, under an loading condition, the base course might move downward a certain distance (the void between the bottom of the base course and the top of subgrade) to fully touch the subgrade and then keep moving down as a fully contact condition. Under an unloading condition, the geogrid stabilized base course and the subgrade rebounded together as a fully bonded composite and then separate lost contact because the base course kept move upward due to the tension of the geogrid. This phenomenon happened only when the permanent deformation became large.

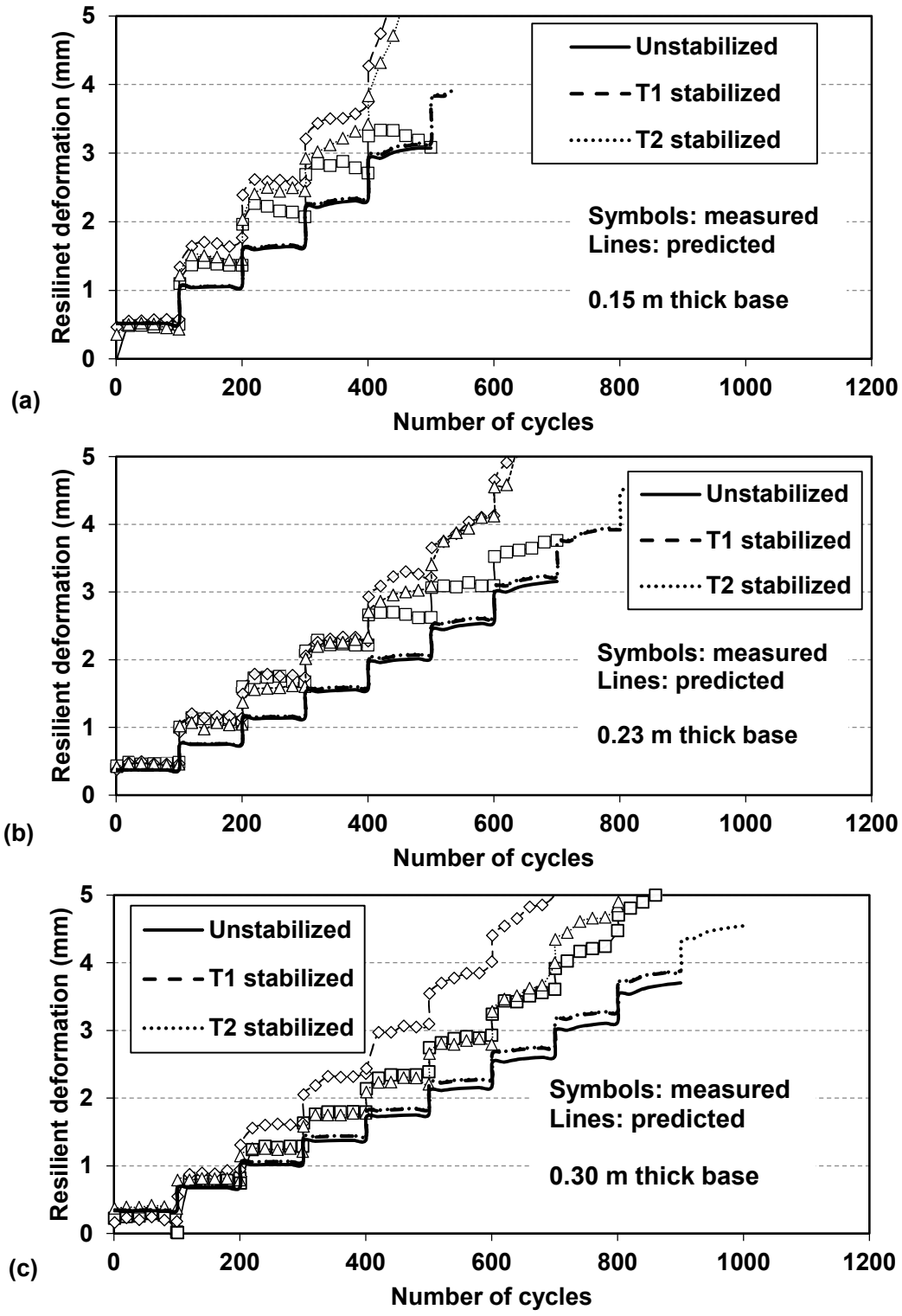

Figure 5.8 Comparison of the measured and predicted surface resilient deformations

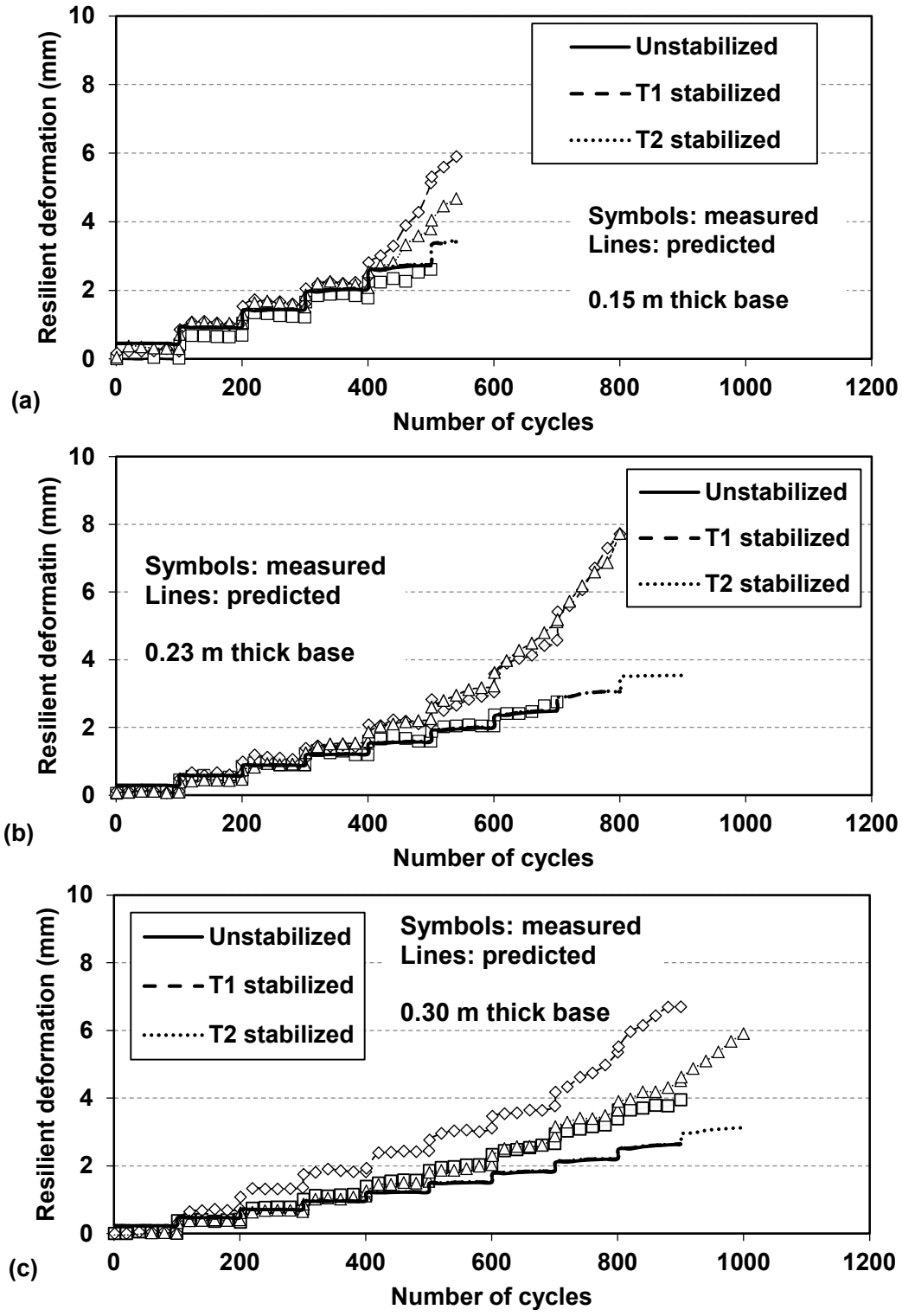

Figure 5.9 Comparison of the measured and predicted subgrade resilient deformations

5.5.3 Surface permanent deformation

Both the base course and the subgrade accumulate permanent deformations under cyclic loading. In this study, the base permanent deformations were estimated based on the original MEPDG soil damage model. The permanent deformations for the subgrade were estimated by the following equations:

$$\begin{cases} PD = f_p \cdot h_{soil} \cdot \varepsilon_v \cdot \left(\frac{\varepsilon_0}{\varepsilon_r}\right) \cdot e^{-\left(\frac{\rho}{N}\right)^{\beta}} \\ Log\beta = -0.61119 - 0.017638W_c \\ \rho = 10^9 \cdot \left(\frac{-4.89285}{1-(10^9)^{\beta}}\right)^{\frac{1}{\beta}} \\ \left(\frac{\varepsilon_0}{\varepsilon_r}\right) = k \cdot \mathrm{CBR}^{(-0.187)} \frac{p}{N_c c_u} \cdot \frac{0.15 \cdot e^{\rho^{\beta}} + 20 \cdot e^{\left(\frac{\rho}{10^9}\right)^{\beta}}}{2} \end{cases}$$

Equation 5.2

where PD = permanent deformation; f_p= reduction factor due to the confinement during the unloading stage; h_{soil} = thickness of soil layer; ($\varepsilon_0/\varepsilon_r$), ρ, and β = parameters of unbound materials; k = calibration factor; ε_v = average vertical strain; W_c = water content of subgrade (%); N_c = the bearing capacity of subgrade; c_u = undrained shear strength of subgrade; and N = number of traffic repetitions.

Table 5.2 shows the calibration factors and model parameters for base courses and subgrade. The test sections with the 0.3 m thick base course were used to calibrate the soil damage models and the calibrated soil damage models were adopted to predict the performant deformations of other test sections.

Table 5.2 Soil parameters used in the model

Soil type		β	ρ	$\left(\frac{\varepsilon_0}{\varepsilon_r}\right)$	k
AB3		0.178	8470	22.6	1.5
Subgrade	2% CBR	0.157	31172	24.2	8
	3% CBR	0.159	26044	24.1	18
	5% CBR	0.163	20910	23.7	18

Figure 5.10 shows the comparison of the predicted and measured subgrade permanent deformations under the cyclic loading with increasing loading intensities. As shown in the figure, the predicted results matched with the measured results well. As compared with those of the unstabilized sections, the permanent deformations of the geogrid stabilized sections were reduced significantly.

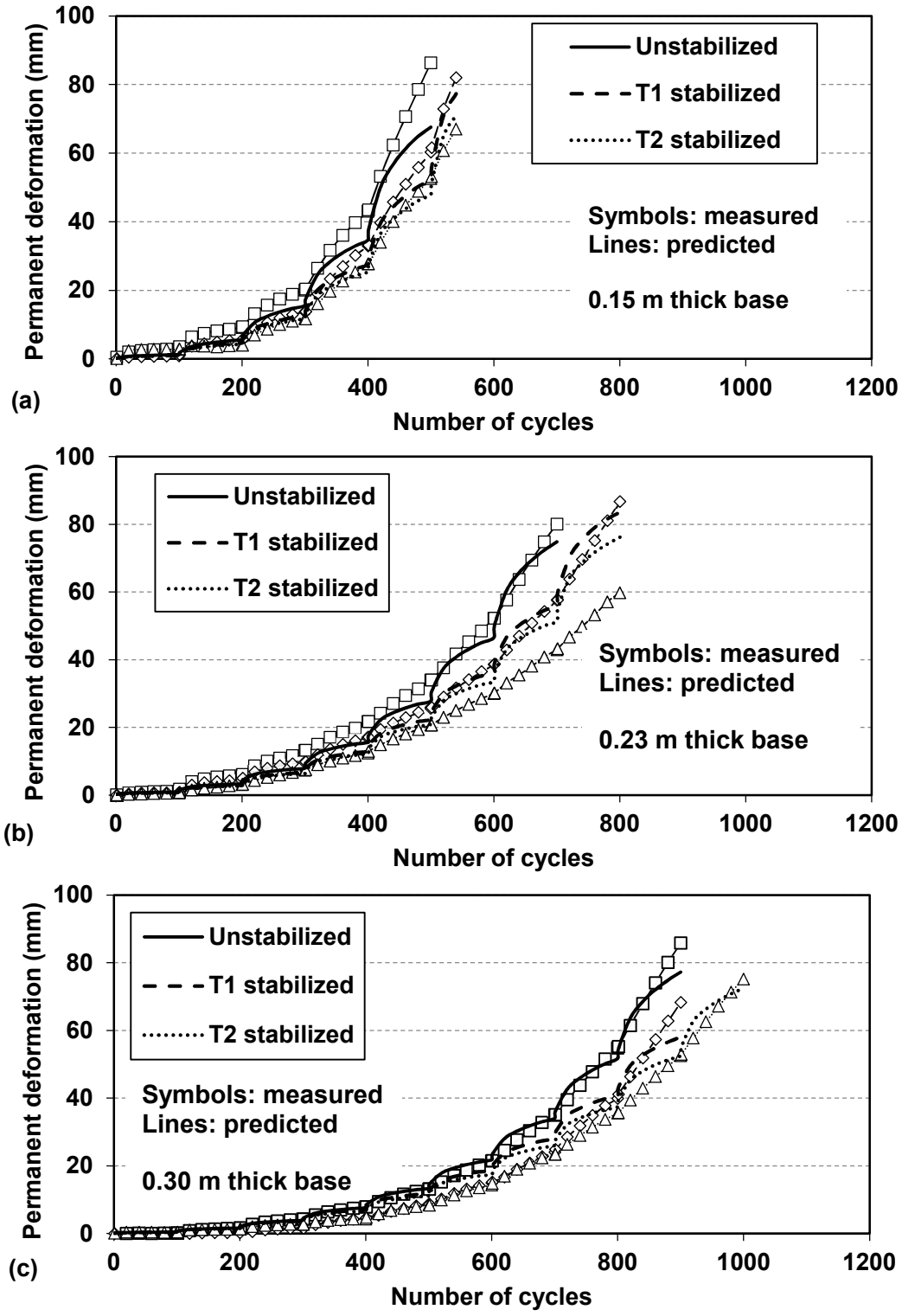

Figure 5.10 Comparison of the measured and predicted surface permanent deformations for the sections with a subgrade CBR of 2%

Since permanent deformation is an important pavement performance index, the model was verified by the measured subgrade permanent deformations from the test sections with subgrade and base courses at different CBR values under a 40 kN cyclic load as well. **Figure 5.11** shows the comparison of predicted and measured subgrade permanent deformations for the test sections of AB3 base courses over subgrade with CBR values of 3% and 5%, respectively. **Figure 5.12** shows the comparison of predicted and measured subgrade permanent deformations for the test sections of AB3-soil mixture base courses over the subgrade with CBR values of 3% and 5%, respectively. The stiffness of the AB3-soil mixture base courses was lower than that of the AB3 base courses. Overall, the predicted subgrade permanent deformations match the measured results well. These comparisons indicate the reliability of the model developed in this study.

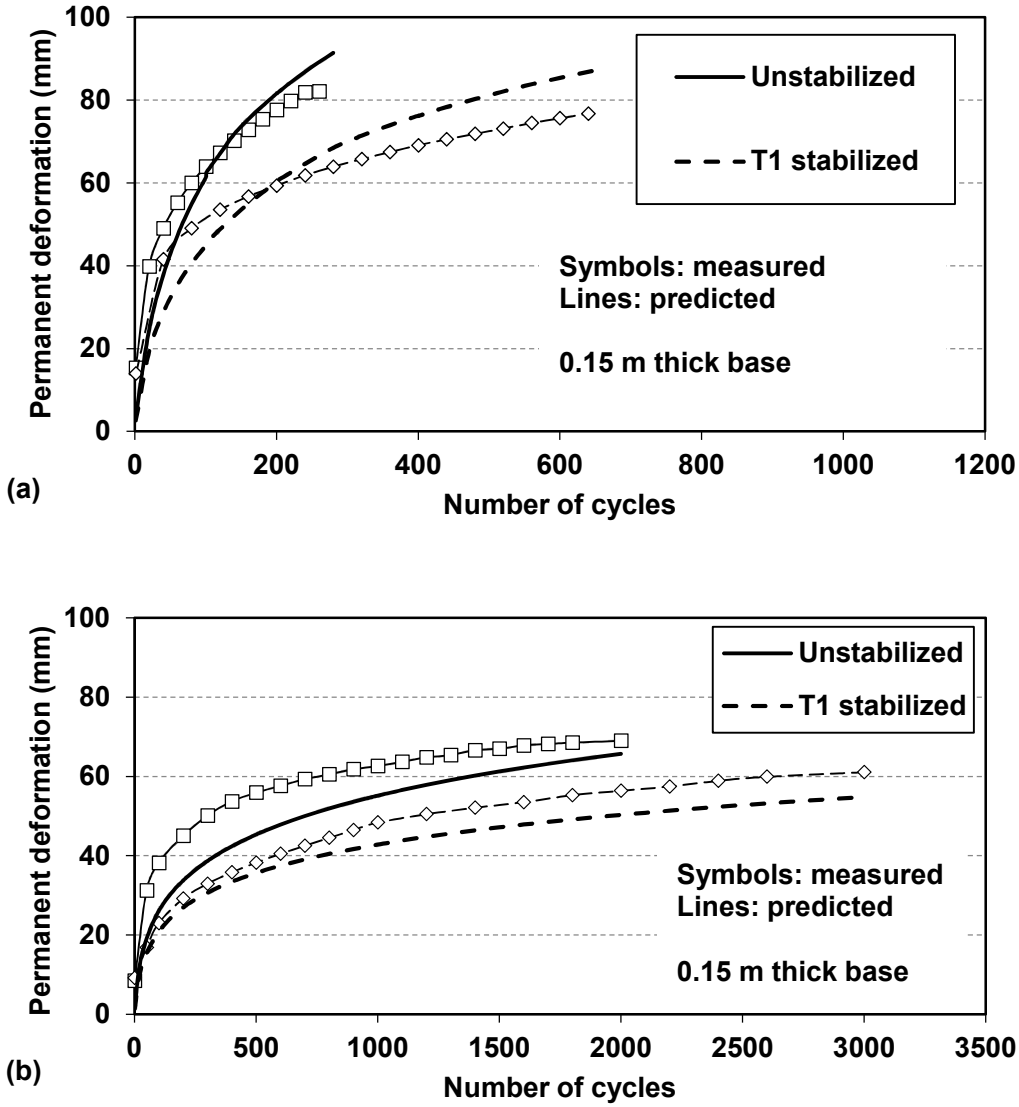

Figure 5.11 Comparison of the measured and predicted surface permanent deformations for the sections of AB3 base courses over subgrade with CBR values of: (a) 3% and (b) 5%

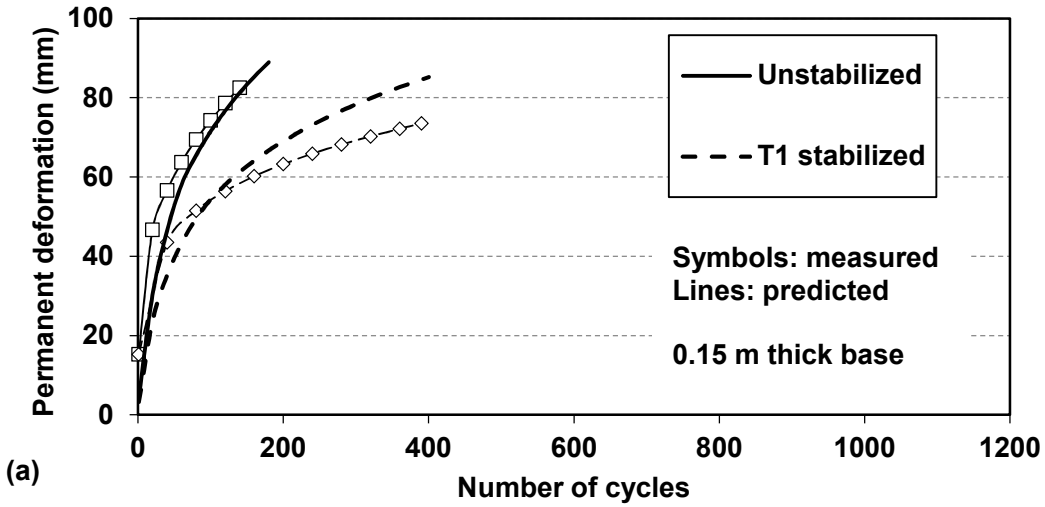

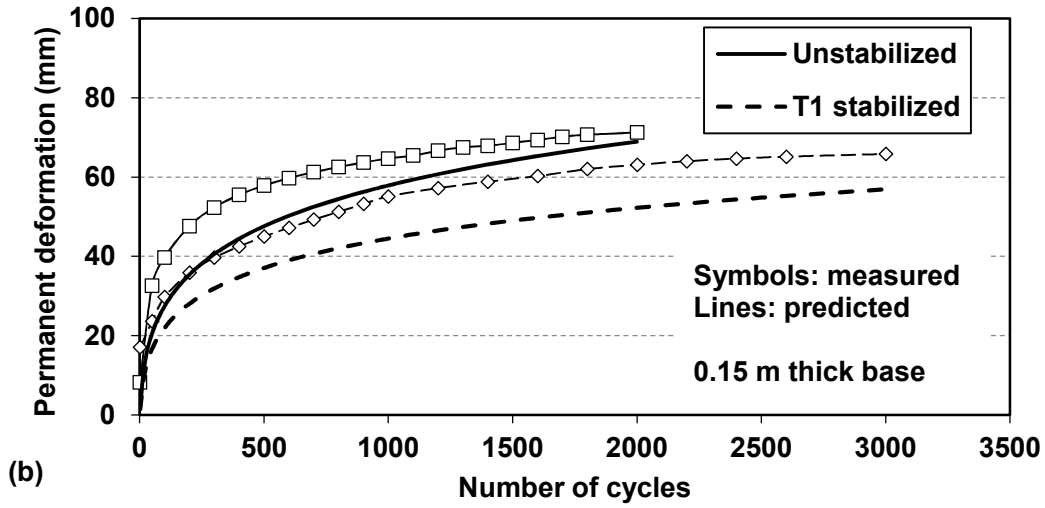

Figure 5.12 Comparison of the measured and predicted surface permanent deformations for the sections of AB3-soil mixture base courses over subgrade with CBR values of: (a) 3% and (b) 5%

Figure 5.13 shows the mechanism of the reduction of permanent deformations due to the inclusion of the geogrid. Basically, the reduction of the permanent deformation includes two parts: reduction due to the confinement during the loading stage and the reduction due to the confinement during the unloading stage. During the loading stage, due to the

inclusion of the geogrid, the total deformation of a geogrid-stabilized section decreases as compared with that of an unstabilized section. During the unloading stage, the additional lateral earth pressure induced by the geogrid is applied to soils so that soils recover more from the total deformation. As a result, the additional reduction occurs in the permanent deformation.

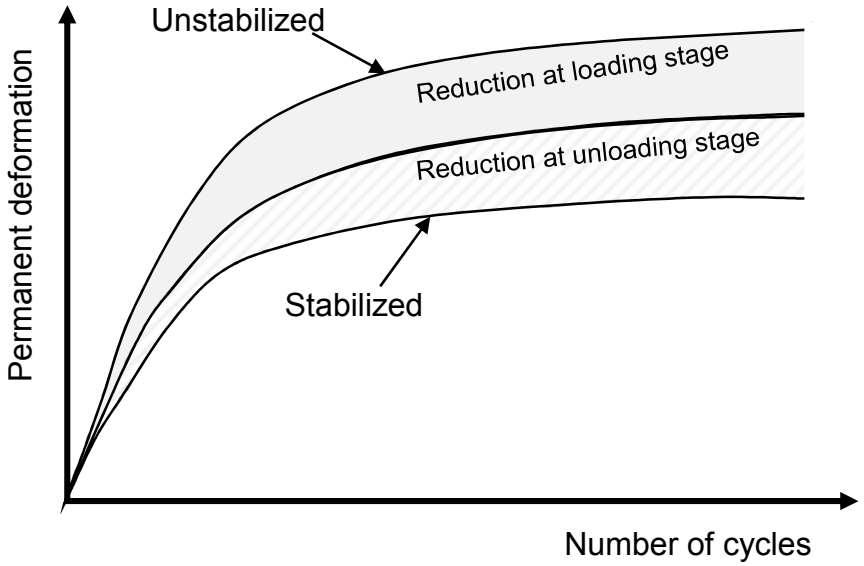

Figure 5.13 Schematic diagram of the mechanism of the reduction of permanent deformation due to the inclusion of the geogrid

5.6 Summary

In this chapter, a Matlab code was programmed to predict the performance of the geogrid stabilized bases over subgrade by considering the geogrid stabilized layered elastic system, the base course modulus degradation, the confinement effect, and the MEPDG soil damage model. Below summarizes the findings in this chapter:

(1) Geogrid induced additional lateral earth pressure coefficient increased with the increase of loading cycles. The increase of the lateral earth pressure coefficient influenced the resilient behavior of the geogrid stabilized base over subgrade. Along the centerline, the soils within the influence range of the geogrid had lower permanent deformations and higher resilient deformations.

(2) The predicted and measured permanent deformations matched well. The predicted resilient deformations in the geogrid stabilized sections were larger than those in the unstabilized sections. This prediction was consistent with the phenomenon observed in laboratory tests. However, the increase of the measured resilient deformations were much larger than that of the predicted resilient deformations in the geogrid stabilized test sections. The possible reason is that the base course and the subgrade might not be in contact at a large permanent deformation during the unloading stage due to the tension in the geogrid. However, in the analytical model, the base course and subgrade were considered fully bonded.

(3) The inclusion of the geogrid reduced the permanent deformation of the geogrid stabilized base over the subgrade by the confinement during the loading stage and the unloading stage.

Chapter 6 Conclusions and Recommendations

6.1 Conclusions from this study

In this study, plate loading tests were conducted on test sections of geogrid-stabilized bases over weak subgrade under cyclic loading (with increasing intensities and constant intensity) and static loading. The test sections were constructed in a geotechnical box with dimensions of 2 m (W) × 2.2 m (L) × 2 m (H) at the University of Kansas. The vertical/lateral stresses and resilient/permanent deformations of the test sections were monitored during the tests.

To predict the roadway performance and compare the predicted results with the measured results of the laboratory tests, an analytical model was developed based on a hypoplastic model and a stabilized layered elastic solution. The MEPDG soil damage model was modified to predict permanent deformations of subgrade. In this process, the confinement and tensioned membrane effects during the loading/unloading stage and the base course degradation were taken into consideration to predict the roadway performance. A Matlab code was programed for the prediction of roadway performance with the increase of loading cycles.

6.1.1 Experimental study

The following conclusions can be drawn from the experimental study:

(1) The vertical stresses at the interface were reduced by the inclusion of geogrid and the reduction became more obvious when a heavier duty of geogrid was included. With the

increase of the base thickness, the vertical stresses at the interface were reduced in both the stabilized and unstabilized sections. The influence of the geogrid was reduced when the base course thickness was increased. In addition, the vertical stresses at the interface increased with the increase of the number of loading cycles due to the deterioration of base courses.

(2) The lateral confinement of the geogrid changed the stress distribution of the radial stress. The radial stress at the bottom of the base and the top of the subgrade increased along the centerline of test section but decreased at locations far away from the center.

(3) The surface permanent deformation was reduced by the inclusion of the geogrid and higher reduction in the permanent deformation was observed with the heavier duty geogrid. Both the subgrade and base course permanent deformations decreased in the stabilized sections. The surface permanent deformations mainly resulted from the subgrade deformations. Additionally, the permanent deformations increased drastically with the increase of loading cycles. This result indicates that the test sections experienced a bearing failure.

(4) The measured resilient deformations of the geogrid stabilized test sections were much larger than those of the unstabilized sections. There are two reasons for this phenomenon: (a) the deformations of the aggregate recovered during the unloading stage in the stabilized sections due to the additional lateral earth pressure induced by the geogrid and (b) the base course might not be in contact with the subgrade at the large permanent deformation due to the tensioned geogrid at the end of the unloading stage.

(5) The permanent deformations of the test sections under the repetitive static load were much lower than those under the cyclic load. The ratio of the permanent deformations under cyclic loading to those under static loading at the same loading intensity increased from 1.7 to 2.0 if the number of cycles per loading stage increased from 100 to 1000.

(6) The test sections with the subgrade CBR at 3% had a higher increase rate of the permanent deformations at a higher number of loading cycles as compared with those with the subgrade CBR at 5%. The test sections with the subgrade CBR at 5% became stable at a higher number of loading cycles, while those with the subgrade CBR at 3% experienced bearing failure. The influence of base quality on the permanent deformations of the test sections with strong subgrade was not as much as that on the test sections with weak subgrade.

(7) With the increase of subgrade CBR, the trend of the permanent deformations of the subgrade changed due to the increase of its bearing capacity. The damage model in the MEPDG was modified by introducing the stiffness and bearing capacity of the subgrade to consider the influence of the bearing capacity of the subgrade. The modified model predicted the subgrade permanent deformations well.

6.1.2 Analytical study

The following conclusions can be drawn from the analytical study:

(1) The solution for the geosynthetic-stabilized transversely-isotropic layered elastic system was derived in this study. With the accumulation of the vertical and lateral deformations, the geogrid caused the increase of lateral earth pressure and the decrease

of the vertical stresses along the centerline of the test sections. Therefore, a higher lateral earth pressure coefficient was considered in the geogrid stabilized sections.

(2) A hypoplastic model was developed to simulate the loading and unloading process of soils under different lateral earth pressure coefficients. With the increase of the lateral earth pressure coefficients, the total strain of a soil element decreased during the loading stage and the resilient strain increased during the unloading stage. This result is consistent with the observed phenomenon in laboratory tests.

(3) The confinement during the unloading stage of the geogrid stabilized sections resulted in the reduction of permanent deformations and the increase of resilient deformations. A reduction factor was applied to the modified MEPDG empirical soil damage model to predict the permanent deformations of subgrade. The predicted and measured permanent deformations matched well.

(4) The predicted resilient deformations of the geogrid stabilized sections were larger than those of the unstabilized sections. This trend is consistent with that of the measured results, but the measured resilient deformations of the stabilized sections were much larger than those of the unstabilized sections. The possible reason is that the base course and the subgrade might not be in touch at the large permanent deformation at the end of the unloading stage due to the tension in geogrid.

6.2 Recommendation for future study

This study identified some areas that need further investigation. These areas are recommended for a further study:

(1) In this study, the interface of base course and subgrade was assumed being fully bonded. In reality, slip may occur at the interface of the base course and the subgrade, especially when the fine content in the base course is high. In addition, at the end of the unloading stage, the geogrid may not be in contact with the subgrade at a large permanent deformation. A further study may consider these issues by changing the continuity condition at the interface.

(2) To investigate the increase of the lateral earth pressure coefficient induced by the geogrid, an elastic solution under a static condition was adopted in this study to simplify the analysis. However, under traffic loading, the geogrid-induced stresses changed with the applied load. A further investigation is needed to fully understand the change of the lateral earth pressure coefficient. In addition, the compaction induced lateral earth pressure was not taken into consideration in this study and such influence needs to be further studied.

(3) The base modulus degradation model adopted in this study was originally used to evaluate the shear modulus degradation under dynamic loading but not for the shear modulus degradation due to the accumulation of permanent deformations under cyclic loading. After redefining the reference shear strain, the model was valid to estimate the base modulus degradation but without a rigorous analytical derivation. A further investigation is needed to develop an analytical base modulus degradation model under cyclic loading.

(4) The hypoplastic model demonstrated the confinement effect of the geogrid during the unloading stage on the resilient behavior of roadway sections, but this simple hypoplastic model did not consider the change of soil properties (such as void ratio) during the loading

process. A further study can adopt a more comprehensive hypoplastic model to capture the change of soil properties.

References

Abu-Farsakh, M., Nazzal, M., Mohammad, L., 2007. Effect of Reinforcement on Resilient and Permanent Deformations of Base Course Material. Transportation Research Record: Journal of the Transportation Research Board 2004, 120-131.

Abu-Farsakh, M.Y., Alshibli, K., Nazzal, M., Seyman, E., 2004. Assessment of in-situ test technology for construction control of base courses and embankments. Louisiana Transportation Research Center Baton Rouge,, LA, USA.

Al-Qadi, I.L., Brandon, T.L., Valentine, R.J., Lacina, B.A., Smith, T.E., 1994. Laboratory evaluation of geosynthetic-reinforced pavement sections.

ASTM, 2009. Standard Test Method for Repetitive Static Plate Load Tests of Soils and Flexible Pavement Components, for Use in Evaluation and Design of Airport and Highway Pavements. ASTM International.

Barenberg, E.J., 1980. Design Procedure for Soil Fabric-Aggregate Systems with Mirafi 500X Fabric.

Barksdale, R.D., 1972. Laboratory evaluation of rutting in base course materials, Presented at the Third International Conference on the Structural Design of Asphalt Pavements, Grosvenor House, Park Lane, London, England, Sept. 11-15, 1972.

Bourdeau, P.L., 1989. Modeling of membrane action in a two-layer reinforced soil system. Computers and Geotechnics 7, 19-36.

Burd, H., 1995. Analysis of membrane action in reinforced unpaved roads. Canadian geotechnical journal 32, 946-956.

Burmister, D.M., 1945a. The general theory of stresses and displacements in layered soil systems. III. Journal of Applied Physics 16, 296-302.

Burmister, D.M., 1945b. The general theory of stresses and displacements in layered systems. I. Journal of Applied Physics 16, 89-94.

Chen, Q.M., Abu-Farsakh, M., Tao, M.J., 2009. Laboratory Evaluation of Geogrid Base Reinforcement and Corresponding Instrumentation Program. Geotechnical Testing Journal 32, 516-525.

Delatte, N.J., 2014. Concrete pavement design, construction, and performance. CRC Press.

Dong, Y.L., Han, J., Bai, X.H., 2011. Numerical analysis of tensile behavior of geogrids with rectangular and triangular apertures. Geotextiles and Geomembranes 29, 83-91.

Espinoza, R.D., 1994. Soil-geotextile interaction: Evaluation of membrane support. Geotextiles and Geomembranes 13, 281-293.

Fellin, W., 2002. Hypoplasticity for beginners. University of Innsbruck.

Giroud, J.-P., Noiray, L., 1981. Geotextile-reinforced unpaved road design. Journal of the Geotechnical Engineering Division 107, 1233-1254.

Giroud, J.P., Han, J., 2004a. Design method for geogrid-reinforced unpaved roads. I. Development of design method. Journal of Geotechnical and Geoenvironmental Engineering 130, 775-786.

Giroud, J.P., Han, J., 2004b. Design method for geogrid-reinforced unpaved roads. II. Calibration and applications. Journal of Geotechnical and Geoenvironmental Engineering 130, 787-797.

Haas, R., Walls, J., Carroll, R., 1988. Geogrid reinforcement of granular bases in flexible pavements.

Han, J., Pokharel, S., Yang, X., Manandhar, C., Leshchinsky, D., Halahmi, I., Parsons, R., 2011. Performance of Geocell-Reinforced RAP Bases over Weak Subgrade under Full-Scale Moving Wheel Loads. Journal of Materials in Civil Engineering 23, 1525-1534.

Hardin, B.O., Drnevich, V.P., 1972. Shear modulus and damping in soils. Journal of the Soil Mechanics and Foundations Division 98, 667-692.

Hart-Davis, A., 2007. Roads and surveying. Discovering Roman Technology. BBC. CO. UK. Retrieved, 04-22.

Heukelom, W., Klomp, A., 1962. Dynamic testing as a means of controlling pavements during and after construction, International conference on the structural design of asphalt pavements.

Holtz, R., Christopher, B.R., Berg, R.R., 1998. Geosynthetic design and construction guidelines. No. FHWA HI-95-038.

Huang, Y.H., 1993. Pavement analysis and design. University of Kentucky. Prentice Hall, inc. USA.

Indraratna, B., Hussaini, S.K.K., Vinod, J.S., 2013. The lateral displacement response of geogrid-reinforced ballast under cyclic loading. Geotextiles and Geomembranes 39, 20-29.

Kavussi, A., Rafiei, K., Yasrobi, S., 2010. Evaluation of PFWD as potential quality control tool of pavement layers. Journal of Civil Engineering and Management 16, 123-129.

Khazanovich, L., Celauro, C., Chadbourn, B., Zollars, J., Dai, S., 2006. Evaluation of Subgrade Resilient Modulus Predictive Model for Use in Mechanistic-Empirical

Pavement Design Guide. Transportation Research Record: Journal of the Transportation Research Board 1947, 155-166.

Kolymbas, D., 1999. Introduction to Hypoplasticity: Advances in Geotechnical Engineering and Tunnelling 1. CRC Press.

Kondner, R.L., 1963. Hyperbolic stress-strain response: cohesive soils. Journal of the soil mechanics and foundations division, ASCE 89, 115-143.

Lay, M.G., 1992. Ways of the World: A History of the World's Roads and of the Vehicles that Used Them. Rutgers university press.

Lekarp, F., Isacsson, U., Dawson, A., 2000. State of the art. II: Permanent strain response of unbound aggregates. Journal of Transportation Engineering 126, 76-83.

Leknitskii, S.G., 1981. Theory of elasticity of an anisotropic body. Mir Publishers.

Leng, J., Gabr, M.A., 2002. Characteristics of geogrid-reinforced aggregate under cyclic load. Transportation Research Record: Journal of the Transportation Research Board 1786, 29-35.

Love, J., Burd, H., Milligan, G., Houlsby, G., 1987. Analytical and model studies of reinforcement of a layer of granular fill on a soft clay subgrade. Canadian geotechnical journal 24, 611-622.

Muki, R., 1960. Asymmetric problems of the theory of elasticity for a semi-infinite solid and a thick plate. Progress in solid mechanics 1, 401-439.

Pasko, T., 1998. Concrete Pavements-Past, Present, and Future, Public Roads, pp. 7-15.

Paute, J., Hornych, P., Benaben, J., 1994. Comportement mécanique des graves non traitées. Bull. de Liaison des Laboratories des Ponts et Chaussees 190, 27-38.

Perkins, S., Christopher, B., Lacina, B., Klompmaker, J., 2011. Mechanistic-Empirical Modeling of Geosynthetic-Reinforced Unpaved Roads. International Journal of Geomechanics 12, 370-380.

Perkins, S., Ismeik, M., 1997. A synthesis and evaluation of geosynthetic-reinforced base layers in flexible pavements: Part I. Geosynthetics International 4, 605-621.

Perkins, S.W., 1999. Geosynthetic reinforcement of flexible pavements: laboratory based pavement test sections.

Perkins, S.W., Christopher, B.R., Cuelho, E., Eiksund, G., Hoff, I., Schwartz, C., Svanø, G., Watn, A., 2004. Development of design methods for geosynthetic reinforced flexible pavements. report prepared for the US Department of Transportation Federal Highway Administration, Washington, DC, FHWA Report Reference Number DTFH61-01-X-00068, 263p.

Pokharel, S.K., 2010. Ph.D. Dissertation. Experimental study on geocell-reinforced bases under static and dynamic loading, CEAE Department. University of Kansas, Lawrence, Kansas.

Qian, Y., Han, J., Pokharel, S., Parsons, R., 2011a. Stress Analysis on Triangular-Aperture Geogrid-Reinforced Bases over Weak Subgrade Under Cyclic Loading. Transportation Research Record: Journal of the Transportation Research Board 2204, 83-91.

Qian, Y., Han, J., Pokharel, S.K., Parsons, R.L., 2011b. Determination of Resilient Modulus of Subgrade Using Cyclic Plate Loading Tests, ASCE Geo-Frontiers 2011. American Society of Civil Engineers, Dallas, Texas.

Qian, Y., Han, J., Pokharel, S.K., Parsons, R.L., 2013. Performance of Triangular Aperture Geogrid-Reinforced Base Courses over Weak Subgrade under Cyclic Loading. Journal of Materials in Civil Engineering 25, 1013-1021.

Rahman, M., Arulrajah, A., Piratheepan, J., Bo, M., Imteaz, M., 2013. Resilient modulus and permanent deformation responses of geogrid-reinforced construction and demolition materials. Journal of Materials in Civil Engineering 26, 512-519.

Rao, C.N., George, V., Shivashankar, R., 2008. PFWD, CBR and DCP Evaluation of Lateritic Subgrades of Dakshina Kannada, India, The 12th International Conference of International Association for Computer Methods and Advances in Geomechanics. Goa: Indian Institute of Technology.

Sharma, R., Chen, Q., Abu-Farsakh, M., Yoon, S., 2009. Analytical modeling of geogrid reinforced soil foundation. Geotextiles and Geomembranes 27, 63-72.

Sun, X., Han, J., Wayne, M.H., Parsons, R.L., Kwon, J., 2014a. Experimental Study on Resilient Behavior of Triaxial Geogrid-Stabilized Unpaved Roads, GeoShanghai 2014. ASCE, Shanghai, pp. 353-362.

Sun, X., Han, J., Wayne, M.H., Parsons, R.L., Kwon, J., 2014b. Quantifying the Benefit of Triaxial Geogrid in Stabilizing Granular Bases over Soft Subgrade under Cyclic Loading at Different Intensities, Geo-Congress 2014. ASCE, pp. 2568-2577.

Sweere, G.T.H., 1990. Unbound granular bases for roads. TU Delft, Delft University of Technology.

Thakur, J.K., Han, J., Pokharel, S.K., Parsons, R.L., 2012. Performance of geocell-reinforced recycled asphalt pavement (RAP) bases over weak subgrade under cyclic plate loading. Geotextiles and Geomembranes 35, 14-24.

Tingle, J., Jersey, S., 2005. Cyclic Plate Load Testing of Geosynthetic-Reinforced Unbound Aggregate Roads. Transportation Research Record: Journal of the Transportation Research Board 1936, 60-69.

Tingle, J., Jersey, S., 2009. Full-Scale Evaluation of Geosynthetic-Reinforced Aggregate Roads. Transportation Research Record: Journal of the Transportation Research Board 2116, 96-107.

Tingle, J.S., Jersey, S.R., 2007. Empirical design methods for geosynthetic-reinforced low-volume roads. Transportation Research Record: Journal of the Transportation Research Board 1989, 91-101.

Tseng, K., Lytton, R.L., 1989. Prediction of permanent deformation in flexible pavement materials. Implication of Aggregates in the Design, Construction, and Performance of Flexible Pavements, ASTM STP 1016, 154-172.

Veverka, V., 1979. Raming van de spoordiepte bij wegen met cen bitumineuze verharding. De Wegentechniek 24, 25-45.

Vokas, C.A., Stoll, R.D., 1987. Reinforced elastic layered systems. Transportation Research Record: Journal of the Transportation Research Board 1153, 1-7.

Wang, Q., 2008. Improvement of structural modeling of flexible pavements for mechanistic-empirical design. ProQuest.

Wang, Z., Jacobs, F., Ziegler, M., 2014. Visualization of load transfer behaviour between geogrid and sand using PFC 2D. Geotextiles and Geomembranes 42, 83-90.

Webster, S.L., 1993. Geogrid reinforced base courses for flexible pavements for light aircraft: Test section construction, behavior under traffic, laboratory tests, and design

criteria. Technical Report GL-93-6. U.S. Army Corps of Engineers,Waterways Experiment Station, Vicksburg, MS, USA.

Yang, X., Han, J., 2012. Analytical Model for Resilient Modulus and Permanent Deformation of Geosynthetic-Reinforced Unbound Granular Material. Journal of Geotechnical and Geoenvironmental Engineering 139, 1443-1453.

Appendix A Geosynthetic-Stabilized Transversely-Isotropic Layered Elastic System

A.1 Introduction

Layered elastic theory has been used in the pavement analysis for decades since Burmister established it. In the current MEPDG design, the pavement responses (i.e. stress, strain, and deformation) under traffic loading are evaluated according to the layered elastic theory at first and then the obtained responses are used to estimate the pavement distresses based on the damage models (empirical models). Even though the elasto-plastic theory and/or other plastic-related theories have been well established, the ME design procedure is suitable to analyze the pavement performance throughout the pavement life due to its simplicity and convenience. Therefore, the layered elastic theory is still widely used in pavement design.

Geosynthetic has been used in subgrade improvement and base course stabilization for many years. However, the geosynthetic-stabilized layered elastic system has not been well established. Moreover, the soil layers usually demonstrate the characteristic of the transverse isotropy and this characteristic becomes more obvious by the inclusion of the geosynthetic. In this chapter, the geosynthetic-stabilized transversely-isotropic layered elastic system is investigated based on the elastic theory. The stress function introduced by Leknitskii was adopted in the derivation. The geosynthetic was assumed to be bonded

together with the base course and subgrade layer at the interface. In addition, the Gauss function was used to simulate the shape of the deformed geosynthetic.

A.2 Governing equations

In the cylindrical coordinate as shown in **Figure 2.3**, the differential equations of equilibrium for an elastic body deformed symmetrically with respect to the z axis, neglecting the body forces, are:

$$\begin{cases} \dfrac{\partial \sigma_\rho}{\partial \rho} + \dfrac{\partial \tau_{\rho z}}{\partial Z} + \dfrac{\sigma_\rho - \sigma_\varphi}{\rho} = 0 \\ \dfrac{\partial \tau_{\rho z}}{\partial \rho} + \dfrac{\partial \sigma_z}{\partial Z} + \dfrac{\tau_{\rho z}}{\rho} = 0 \end{cases}$$

Equation A.1

where σ_ρ, σ_φ, and σ_z are the normal stress components in the radial, tangential and vertical directions, respectively. $\tau_{\rho z}$ is the component of the shear stress on the surface of a cylinder with a radius of ρ in the direction of the z axis.

The strains are related to the displacement components in the radial and vertical directions, expressed by *u* and *w*, in the following expressions:

$$\begin{cases} \varepsilon_\rho = \dfrac{\partial u}{\partial \rho} \\ \varepsilon_\varphi = \dfrac{u}{\rho} \\ \varepsilon_z = \dfrac{\partial w}{\partial Z} \\ \gamma_{\rho z} = \dfrac{\partial u}{\partial Z} + \dfrac{\partial w}{\partial \rho} \end{cases}$$

Equation A.2

The generalized Hooke's law of a transversely isotropic body is:

$$\varepsilon = C\sigma \qquad \textbf{Equation A.3}$$

where

$$C = \begin{bmatrix} \frac{1}{E_1} & \frac{-\mu_0}{E_1} & \frac{-\mu_2}{E_2} & 0 & 0 & 0 \\ \frac{-\mu_0}{E_1} & \frac{1}{E_1} & \frac{-\mu_2}{E_2} & 0 & 0 & 0 \\ \frac{-\mu_1}{E_1} & \frac{-\mu_1}{E_1} & \frac{1}{E_2} & 0 & 0 & 0 \\ 0 & 0 & 0 & \frac{1}{G'} & 0 & 0 \\ 0 & 0 & 0 & 0 & \frac{1}{G'} & 0 \\ 0 & 0 & 0 & 0 & 0 & 2\left(\frac{1}{E_1} + \frac{\mu_0}{E_1}\right) \end{bmatrix}$$

where E_1 is the modulus in the plane of isotropy, E_2 is the modulus in the direction normal to the plane of isotropy, μ_0 is Poisson's ratio characterizing contraction in the plane of isotropy when tension is applied in this plane; μ_1 is Poisson's ratio characterizing contraction in the plane normal to the plane of isotropy when tension is applied in the plane of isotropy; μ_2 is Poisson's ratio characterizing contraction in the plane of isotropy when tension is applied in a direction normal to the plane of isotropy; G' is the shear modulus of the plane perpendicular to the plane of isotropy.

Considering the following equations, there are four independent parameters totally:

$$\frac{\mu_2}{E_2} = \frac{\mu_1}{E_1} \qquad \textbf{Equation A.4}$$

$$G' = \frac{E_1 E_2}{E_1(1 + 2\mu_2) + E_2} \qquad \textbf{Equation A.5}$$

The generalized Hooke's law of a transversely isotropic body can be expressed in the following form:

$$\sigma = D\varepsilon$$ **Equation A.6**

$$\mathrm{D} = \begin{bmatrix} a & b & c & 0 & 0 & 0 \\ b & a & c & 0 & 0 & 0 \\ c & c & d & 0 & 0 & 0 \\ 0 & 0 & 0 & \frac{f}{2} & 0 & 0 \\ 0 & 0 & 0 & 0 & \frac{f}{2} & 0 \\ 0 & 0 & 0 & 0 & 0 & \frac{a-b}{2} \end{bmatrix}$$

where

$$a = \frac{E_1(\mu_1\mu_2 - 1)}{\mu_0^{\,2} + 2\mu_0\mu_1\mu_2 + 2\mu_1\mu_2 - 1}$$

$$b = \frac{-E_1(\mu_1\mu_2 + \mu_0)}{\mu_0^{\,2} + 2\mu_0\mu_1\mu_2 + 2\mu_1\mu_2 - 1}$$

$$c = \frac{-E_2\mu_1}{\mu_0 + 2\mu_1\mu_2 - 1}$$

$$d = \frac{E_2(\mu_0 - 1)}{\mu_0 + 2\mu_1\mu_2 - 1}$$

$$f = 2G$$

By substituting **Equation A.2** into **Equation A.6**, the expressions of the stresses in terms of the displacements can be rewritten as **Equation A.7:**

$$\begin{cases} \sigma_\rho = a\dfrac{\partial u}{\partial \rho} + b\dfrac{u}{\rho} + c\dfrac{\partial w}{\partial z} \\ \sigma_\varphi = b\dfrac{\partial u}{\partial \rho} + a\dfrac{u}{\rho} + c\dfrac{\partial w}{\partial z} \\ \sigma_z = c\dfrac{\partial u}{\partial \rho} + c\dfrac{u}{\rho} + d\dfrac{\partial w}{\partial z} \\ \tau_{\rho z} = \dfrac{f}{2}\left(\dfrac{\partial u}{\partial z} + \dfrac{\partial w}{\partial \rho}\right) \end{cases}$$

Equation A.7

By introducing a stress function ϕ, the displacements can be expressed as

$$\begin{cases} u = m_1 \dfrac{\partial^2}{\partial \rho \partial z}\phi \\ w = m_2 \dfrac{\partial^2}{\partial \rho^2}\phi + \dfrac{m_3}{\rho}\dfrac{\partial}{\partial \rho}\phi + m_4 \dfrac{\partial^2}{\partial z^2}\phi \end{cases}$$

Equation A.8

where m_1, m_2, m_3, and m_4 are the parameters related to material properties.

By substituting **Equations A.7** and **A.8** into the equations of the equilibrium, **Equation A.1**, the parameters, m_1, m_2, m_3, and m_4, can be determined:

$$\begin{cases} m_1 = -1 \\ m_2 = \dfrac{2a}{f + 2c} \\ m_3 = \dfrac{2a}{f + 2c} \\ m_4 = \dfrac{f}{f + 2c} \end{cases}$$

Equation A.9

Moreover, from the second equation of equilibrium, a partial differential equation of the stress function can be obtained, as shown in **Equations A.7**.

$$\left(\frac{\partial^2}{\partial \rho^2} + \frac{1}{\rho}\frac{\partial}{\partial \rho} + \frac{1}{\lambda_1^2}\frac{\partial^2}{\partial z^2}\right)\left(\frac{\partial^2}{\partial \rho^2} + \frac{1}{\rho}\frac{\partial}{\partial \rho} + \frac{1}{\lambda_2^2}\frac{\partial^2}{\partial z^2}\right)\phi = 0$$

Equation A.10

where

$$\lambda_1 = \pm\frac{1}{2}\left(\frac{2}{af}\left(ad - cf - c^2\right) - \sqrt{\left(\frac{2}{af}\left(ad - cf - c^2\right)\right)^2 - 4\frac{d}{a}}\right),$$

$$\lambda_2 = \pm\frac{1}{2}\left(\frac{2}{af}\left(ad - cf - c^2\right) + \sqrt{\left(\frac{2}{af}\left(ad - cf - c^2\right)\right)^2 - 4\frac{d}{a}}\right).$$

When λ_1 and λ_2 are different, the stress function $\phi(\rho, z)$ can be expressed as

$$\varphi(\rho, z) = \int_0^\infty \mathrm{m}(\mathrm{A_m e}^{\lambda_1 \mathrm{mz}} + \mathrm{B_m e}^{\lambda_2 \mathrm{mz}} + \mathrm{C_m e}^{-\lambda_1 \mathrm{mz}} + \mathrm{E_m e}^{-\lambda_2 \mathrm{mz}})\mathrm{J}_0(\mathrm{m}\rho)\mathrm{dm} \quad \textbf{Equation A.11}$$

When λ_1 = λ_2 = λ, the stress function $\phi(\rho, z)$ can be expressed as

$$\varphi(\rho, z) = \int_0^\infty \mathrm{m}(\mathrm{A_m e}^{\lambda \mathrm{mz}} + \mathrm{B_m z e}^{\lambda \mathrm{mz}} + \mathrm{C_m e}^{-\lambda \mathrm{mz}} + \mathrm{E_m z e}^{-\lambda \mathrm{mz}})\mathrm{J}_0(\mathrm{m}\rho)\mathrm{dm} \quad \textbf{Equation A.12}$$

If λ_1 = λ_2 = λ, the transversely isotropic problem becomes a fully isotropic problem. Burmister applied the stress function of **Equation A.12** and developed the layered elastic theory.

In this study, the transversely isotropic body was investigated and therefore λ_1 and λ_2 are different. **Equation A.11** shows the stress function used in this study. The stresses and displacements yield:

$$\sigma_\rho = \int_0^\infty M1dm \qquad \sigma_\varphi = \int_0^\infty M2dm \qquad \sigma_z = \int_0^\infty M3dm$$

$$\tau_{\rho z} = \int_0^\infty M4dm \qquad u = \int_0^\infty M5dm \qquad w = \int_0^\infty M6dm \quad \textbf{Equation A.13}$$

where M1=

$$\frac{1}{(f+2c)\,\rho}\left(-2m\left(\left(\frac{1}{2}f+c\right)(a-b)\left[\left(A\,m\,e^{\lambda 1\,m\,z}-C\,m\,e^{-\lambda 1\,m\,z}\right)\lambda 1+\lambda 2\,m\left(B\,e^{\lambda 2\,m\,z}-E\,e^{-\lambda 2\,m\,z}\right)\right]m\right)\text{BesselJ}(1,m\,\rho)+f\,\rho\left(a\left[\left(A\,m\,e^{\lambda 1\,m\,z}-C\,m\,e^{-\lambda 1\,m\,z}\right)\lambda 1+\lambda 2\,m\left(B\,e^{\lambda 2\,m\,z}-E\,e^{-\lambda 2\,m\,z}\right)\right]m^3+\left[\left(A\,m^3\,e^{\lambda 1\,m\,z}-C\,m^3\,e^{-\lambda 1\,m\,z}\right)\lambda 1^3+\lambda 2^3\,m^3\left(B\,e^{\lambda 2\,m\,z}-E\,e^{-\lambda 2\,m\,z}\right)\right]c\,m\right)\text{BesselJ}(0,m\,\rho)\right)$$

M2=

$$\frac{1}{(f+2c)\,\rho}\left(2m\left(\left(\frac{1}{2}f+c\right)(a-b)\left[\left(A\,m\,e^{\lambda 1\,m\,z}-C\,m\,e^{-\lambda 1\,m\,z}\right)\lambda 1+\lambda 2\,m\left(B\,e^{\lambda 2\,m\,z}-E\,e^{-\lambda 2\,m\,z}\right)\right]m\right)\text{BesselJ}(1,m\,\rho)-2\left(\left[\left(A\,m\,e^{\lambda 1\,m\,z}-C\,m\,e^{-\lambda 1\,m\,z}\right)\lambda 1+\lambda 2\,m\left(B\,e^{\lambda 2\,m\,z}-E\,e^{-\lambda 2\,m\,z}\right)\right]\left(-\frac{1}{2}bf+c(a-b)\right)m^3-\frac{1}{2}f\left[\left(A\,m^3\,e^{\lambda 1\,m\,z}-C\,m^3\,e^{-\lambda 1\,m\,z}\right)\lambda 1^3+\lambda 2^3\,m^3\left(B\,e^{\lambda 2\,m\,z}-E\,e^{-\lambda 2\,m\,z}\right)\right]c\,m\right)\rho\,\text{BesselJ}(0,m\,\rho)\right)$$

M3=

$$\frac{1}{(f+2c)\,\rho}\left(-2\left(\left[\left(A\,m\,e^{\lambda 1\,m\,z}-C\,m\,e^{-\lambda 1\,m\,z}\right)\lambda 1+\lambda 2\,m\left(B\,e^{\lambda 2\,m\,z}-E\,e^{-\lambda 2\,m\,z}\right)\right]\left(-\frac{1}{2}cf-c^2+a\,d\right)m^3-\frac{1}{2}f\left[\left(A\,m^3\,e^{\lambda 1\,m\,z}-C\,m^3\,e^{-\lambda 1\,m\,z}\right)\lambda 1^3+\lambda 2^3\,m^3\left(B\,e^{\lambda 2\,m\,z}-E\,e^{-\lambda 2\,m\,z}\right)\right]d\,m\right)\rho\,\text{BesselJ}(0,m\,\rho)\right)$$

M4=

$$\frac{1}{f+2c}\left(m^2\,\text{BesselJ}(1,m\,\rho)f\left(a\,m^2\left[A\,e^{\lambda 1\,m\,z}+B\,e^{\lambda 2\,m\,z}+C\,e^{-\lambda 1\,m\,z}+E\,e^{-\lambda 2\,m\,z}\right]+c\left[\left(A\,m^2\,e^{\lambda 1\,m\,z}+C\,m^2\,e^{-\lambda 1\,m\,z}\right)\lambda 1^2+\lambda 2^2\,m^2\left(B\,e^{\lambda 2\,m\,z}+E\,e^{-\lambda 2\,m\,z}\right)\right]\right)\right)$$

M5=

$$m^2\,\text{BesselJ}(1,m\,\rho)\left[A\,\lambda 1\,m\,e^{\lambda 1\,m\,z}+B\,\lambda 2\,m\,e^{\lambda 2\,m\,z}-C\,\lambda 1\,m\,e^{-\lambda 1\,m\,z}-E\,\lambda 2\,m\,e^{-\lambda 2\,m\,z}\right]$$

M6=

$$-\frac{1}{f+2c}\left(2\,\text{BesselJ}(0,m\,\rho)\,m\left(a\,m^2\left[A\,e^{\lambda 1\,m\,z}+B\,e^{\lambda 2\,m\,z}+C\,e^{-\lambda 1\,m}\right.\right.\right.$$
$$\left.\left.+E\,e^{-\lambda 2\,m\,z}\right]-\frac{1}{2}\left[\left(A\,m^2\,e^{\lambda 1\,m\,z}+C\,m^2\,e^{-\lambda 1\,m\,z}\right)\lambda 1^2+\lambda 2^2\,m^2\left(B\,e^{\lambda 2\,m\,z}+E\,e^{-\lambda 2\,m\,z}\right)\right]f\right)\right)$$

A.3 Model simplification

Figure A.1 shows the deformed two-layer system under a distributed load. Due to the accumulated permanent deformation, the analysis of the two-layer system became difficult since the geometry condition of the system is complex. However, the accumulated deformation, w, is much less than the span of the deformation along the interface. It is reasonable to neglect the geometry nonlinearity. The confinement and tensioned membrane effects of the geosynthetic in a deformed condition can be simulated as external stresses at the interface. **Figure A.2** is the simplified two-layer system. In Figure 4.2, $\Delta\tau(u)$ represents the confinement effect of the geosynthetic in terms of the lateral displacement, u, and $\Delta\sigma(w)$ represents the tensioned membrane effect in terms of the accumulated vertical deformation, w.

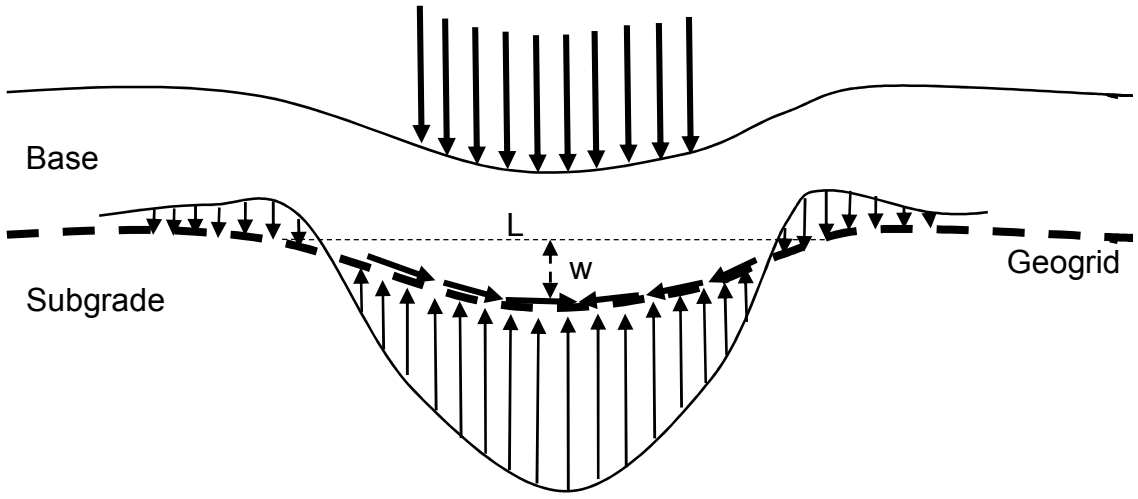

Figure A.1 Deformed two-layer system

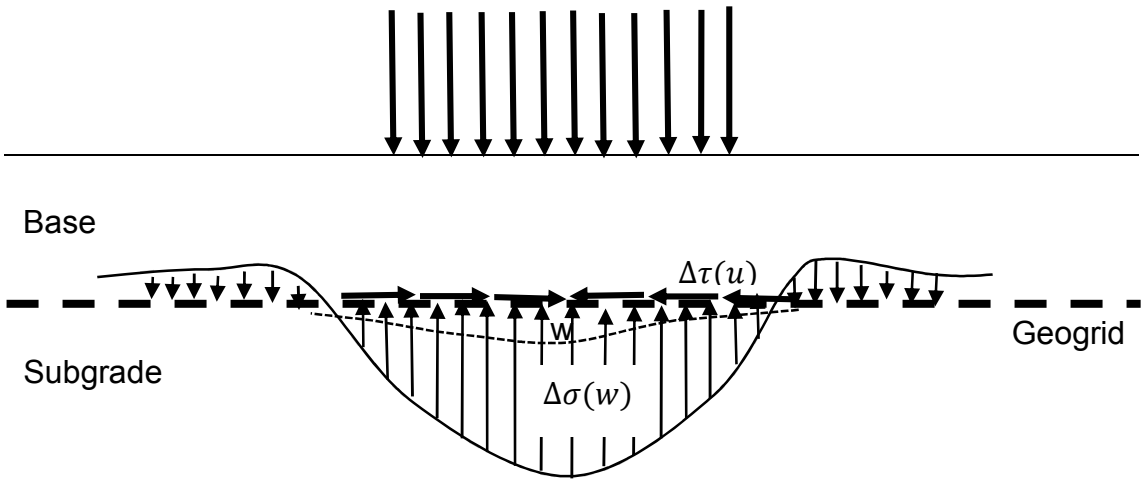

Figure A.2 Simplified model for the deformed two-layer system

A.4 Analysis

Boundary and continuity condition

The boundary and continuity conditions used in Burmister's study are applied to the transversely isotropic layered elastic system. For a model in a coordinate system as shown in Figure 4.3, the boundary and continuity conditions of the layered system are presented in Chapter Section 2.3.

With the inclusion of the geosynthetic at the interface of the base course and the subgrade, the continuity conditions at the interface should be modified to consider the effect of the geosynthetic. Assuming the geosynthetic is bonded with the base course and the subgrade on both sides, the continuity conditions of displacements do not change; however, those of the normal stresses and shear stresses should be modified to consider the tensioned membrane effect and the confinment effect, respectively. The continuity conditions for the geosynthetic-stabilized two-layer system are

At z = 0,

Vertical settlements, $w_1 = w_2$,

Horizontal displacements, $u_1 = u_2$,

Shearing stresses,$\tau_{\rho z1} - \tau_{\rho z2} = \Delta\tau(u)$.

Normal stresses, $\sigma_{z1} - \sigma_{z2} = \Delta\sigma(w)$,

Where $\Delta\tau(u)$ represents the confinement effect in terms of the lateral deformation, u; $\Delta\sigma(w)$ represents the tensioned membrane effect in terms of the vertical deformation, w. To mobilize the tensioned membrane effect, a comparatively large deformation is required.

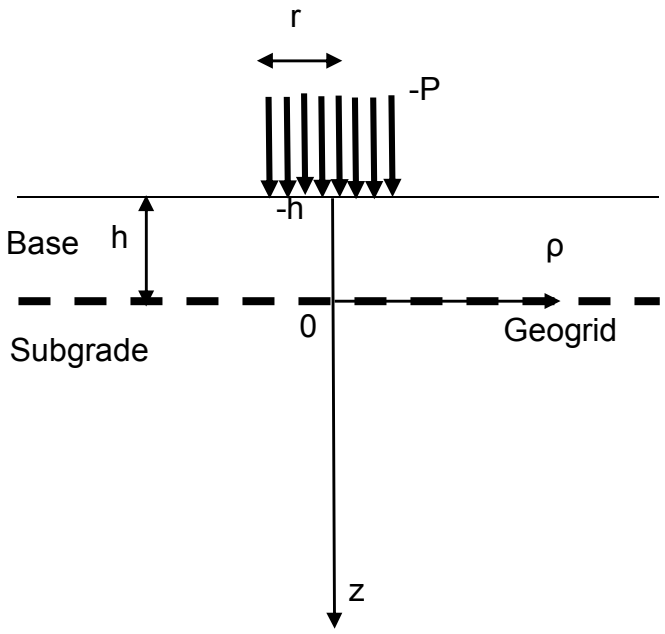

Figure A.3 Two-layer model in the coordinate system

For a two-layer system, there are eight integral constants totally. Due to zero stress and strain at the infinite depth, the integral constants are reduced to six and therefore six linear

equations are needed. To obtain linear equations, Hankel's transform needs to be applied to equations governed by the boundary and continuity conditions to remove the symbol of integral and obtain linear equations in terms of integral constants.

Take the boundary condition at $z = -h$ as an example.

$$\sigma_z = \int_0^\infty M3dm = -p \qquad \textbf{Equation A.14}$$

Applying the zero order of Hankel transform on Equation 4.14, the equation yields

$$\frac{M3}{mJ_0(m\rho)} = -\int_0^\infty pmJ_0(m\rho)dm = -\frac{paJ_1(ma)}{m} \qquad \textbf{Equation A.15}$$

where, a is the radius of the loading area. If the loading plate is rigid, **Equation 2.13** is the zero-order Hankel transformed contact pressure.

Tensioned membrane and confinement effects

Tensioned membrane effect is a complex large-deformation elastic problem. In the conventional elastic theory, the tensioned membrane effect was analyzed without surface frictions on the membrane. Both the strains induced by lateral movement and vertical deflection contributed to the membrane support in the vertical direction. However, for the geogrid, the strains induced by the lateral movement of the geogrid will apply confinement to soils. In other words, the tension due to the lateral movement of the geogrid will be balanced by the frictions at the interface. Therefore, this part of tension should not apply additional membrane support to soils. Another part of tension, induced by the vertical deflection of the geogrid, is considered as the source of the tensioned membrane effect.

In this study, the lateral movement induced tension was assumed to provide a confinement effect to soils and the vertical deflection induced tension was assumed to

provide the tensioned membrane support. The total contribution of the geosynthetic was the combination of these two effects. **Figure A.4** shows the schematic diagram of the deformed geosynthetic element.

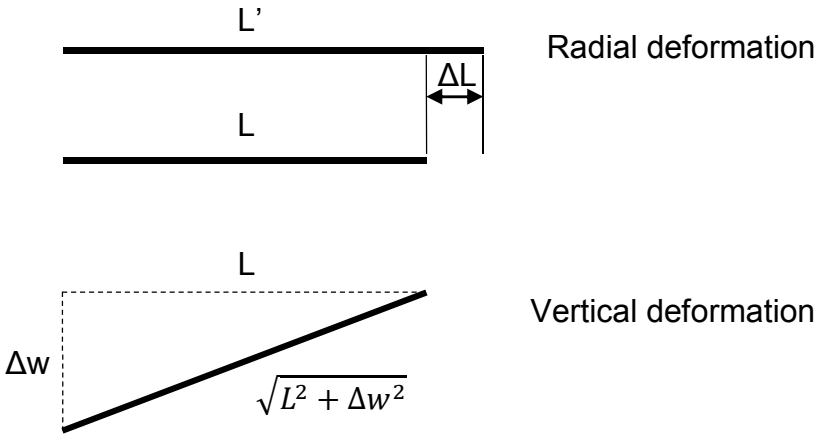

Figure A.4 Schematic diagram of the deformed geosynthetic element

The strains of the geosynthetic due to the radial deformation and the vertical deformation are expressed as follows:

Due to the radial deformation,

$$\begin{cases} \varepsilon_{\rho} = \dfrac{\partial \mathrm{u}}{\partial \rho} \\ \varepsilon_{\varphi} = \dfrac{\mathrm{u}}{\rho} \end{cases} \qquad \textbf{Equation A.16}$$

Due to the vertical deformation,

$$\begin{cases} \varepsilon_{\rho} = \dfrac{\sqrt{L^2 + \Delta w^2} - L}{L} = \sqrt{1 + \left(\dfrac{\Delta w}{L}\right)^2} - 1 \approx \dfrac{1}{2}\left(\dfrac{\partial \mathrm{w}}{\partial \rho}\right)^2 \\ \varepsilon_{\varphi} = 0 \end{cases} \qquad \textbf{Equation A.17}$$

Based on the theory for a thin plate under a large deformation, if the term which considers the flexure stiffness of the plate is neglected, the equation for the thin plate becomes the tensioned membrane equation:

$$D\nabla^4 w - \left[N_\rho \frac{\partial^2 w}{\partial \rho^2} + N_\varphi \left(\frac{1}{\rho} \frac{\partial w}{\partial \rho} + \frac{1}{\rho^2} \frac{\partial^2 w}{\partial \varphi^2} \right) + 2N_{\rho\varphi} \frac{\partial}{\partial \rho} \left(\frac{1}{\rho} \frac{\partial w}{\partial \varphi} \right) \right] = \Delta\sigma(w) \qquad \textbf{Equation A.18}$$

Under the asymmetric condition, **Equation A.18** can be further organized as follows:

$$- \left[N_\rho \frac{\partial^2 w}{\partial \rho^2} + N_\varphi \left(\frac{1}{\rho} \frac{\partial w}{\partial \rho} \right) \right] = \Delta\sigma(w) \qquad \textbf{Equation A.19}$$

Considering the generalized Hooke's law of the geosynthetic sheet, the strains in the geosynthetic can be expressed in terms of the forces in the radial and tangential directions.

$$\varepsilon_\rho = \frac{\sigma_\rho - \mu_g \sigma_\varphi}{E_g} = \frac{N_\rho - \mu_g N_\varphi}{E_g h_g}$$
$$\varepsilon_\varphi = \frac{\sigma_\varphi - \mu_g \sigma_\rho}{E_g} = \frac{N_\varphi - \mu_g N_\rho}{E_g h_g} \qquad \textbf{Equation A.20}$$

By substituting the strains induced by the vertical displacement into **Equation A.20** and **Equation A.19**, **Equation 4.19** yields

$$- \frac{E_g h_g}{2(1 - \mu_g^2)} \left(\frac{\partial w}{\partial \rho} \right)^2 \left[\frac{\partial^2 w}{\partial \rho^2} + \mu_g \left(\frac{1}{\rho} \frac{\partial w}{\partial \rho} \right) \right] = Q(w(\rho)) \qquad \textbf{Equation A.21}$$

In this study, the Gauss function, **Equation A.22**, was chosen to simulate the deformed shape of the geosynthetic under a wheel load.

$$w(\rho) = \delta e^{-\frac{\rho^2}{\xi^2}} \qquad \textbf{Equation A.22}$$

where δ is the permanent deformation at the center; ξ is a coefficient, which can be determined as $\sqrt{2}d$, where d is the inflection point distance of the deformed shape. The inflection point distance was assumed to be the same as that from an elastic solution. The inflection point distances for the sections with varying layer thicknesses and modulus ratios are presented in **Figure A.5**. This chart was based on a rigid plate with a 0.3 m diameter.

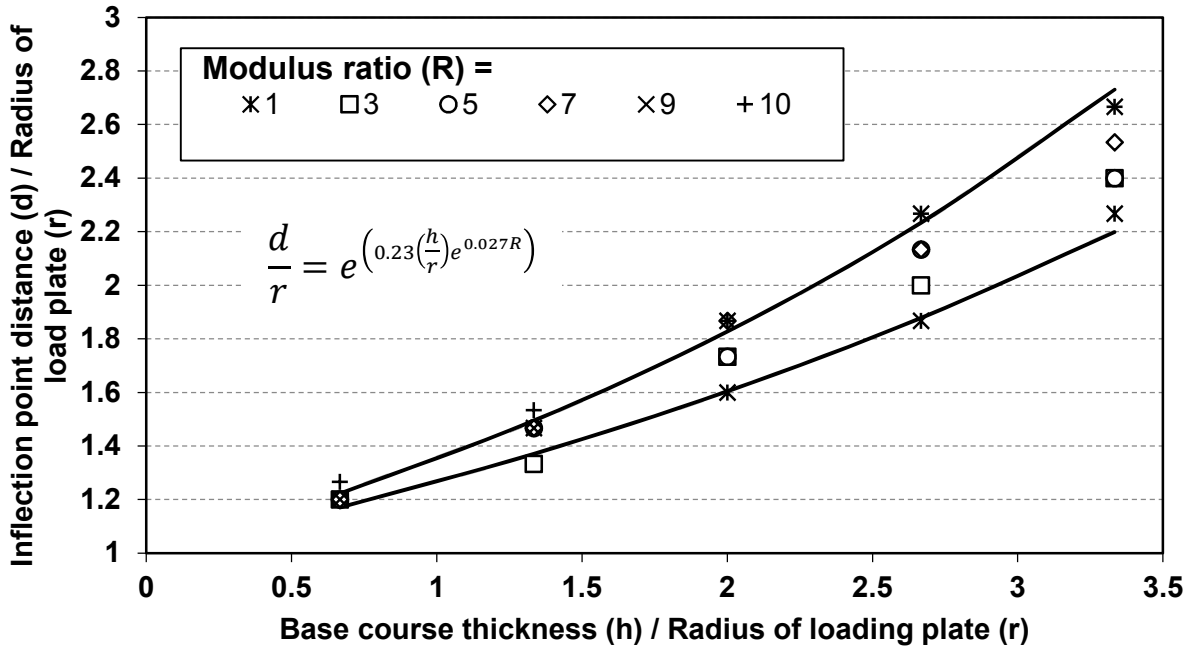

Figure A.5 Schematic diagram of the deformed geosynthetic element

Substituting the expression of the geosynthetic shape, **Equation A.22**, to the equation of the tensioned membrane effect, **Equation A.21**, the vertical support due to the tensioned membrane effect yields

$$Q(\rho) = \frac{4\,Eg\,hg\,\rho^2\,\delta^3\left(\left(1+\mu g\right)\xi^2 - 2\rho^2\right)\left(e^{-\frac{\rho^2}{\xi^2}}\right)^3}{\left(-1+\mu g^2\right)\xi^8} = Con1\cdot\rho^2\cdot e^{-\alpha\cdot\rho^2} - Con2\cdot\rho^4\cdot e^{-\alpha\cdot\rho^2} \quad \textbf{Equation A.23}$$

where $\frac{4\,Eg\cdot hh\cdot\delta^3\,(1+\mu)}{(-1+\mu^2)\,\xi^6} = Con1,\ \frac{3}{\xi^2} = \mathrm{a},\ \frac{8\,Eg\,hh\,\delta^3}{(-1+\mu^2)\,\xi^8} = Con2$.

As mentined in the previous section, the Hankel transform needs to be applied on each boundary and/or continuity condition to obtain a group of linear equations with the integral constants.

By applying the zero-order Hankel transform, the equilibrium of the vertical stresses at the interface yields

$$\frac{\mathrm{M3}_{layer1}-\mathrm{M3}_{layer2}}{mJ_0(m\rho)} = \int_0^\infty Q(\rho)mJ_0(m\rho)dm \qquad \textbf{Equation A.24}$$

The right hand of **Equation A.24** can be expressed in the form of **Equation A.25**.

$$\int_0^\infty \mathrm{x}^\mu \mathrm{e}^{-\alpha\mathrm{x}^2} \mathrm{J}_\nu(\beta\mathrm{x})\mathrm{dx} = \frac{\Gamma\left(\frac{1}{2}\nu + \frac{1}{2}\mu + \frac{1}{2}\right)}{\beta\alpha^{\frac{1}{2}\mu}\Gamma(\nu+1)} \exp\left(-\frac{\beta^2}{8\alpha}\right)\mathrm{M}_{\frac{1}{2}\mu,\frac{1}{2}\nu}\left(\frac{\beta^2}{4\alpha}\right) \qquad \textbf{Equation A.25}$$

where Γ represents the gamma function, M represents the Whittaker function, and J represents the Bessel function. After applying the Hankel transform, the continuity condition of the vertical stresses at the interface (i.g. **Equation A.24**) yields

$$\frac{\mathrm{M3}_{layer1}-\mathrm{M3}_{layer2}}{mJ_0(m\rho)} = Q(m) = \frac{1}{32}\frac{1}{a^{9/2}m}\left(\mathrm{e}^{-\frac{1}{4}\frac{m^2}{a}}\sqrt{\frac{m^2}{a}}\left(-4a^2m^2+16a^3\right)Con1 + Con2\left(m^4 - 16m^2a + 32a^2\right)\right)$$

Equation A.26

Confinement effect

The equilibrium of the geosynthetics in the radial direction is

$$\frac{\partial N_\rho}{\partial \rho} + \frac{N_\rho - N_\varphi}{\rho} = \Delta\tau(u) \qquad \textbf{Equation A.27}$$

Equation A.14 shows the strains of the geosynthetic due to the lateral displacement. According to the Hooke's law, the lateral confinement of the geosynthetic yields

$$\Delta\tau(\mathrm{u}) = \frac{\mathrm{E_g h_g}}{(1 - \mu_g^{\,2})}\left(\frac{\partial^2 \mathrm{u}}{\partial \rho^2} + \frac{1}{\rho}\frac{\partial \mathrm{u}}{\partial \rho} - \frac{\mathrm{u}}{\rho^2}\right) \qquad \textbf{Equation A.28}$$

The continuity condition based on the equilibrium of the shear stresses at the interface is

$$\tau_{\rho z1} - \tau_{\rho z2} = \Delta\tau(\mathrm{u}) \qquad \textbf{Equation A.29}$$

Substituting $\Delta\tau(u)$ into the continuity condition of **Equation A.28** and applying Hankel transform, the equation will be converted to a linear equation in terms of the integral constants.

In the process of the accumulation of the vertical permanent deformation, the radial permanent deformation can accumulate as well. The accumulated lateral permanent deformation of the base course at the interface applies an additional tension to the geosynthetic, in addition to the tension applied by the elastic deformation during the loading stage. Therefore, the confinement effect of the geosynthetic can be expressed as follows:

$$\Delta\tau(u^* + u) = \frac{E_g h_g}{(1-\mu_g^2)}\left(\frac{\partial^2 u^*}{\partial\rho^2} + \frac{1}{\rho}\frac{\partial u^*}{\partial\rho} - \frac{u^*}{\rho^2}\right) + \frac{E_g h_g}{(1-\mu_g^2)}\left(\frac{\partial^2 u}{\partial\rho^2} + \frac{1}{\rho}\frac{\partial u}{\partial\rho} - \frac{u}{\rho^2}\right)$$

Equation A.30

where u* represents the radial permanent deformation and u represents the radial elastic deformation. The term of u* can be considered as an external shear stress applied at the interface and u has to be compatible with the base course and subgrade layers at the interface. If considering the slip between the geogrid and soils, a reduction factor can be applied to the lateral permanent deformation.

Assume that there is no volume change at the bottom of the base course during the deformation. **Equation A.31** expresses the volume strain of soils.

$$\varepsilon_\rho^p + \varepsilon_z^p + \varepsilon_\varphi^p = 0 \qquad \textbf{Equation A.31}$$

$$\frac{\partial u^*}{\partial\rho} + \frac{u^*}{\rho} + \varepsilon_z^p = 0 \qquad \textbf{Equation A.32}$$

The relationship between u_p and ε_z^p can be obtained by solving this differential equation,

$$u^* = -\frac{1}{2}\rho\varepsilon_z^p \qquad \textbf{Equation A.33}$$

According to the current MEPDG soil damage model and the assumed deformation shape of the geogrid, the vertical permanent strain along the interface yields

$$\varepsilon_z^p = k\varepsilon_v^0 \frac{\varepsilon_0}{\varepsilon_{v0}} e^{-\frac{\rho^2}{\xi^2}-\left(\frac{\rho_{MEPDG}}{N}\right)^\beta} \qquad \textbf{Equation A.34}$$

The lateral permanent displacement can be expressed as

$$u^* = -\frac{1}{2}\rho\varepsilon_z^p = -\frac{1}{2}k\rho\varepsilon_v^0\frac{\varepsilon_0}{\varepsilon_{v0}}e^{-\frac{\rho^2}{\xi^2}-\left(\frac{\rho_{MEPDG}}{N}\right)^\beta} \qquad \textbf{Equation A.35}$$

Substituting u* into **Equation A.30**, the confinement effect due to both the permanent and elastic deformation of the geosynthetic can be obtained. Similarly, the Hankel transform needs to be applied.

After reorganizing the six equations obtained from the boundary condition and the continuity condition, the integral constants can be determined.

By substituting the identified integral constants into **Equation A.13**, the expressions of the stresses and displacements can be obtained in the form of the integration. The technique of the numerical integral needs to be adopted to determine stresses and strains.